

Borlaff et al.: The missing light of the Hubble Ultra Deep Field

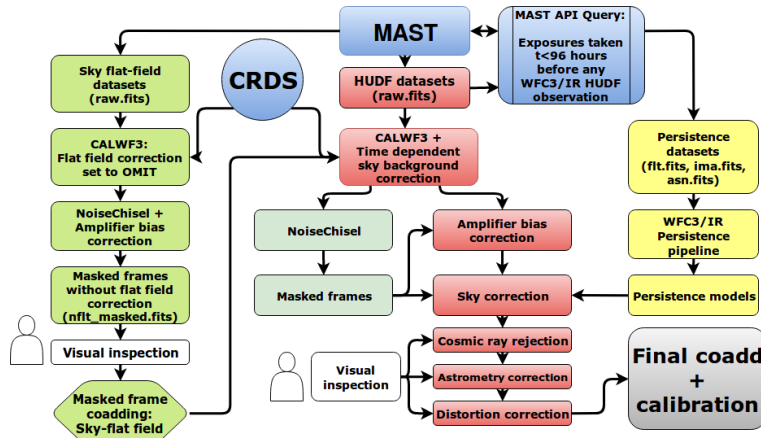


Fig. 1: An illustrative flowchart for the ABYSS HUDF reduction pipeline. Each major step in the pipeline discussed in the text is shown. The full process can be divided in three major branches: *Green steps*: sky flat field creation. *Yellow steps*: modelling of the extended persistence arrays. *Red steps*: main reduction of the HUDF exposures. *Blue steps*: required queries to the MAST or the CRDS database.

- Creation of sky flat fields for the four filters. This process is fully described in Sect. 2.4.
- Creation of a catalogue of all WFC3/IR datasets that may affect our mosaics (including calibration exposures) to generate a set of improved persistence models for each exposure of the HUDF. We detail this process in Sect. 2.5.
- Download and reduction of all the WFC3/IR datasets that include observations using the F105W, F125W, F140W and F160W filters on the HUDF.

For each individual exposure, we conduct the following steps. We refer the reader to the corresponding sections for a detailed description:

1. Preliminary calibration (bias, dark, flat field), including a time variation sky background correction (see Sects. 2.1 and 2.6).
2. Create masked frames for each exposure (Sects. 2.2 and 2.7).
3. Perform amplifier level correction (Sect. 2.3).
4. Perform sky correction for each readout, using the individual masks and robust statistical estimators (Sect. 2.8).
5. Perform cosmic rays rejection and alignment of each exposure. (Sect. 2.9).
6. Transformation of the corrected frames into a geometric distortion corrected frame, combination and calibration of the final mosaic (Sect. 2.10).

2.1. Initial data and preliminary calibration

For the present work, we started downloading all the individual exposures of the WFC3 (symbolized here by `raw.fits`)

within $r < 3 \text{ arcmin}$ radius of the original HUDF center coordinates ($\alpha = 3\text{h}32\text{m}39.0\text{s}$, $\delta = -27^\circ47'29.1''$, J2000). In order to do that, we make use of The Barbara A. Mikulski Archive for Space Telescopes (MAST)¹. MAST allows to perform queries with multiple constraints, such as sky-coordinates (α, δ), telescope, instrument, detector, filter, proposal ID and observation date. Given the large number of files to download, we used the MAST Python API². The MAST API allows for programmatic queries and implement them easily into any Python code. We included MAST API subroutines into our pipeline to automatically download required files from MAST when needed.

Subsequently, we made use of the HST Calibration Reference Data System³ (CRDS, Greenfield & Miller 2016) to download the best reference files available for each individual exposure of the HUDF. The CRDS is publicly available and can be installed as part of AstroConda⁴. For HST, CRDS has a command line tool that assigns and automatically downloads the best reference files to the FITS headers of the `raw.fits` files. We processed all our `raw.fits` files using the Space Telescope Science Data Analysis System (STSDAS) task `calwf3`, `calwf3` is available as part of the `stsci_python` package on AstroConda, and it corrects for instrumental effects and generates calibrated

¹ MAST is managed by Space Telescope Science Institute (STScI) and is publicly available at <https://mast.stsci.edu/portal/Mashup/Clients/Mast/Portal.html>

² MAST Python API: <https://mast.stsci.edu/api/v0/> ³ HST Calibration Reference Data System: <https://hst-crds.stsci.edu/> ⁴ AstroConda is a free Conda channel maintained by the Space Telescope Science Institute (STScI). It provides tools and utilities required to process and analyse data from the Hubble Space Telescope (HST), James Webb Space Telescope (JWST), and others: <http://AstroConda.readthedocs.io/>

Este documento incorpora firma electrónica, y es copia auténtica de un documento electrónico archivado por la ULL según la Ley 39/2015.
Su autenticidad puede ser contrastada en la siguiente dirección <https://sede.ull.es/validacion/>

Identificador del documento: 1630219

Código de verificación: NYPyuzSi

Firmado por: ALEJANDRO SERRANO BORLAFF
 UNIVERSIDAD DE LA LAGUNA

Fecha: 26/10/2018 14:33:01

Juan Esteban Beckman Abramson
 UNIVERSIDAD DE LA LAGUNA

26/10/2018 14:36:58

MARIA DEL CARMEN ELICHE MORAL
 UNIVERSIDAD DE LA LAGUNA

26/10/2018 15:46:09

JOAN FONT SERRA
 UNIVERSIDAD DE LA LAGUNA

26/10/2018 18:46:53

A&A proofs: manuscript no. output

frames. In addition, `calwf3` can process multiple readouts for the same exposure to create improved data products.

For WFC3/IR observations, it is possible to sample the signal multiple times as an exposure accumulates, before the end of the exposure. This allows to 1) to record the signal of a pixel before it saturates, 2) to perform a better cosmic-ray rejection and 3) to reduce the net effective read noise. This observation mode is named `MULTIACCUM`, and is the default observation mode for WFC3/IR. Each `.raw.fits` file contains the information of each readout (up to 16) of the chip during a certain exposure. The individual processing steps that `calwf3` performs for each readout are:

1. Flagging of known bad pixels in the data quality (DQ) array.
2. Identification of pixels in the initial read that contain detectable source signal.
3. Subtraction of bias drifts using the reference pixels.
4. Subtraction of the zeroth (first) read.
5. Estimation of the noise model for each pixel and record in the error (ERR) array.
6. Photometric non-linearity and saturated pixels correction.
7. Subtraction of dark image.
8. Calculation of the photometric header keyword values for flux conversion.
9. Conversion of the data from counts to count rates.

After this, `calwf3` uses each readout of the `MULTIACCUM` mode to create a single image for each individual exposure. This is done by analysing the count differences between readout as a function of time (up-the-ramp fitting). This new array represents the best-fit count rate for each pixel. Finally, the pipeline performs flat fielding and gain conversion (transforming from counts to count-rates). The final result is an `.flt.fits` file, which contains the science best-fit count-rate array (SCI), the error array (ERR), a data-quality array (which flags bad-pixels and cosmic rays), the number of samples (SAMP) and integration time (TIME) arrays. Each one of the `calwf3` steps can be omitted or performed by switching their corresponding keywords in the headers of the `.raw.fits` files of each exposure. For those frames that are going to be used here to calculate our dedicated sky-flat, we set the corresponding keyword (`FLATCORR`) to "OMIT" prior to their processing.

2.2. Image masking

In order to create the sky flat field models, estimate the sky level of each exposure and obtain the final catalogue, we require an accurate masking of the individual sources in the images. For this task we used Gnuastro's¹ program (version 0.5) for detection and segmentation: NoiseChisel (Akhlaghi & Ichikawa 2015). NoiseChisel is a recently developed free software to detect signal in astronomical images based on erosion of pixels. This method is non-parametric, allowing to efficiently detect astronomical objects with irregular morphologies that are immersed in noise. In addition to this, NoiseChisel algorithm is based on the properties of the image noise (not only on those of the signal dominated pixels) reducing the input from the user and thus it is extremely robust against the sky level value or the properties of the sources to mask, making it an excellent choice for highly different exposures, such as the ones analysed in this paper. NoiseChisel accepts FITS files as input, and returns a multi-extension FITS file that contains: 1) the input image, 2)

¹ GNU Astronomy Utilities (ascl.net/1801.009) project is part of the Free Software Foundation and is freely available at: <https://www.gnu.org/software/gnuastro/>

Article number, page 4 of 36

the segmentation map with the detection labels for each object, 3) a secondary segmentation map for the clumps inside each detection, 4) NoiseChisel estimation of the final sky value on each pixel, and 5) the standard deviation for each pixel. The final results are based on version 0.5 of Gnuastro. The masking of each individual exposure is performed as follows:

1. In order to properly detect sources in the input images with NoiseChisel they have to be flat field corrected. Otherwise, we would not have a similar sensitivity across the detector, and our results would be biased. We perform preliminary calibration of the `.raw.fits` files, including flat field calibration. During the creation of our own sky flat fields, we have to correct the images before masking. For this step, we use the official MAST flat fields. After the sky flat fields are created, if the input image is a HUDF exposure, we use our own sky-flat fields.
2. We create the segmentation maps for each `.flt.fits` image using NoiseChisel with default configuration (tile size equal to 50×50 pixels).
3. If the images are being masked for the generation of the sky flat fields, we multiply back the images by its corresponding official MAST flat fields. The result of this process is a properly masked flat field uncorrected exposure.

In Fig. 2 we show an example of the masking process of a F160W exposure, included in the HUDF field (`ib5x2elbq`, PID 11563). The top left panel represents the `.flt.fits` file after preliminary calibration through `calwf3`, but before flat field correction (see Sect. 2.1). The top right panel shows the same `.flt.fits` file after flat field correction. After this step, we analyse the flat field corrected `.flt.fits` image with NoiseChisel, which produces a segmentation map for each exposure. We identify all the pixels that are included as part of a source obtaining a masked, flat field uncorrected `.flt.fits` file, ready to be combined for the creation of a sky flat field. We show this final masked frame in the bottom-left panel of Fig. 2. In order to illustrate the accuracy of the segmentation map results, we compare in the bottom panels the NoiseChisel mask with the `.flt.fits` image convolved by a Gaussian kernel with $\sigma = 5$ pixels. It is clearly visible that this process accurately masks objects with very different ranges of size, even if part of them (or the whole object) is not visible in the non-convolved frame. We refer the reader to Sect. 2.8 for a systematic benchmark analysis of the masking procedure effect on the sky background subtraction and its comparison with other methods.

2.3. Amplifier relative gain correction

The WFC3/IR detector contains 1024×1024 pixels, which are divided into four quadrants of 512×512 pixels. There is a border of 5 non-illuminated pixels around the edges of the detector, which are used to provide constant-voltage reference values for the detector. Due to this, the light exposed area of the detector includes 1014×1014 , divided in four 507×507 pixels. Although the default pipeline corrects for differences in gain between the four different sections of the WFC3/IR detector, it is common to see residual differences in the flat field corrected images and especially in the combined mosaics. The amplitude and sign of these differences between amplifiers may vary from dataset to dataset, and can produce significant effects in both the final images and the sky flat fields.

In order to correct for this effect we have to calculate the median differences in flux between each section of the chip and

Este documento incorpora firma electrónica, y es copia auténtica de un documento electrónico archivado por la ULL según la Ley 39/2015.
Su autenticidad puede ser contrastada en la siguiente dirección <https://sede.ull.es/validacion/>

Identificador del documento: 1630219

Código de verificación: NYPyuzSi

Fecha: 26/10/2018 14:33:01

Firmado por: ALEJANDRO SERRANO BORLAFF
 UNIVERSIDAD DE LA LAGUNA

Juan Esteban Beckman Abramson
 UNIVERSIDAD DE LA LAGUNA

MARIA DEL CARMEN ELICHE MORAL
 UNIVERSIDAD DE LA LAGUNA

JOAN FONT SERRA
 UNIVERSIDAD DE LA LAGUNA

26/10/2018 14:36:58

26/10/2018 15:46:09

26/10/2018 18:46:53

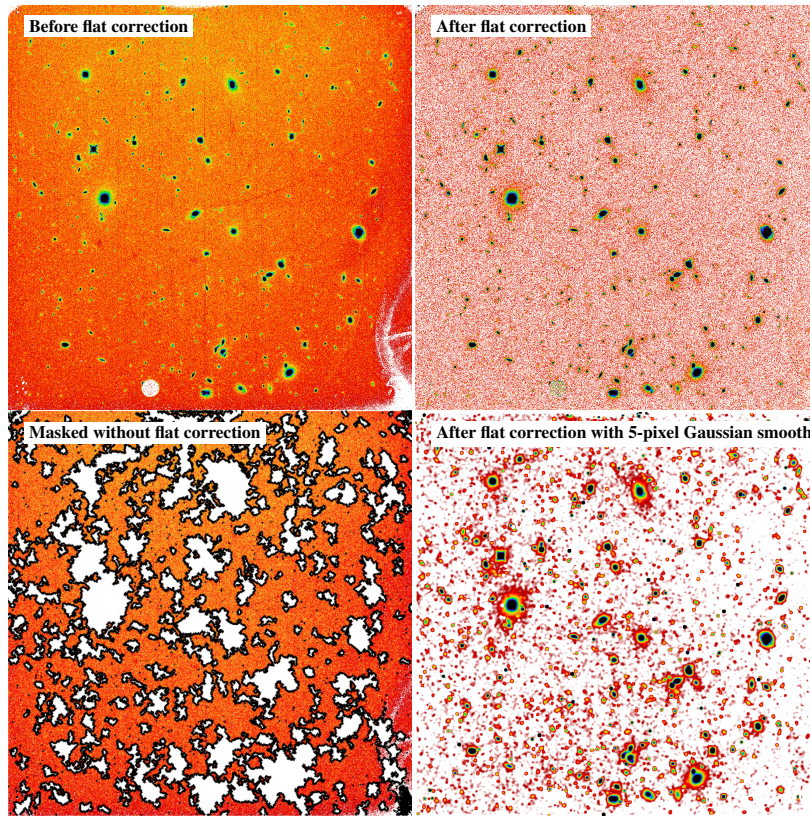


Fig. 2: Top left: Pre-calibrated frame, without flat field correction. Top right: Pre-calibrated frame, with flat field correction applied. Bottom left: Masked frame without flat field correction. Bottom right: Flat field corrected frame with Gaussian smoothing. Notice that NoiseChisel (Akhlaghi & Ichikawa 2015) efficiently detects objects with very different shapes and sizes, masking the outskirts and diffuse regions that are barely visible even in the convolved frame.

compensate them. We cannot simply use the median values for the full area covered by each section, because that would result in a wrong estimate of the median bias if there are large scale gradients across the detector. Instead, we calculate the ratios between columns or rows of pixels at equal distances to the frontier between chips. Then we estimate the weighted median of the resulting array of ratios, where the weights are equal to the inverse distance of each pixel to the frontier of the chip. By doing this, we ensure that the differences between pixels which contribute the most are the closest ones to the frontier, but we still make use

of all the information available in the image. We set as reference the A section of the chip (top left) and correct the remaining sections (*B*, *C* and *D*) to it. The weighted sky-levels for each frontier between chips are labelled with two letters, being the first letter the one to which the pixels of the sample belong (see Fig. 3). The correction factors are:

$$\delta_{AB} = \left\langle \frac{\overrightarrow{AB}}{\overrightarrow{BA}} \right\rangle, \quad (1)$$

Article number, page 5 of 36

Este documento incorpora firma electrónica, y es copia auténtica de un documento electrónico archivado por la ULL según la Ley 39/2015.
Su autenticidad puede ser contrastada en la siguiente dirección <https://sede.ul.es/validacion/>

Identificador del documento: 1630219

Código de verificación: NYPyuzSi

Firmado por: ALEJANDRO SERRANO BORLAFF
 UNIVERSIDAD DE LA LAGUNA

Fecha: 26/10/2018 14:33:01

Juan Esteban Beckman Abramson
 UNIVERSIDAD DE LA LAGUNA

26/10/2018 14:36:58

MARIA DEL CARMEN ELICHE MORAL
 UNIVERSIDAD DE LA LAGUNA

26/10/2018 15:46:09

JOAN FONT SERRA
 UNIVERSIDAD DE LA LAGUNA

26/10/2018 18:46:53

A&A proofs: manuscript no. output

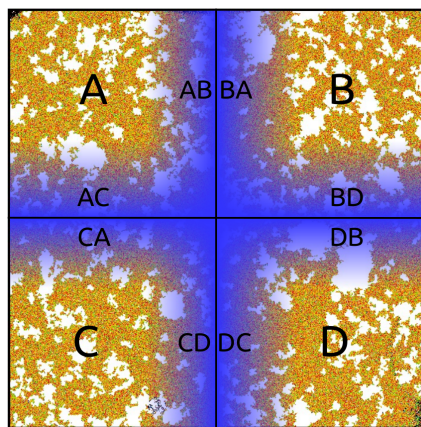


Fig. 3: Amplifier gain correction diagram. We label each one of the four 507×507 pixel sections of the WFC3/IR detector as A, B, C, D (see figure). We represent with a blue transparent gradient the weights (bluer represents higher weights) applied to the corresponding pixels of each region, labelled accordingly. The white regions in the background are masked pixels, either because they are part of a light source or are affected by persistence. We do not include those pixels in the amplifier gain correction estimation.

$$\delta AC = \langle \frac{\overrightarrow{AC}}{\overleftarrow{CA}} \rangle, \quad (2)$$

$$\delta CD = \langle \frac{\overrightarrow{CD}}{\overleftarrow{DC}} \rangle, \quad (3)$$

$$\delta BD = \langle \frac{\overrightarrow{BD}}{\overleftarrow{DB}} \rangle, \quad (4)$$

where the \rightarrow and \leftarrow mean the original and axis reversed arrays, respectively, and the $\langle \rangle$ represents the weighted mean by the distance of each pixel to the frontier between chips. By using these, we can calculate the δAD correction factor as follows:

$$\delta AD1 = \delta AB \cdot \delta BD, \quad (5)$$

$$\delta AD2 = \delta AC \cdot \delta CD, \quad (6)$$

$$\delta AD = \frac{\delta AD1 + \delta AD2}{2}, \quad (7)$$

In addition, as in the case of sky-correction, we must avoid contamination by the objects in the field of view and persistence. In order to avoid such effects, we masked all the pixels flagged as part of sources by NoiseChisel (see Sect. 2.2). Additionally, for the HUDF field images, we also flagged all those pixels affected by persistence according to our custom-improved models (see Sect. 2.5). Finally, we applied this amplifier gain correction to all the exposures used in this study before the final sky-subtraction.

Article number, page 6 of 36

2.4. Sky flat fielding

In order to measure the relative sensitivity of the pixels of a detector (flat field), the optimal process would be to observe a uniform external source of light. Although this is certainly not possible in most cases, there are several strategies to reproduce these conditions or to compensate for any possible inhomogeneities in the illumination. In ground-based observations, the combination of several out-of-focus dome images is the easiest way to estimate the flat field. Observations of the twilight sky at the start and the end of the night (twilight flats) are a reasonable alternative to avoid the possible inhomogeneities and gradients caused by the dome of the telescope. However, neither dome flats nor twilight flats are free of gradients due to non-perfect flat illumination, and the latter suffer from time variation of the sky background level. In space, twilight flats are possible using dark Earth limb observations (see e.g., HST Cycle 17 WFC3 calibration proposal 11917) or the moonlit illuminated earth (Bohlin et al. 2008). For WFC3, high signal-to noise ground-based flat fields (Bushouse 2008) were generated prior to launch in the CASTLE HST simulator (hereafter CASTLE LP-flats). Nevertheless, the CASTLE simulator is not a perfect replica of the optical path and conditions of HST. Observations of the star clusters Omega-Cen and 47 Tuc (proposals CAL-11453 and CAL-11928) demonstrated that the CASTLE LP-flats were not able to correct the large scale structure in WFC3/IR channel (Pirzkal et al. 2011).

An alternative to these strategies is to take advantage of the observations previously accumulated. Sky background in the near IR is high enough, even in space, to use it as a uniform source of light. However, diffuse objects and the extended point spread function can introduce severe biases in the median images. It is because of this, that careful masking of any source in the field-of-view is necessary to avoid contamination in the final calibration images. In addition to this, not all the images are suitable for this analysis, because the flux of the sky background is relatively low ($\sim 0.3 - 1.0 \text{ e}^- \text{s}^{-1} \text{pix}^{-1}$, see Pirzkal et al. 2011). Thus, creating accurate sky-flat fields requires the combination of a large number of exposures. The standard method to create sky-flats from observations is to calculate the median of the masked science images. In ground-based observations, a master-flat per night is created by using the corresponding normalised science images of that night. The reason of this is to avoid any unwanted effects due to slight changes of focus, weather conditions, or vignetting. The high stability of space telescopes compared to the ground-based ones permits the making of sky-flat fields using images that have been taken over longer time periods. Moreover, the use of sky-flat fields have the advantage that they are measuring the relative sensitivity between pixels at the same intensity level of the images that have to be corrected. This accounts for any possible spatial differences in the linearity across the detector as a function of the input intensity.

In Pirzkal et al. (2011), the authors used the observations taken between 2009 and 2010 with WFC3/IR to create a second order correction to the CASTLE LP-flats (delta sky flat or SD-flats). In order to do that, they first identified a large number of datasets with exposure times longer than 300s. Secondly, they aggressively masked all the sources in the images with SExtractor (Bertin & Arnouts 1996) in the field of view. This step was repeated for several hundreds of images per filter. Finally the masks were normalised and combined to the CASTLE-LP flats, creating the new SD-flats. Although the SD-flats for the F160W included nearly a thousand masked images, some of the other filters did not have enough data to create a reliable flat field,

Este documento incorpora firma electrónica, y es copia auténtica de un documento electrónico archivado por la ULL según la Ley 39/2015.
Su autenticidad puede ser contrastada en la siguiente dirección <https://sede.ull.es/validacion/>

Identificador del documento: 1630219

Código de verificación: NYPyuzSi

Fecha: 26/10/2018 14:33:01

Firmado por: ALEJANDRO SERRANO BORLAFF
 UNIVERSIDAD DE LA LAGUNA

Juan Esteban Beckman Abramson
 UNIVERSIDAD DE LA LAGUNA

MARIA DEL CARMEN ELICHE MORAL
 UNIVERSIDAD DE LA LAGUNA

JOAN FONT SERRA
 UNIVERSIDAD DE LA LAGUNA

26/10/2018 14:36:58

26/10/2018 15:46:09

26/10/2018 18:46:53

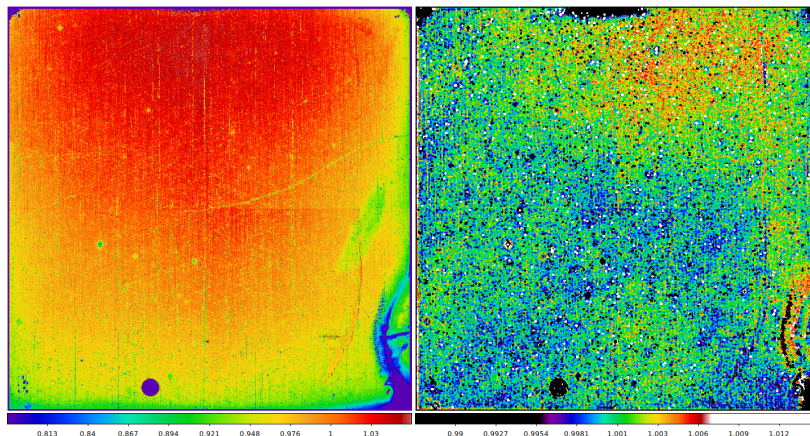


Fig. 4: Sky flat field analysis for the F160W filter. *Left panel:* Absolute sky flat field measured for the June 2009 to July 2013 period, using the datasets corresponding to the proposal IDs listed in Table 1. *Right panel:* Ratio of our sky flat field for the F160W to its corresponding MAST SD flat field uc721145i. Notice the different colour scale, spanning only a $\sim 1\%$ for the flat field ratio panel. The right panel was smoothed with a 3 pixel wide Gaussian kernel to enhance the differences between different regions.

which was the case for F105W, F110W and F140W, where only ~ 100 datasets were used. For these filters, the signal-to-noise ratio was too low and the masking process left no available data in some regions of the detector, creating holes were the corresponding SD-flat had no data. Finally, in order to reach a reliable final SD-flat solution, the authors opted to combine the ~ 2000 datasets from all the filters into one SD-flat (grey SD-flat, hereafter). In addition to this, they smoothed the grey SD-flat by using a $\sigma = 10$ pixel kernel before combination with the CASTLE LP-flats. The authors did not find any significant dependence on the filter or variation of the flat fields with time between 2009 and 2010. They successfully tested the improved flat field with 32 F160W datasets from the HUDF proposal 11563, removing a large scale cross-like structure in the background. These combined CASTLE LP-flats + SD-flat fields were included into the calibration database system in December 7th, 2010, until present date.

In this paper, we follow a similar procedure as the presented in Pirzkal et al. (2011). We generate a sky flat field per filter by combination of exposures between 55000 (June 2009) to 56500 (July 2013). Additionally, we create a second flat for the F105W filter considering observations between 56500 and 58000 (April 2017). Due to the small size of the dithering pattern, and the fact that all images were taken with very similar rotation angles, we cannot create a sky-flat field just by using the exposures from the HUDF observation programs. To tackle this problem, we selected the deep observations as the AEGIS, COSMOS, GOODS-N, GOODS-S, and UDS fields. We also included multiple exposures from other fields that were taken in the 96 hours before the HUDF exposures. We list the amount of exposures per filter,

time-period, and the proposal IDs of all the images used for each flat field in Table 1.

In Fig. 4 we present an example of our results. In the left panel we show our absolute sky-flat field for the F160W filter, according to the robust median of the masked datasets from Table 1. In the right panel we show the ratio between our sky flat field and its corresponding SD-flat from MAST. Notice that both panels have different colour scales, and that the right panel has been convolved with a 3 pixel wide Gaussian kernel in order to enhance the differences between flats. We do not find differences larger than $\sim 1\%$, but there is a significant coherent large scale variation, in addition to residuals on the bottom-right corner of the detector (wagon-wheel).

2.5. Persistence correction

A known effect that affects HgCdTe IR array detectors (as is the case of the WFC3/IR) is persistence. Persistence shows up as an afterglow on the pixels that were exposed to a bright source of light in a previous exposure. This charges arise from imperfections in the photo-diodes of IR detectors (Smith et al. 2008a,b). Neither non-destructive read-out nor resets can change significantly the rate at which this charge is released. These bright sources then re-appear in the following exposures as ghost images in the same regions of the detector. The intensity of this effect decays with time and eventually becomes negligible. Even so, persistence is an important effect to take into account as it may create false detections in science images. The effect of persistence and thus the accuracy of its correction becomes more challenging as we move towards lower surface brightness ranges.

Article number, page 7 of 36

Este documento incorpora firma electrónica, y es copia auténtica de un documento electrónico archivado por la ULL según la Ley 39/2015.
Su autenticidad puede ser contrastada en la siguiente dirección <https://sede.ull.es/validacion/>

Identificador del documento: 1630219

Código de verificación: NYPyuzSi

Firmado por: ALEJANDRO SERRANO BORLAFF
UNIVERSIDAD DE LA LAGUNA

Fecha: 26/10/2018 14:33:01

Juan Esteban Beckman Abramson
UNIVERSIDAD DE LA LAGUNA

26/10/2018 14:36:58

MARIA DEL CARMEN ELICHE MORAL
UNIVERSIDAD DE LA LAGUNA

26/10/2018 15:46:09

JOAN FONT SERRA
UNIVERSIDAD DE LA LAGUNA

26/10/2018 18:46:53

A&A proofs: manuscript no. output

Sky-flat (1)	Period (2)	No. of exposures (3)	Proposal IDs (4)
F105W A	55000 - 56500	719	11563, 11584, 11738, 12060, 12065, 12067, 12068, 12069, 12099, 12100, 12101, 12102, 12103, 12104, 12184, 12286, 12442, 12451, 12452, 12453, 12454, 12455, 12456, 12457, 12458, 12459, 12460, 12461, 12496, 12498, 12553, 12590, 12787, 12788, 12789, 12790, 12791, 12949, 13063
F105W B	56500 - 58000	747	13386, 13420, 13459, 13495, 13496, 13641, 13677, 13687, 13718, 13767, 13779, 13790, 13792, 14037, 14096, 14122, 14227, 14327, 14808
F125W	55000 - 56500	1811	11144, 11149, 11189, 11359, 11520, 11557, 11563, 11678, 11700, 11702, 12025, 12028, 12036, 12060, 12061, 12062, 12063, 12064, 12065, 12066, 12067, 12068, 12069, 12099, 12100, 12101, 12102, 12103, 12265, 12286, 12329, 12440, 12443, 12444, 12445, 12451, 12452, 12453, 12454, 12459, 12460, 12461, 12572, 12590, 12616, 12960, 13063
F140W	55000 - 56500	875	11359, 11600, 11696, 12067, 12068, 12099, 12100, 12101, 12102, 12103, 12166, 12177, 12190, 12203, 12217, 12328, 12330, 12452, 12458, 12459, 12461, 12471, 12498, 12544, 12547, 12568, 12726, 12896, 13063
F160W	55000 - 56500	1727	11142, 11149, 11189, 11359, 11520, 11563, 11584, 11647, 11663, 11694, 11696, 11700, 11702, 11735, 11738, 11838, 11840, 12028, 12036, 12055, 12060, 12061, 12062, 12063, 12064, 12065, 12066, 12067, 12068, 12069, 12072, 12075, 12099, 12100, 12101, 12102, 12104, 12167, 12194, 12195, 12197, 12224, 12265, 12267, 12283, 12286, 12292, 12307, 12329, 12378, 12440, 12443, 12444, 12445, 12447, 12451, 12452, 12453, 12454, 12459, 12461, 12498, 12502, 12590, 12613, 12616, 12686, 12709, 12764, 12866, 12990, 13063

Table 1: Summary of the exposures used for the sky flat field analysis. Columns: 1) Flat field identifier. 2) Exposure date limits used for the selection of the datasets for each flat field. 3) Number of exposures used for each flat field. 4) Proposal IDs of the exposures used. We remark that not all the images of a given proposal ID were used in its corresponding flat field. A careful visual inspection of each one of the images was carried out by the authors, before image combination.

Persistence is an intrinsic effect of the WFC3/IR detector and thus it cannot be avoided, but it can be partially corrected afterwards. STScI MAST WFC3 Persistence Project¹ provides the necessary tools to check if a certain exposure was affected by persistence and a complete set of models to correct the effects. The current method of persistence correction of WFC3/IR consists in modeling the number of electrons that would be created by persistence in each pixel by all the previous exposures (up to a certain time) that were taken before the one to correct (Long et al. 2012). These models are pre-calculated for all WFC3/IR exposures and publicly available through MAST. Nevertheless, these models only take into account the exposures that were taken up to 16 hours before for the creation of the persistence model (Dr. Knox Long, private communication).

In Long et al. (2015) the authors published an improved pipeline to create persistence models for WFC3/IR. The initial models predicted persistence only based on the observed flux and the time between exposures (Long et al. 2012). Nevertheless, in Long et al. (2013a,b), the authors carried out a set of experiments where they demonstrated that the persistence depended also with the amount of exposures taken and the time that a pixel remained filled with charge. Based on these findings, the authors developed a more accurate prediction of persistence in the IR channel of WFC3. This new pipeline was included into the set of software tools used to estimate the persistence in all WFC3/IR images and also was made publicly available².

In this paper, we make use of the last update to date (git commit hash b0b9cbeaf7, 26 Jan 2016) of the prediction software made by STScI in order to create a set of dedicated persistence

models for each individual exposure of the HUDF. We increase the lookback time from 16 hours to 96 hours to take into account the longest time that our computer resources permit to create the persistence models, using the default observational "A-gamma" model (Long et al. 2015). To do that, we downloaded all the exposures taken with WFC3/IR 96 hours before each exposure of the HUDF. Finally, we run the persistence pipeline for each exposure in the HUDF field. The software creates the persistence models and automatically stores them in their corresponding FITS files.

We show two examples of the improvement of the persistence models in Fig. 5. The left column shows the improved persistence models for the exposures of the HUDF `iB5x22b8q` and `iCxt25byq`. The right column shows their corresponding MAST official persistence models taking into account the previous 16 hours. In the first case `iB5x22b8q`, the persistence model (top-left panel) is dominated by a large gradient produced by a set of calibration observations (Cycle 17, CAL/WFC3 category, 11915 - IR Internal Flat Fields, PI: Bryan Hilbert³). These observations were meant to create a new set of flat fields for WFC3/IR using the internal tungsten flat field lamp to illuminate the detector. As a consequence of this, the camera was flooded with persistence just 18 hours before the observations of the HUDF with the F105W filter. Unfortunately, the results of the proposal 11915 were never published (Ben Sunquist, WFC3 Help Desk, private communication). Many of the HUDF exposures of the F105W filter were left unusable because of this calibration program, since we are interested on the lowest surface brightness limit, and we cannot rely on the persistence correction to fully correct the images. This effect does not appear in the official

¹ WFC3 Persistence Project: <https://archive.stsci.edu/prepds/persist/>

² STScI Persistence repository: <https://github.com/klong/Persistence/wiki>

³ A detailed overview of proposal 11915 can be found in: <http://www.stsci.edu/hst/phase2-public/11915.pdf>

Firmado por: ALEJANDRO SERRANO BORLAFF <i>UNIVERSIDAD DE LA LAGUNA</i>	Fecha: 26/10/2018 14:33:01
Juan Esteban Beckman Abramson <i>UNIVERSIDAD DE LA LAGUNA</i>	26/10/2018 14:36:58
MARIA DEL CARMEN ELICHE MORAL <i>UNIVERSIDAD DE LA LAGUNA</i>	26/10/2018 15:46:09
JOAN FONT SERRA <i>UNIVERSIDAD DE LA LAGUNA</i>	26/10/2018 18:46:53

Borlaff et al.: The missing light of the Hubble Ultra Deep Field

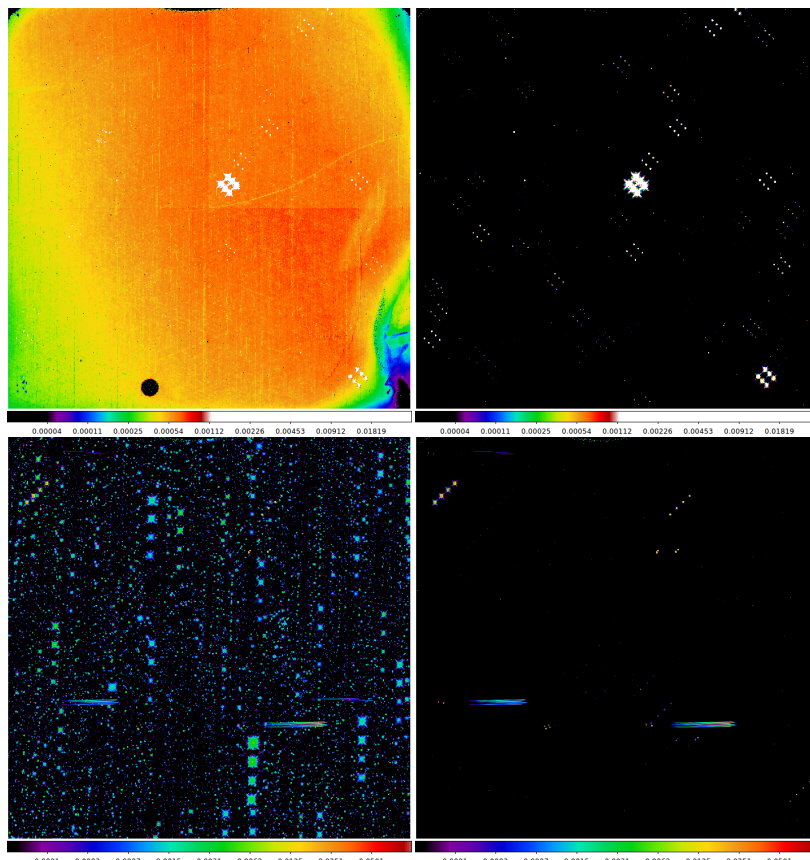


Fig. 5: Comparison between the WFC3/IR persistence models calculated taking into account 96 hours of previous observations (left column) and the persistence models available at MAST, with a limit of 16 hours of lookback time (right column). *Top panels:* Persistence models for dataset `ib5rx22b8q`. *Bottom panels:* Persistence models for dataset `ictxt25byq`. The images corresponding to the same dataset are at the same colour scale. Note on the top left panel a background of persistence covering the complete field of view caused by the flat calibration lamp in the previous hours to the observation of the HUDF, not detected on the persistence model available at MAST (top right panel).

MAST persistence arrays (top-right panel), due to the 16 hours limit for the lookback calculation of persistence, and thus, were not taken into account in the previous versions of the HUDF.

Nevertheless, large scale gradients can hardly affect the results for high- z , unresolved objects. In that case, the observers

must pay more attention to flag any point-like source of light that may be caused by persistence. In the bottom panels of Fig. 5 we show another example (`ictxt25byq`) of the improvement of our persistence models. We identify two major causes of the persistence contamination, proposals 14074 (Opening the Window

Article number, page 9 of 36

Este documento incorpora firma electrónica, y es copia auténtica de un documento electrónico archivado por la ULL según la Ley 39/2015.
Su autenticidad puede ser contrastada en la siguiente dirección <https://sede.ull.es/validacion/>

Identificador del documento: 1630219

Código de verificación: NYPyuzSi

Firmado por: ALEJANDRO SERRANO BORLAFF
 UNIVERSIDAD DE LA LAGUNA

Fecha: 26/10/2018 14:33:01

Juan Esteban Beckman Abramson
 UNIVERSIDAD DE LA LAGUNA

26/10/2018 14:36:58

MARIA DEL CARMEN ELICHE MORAL
 UNIVERSIDAD DE LA LAGUNA

26/10/2018 15:46:09

JOAN FONT SERRA
 UNIVERSIDAD DE LA LAGUNA

26/10/2018 18:46:53

A&A proofs: manuscript no. output

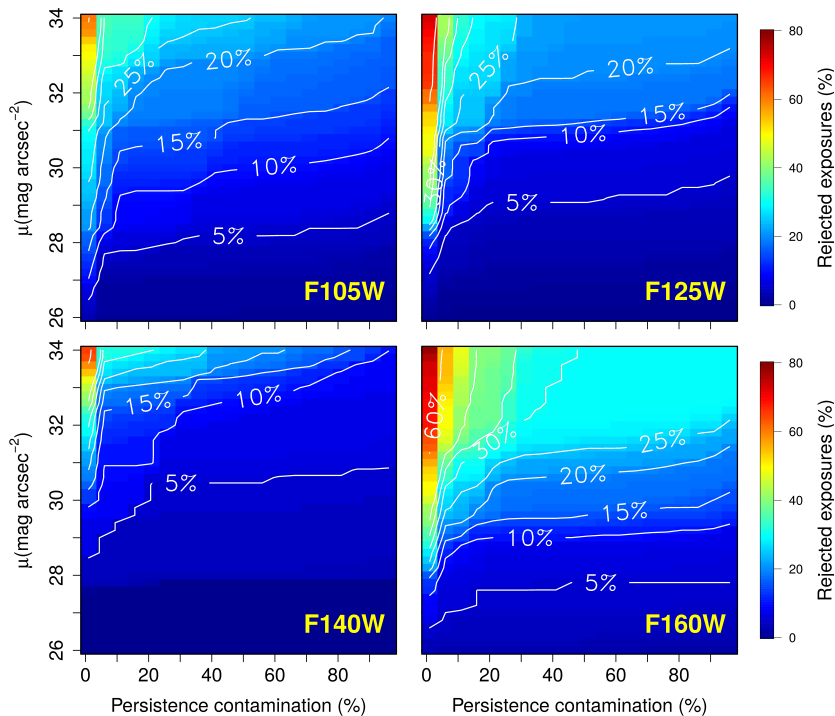


Fig. 6: Analysis of persistence contamination on the WFC3/IR HUDF exposures. In colour bins and white labelled contours, we represent the fraction of exposures that present a certain level of surface brightness contamination by persistence or higher (vertical axis) as a function of the fraction of the total amount of pixels that are affected (horizontal axis), for the F105W (top left), F125W (top right), F140W (bottom left) and F160W (bottom right) bands.

on Galaxy Assembly: Ages and Structural Parameters of Globular Clusters Towards the Galactic Bulge, PI: Roger Cohen) and the WFC3/G102 grism observations of proposal 14227 (Cycle 23 proposal 14227: The CANDELS Lyman-alpha Emission At Reionization Experiment, PI: Casey Papovich), which ended just ~ 3 minutes before the start the HUDF exposure `icx25byq`. The former one (which ended 40 hours before the HUDF exposure, hence, was not taken into account for persistence) is responsible for the star-like sources across the detector, and the latter one for the two elongated sources.

In Fig. 6 we analyse the persistence contamination level of the WFC3/IR exposures of the HUDF. We measured the amount of pixels that were affected by persistence as a function of the surface brightness contamination that this effect creates. The expected surface brightness level created only by persistence is estimated using the persistence flux predicted by the models.

We then determine the fraction of each image that is affected as a function of the surface brightness persistence contamination level. We found that the F160W and F105W are the filters most affected by this issue. For F160W band, $\sim 17\%$ of the images present at least half of the image contaminated at surface brightness of $\mu = 30 \text{ mag arcsec}^{-2}$. The filter less affected by persistence is F140W, with less than $\sim 5\%$ of the images with that level of contamination on at least half of the image. Given that the persistence models are an approximation to the real level of persistence, and they do not fully correct for all the contamination, the general recommendation by STScI is to use them to correct the images and flag those pixels affected up to a certain level, that has to be chosen depending on the science target. After correcting all the images with our improved persistence models, we chose a conservative compromise between losing exposure time and possible contamination by the persistence residuals. We

Article number, page 10 of 36

Este documento incorpora firma electrónica, y es copia auténtica de un documento electrónico archivado por la ULL según la Ley 39/2015.
Su autenticidad puede ser contrastada en la siguiente dirección <https://sede.ull.es/validacion/>

Identificador del documento: 1630219

Código de verificación: NYPyuzSi

Firmado por: ALEJANDRO SERRANO BORLAFF
 UNIVERSIDAD DE LA LAGUNA

Fecha: 26/10/2018 14:33:01

Juan Esteban Beckman Abramson
 UNIVERSIDAD DE LA LAGUNA

26/10/2018 14:36:58

MARIA DEL CARMEN ELICHE MORAL
 UNIVERSIDAD DE LA LAGUNA

26/10/2018 15:46:09

JOAN FONT SERRA
 UNIVERSIDAD DE LA LAGUNA

26/10/2018 18:46:53

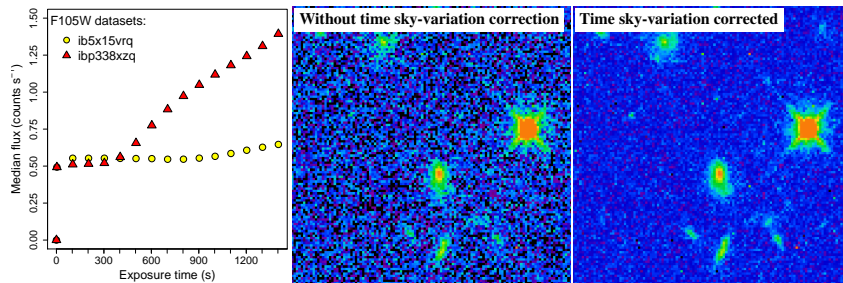


Fig. 7: Example of the effects of time varying sky background in two different datasets of WFC3/IR in the F105W band. *Left panel:* Median background flux of ibp5x15vrq (yellow circles) and ibp338xzq (red triangles). While the dataset ibp5x15vrq shows a nearly constant flux on all the different readouts ($\sim 0.50 \text{ counts s}^{-1}$), ibp338xzq is clearly affected by time variation of the sky background, increasing from $\sim 0.50 \text{ counts s}^{-1}$ to $\sim 1.3 \text{ counts s}^{-1}$ after 400s from the start of the exposure. *Middle panel:* Sky-corrected ibp338xzq `flt.fits` image without time-varying sky background correction applied. *Right panel:* Sky-corrected ibp338xzq `flt.fits` image accounting for the time-varying sky background correction. Both images are set to the same colour scale.

reject all the images that present more than 50% of the pixels affected at surface brightness brighter than $\mu = 30 \text{ mag arcsec}^{-2}$ (this removes a 10%, 8%, 5% and 17% of the total amount of exposures from the F105W, F125W, F140W and F160W filter respectively). Finally, we flag any pixel in the valid images that presents a persistence surface brightness larger than $\mu = 30 \text{ mag arcsec}^{-2}$.

We conclude that our persistence models are more robust and include many potential persistence sources that were not taken into account in the previous versions of the HUDF mosaics. The reason for this is that we used a four times larger look-back time for the persistence calculation than the official MAST persistence models and the last WFC3 Persistence pipeline as presented in Long et al. (2015).

2.6. Time-dependent sky background variation

During long exposures, sky background can vary noticeably, introducing a non-linear component to the count rates calculated by `calwf3`. This causes non-Gaussian properties in the `flt.fits` frames of many exposures, with a severe impact in the depth of the final product. This problematic effect is specially common in F105W filter observations. The reason for this is the presence of atmospheric He 10,830Å emission line in the upper atmosphere (Brammer et al. 2014). This emission line falls into the F105W and F110W filters and both HST WFC3/IR grisms. The effect is strongest at low Earth limb angles and under direct sunlight, and usually negligible in the Earth's shadow, but sometimes can be strong even when observing at 40 degrees above the Earth limb. In the worse case scenario, the He 10,830Å line fully dominates the sky background emission (see Dressel 2012, Figure 7.13). Observations with long exposure times will approach closer to the Earth's limb and will be potentially more contaminated by Earth's scattered light and atmospheric emission.

The pixels of those exposures affected by time-dependent sky background will be wrongly classified by `calwf3` as cosmic rays, thus impeding any type of alignment (see Sect. 2.9). In

order to correct for this effect, we follow a similar procedure as in the Sect. 3.2 of Koekemoer et al. (2012). We take advantage of the flexibility of `calwf3` to stop and re-start the calibration process at any point, and we subtract the sky background of each independent readout for each exposure (typically 16 readout per exposure), before the cosmic ray rejection process (steps 7 and 8 of Sect. 2.1). We perform this correction in four steps:

1. We run `calwf3`, stopping the procedure before the "up-the-ramp" fitting and the cosmic rays identification (Sect. 2.1).
2. We individually estimate and subtract the sky background emission from each readout of the intermediate `ima.fits` files.
3. We resume `calwf3`, obtaining a first approximation to the `flt.fits` file.
4. We use this first `flt.fits` combined image to create an object mask, using `NoiseChisel` (see Sect. 2.2)
5. We run again steps 1-3, using this mask to have a better determination of the sky background on each readout. The output is the final `flt.fits` file.

The final sky-background level for each exposure is calculated as the median sky value of the half of the readouts with less differences between them (first or second half). Note that this constant sky level will be subtracted in a later step. By doing this, we successfully corrected most of the exposures affected by this effect. We must note that this correction is only valid if the time variation of sky background is flat, this is, it does not include any variation of a large scale gradient across the image. We visually inspected each dataset and rejected those exposures that were clearly affected by sky background gradients. We show in Fig. 7 an example of an exposure affected by time variation of the sky background. The left panel shows the median flux for two different exposures as a function of the readout time. In an ideal case, the background count rate should be zero or at least constant, but exposure ibp338xzq shows a clear increase on the sky background flux starting at ~ 400 s from the start of the exposure. Running the standard `calwf3` pipeline leads to the image

Este documento incorpora firma electrónica, y es copia auténtica de un documento electrónico archivado por la ULL según la Ley 39/2015.
Su autenticidad puede ser contrastada en la siguiente dirección <https://sede.ull.es/validacion/>

Identificador del documento: 1630219

Código de verificación: NYPyuzSi

Fecha: 26/10/2018 14:33:01

Firmado por: ALEJANDRO SERRANO BORLAFF
 UNIVERSIDAD DE LA LAGUNA

Juan Esteban Beckman Abramson
 UNIVERSIDAD DE LA LAGUNA

MARIA DEL CARMEN ELICHE MORAL
 UNIVERSIDAD DE LA LAGUNA

JOAN FONT SERRA
 UNIVERSIDAD DE LA LAGUNA

26/10/2018 14:36:58

26/10/2018 15:46:09

26/10/2018 18:46:53

A&A proofs: manuscript no. output

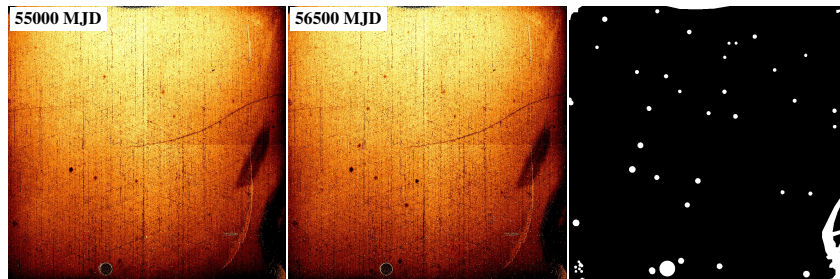


Fig. 8: Example of identification using two extreme flat fields, calculated for June 2009 (55000 MJD, left panel) and July 2013 (56500 MJD, central panel). Right panel: Final Data Quality array. We represent in white those regions of the detector labelled as bad pixels. Note that this data quality array has to be combined with the individual data quality arrays from each individual exposure, containing the cosmic rays masks, the pixels affected by persistence, and the default time-dependent WFC3/IR blobs.

shown in the central panel of Fig. 7, where the sky background has a high-noise level which is not well represented by a Gaussian approximation. We present in the right panel the same exposure corrected by the procedure described above. We stress that both images are calculated from the same `raw.fits` file, and are represented with the same colour scale.

In conclusion, this procedure allows us to successfully correct for the effect of time-variation of the sky background, which is a common issue in HST WFC3/IR exposures.

2.7. Extended data quality array

In order to avoid systematic biases due to the presence of defects in some regions of the detector, we created a manual data quality mask to flag those regions were the flat field cannot fully correct the differences in sensitivity. Besides the effect of those regions of the detector known to have lower sensitivity (wagon wheel, death star), we must pay attention to the presence of the WFC3/IR blobs. These blobs are regions that appear sporadically and cumulatively over the detector and present 5–10% less sensitivity on the detector (Pirzkal et al. 2010). Blobs are not related to any damage on the detector, but rather to particles that stick to the mirror of the Channel Select Mechanism (Calvi 2014). Their effect is strong enough to become a problem in the final mosaics. One of the most important problems is that the WFC3/IR blobs appear as a function of time. Although there is a continuous monitoring of the presence of new IR blobs (Pirzkal & Hilbert 2012), their appearance cannot be predicted.

To avoid including frames affected by blobs that were not flagged yet, we conservatively decided to mask manually those pixels with the largest blobs regardless of the epoch when the exposure was taken. We created a set of 16 sky-flat fields per filter (every 100 days, since 55000 to 56500 MJD) as a function of time in order to visually track the appearance of blobs (see Sect. 2.4). We show an example of the time-dependent flat fields used for the selection process in the left and central panels of Fig. 8. Notice that in the central panel, there are several additional IR blobs visible in the sky flat field. We carefully flagged any region with clear time variation according to our time-dependent flat fields and added them to our master data quality array, which is shown in the right panel of Fig. 8. We

also flagged those regions with low sensitivity or none at all, which are clearly seen in the flat fields (wagon wheel, death star, the unbounded pixels of the top corners and middle strip, and the seven point-like damaged regions on the low left regions, see Dressel 2012, Chapter 5.7.7). Finally, we flag in the individual Data Quality (DQ) extension of all `flt.fits` files all the pixels included in our extended data quality array and mask from the individual images before sky-subtraction and co-addition.

2.8. Sky-subtraction

In this Section we describe the methods used to remove the sky background from the individual exposures and the final mosaics of the HUDF. We divide this task in two parts: flat sky background estimation (constant across the detector, Sect. 2.8.1) and removal of large scale residual gradients with a two-dimensional sky background (Sect. 2.8.2).

2.8.1. Flat sky-subtraction

A key step in the reduction process of astronomical images is the matching of the sky background level before the final co-adding of the individual frames. Because the near IR background is brighter than in the visible and its time variation is higher, this step can be particularly complicated even for space-based observations. Furthermore, for observations of extended sources or very crowded fields – such as the case of WFC3/IR observations of the HUDF – there are many low-surface brightness features that are buried deep under the 1σ noise levels of the individual images, only detectable in the final mosaics. Extended discs, stellar halos, and diffuse objects are extremely hard to mask and they contribute to bias the distribution of the pixels selected for sky background determination toward higher values. This leads to a common tendency to over-subtract in the reduction of deep images. Moreover, a biased determination of the sky background level of the different images before co-adding can greatly affect the final mosaic by including additional noise and thus distorting low surface brightness features of the final image. In this section we describe our flat sky background determination method and compare the results with other standard methods including the method applied by default in Astrodrizzle.

Article number, page 12 of 36

Este documento incorpora firma electrónica, y es copia auténtica de un documento electrónico archivado por la ULL según la Ley 39/2015.
Su autenticidad puede ser contrastada en la siguiente dirección <https://sede.ull.es/validacion/>

Identificador del documento: 1630219

Código de verificación: NYPyuzSi

Fecha: 26/10/2018 14:33:01

Firmado por: ALEJANDRO SERRANO BORLAFF
 UNIVERSIDAD DE LA LAGUNA

Juan Esteban Beckman Abramson
 UNIVERSIDAD DE LA LAGUNA

MARIA DEL CARMEN ELICHE MORAL
 UNIVERSIDAD DE LA LAGUNA

JOAN FONT SERRA
 UNIVERSIDAD DE LA LAGUNA

26/10/2018 14:36:58

26/10/2018 15:46:09

26/10/2018 18:46:53

Borlaff et al.: The missing light of the Hubble Ultra Deep Field

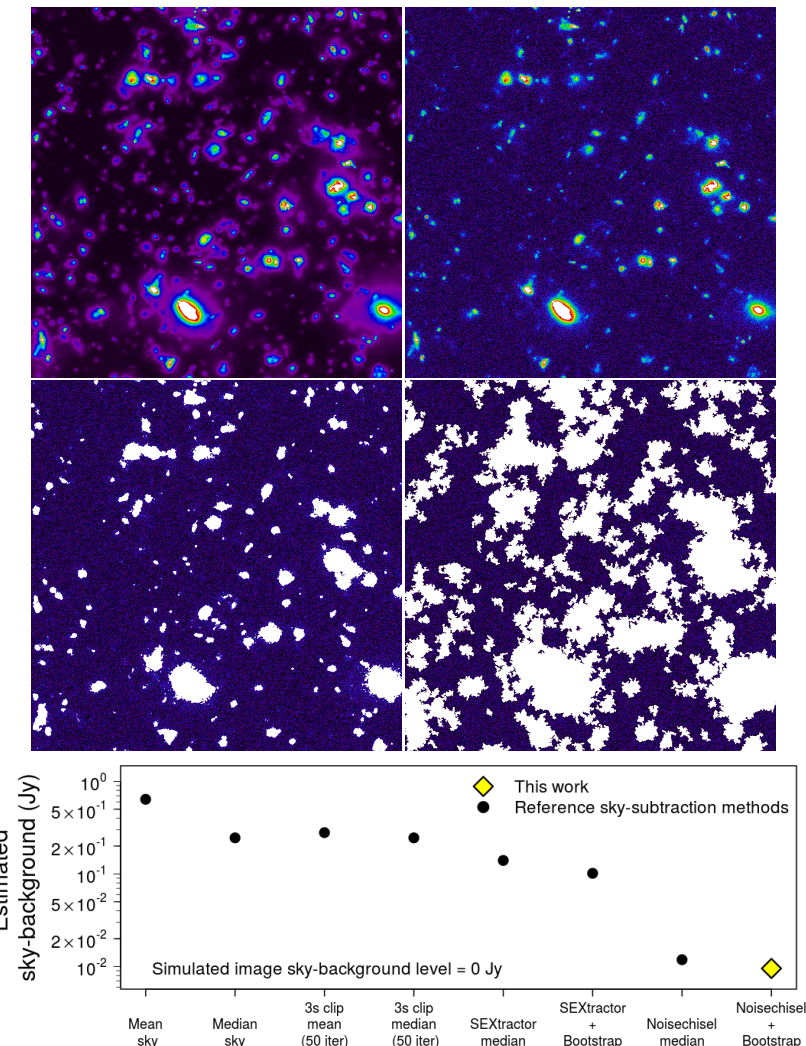


Fig. 9: Comparison of sky-subtraction methods, over a section of the Illustris simulation images. *Top-left panel:* Simulated Illustris Deep Field B section. *Top-right panel:* Same image with a 1 Jy wide Poissonian noise added. *Middle-right panel:* Simulated Illustris Deep Field B with noise masked with SExtractor (1 σ threshold level). *Middle-left panel:* Same image masked with NoiseChisel (default configuration). *Bottom panel:* Estimated sky background as a function of different methods. *Black dots:* Reference methods. *Yellow diamond:* Method applied in the present paper. Notice that all methods overestimate the true sky background level, which is equal to zero in the simulated image. See the legend and axis for details.

Article number, page 13 of 36

Este documento incorpora firma electrónica, y es copia auténtica de un documento electrónico archivado por la ULL según la Ley 39/2015.
Su autenticidad puede ser contrastada en la siguiente dirección <https://sede.ull.es/validacion/>

Identificador del documento: 1630219

Código de verificación: NYPyuzSi

Firmado por: ALEJANDRO SERRANO BORLAFF
UNIVERSIDAD DE LA LAGUNA

Fecha: 26/10/2018 14:33:01

Juan Esteban Beckman Abramson
UNIVERSIDAD DE LA LAGUNA

26/10/2018 14:36:58

MARIA DEL CARMEN ELICHE MORAL
UNIVERSIDAD DE LA LAGUNA

26/10/2018 15:46:09

JOAN FONT SERRA
UNIVERSIDAD DE LA LAGUNA

26/10/2018 18:46:53

A&A proofs: manuscript no. output

We first select those pixels that will be used to calculate a flat sky background level by using the masks created with NoiseChisel (see Sect. 2.2). In addition, we remove (set as NaN) from the sample those pixels that are flagged as bad pixels in the DQ array of each image, including those in the extended DQ array (see Sect. 2.7). We also remove those pixels affected by persistence, according to the custom models calculated in Sect. 2.5, flagging all pixels that present a persistence surface brightness brighter than $\mu = 30 \text{ mag arcsec}^{-2}$. Then, we calculate the probability density distribution of the median value of the sky background level by using random re-sampling with replacement (bootstrapping). One of the main benefits of the resampling methods is to avoid any assumptions of normality on the sample and hence obtain a more accurate distribution for certain statistics. In addition, the shape of the resulting probability distributions gives us information about the presence of outliers and irregularities. This method is much accurate than the sigma clipping methods applied by default by Astrodrizzle (Koekemoer 2002), as the main source of bias for a masked array are not the brightest pixels in the image, but the unmasked outskirts of the largest and most diffuse objects in the field of view. Those contaminated pixels are well below the 1σ interval of the sky background probability distribution. Careful masking based on the noise-based non-parametric algorithms such as NoiseChisel combined with robust statistic methods such as bootstrapping provides much more accurate estimations of the sky level.

We present a systematic comparison of multiple sky-subtraction methods on Fig. 9. In order to make a reasonable experiment, we used the simulated images of the Illustris Project¹ (Vogelsberger et al. 2014; Nelson et al. 2015). The Illustris project is a large cosmological simulation of galaxy formation, which simulates a volume of $(106.5 \text{ Mpc})^3$, since $z = 127$ to $z = 0$. The project made available a set of model deep images² simulating the observations of HST/ACS and WFC3 detectors, JWST/MIRI and WFIRST. We took a section of the same size of WFC3 exposure frames (1014×1014) of the WFC3 F160W Illustris Field B. We added Poissonian noise with a standard deviation equal to 1 Jy . Note that this choice is arbitrary and only for testing purposes. In the bottom panel of Fig. 9 we compare the following sky-subtraction methods:

1. Mean of the unmasked image.
2. Median of the unmasked image.
3. 3σ sigma clipped (50 iterations) mean of the unmasked image.
4. 3σ sigma clipped (50 iterations) median of the unmasked image.
5. Median of the SExtractor masked image (using 1σ detection limit for sources).
6. Bootstrapping median of the SExtractor masked image (using 1σ detection limit for sources).
7. Median of the Noisechisel masked image (default configuration).
8. Bootstrapping median of the Noisechisel masked image.

We remark that the sky background of the simulated image is equal to zero. This means that the methods that measure sky background levels closer to zero can be classified as better than those that predict higher levels. We found several interesting results: 1) every single tested sky-correction method systematically overestimates the true sky level, which for this simulation equals to zero Jy (see also Ji et al. 2018, for a similar result based

a 2D fitting modelling method). 2) NoiseChisel is extremely efficient to remove the outer and dim regions of the simulated galaxies. The difference with respect to sigma clipping (or median sky methods) is larger than one order of magnitude. 3) Bootstrapping does not add a significant improvement to the estimation of the median value, although it is still less biased than a simple median (only 2.5% less biased), even with NoiseChisel masked images. 4) As expected, sigma clipping is not a reliable method for sky-subtraction. The reason to this is that the main bias contributors to the sample of pixels are precisely those pixels which are well below the 1σ level, and thus those are not masked in the process. Finally, we choose the best subtraction method from those analysed (Bootstrapping + NoiseChisel masking) to estimate the final sky value of each exposure before co-addition.

2.8.2. Two-dimensional sky-subtraction and diffuse light gradients

As we increase the depth of astronomical images, any analysis is less affected by the statistical uncertainties of the sky noise and become more dominated by systematic biases (PSF wings, sky gradients, or diffuse scatter light contamination). As a consequence of this, measuring the structure of objects with small but resolved angular sizes in highly crowded fields (such as the HUDF) is a increasingly challenging task. Even in an ideal case without any noise or residual sky background gradients, the structure of small objects is influenced by the presence of other objects in the field of view. For example, most of the objects with small angular sizes from Illustris simulation are on top of the extended wings of a larger close companion (see Fig. 9).

Besides the scatter light caused by real sources, no astronomical image is absolutely free of artificial sky gradients, and their effects can only be partially corrected. One of the most common methods for tackling with this problem is the subtraction of a two-dimensional sky background, by using n -degree polynomial fits, bicubic-spline interpolation on a mesh grid (i.e., SExtractor), or multiple subtractions of median filtered masked frames with different grid sizes (see Sects. 4.1 and 3.4 from Koekemoer et al. 2012; Illingworth et al. 2013, respectively). Most, if not all of these methods have to assume some kind of minimum spatial scale for the variation of the sky background (i.e., mesh grid for SExtractor). Any sky background variations larger than this minimum spatial scale will be fitted and subtracted from the corrected image, at least partially, regardless of their astronomical or instrumental nature. Correspondingly, smaller scales will contain an unknown fraction of artificial sky-gradient residuals and real astronomical diffuse light. Therefore, such methods cannot subtract a two-dimensional sky background that fully preserves the outskirts at all angular scales.

As stated before, highly aggressive sky background subtraction methods allow to obtain very flat final mosaics on small spatial scales. While this can be an asset for photometry of unresolved objects, HUDF contains objects of very different sizes (from ~ 20 arcsec to a fraction of arcsec in diameter). Such methods present the disadvantage of removing the outer parts of the largest objects, which are the primary objective of this paper. In Illingworth et al. (2013) and Koekemoer et al. (2012), the authors decided to calculate a non-flat sky background correction in order to remove residual background features. The chosen sky background spatial scale ranged from 100 pixels (13 arcsec, HUDF12) to 39 pixels (5 arcsec, XDF). The process consisted in the subtraction of two-dimensional sky background arrays, after masking the individual images. In the case of the XDF, the sky background of all the masked images was stacked and subtracted

¹ The Illustris Simulation: <http://www.illustris-project.org/>

² The Illustris ultra deep fields are publicly available at <https://archive.stsci.edu/prepds/illustris/index.html>

Este documento incorpora firma electrónica, y es copia auténtica de un documento electrónico archivado por la ULL según la Ley 39/2015.
Su autenticidad puede ser contrastada en la siguiente dirección <https://sede.ull.es/validacion/>

Identificador del documento: 1630219

Código de verificación: NYPyuzSi

Fecha: 26/10/2018 14:33:01

Firmado por: ALEJANDRO SERRANO BORLAFF
 UNIVERSIDAD DE LA LAGUNA

Juan Esteban Beckman Abramson
 UNIVERSIDAD DE LA LAGUNA

MARIA DEL CARMEN ELICHE MORAL
 UNIVERSIDAD DE LA LAGUNA

JOAN FONT SERRA
 UNIVERSIDAD DE LA LAGUNA

26/10/2018 14:36:58

26/10/2018 15:46:09

26/10/2018 18:46:53

Borlaff et al.: The missing light of the Hubble Ultra Deep Field

from the individual images. Masking the frames previous to sky background correction partially reduces the over subtraction of the source on the images. Nevertheless –while detectable on the final mosaics– the outskirts of the largest objects extend far beyond the 1σ limit of the individual images, and thus usually get included in the two-dimensional sky background fit, biasing the final result.

Since our primary objective is to recover the outskirts of galaxies in the HUDF at lower redshifts ($z \sim 0.6 - 1$), we have to be more careful with our sky-subtraction techniques. Akhlaghi & Ichikawa (2015, see Appendix A.6) show that even extensively used model-based methods to calculate the background, such as SExtractor (Bertin & Arnouts 1996), fail to interpolate the sky level for the corners of the detector, unless the observers perform a careful and individual setting of the mesh size (BACK_SIZE) for each image. This process may depend on the objects and their position on the detector. For this paper, we set the parameters of NoiseChisel checking the spatial distribution of the valid tiles (a subset or a section of the input array) for sky background estimation. We refer the reader to Gnuastro tutorial 2.3 - Detecting large extended targets¹ for a detailed tutorial on detecting the low surface brightness wings of extended sources on astronomical images and using NoiseChisel to avoid systematic biases on sky subtraction. In our configuration, NoiseChisel calculates the sky background over square sections of the image called tiles, removing from the analysis those tiles which present significant differences between the mode and the median. The distance between valid tiles depends on the signal to noise ratio and the distribution of the sources on the image, being less valid tiles (or none) on more crowded regions of the image. For the individual images we set the tile size to 100 pixels, with the smoothwidth parameter fixed to 5 and a mode-median quantile difference equal to 0.005. The needed number of neighbour tiles for interpolation was set to 5. We modified those parameters until no valid tiles were accepted by the program near the most extended objects. As a final step, we subtracted a final sky background gradient for each mosaic, using again a tile size of 100 pixels with smoothwidth equal to 5 and the mode-median quantile difference equal to 0.01.

We conclude that as a consequence of protecting the outskirts of the largest objects in our reduction process, we cannot neglect the presence of artificial sky-gradient residuals with spatial scales of several hundreds of pixels or smaller. This is an inevitable consequence of the reduction process that has to be corrected on a case-by-case basis, taking into account the intensity, shape, angular size, and environment of each object to study. In Sect. 3 we provide some examples to illustrate the benefits of our dedicated mosaics and discuss the required corrections to analyse diffuse light contaminated objects.

2.9. Image alignment

The astrometric solution of the HST images is precise up to a fraction of arcsec (typically 2–5 pixels, Gonzaga et al. 2012). As a consequence, when comparing images from different visits, it is usual to see that they are not exactly aligned. In order to exploit the full resolving capabilities of WFC3, we need to carefully re-align the images of different visits to a single reference world coordinate system solution (WCS hereafter). To perform this correction we use Tweakreg². Tweakreg is task part of

¹ Gnuastro 2.3 Tutorial - Detecting large extended targets: https://www.gnu.org/s/gnuastro/manual/html_node/Detecting-large-extended-targets.html

² Tweakreg is publicly available at: <http://drizzlepac.readthedocs.io/en/deployment/tweakreg.html>

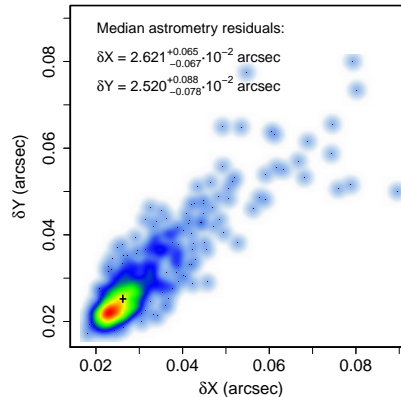


Fig. 10: Colour coded density two-dimensional distribution of the astrometry dispersion of the residuals on the HUDF dataset, according to Tweakreg. The black cross represents the median value for the astrometry residuals, in arcsec. Consult the values on the panel.

Drizzlepac and it allows the user to align sets of images to each other and/or an external astrometric reference frame or image. In this paper, we perform this correction following the method presented on Lucas & Hilbert (2015) and Lucas (2015):

1. We generate four reference catalogues (F105W, F125W, F140W and F160W) for the XDF final mosaics using SExtractor (Bertin & Arnouts 1996). We iteratively increased the threshold level (DETECT_THRESH and ANALYSIS_THRESH) from 1σ to 3σ in order to remove spurious sources that may affect the final solution.
2. We group the individual exposures by visits, using AstroDrizzle to correct for cosmic rays. We use AstroDrizzle to analyse each group of images from the same visit and filter and substitute the identified cosmic rays and flagged pixels with the binned median of the group (see Chapter 4.2.7 of Gonzaga et al. 2012)
3. We generate one catalogue per exposure to correct using the cosmic ray corrected frames.
4. We use Tweakreg to find the necessary shift and scaling for each exposure. The program uses the cosmic rays cleaned image, their corresponding source catalog and the reference catalog to its filter, and it matches the astrometry of the individual images to the XDF mosaic.
5. We repeat the previous process, visually checking for misalignments during each iteration and modifying the sigma level of the catalogues and the searching radius of Tweakreg.
6. Finally, we copy the astrometric solution to the `flt.fits` files.

One of the outputs from Tweakreg is the residuals of the positions for each object and its reference object according to the

Article number, page 15 of 36

Este documento incorpora firma electrónica, y es copia auténtica de un documento electrónico archivado por la ULL según la Ley 39/2015.
Su autenticidad puede ser contrastada en la siguiente dirección <https://sede.ull.es/validacion/>

Identificador del documento: 1630219

Código de verificación: NYPyuzSi

Fecha: 26/10/2018 14:33:01

Firmado por: ALEJANDRO SERRANO BORLAFF
 UNIVERSIDAD DE LA LAGUNA

Juan Esteban Beckman Abramson
 UNIVERSIDAD DE LA LAGUNA

MARIA DEL CARMEN ELICHE MORAL
 UNIVERSIDAD DE LA LAGUNA

JOAN FONT SERRA
 UNIVERSIDAD DE LA LAGUNA

26/10/2018 14:36:58

26/10/2018 15:46:09

26/10/2018 18:46:53

A&A proofs: manuscript no. output

final astrometric solution for each dataset. In order to measure the average precision that we achieve on our images, we measure the median dispersion of the residuals on all our datasets. The results are shown in Fig. 10. The median dispersion of the residuals is ~ 0.2 pixels on both directions of the array, which corresponds to ~ 0.025 arcsec. We conclude that our images are sufficiently well-aligned to use a final pixel scale of the mosaics is equal to 0.06 arcsec, which is the same used by HUDF12 and XDF teams.

2.10. Image combination: Bootlma

Image combination is one of the most common tasks for astronomers. Avoiding systematic biases at this step can be a challenging task. Ground and space based surveys are subdued to a large number of time dependent conditions, either external, such as the effect of cosmic rays, the variation of the sky background or stray-light contamination, that may affect in the form of gradients, or internal, such as variations on the sensitivity of the detector or the position of the different objects over the detector. All these effects produce large variations on the final mosaics, and their typical time-scale can vary between the length of the exposure time to years. The most common methods for co-adding are different types of robust median. Most (if not all) HST images rely on the `imcombine` task of AstroDrizzle (Koekemoer 2002). AstroDrizzle allows the user to use different methods of image combination. The recommended method for a large number of images (more than ten) is "imedian", which corresponds to the median value for each pixel, with the exception of those regions were all pixels were flagged as bad. In that case, the algorithm returns the last value of the stack. This will prevent to have holes in the center of stars, for example.

Nevertheless, this type of processes does not provide accurate uncertainties for the final mosaics, which are extremely useful for many scientific objectives (i.e., measuring the local sky noise, performing accurate photometry, or two-dimensional decomposition). For that objective, we created Bootlma. Bootlma is a set of programs written in Python and HTCondor¹ to perform image combination through Bootstrapping. We use this program for the flat field combination and to create the final mosaics. The main task of Bootlma is the robust combination of a large number of images and estimation of their uncertainties. Such task is computationally expensive, and we optimised it to work in parallel processors and specially, HTCondor. We can summarise in two the main reasons for using bootstrapping to calculate the median images:

1. It estimates a robust measurement of the confidence intervals, which are provided with the final mosaics and flats obtained with this task, which are extremely useful in the case of deep imaging studies.
2. It allows to combine images using weights. This is particularly useful for the HUDF, where multiple observing programs used different exposure times. This also means that the observing sample does not present a pure Gaussian distribution and has to be treated with non-parametric methods.

A previous step to image combination is the distortion correction. The images produced by WFC3 are affected by geometric distortion, caused by the tilt of the image surface with respect to the path of light (Kozhurina-Platais et al. 2012). If the distortion correction is not applied or accurate enough, the image

¹ HTCondor is an open-source high-throughput management system for computing-intensive jobs: <https://research.cs.wisc.edu/htcondor/index.html>

Article number, page 16 of 36

combination will produce blurred images and distort the PSF. AstroDrizzle drizzling code corrects for this geometric distortion using the calibration IDCTAB files, with a precision of 0.1 pixels. After geometric transformation, AstroDrizzle reassigns each pixel to a new and undistorted pixel grid (Fruchter & Hook 1998). This process is called drizzling. The new pixel grid can take advantage of the dithering in order to reconstruct a final image with smaller pixel scale by oversampling the input data. We refer the reader to Chapter 6.3 of Gonzaga et al. (2012) for a detailed description of this process. The fraction by which each input pixel is shrunk before being drizzled onto the input image is controlled by the `final_pixfrac` parameter, which we set to 0.8, following the prescriptions for the HUDF12 and the XDF. We choose the Gaussian kernel to distribute the flux of each input pixel onto the new pixel grid. Finally, we obtain a new set of images, corrected for geometric distortion, with a pixel scale of 0.06 arcsec, and aligned into a common pixel grid, ready for image combination.

Bootlma performs the median image as follows: first, we register exposure time and date for all the input images. Images are re-ordered as a function of time, to simplify visual inspection. Second, we create an hdf5 datacube, where we store all the individual image arrays, along with their exposure time and date. We choose hdf5 format instead of fits because of its optimal performance with extremely large files (> 1 Tb) and optimization to access to chunks of the information inside an object, without loading all the data into the computer RAM. Once the master hdf5 file is created, we calculate a robust median value along the date direction using a Python-HTCondor program built for this purpose. We use the weight images created with Astrodrizzle for each image weights during random re-sampling, as they take into account the exposure time and the fraction of counts that correspond to each pixel in the new drizzle grid for each pixel from each original pixel grid. Notice that our datacube contains "holes" (i.e., NaN values due to persistence masking and bad pixels). This prevents us from using random re-sampling directly over the full set of images, because all bootstrapping simulations would not have the same amount of pixels. Each pixel of the image has a different sample size, and thus requires independent analysis. Finally, we reconstruct the final image into a single frame.

We conclude that our method allows to obtain precise error frames, extremely useful for many science cases while performing robust combination of the images into the final mosaics. In the FITS files that contain the ABYSS images, we included two additional FITS extensions that contain the $+1\sigma$ and -1σ uncertainty intervals for each pixel in the field of view.

3. Results and discussion

3.1. General properties

In this section we detail the morphological and photometric properties of the newly reduced mosaics, which we present in the colour image of Fig. 11. We compare the results from our images to the original HUDF12 (Koekemoer et al. 2012) and the XDF (Illingworth et al. 2013) mosaics.

3.1.1. Recovering the low-surface brightness structure

In Figs. 12 and 13 we perform a comparison of the low surface brightness properties of the three different versions of the mosaics compared in this paper: HUDF12, XDF and our dedicated version of the HUDF mosaics which we called ABYSS. We per-

Este documento incorpora firma electrónica, y es copia auténtica de un documento electrónico archivado por la ULL según la Ley 39/2015.
Su autenticidad puede ser contrastada en la siguiente dirección <https://sede.ull.es/validacion/>

Identificador del documento: 1630219

Código de verificación: NYPyuzSi

Fecha: 26/10/2018 14:33:01

Firmado por: ALEJANDRO SERRANO BORLAFF
 UNIVERSIDAD DE LA LAGUNA

Juan Esteban Beckman Abramson
 UNIVERSIDAD DE LA LAGUNA

MARIA DEL CARMEN ELICHE MORAL
 UNIVERSIDAD DE LA LAGUNA

JOAN FONT SERRA
 UNIVERSIDAD DE LA LAGUNA

26/10/2018 14:36:58

26/10/2018 15:46:09

26/10/2018 18:46:53

Borlaff et al.: The missing light of the Hubble Ultra Deep Field

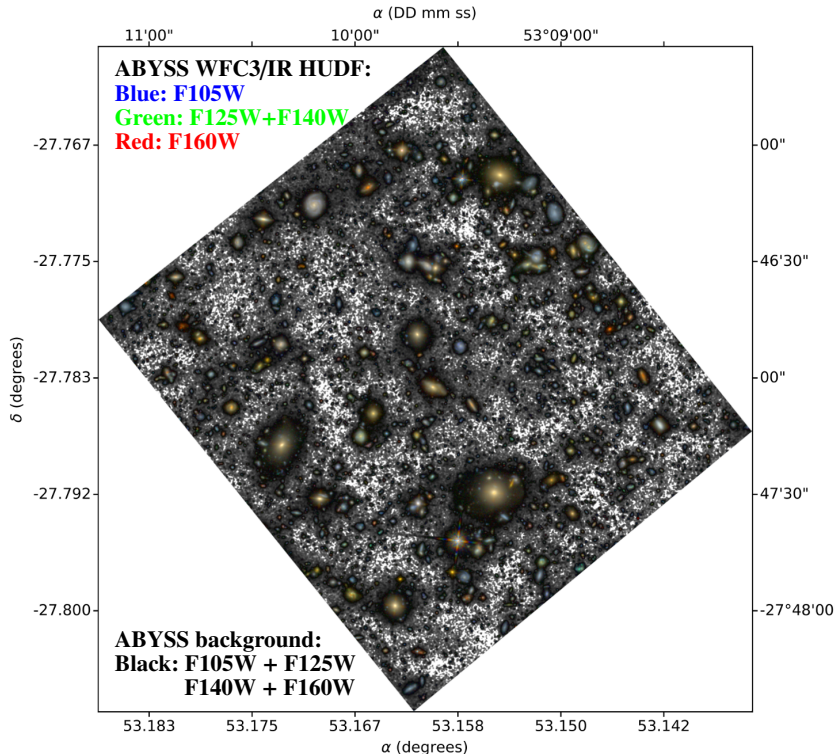


Fig. 11: Luminance-RGB image showing the full depth of the mosaics of the ABYSS version of the HUDF WFC3/IR. The high signal-to-noise parts of the mosaics are represented with colours (Red: F160W, Green: mean of F125W and F140W bands, Blue: F105W). The low signal-to-noise regions are represented in as a black and white background (black regions are brighter than white regions) according to the mean image of the four mosaics (F105W, F125W, F140W, F160W) of the mosaics of the ABYSS (covering HUDF, deep WFC3/IR region).

form the same analysis for the four available filters. In order to reduce the noise and enhance the differences between our mosaics and the previous versions in the low-surface brightness regions, we have re-sampled the image binning the data to 0.6 arcsec boxes (10×10 pixels).

Visual inspection of the binned difference frames reveals that the XDF mosaics present large over-subtracted regions, which are centred over the regions where the most extended objects are. They are easily identifiable in the difference intensity images that we present on Figs. 12 (for F105W and F125W) and 13 (for F140W and F160W). Comparing the light distribution of the largest objects from the ABYSS mosaics and the morphology

of the difference intensity images for the XDF we find that they create almost a mirror image of the intensity mosaics. Moreover, the distribution of the residuals for the XDF is strikingly similar in the four filters, being more clear in the F105W and more noisy in the F140W (this is an expected effect due to the relative depth of the mosaics).

Although, in principle, this effect may be caused both by over-subtraction in the regions around the largest objects of the XDF or by under-subtraction in our ABYSS version, because we also applied a two-dimensional sky background correction to our mosaics, as Illingworth et al. (2013, see Sect. 2.8.2), it is highly unlikely that the correction that we applied generate

Article number, page 17 of 36

Este documento incorpora firma electrónica, y es copia auténtica de un documento electrónico archivado por la ULL según la Ley 39/2015.
Su autenticidad puede ser contrastada en la siguiente dirección <https://sede.ull.es/validacion/>

Identificador del documento: 1630219

Código de verificación: NYPyuzSi

Firmado por: ALEJANDRO SERRANO BORLAFF
 UNIVERSIDAD DE LA LAGUNA

Fecha: 26/10/2018 14:33:01

Juan Esteban Beckman Abramson
 UNIVERSIDAD DE LA LAGUNA

26/10/2018 14:36:58

MARIA DEL CARMEN ELICHE MORAL
 UNIVERSIDAD DE LA LAGUNA

26/10/2018 15:46:09

JOAN FONT SERRA
 UNIVERSIDAD DE LA LAGUNA

26/10/2018 18:46:53

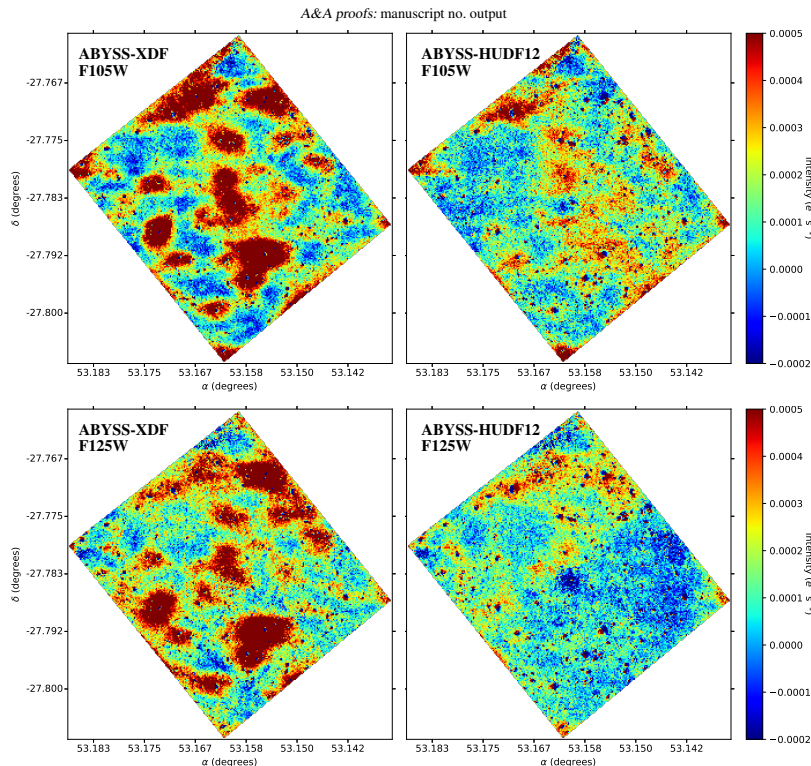


Fig. 12: Comparison of the ABYSS mosaics of the HUDF WFC3/IR and the previous releases. Each plot represents the intensity difference between our version of the mosaics (ABYSS) and the reference versions (left panels: XDF, right panels: HUDF12), for the F105W filter (top panels) and the F125W filter (bottom panels). See the colour bar for reference.

under-subtraction around the largest objects. First, because the typical scale-length of our gradients is 1/3 or 1/2 of the field-of-view, much larger than the size of the largest objects on the HUDF, while the variations that we detect on the binned difference frames are much smaller. And secondly and most importantly, two-dimensional sky-subtraction tends to fit the extended light of the galaxies, over subtracting these regions, not the opposite effect.

Interestingly, we found that the HUDF12 presents a similar effect at a lower scale. The distribution of residuals for the F105W and the F140W filters are similar for the XDF and the HUDF12 mosaics when comparing with our mosaics, although the differences are less intense. Inspecting the difference intensity images corresponding to those mosaics (right panels of Figs. 12 and Figs. 13), we can easily see how the extended light around one of the largest elliptical galaxies, HUDF-5 ($\alpha = 53.15545$, $\delta = -27.79150$, Buitrago et al. 2016), was over

subtracted, similarly as in the case of the XDF mosaics. Nevertheless, the west region of the F125W of the HUDF12 is less over subtracted than the rest, presenting a lower level of residual intensity in Fig. 12. We found a similar effect in the south-east region of the HUDF12 F160W mosaic (see Fig. 13), where the HUDF12 predicts more flux than our own mosaics. Neither this effect nor the discussed on F125W was found when comparing to the XDF, suggesting that the issue is due to the HUDF12 mosaics.

As an illustrative exercise, we calculated the equivalent integrated magnitude of the light recovered on the low surface brightness regions of the ABYSS HUDF mosaics, compared to the previous versions. In order to do that, first we calculate the mean surface brightness on 1.2 arcsec boxes (20 pixels). Due to the fact that small differences in magnitude at the brightest cores of the galaxies may dominate over the differences on the dimmest regions of the images, we select only the regions

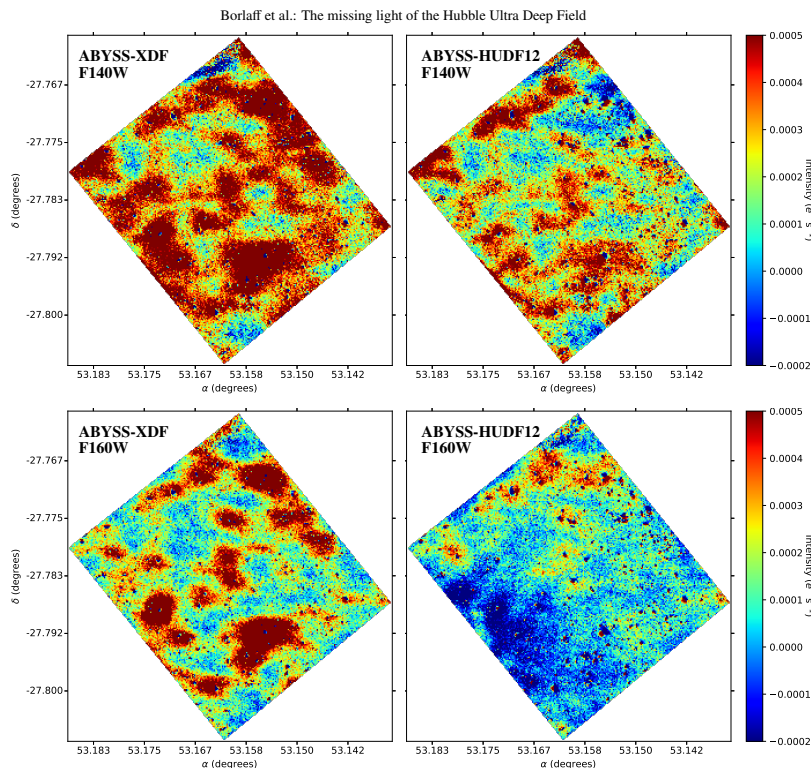


Fig. 13: Comparison of the ABYSS mosaics of the HUDF WFC3/IR and the previous releases. Each plot represents the intensity difference between our ABYSS mosaics of the HUDF WFC3/IR and the previous reductions (left panels: XDF, right panels: HUDF12), for the F140W filter (top panels) and the F160W filter (bottom panels). See the colour bar for reference.

were the mean surface brightness is lower than $\bar{\mu} = 26$ mag arcsec $^{-2}$ for each individual filter. Finally, we integrate the difference in flux between our mosaics and the reference images (XDF and HUDF12). We show the resulting equivalent magnitudes in Fig. 14. We found that the amount of recovered light is equivalent to a ~ 19 mag source when comparing to the XDF and to a ~ 20 mag for the HUDF12. This is comparable to the brightness of some of the largest objects in the HUDF. This result is nearly constant for all the filters, although we found that the integrated magnitude for the F125W and F160W images of the HUDF12 is dimmer, in agreement with the results found on the difference maps (see Figs. 12 and 13). We must remark that this result highly depends on the size of the image. In a larger area, the total magnitude missing will be larger. In this sense, the values provided here should serve only to compare the equivalent effect of over-subtraction of low surface brightness features on brighter sources.

We conclude that our images successfully recover most of the extended light around the largest objects from the HUDF WFC3/IR. The recovered light is easily identified as positive counts when subtracting the previous versions of the mosaics from the ABYSS HUDF WFC3/IR images around these objects.

3.1.2. Photometric consistency with previous HUDF WFC3/IR images

In this section we study the photometric properties of the final mosaics, comparing with the results from the previous reductions of the WFC3/IR mosaics for the HUDF. In order to do that, we measure and compare the magnitude of ~ 2500 objects on the HUDF and identified using NoiseChisel and measured using MakeCatalog (both part of Gnuastro, see Akhlaghi 2016 for a discussion about separate detection and catalog production on astronomical surveys). We created a catalogue per filter and re-

Article number, page 19 of 36

Este documento incorpora firma electrónica, y es copia auténtica de un documento electrónico archivado por la ULL según la Ley 39/2015.
Su autenticidad puede ser contrastada en la siguiente dirección <https://sede.ull.es/validacion/>

Identificador del documento: 1630219

Código de verificación: NYPyuzSi

Firmado por: ALEJANDRO SERRANO BORLAFF
 UNIVERSIDAD DE LA LAGUNA

Fecha: 26/10/2018 14:33:01

Juan Esteban Beckman Abramson
 UNIVERSIDAD DE LA LAGUNA

26/10/2018 14:36:58

MARIA DEL CARMEN ELICHE MORAL
 UNIVERSIDAD DE LA LAGUNA

26/10/2018 15:46:09

JOAN FONT SERRA
 UNIVERSIDAD DE LA LAGUNA

26/10/2018 18:46:53

A&A proofs: manuscript no. output

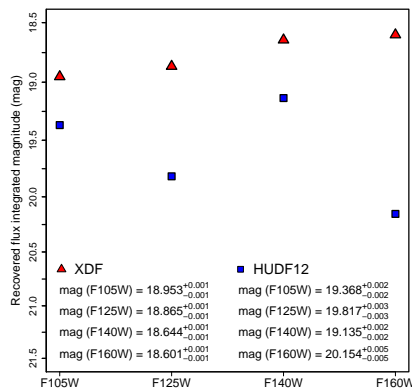


Fig. 14: The missing light of the HUDF measured as the integrated magnitude of the regions with $\bar{\mu} > 26 \text{ mag arcsec}^{-2}$. These are calculated with the difference images between the ABYSS mosaics and the XDF (red triangles) and the HUDF12 (blue squares). See the legend for the values and uncertainties of the different bands.

duction set (12 final catalogs in total). We provide the number of objects identified on the mosaics created for this test on the legend of each panel in Fig. 15.

The NoiseChisel segmentation maps are highly dependent on the shape and amount of extended light of the objects. Because of this reason, we used one mosaic per filter to calculate the segmentation maps. In this case, we used the mosaics from the HUDF12. Notice that the exact photometry of the objects depends on this choice, but not the conclusions from this test. Thus, the segmentation maps are fixed for the three versions used to compare and independent for each one of the four filters. Finally, MakeCatalog calculates the integrated magnitude, correcting for the local sky background for each object.

In Fig. 15 we compare the differences in magnitude between our reduction and the HUDF12 and the XDF mosaics. We found that the median differences between the magnitudes are $\Delta m_{\text{HUDF12-ABYSS}} = 0.026^{+0.016}_{-0.013} \text{ mag}$ when comparing to the HUDF12 versions of the mosaics, and slightly larger ($\Delta m_{\text{XDF-ABYSS}} = 0.067^{+0.008}_{-0.008} \text{ mag}$) when comparing with the XDF mosaics. These differences are negligible and (most importantly) not systematic. The objects in our filters are not systematically brighter or dimmer than in the previous releases. In addition, we found that they are compatible with the differences that we found when comparing the XDF with the HUDF12 mosaics using the same method and apertures ($\Delta m_{\text{F105W}} = 0.071^{+0.006}_{-0.006}$, $\Delta m_{\text{F125W}} = 0.047^{+0.005}_{-0.005}$, $\Delta m_{\text{F140W}} = -0.030^{+0.003}_{-0.003}$, $\Delta m_{\text{F160W}} = 0.021^{+0.005}_{-0.004}$).

We conclude that the photometric analysis in fixed apertures does not reveal any systematic bias or significant differences when comparing to the results and differences between the previous versions of the HUDF mosaics.

3.1.3. Surface brightness limiting magnitude maps

In Fig. 16 we present the surface brightness limiting magnitude maps, calculated using the standard deviation estimation of NoiseChisel for the F105W, F125W, F140W, and F160W mosaics. We find that despite removing a large amount of pixels because of persistence and gradient corrections, the relative depth between filters has not notably changed. We summarise the results in Table 2. In our version, as well as in the previous releases, the deepest filter is the F105W band ($\mu_{lim} = 32.89^{+0.01}_{-0.02} \text{ mag arcsec}^{-2}$, 3σ in $10 \times 10 \text{ arcsec}$ boxes), followed by F140W ($\mu_{lim} = 32.54^{+0.03}_{-0.01} \text{ mag arcsec}^{-2}$), F125W ($\mu_{lim} = 32.58^{+0.01}_{-0.02} \text{ mag arcsec}^{-2}$), and F160W ($\mu_{lim} = 32.52^{+0.01}_{-0.02} \text{ mag arcsec}^{-2}$). The relative differences between the surface brightness limiting magnitudes for the same filters of different versions are very small. We note that even after the extremely conservative selection criteria that we have carried out to select the images and the valid pixels (mainly due to persistence effects), our final mosaics present compatible limiting magnitudes than previous HUDF releases. The limiting magnitude for the ABYSS F105W image is 0.01 mag arcsec $^{-2}$ deeper than in the XDF and 0.04 mag arcsec $^{-2}$ deeper when comparing with the F105W HUDF12 image. The F160W image is the most affected presenting a limiting magnitude 0.15 mag arcsec $^{-2}$ brighter than in the XDF and HUDF12. This is because the F160W images are more affected by persistence effects (see Sect. 2.5). Finally, the F125W presents a compatible depth with XDF and HUDF12, while our F140W mosaic is slightly deeper ($\sim 0.06 \text{ mag arcsec}^{-2}$) than the previous reductions (see Fig. 16).

Nevertheless, the above limiting surface brightness magnitude should be understood as the formal limiting magnitude and not the effective ones from the images. The effective limiting magnitudes are affected by systematic effects (such as sky oversubtraction) not included in this measurement of the pixel noise. The surface brightness limiting magnitude is position dependent over the field of view, with differences of almost 0.5 mag arcsec $^{-2}$. It is notable the presence of a shallower region on our mosaics on the north corner, due to the effect of conservative masking of the WFC3/IR chip cosmetic defect called the "wagon wheel" (see Sect. 2.7). We find that this region can present a surface brightness limiting magnitude $\sim 1 \text{ mag arcsec}^{-2}$ brighter than the rest of the mosaics. Any analysis including data from this region should be done carefully.

The side effect of our reduction process to avoid systematic biases (in particular, removal of persistence contamination) is that the F160W mosaic present slightly brighter formal limiting surface brightness than the previous versions of the HUDF, if we only take into account the pixel noise. Nevertheless, as shown in Sect. 3.1.1, those previous reductions were dominated by systematic biases, much larger than the relative differences found in surface brightness limiting magnitude. As a result of this, our mosaics contain much more information on the outskirts of the extended objects of the HUDF than any previous version of the data. We will comment on this in Sect. 3.2. We find that the conservative persistence masking and removal of gradients that we have performed do not affect significantly the depth of our mosaics, which present surface brightness limiting magnitudes similar to those from the previous versions of the HUDF, while reducing the systematic biases.

3.2. Surface brightness profiles

In this section we study the surface brightness profiles of several objects (see Table 3) from the HUDF, comparing the results from

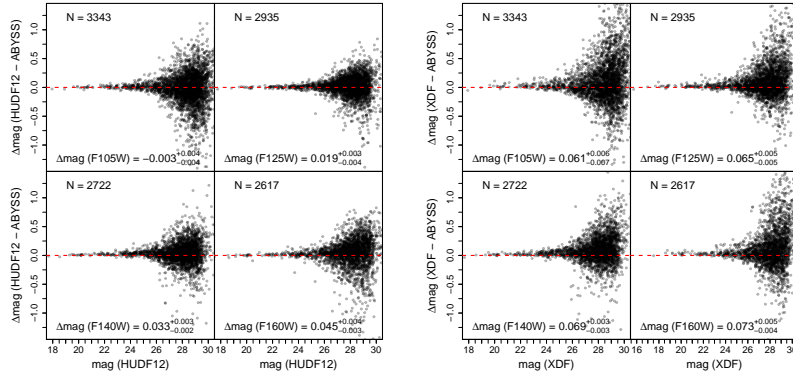


Fig. 15: Comparison of the HUDF photometry of several sources for our ABYSS reduction and the previous releases. Each panel shows the magnitude differences with their corresponding reference catalogue as a function of the object magnitude. *Left panel:* ABYSS vs. HUDF12. *Right panel:* ABYSS vs. XDF. The magnitudes are measured using fixed non-parametric apertures in each object and filter calculated with Gnuastro using the HUDF12 segmentation maps.

Filter	No. exposures	Exposure time [s]	μ_{lim} ABYSS [mag arcsec $^{-2}$]	μ_{lim} XDF [mag arcsec $^{-2}$]	μ_{lim} HUDF12 [mag arcsec $^{-2}$]
(1)	(2)	(3)	(4)	(5)	(6)
F105W	264	312072	32.888 $^{+0.013}_{-0.018}$	32.877 $^{+0.017}_{-0.017}$	32.846 $^{+0.021}_{-0.017}$
F125W	234	175837	32.539 $^{+0.031}_{-0.014}$	32.517 $^{+0.026}_{-0.027}$	32.503 $^{+0.026}_{-0.024}$
F140W	103	86352	32.585 $^{+0.012}_{-0.024}$	32.517 $^{+0.014}_{-0.017}$	32.521 $^{+0.013}_{-0.012}$
F160W	271	234696	32.522 $^{+0.013}_{-0.016}$	32.677 $^{+0.018}_{-0.020}$	32.660 $^{+0.018}_{-0.019}$

Table 2: Summary of the data used to create the ABYSS HUDF WFC3/IR mosaics and surface brightness limiting magnitude comparison with previous mosaics. *Columns:* 1) Filter identifier. 2) Number of exposures included in the final mosaic. 3) Total exposure time. 4) Median surface brightness limiting magnitude (3σ measured on 10×10 arcsec 2 boxes) for the ABYSS mosaics. 5) Median surface brightness limiting magnitude for the XDF mosaics, measured in the same way. 6) Median surface brightness limiting magnitude for the HUDF12 mosaics, measured in the same way. The surface brightness limits shown here refer to the pixel noise of the images and do not account for systematic effects.

our reduction and the previous releases of the mosaics. First, in Sect. 3.2.1 we focus our attention on those objects with large angular sizes, which are more sensitive to over-subtraction and the primary target of the reduction process applied on this work. We start with HUDF-5, the largest one from our sample ($z = 0.607$, following the nomenclature from Buitrago et al. 2016) and one of the objects most affected by the sky over-subtraction of the previous versions, continuing with HUDF-1 ($z = 0.618$), HUDF-2 ($z = 0.619$), and ABYSS-1 ($z = 0.622$), a spiral galaxy from Elmegreen et al. (2005). Finally, we will study whether there are significant changes on the structure of the objects with smaller ($R_{lim} < 10$ arcsec) angular sizes in Sect. 3.2.2. For this, we have selected two additional spiral galaxies from Elmegreen et al. (2005): ABYSS-2 ($z = 0.607$) and ABYSS-3 ($z = 1.28$). We show the cutouts of the targets in Fig. 17. The main selection

criteria for the spiral galaxies was the relative isolation to avoid light contamination from nearby sources. We refer to Table 3 for the sky coordinates, main properties, and IAU ID.

In order to properly analyse the surface brightness profiles of the target objects we first performed a careful manual masking of all the nearby objects. These masks were created using the sum of all the four filters. For consistency, we use the same masks for every filter and version of the HUDF. Secondly, we analysed the surface brightness profiles of each galaxy using concentric elliptical apertures. We take into account both the uncertainties of the intensity dispersion along the elliptical aperture and the intrinsic uncertainty of each pixel (sky noise) using bootstrapping and Monte Carlo simulations. The sky noise is measured on each mosaic independently, using the standard deviation maps used for the limiting magnitude analysis (see Sect. 3.1.3). Finally, to

Este documento incorpora firma electrónica, y es copia auténtica de un documento electrónico archivado por la ULL según la Ley 39/2015.
Su autenticidad puede ser contrastada en la siguiente dirección <https://sede.ull.es/validacion/>

Identificador del documento: 1630219

Código de verificación: NYPyuzSi

Firmado por: ALEJANDRO SERRANO BORLAFF
 UNIVERSIDAD DE LA LAGUNA

Fecha: 26/10/2018 14:33:01

Juan Esteban Beckman Abramson
 UNIVERSIDAD DE LA LAGUNA

26/10/2018 14:36:58

MARIA DEL CARMEN ELICHE MORAL
 UNIVERSIDAD DE LA LAGUNA

26/10/2018 15:46:09

JOAN FONT SERRA
 UNIVERSIDAD DE LA LAGUNA

26/10/2018 18:46:53

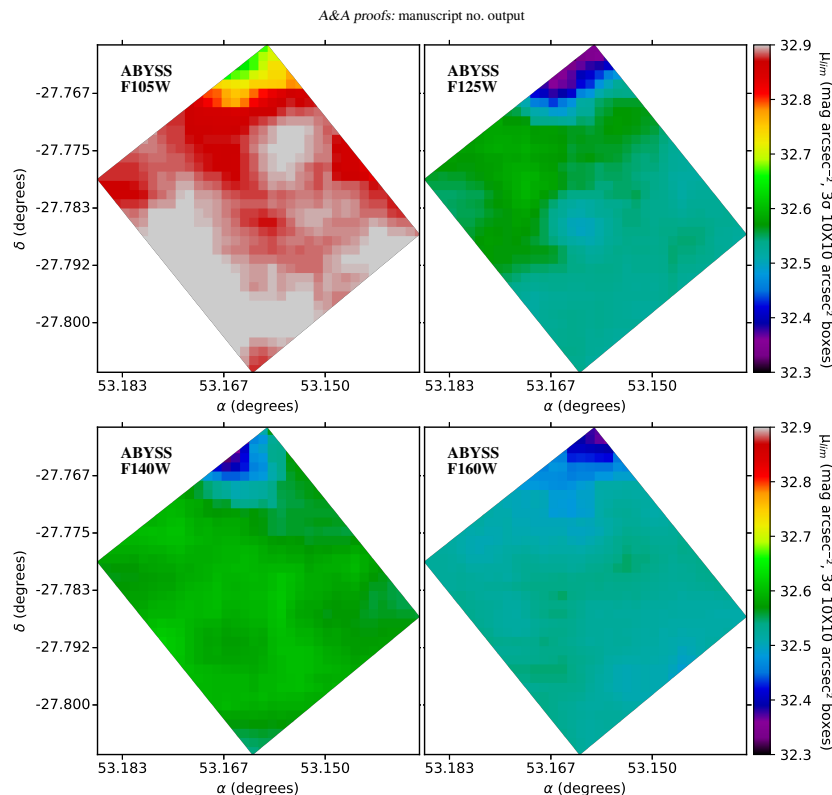


Fig. 16: Surface brightness limiting magnitude maps for the ABYSS mosaics of HUDF. From top to bottom and left to right, F105W, F125W, F140W, and F160W bands. Each panel represents in colour scale the surface brightness limiting magnitude for each mosaic, measured as the 3σ upper limit of the sky level on $10 \times 10 \text{ arcsec}^2$ boxes (Trujillo & Fliri 2016), as a function of the position on the mosaics. All the panels are at the same scale (see the colour bar on the right panels for reference).

improve the sky estimation we subtract the local sky level using the median value of all the valid apertures that are beyond a certain limit (Pohlen & Trujillo 2006), which is set at 140 kpc for HUDF-2 and HUDF-5, following the method described on Buitrago et al. (2016). For the three spiral galaxies (ABYSS-1, ABYSS-2 and ABYSS-3) and HUDF-1 (notably smaller than HUDF-2 and HUDF-5), we measure the local sky level beyond 80 kpc, which is well beyond the visual limit of the objects. The geometric parameters for the profiles (position angle and axis ratio) were calculated using SExtractor. We detail the position angles, axis ratios, and the local sky region limit for each object in Table 3. We remark that in order to do a fair comparison we apply the same masks, geometric parameters, elliptical aperture algorithm, and local sky level region to all the mosaics, regard-

less of their wavelength and version. For the sake of simplicity, we do not apply any type of PSF correction. The main objective of the surface brightness profile analysis that we present here is to illustrate the differences on the low surface brightness regions of the different mosaics. The differences of the PSF between the three versions studied are minimal, as they are created from similar datasets. Thus, any attempt to correct the individual images from PSF effect would introduce additional uncertainties. We will study the shape of the surface brightness profiles of the galaxies on the HUDF according to the new mosaics in a forthcoming paper (Borlaff et al. in prep).

Borlaff et al.: The missing light of the Hubble Ultra Deep Field

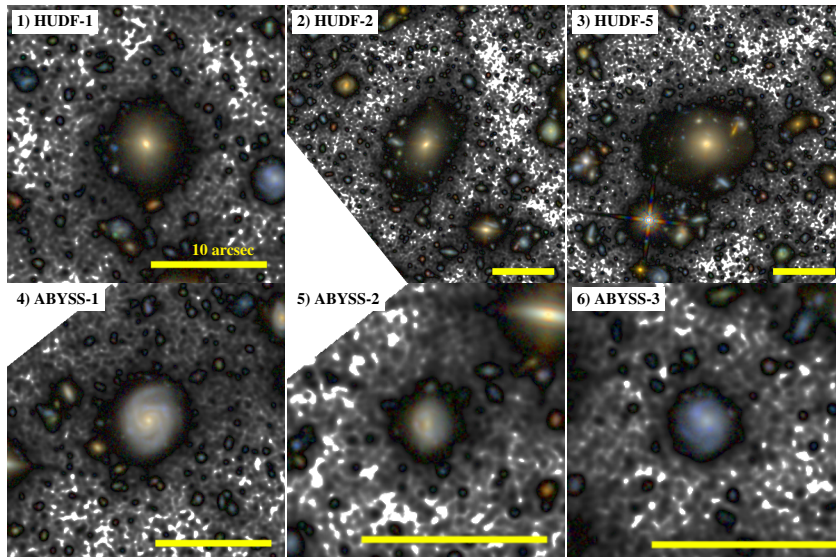


Fig. 17: Luminance-RGB images of the selected targets for the surface brightness profile analysis: Top row, from left to right: 1) HUDF-1 (24×24 arcsec), 2) HUDF-2 (45×45 arcsec), 3) HUDF-5 (45×45 arcsec). Bottom row, from left to right: 1) ABYSS-1 (24×24 arcsec), 2) ABYSS-2 (15×15 arcsec), 3) ABYSS-3 (15×15 arcsec). The yellow segment represents 10 arcsec in all images. The high signal-to-noise parts of the mosaics are represented with colours (red: F160W, green: mean of F125W and F140W bands, blue: F105W). The low signal-to-noise regions are represented as a black and white background (black regions are brighter than white regions) according to the mean image of the four mosaics (F105W, F125W, F140W, F160W).

ID (1)	IAU ID (2)	MUSE ID (3)	α (4) (degrees)	δ (5) (degrees)	z (6)	PA (7) (degrees)	b/a (8)	Sky background limiting radius (9) (kpc)
HUDF-1	J033237.30-274729.3	5	53.16164	-27.78025	0.618	-14.18	0.878	80
HUDF-2	J033241.40-274717.1	870	53.17254	-27.78812	0.619	-30.61	0.599	140
HUDF-5	J033237.30-274729.3	862	53.15545	-27.79150	0.667	75.18	0.900	140
ABYSS-1	J033240.78-274615.6	1	53.16993	-27.77106	0.622	-15.82	0.884	80
ABYSS-2	J033242.25-274625.3	916	53.17606	-27.77371	1.288	-3.31	0.890	80
ABYSS-3	J033237.96-274651.9	7	53.15815	-27.78109	0.620	64.69	0.860	80

Table 3: Selected targets for the surface brightness profile comparison of the HUDF WFC3/IR mosaics. Columns: 1) ID, 2) IAU ID, 3) MUSE catalog ID, 4) Right ascension (degrees), 5) Declination (degrees), 6) Spectroscopic z from the MUSE HUDF catalog (Bacon et al. 2017), 7) Position angle (degrees, anti-clockwise from North), 8) Axis ratio of the minor over the major axis, 9) Minimum galactocentric radius used to calculate the local sky background (kpc).

3.2.1. Surface brightness profiles of large objects

HUDF-5 (Buitrago et al. 2016) is an elliptical galaxy ($z = 0.667$, $\log_{10}(M/M_\odot) = 11.19^{+0.09}_{-0.05}$) and one of the brightest objects from the HUDF. It presents a noticeable shell envelope, and is one

of the objects most affected by the aggressive sky subtraction from the previous releases. In Figs. 18 and 19 we represent the intensity images of the six targets in the F105W filter (which is the deepest mosaic in our reduction) in three different panels, for the ABYSS, HUDF12, and XDF version of the mosaics. On top

Article number, page 23 of 36

Este documento incorpora firma electrónica, y es copia auténtica de un documento electrónico archivado por la ULL según la Ley 39/2015.
Su autenticidad puede ser contrastada en la siguiente dirección <https://sede.ull.es/validacion/>

Identificador del documento: 1630219

Código de verificación: NYPyuzSi

Firmado por: ALEJANDRO SERRANO BORLAFF
UNIVERSIDAD DE LA LAGUNA

Fecha: 26/10/2018 14:33:01

Juan Esteban Beckman Abramson
UNIVERSIDAD DE LA LAGUNA

26/10/2018 14:36:58

MARIA DEL CARMEN ELICHE MORAL
UNIVERSIDAD DE LA LAGUNA

26/10/2018 15:46:09

JOAN FONT SERRA
UNIVERSIDAD DE LA LAGUNA

26/10/2018 18:46:53

A&A proofs: manuscript no. output

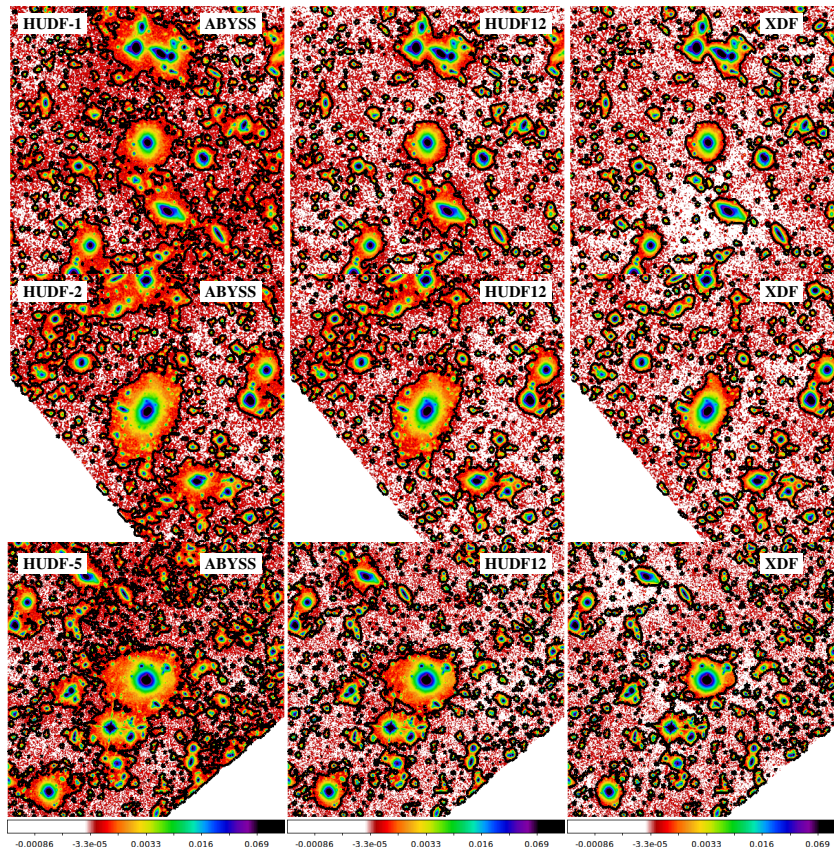


Fig. 18: F105W intensity images of HUDF-1 (top row, 54×54 arcsec), HUDF-2 (central row, 54×54 arcsec), and HUDF-5 (bottom row, 72×72 arcsec) for our version of the HUDF mosaics (ABYSS, left column), the HUDF12 mosaics (Koekemoer et al. 2012, central column), and the XDF mosaics (Illingworth et al. 2013, right column). The black contours represent the $\mu_{F105W} = 29$ mag arcsec $^{-2}$ isophote. All images are at the same colour scale.

of each panel we represent with black contours their respective $\mu = 29$ mag arcsec $^{-2}$ isophotes. We observe that: 1) the $\mu = 29$ mag arcsec $^{-2}$ isophotal contours are more extended in our reduction than in the previous versions of the mosaics, specially when compared to the XDF; and 2) the new diffuse light tends to appear around the largest objects on the field-of-view, while the objects with small angular size almost do not change their respective contours. This is a expected result, as aggressive sky-

subtraction tends to affect mostly to the envelopes of the largest objects.

Nevertheless, we note that the intensity images are not a direct proxy of the shape of the surface brightness profile, as they are not corrected by the small sky residuals that appear on the surface brightness profiles (local sky background). The same effect shown on Figs. 18 and 19 could be caused by sky background under-subtraction on our mosaics. In order to confirm the validity of these findings, we must analyse the surface bright-

Borlaff et al.: The missing light of the Hubble Ultra Deep Field

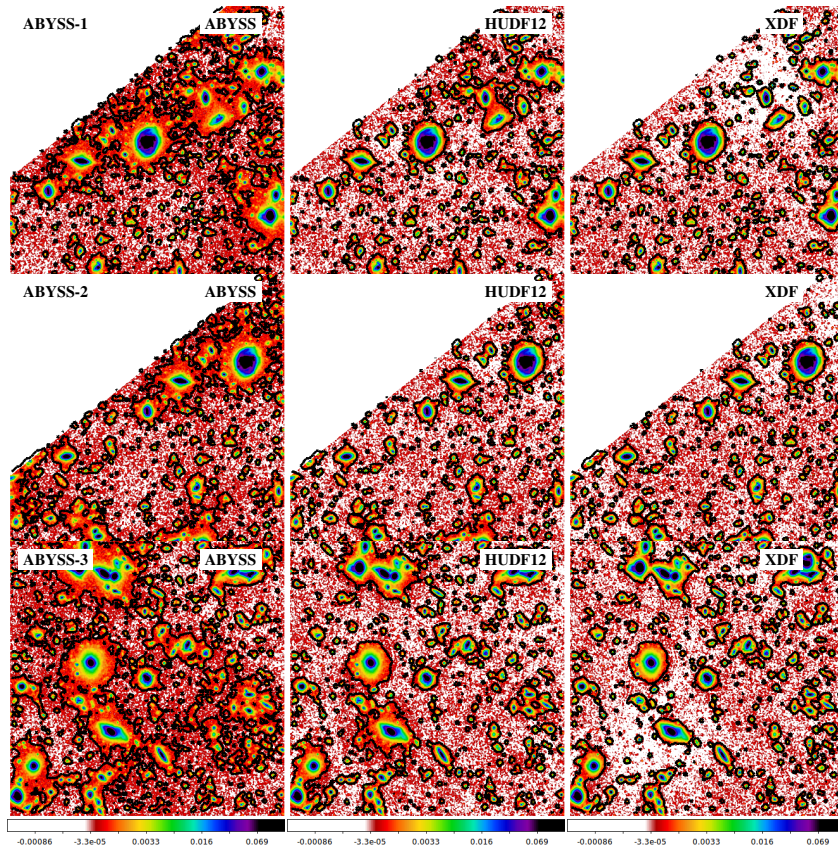


Fig. 19: F105W intensity images of ABYSS-1 (top row), ABYSS-2 (central row), and ABYSS-3 (bottom row) for our version of the HUDF mosaics (ABYSS, left column), the HUDF12 mosaics (Koekemoer et al. 2012, central column), and the XDF mosaics (Illingworth et al. 2013, right column). The field of view is 54×54 arcsec on all the images. The black contours represent the $\mu_{F105W} = 29$ mag arcsec $^{-2}$ isophote. All images are at the same colour scale.

ness profiles corrected by the local sky background of the target galaxy. In Fig. 20 we show the results of the surface brightness analysis for HUDF-5. We found several interesting results:

1. Even after applying a local sky level correction, the XDF mosaics present a significant over-subtraction when comparing to the HUDF12 or our dedicated mosaics. This effect is noticeable at surface magnitudes fainter than $\mu \sim 26 - 27$ mag arcsec $^{-2}$.
2. Our dedicated mosaics recover a significant amount of light when compared to the HUDF12 mosaics and the XDF. The maximum differences in surface brightness range from $\Delta\mu = 0.5 - 1.25$ mag arcsec $^{-2}$, being higher for the deeper images (F105W and F160W).
3. Interestingly, the XDF version of the F140W mosaic appears to be less over-subtracted than the rest of the filters, obtaining a limiting radius at $R \sim 10$ arcsec, while the rest of the filters reaches only $R \sim 8$ arcsec.

Article number, page 25 of 36

Este documento incorpora firma electrónica, y es copia auténtica de un documento electrónico archivado por la ULL según la Ley 39/2015.
Su autenticidad puede ser contrastada en la siguiente dirección <https://sede.ull.es/validacion/>

Identificador del documento: 1630219

Código de verificación: NYPyuzSi

Firmado por: ALEJANDRO SERRANO BORLAFF
 UNIVERSIDAD DE LA LAGUNA

Fecha: 26/10/2018 14:33:01

Juan Esteban Beckman Abramson
 UNIVERSIDAD DE LA LAGUNA

26/10/2018 14:36:58

MARIA DEL CARMEN ELICHE MORAL
 UNIVERSIDAD DE LA LAGUNA

26/10/2018 15:46:09

JOAN FONT SERRA
 UNIVERSIDAD DE LA LAGUNA

26/10/2018 18:46:53

A&A proofs: manuscript no. output

4. For the F105W, F125W, and F160W images, the surface brightness profiles of ABYSS extend much further out (up to $R \sim 25$ arcsec in the F105W and F160W bands) than in the HUDF12 and specially than the XDF mosaics, where the limit is almost 1/3 smaller than the limiting radius of the ABYSS mosaics.

The general agreement up to a certain radius of the HUDF12 and our reduction, contrary to the results obtained with the XDF, is a quantitative proof of that the latter mosaics present a high and systematic over-subtraction of the outskirts around the most extended objects, such as HUDF-5. The over-subtraction can be as high as $\Delta\mu \sim 1.5$ mag arcsec $^{-2}$ at a surface brightness magnitude of $\mu \sim 28$ mag arcsec $^{-2}$ for the XDF mosaics even after applying local sky correction. We obtain a similar result for the HUDF12 mosaics at $\mu \sim 29$ mag arcsec $^{-2}$. This result demonstrates that the depth of previous reductions was dominated by systematic biases rather than the sky noise. We also found interesting that the surface brightness profile of the shallower mosaic (F140W) of XDF presents $S/N > 3$ to larger galactocentric radius than the rest of the filters, which are much deeper. In addition, visual inspection of the surface brightness profiles from our images reveals that they tend to reach the sky level smoothly, following the general shape of the surface brightness profile, rather than showing a sharp down-bending profile at the outskirts as observed on the XDF profiles.

In Fig. A.1 we represent the surface brightness profiles of HUDF-1, another one of the elliptical galaxies studied in Buitrago et al. (2016). We found a very similar result as in the case of HUDF-5. The surface brightness profiles of the ABYSS mosaics recover a significant extension that has been completely removed in the case of XDF and HUDF12. Again, we find that the XDF is the most affected by over subtraction, with $\Delta\mu \sim 1.5$ mag arcsec $^{-2}$ with respect to the ABYSS profile at a surface brightness magnitude of $\mu \sim 29$ mag arcsec $^{-2}$. We recover also a significant amount of light compared to the HUDF12, reaching $\Delta\mu \sim 1.5$ mag arcsec $^{-2}$ at the limiting radius in the F105W and $\Delta\mu \sim 1$ mag arcsec $^{-2}$ in the rest of the images. The XDF profiles show a down-bending break that is not that strong in the HUDF12, and it is completely removed in our version of the mosaics, where the surface brightness profile reaches the sky level smoothly, following a nearly exponential shape.

We show the surface brightness profile analysis of HUDF-2 in Fig. A.2. For this object we detect a similar over subtraction of the XDF profiles. The XDF F160W surface brightness profile reaches $S/N = 3$ at half the extension of the ABYSS and HUDF12 profiles. Interestingly, we found that the ABYSS and HUDF12 profile agree remarkably well for this object, reaching the limiting S/N at very similar radius ($R_{lim} \sim 13$ arcsec, with the exception of F125W and F160W which extends to $R \sim 15.5 - 16$ arcsec). In F160W, we observe that the HUDF12 surface brightness profile is $\Delta\mu \sim 0.3$ mag arcsec $^{-2}$ brighter than the ABYSS between $R = 4$ and $R = 13$ arcsec. For the rest of the filters, the ABYSS surface brightness profiles are $\Delta\mu \sim 0.3$ brighter than the HUDF12 ones beyond $R > 11$ arcsec. This result agrees with the observed difference maps (see Sect. 3.1.1), where we detected more flux on the southern section of the F160W HUDF12 image than in our F160W ABYSS mosaic.

We continue the analysis with the spiral galaxy ABYSS-1 (see Table 3, and bottom left panel of Fig. 17). In Fig. A.3 we compare the surface brightness profiles based on our own reduction of the HUDF mosaics (ABYSS), the HUDF12, and the XDF, for the four different filters (F105W, F125W, F140W and F160W). We summarise the results in several points:

1. As in the case of HUDF-5, the surface brightness profiles from our dedicated mosaics present higher intensity and signal-to-noise ratio on the outskirts, up to radius of $R \sim 7 - 7.5$ arcsec. Similarly to the previous case, the maximum differences in surface brightness range from $\Delta\mu = 0.5 - 1.5$ mag arcsec $^{-2}$.
2. The F140W band surface brightness profiles for the ABYSS and XDF version of the mosaics present a more similar shape than in the previous cases.
3. The surface brightness profiles of the four filters of the ABYSS mosaics and the F140W from XDF suggest the presence of an extended component clearly detectable at $R > 5.5$ arcsec, which could be due to PSF effects or an extended stellar halo. The effect is less clear in the F125W image, which reaches $S/N = 3$ at $R \sim 6$ arcsec.
4. There is a clear discrepancy between different filters on the shapes of the profiles for the XDF version of the mosaics, being the F140W the most extended of all XDF surface brightness profiles and the only approaching our own reduction.

The presence of an extended component detectable beyond $R = 5$ arcsec in these surface brightness profile does not necessarily imply that it is associated with a physical component (i.e., a stellar halo). In order to identify the true nature of such extended light it would be necessary to estimate the amount of PSF scattered light from the nearby objects and the ABYSS-1 galaxy itself, in a similar way as done in Trujillo & Fliri (2016). As demonstrated in that work, the scattered light of the sources creates a background of light that contaminates the images and the surface brightness profiles. Assuming that the observer knows the behaviour of the PSF, it is possible to model and correct it, recovering the true shape of the objects to a certain degree (see Borlaff et al. 2017, for a similar work with HST/ACS data on GOODS-N). Nevertheless, such field of scattered light can be easily mistaken with the sky background. Removing it from the final mosaics in the reduction process neglects the possibility of recovering the information at the very low surface brightness limits.

A detailed analysis of the new low surface brightness structures is well beyond the scope of the present paper and will be addressed in a forthcoming paper (Borlaff et al. in prep). We conclude that the surface brightness profiles that we present are a valid benchmark between the different reduction processes, as they use the same masks and surface brightness profile analysis and local sky background correction procedure. In addition, we found that our reduction process allows us to recover up to $\Delta\mu \sim 1 - 1.5$ mag arcsec $^{-2}$ on the surface brightness profiles when compared to the previous versions of the HUDF WFC3/IR mosaics and almost twice the radial size when compared to the XDF surface brightness profiles, even after local sky background correction.

3.2.2. Surface brightness profiles of small objects

In this section we will analyse the properties of the surface brightness profiles of ABYSS-2 and ABYSS-3 (see Table 3), two spiral galaxies with smaller angular sizes compared to the previous targets. The main objective is to do a consistency test and determine if there is any significant differences on the surface brightness profiles of such objects when comparing to the previous versions of the mosaics.

In Fig. A.4 we show the surface brightness profiles of the spiral galaxy ABYSS-2. Given that the aggressive sky background correction applied on the previous versions of the HUDF affected

Article number, page 26 of 36

Este documento incorpora firma electrónica, y es copia auténtica de un documento electrónico archivado por la ULL según la Ley 39/2015.
Su autenticidad puede ser contrastada en la siguiente dirección <https://sede.ull.es/validacion/>

Identificador del documento: 1630219

Código de verificación: NYPyuzSi

Fecha: 26/10/2018 14:33:01

Firmado por: ALEJANDRO SERRANO BORLAFF
 UNIVERSIDAD DE LA LAGUNA

Juan Esteban Beckman Abramson
 UNIVERSIDAD DE LA LAGUNA

MARIA DEL CARMEN ELICHE MORAL
 UNIVERSIDAD DE LA LAGUNA

JOAN FONT SERRA
 UNIVERSIDAD DE LA LAGUNA

26/10/2018 14:36:58

26/10/2018 15:46:09

26/10/2018 18:46:53

Borlaff et al.: The missing light of the Hubble Ultra Deep Field

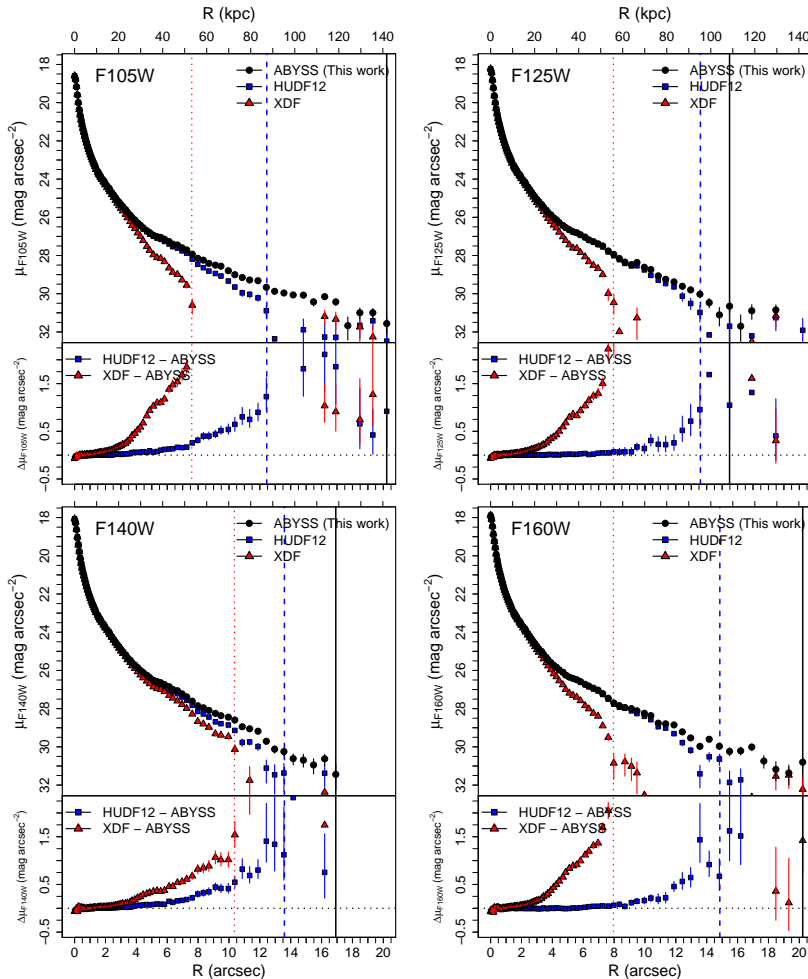


Fig. 20: Comparison of the surface brightness profiles of the elliptical galaxy HUDF-5 ($\alpha = 53.15545$, $\delta = -27.79150$, Buitrago et al. 2016) for the F105W (top left), F125W (top right), F140W (bottom left) and F160W filters (bottom right), using our own reduction of the HUDF WFC3 mosaics (ABYSS, black dots), the HUDF12 (Koekemoer et al. 2012, blue squares) and the XDF (Illingworth et al. 2013, red triangles). The top plot of each panel shows the surface brightness profile for each reduction. Black solid, blue dashed and red dotted lines represent the elliptic aperture with largest semi-major axis that presents a signal-to-noise ratio higher than 3 over the sky-level. The bottom plot represents the difference in magnitude of each previous reduction with the ABYSS version of the mosaics as a function of galactocentric radius. Consult the legend on the figure.

Article number, page 27 of 36

Este documento incorpora firma electrónica, y es copia auténtica de un documento electrónico archivado por la ULL según la Ley 39/2015.
 Su autenticidad puede ser contrastada en la siguiente dirección <https://sede.ull.es/validacion/>

Identificador del documento: 1630219

Código de verificación: NYPyuzSi

Firmado por: ALEJANDRO SERRANO BORLAFF
 UNIVERSIDAD DE LA LAGUNA

Fecha: 26/10/2018 14:33:01

Juan Esteban Beckman Abramson
 UNIVERSIDAD DE LA LAGUNA

26/10/2018 14:36:58

MARIA DEL CARMEN ELICHE MORAL
 UNIVERSIDAD DE LA LAGUNA

26/10/2018 15:46:09

JOAN FONT SERRA
 UNIVERSIDAD DE LA LAGUNA

26/10/2018 18:46:53

A&A proofs: manuscript no. output

specially to the most extended objects, the surface brightness profiles of more compact objects should be more similar than the large objects, regardless of the version of the mosaics. Indeed, we find that the structure of the surface brightness profiles is more similar in the case of ABYSS-2 than in the previous ones, especially in comparison with HUDF-5. The surface brightness differences are reduced to $\Delta\mu \sim 0.5$ mag arcsec $^{-2}$ at the limiting radius, and the relative differences between the HUDF12 and the XDF are notably smaller. Moreover, we still detect that the F140W profile of XDF has a more similar shape to our surface brightness profiles of ABYSS mosaics, suggesting that the over-subtraction could be less aggressive in this filter than in the rest. In addition to these results, we detect a tail of extended light in the ABYSS mosaics (possibly due to PSF scattered light) which dominates the surface brightness profile from $R \sim 2 - 2.5$ arcsec and it is not visible on the previous versions on the HUDF. This result is compatible with the analysis of ABYSS-1.

Finally, we analyse the surface brightness profile of ABYSS-3 (see Fig. A.5). This is the smallest object of all the six selected galaxies. The surface brightness profile shows a clear exponential decline without deviations (with small signs of a down-bending at $R \sim 1.5$ arcsec) until the limiting radius. We find no signs of a bulge at the inner regions. For this object we find a remarkably good agreement between the three versions of the mosaics, obtaining very similar limiting radii for all of them on each band ($R_{lim} \sim 2.8 - 3.2$ arcsec) and no significant differences on the surface brightness profiles along all the visible radius. We do not find signs of extended scattered light, in contrast to the profiles of ABYSS-2.

Therefore, the photometry and structure of objects with relatively small angular sizes is similar and compatible to that observed in the previous versions of the HUDF. This analysis provides a consistency test, demonstrating that our mosaics preserve the properties of the small objects while recovering the extended light from the largest sources in the field of view. The results provided here demonstrate that the cause of the differences in flux between the XDF and HUDF12 is a systematic bias caused by over-subtraction of the sky background. We show that our reduction pipeline provides a viable process to reduce systematic biases prior to the co-adding of the final mosaics. This process reduces the need for sky background subtraction, while preserving the structure of the brightest galaxies and their extended envelopes, maintaining the limiting magnitude of the faintest objects at the same time.

4. Conclusions

The low surface brightness Universe is the next frontier for many studies in galaxy evolution and cosmology. Many observational and theoretical works demonstrate that there are very extended and complex structures larger than the visible size of their host galaxies below the limiting magnitude of most current surveys. Moreover, the cosmological dimming substantially limits our capabilities to study the structure of extended objects at high redshift, most of which are only accessible through space-based observations. It is then mandatory to improve the reduction techniques of the cosmological deep fields from HST and other space telescopes. In this paper we test a number of corrections to improve the low surface brightness limits of the HUDF WFC3/IR mosaics. We have obtained a dedicated version of the images which we named ABYSS which we made publicly available for the benefit and use of all the astronomical community. We found several interesting results:

1. The XDF version of the HUDF WFC3/IR mosaics is dominated by a systematic bias in the form of a significant over-subtraction of the sky background around the objects with large angular size. A similar result (to a lesser extent) is obtained for the HUDF12. We successfully recover a significant amount of over-subtracted diffuse light around the largest objects of the HUDF, not detected by the previous versions of the mosaics. The integrated magnitude of the recovered light is equivalent to a $m \sim 19$ mag object for the XDF and $m \sim 20$ mag for the HUDF12 mosaics, comparable to the brightest galaxies on the image.

2. A significant fraction of the images of the HUDF are (at least partially) affected by persistence effects at the very low surface brightness regime, biasing the sky background estimation. The cause of this is the observation of bright sources (astronomical or calibration runs) in the previous hours to the scheduled HUDF observations.

3. We propose and test a sky background correction method, based on careful masking using noise-based, non-parametric methods as Gnuastro/NoiseOhisel to detect and flag the extended envelopes of the sources on the field of view. We demonstrate that this method can improve the sky background determination more than one order of magnitude.

4. We studied the surface brightness profiles of six objects in the HUDF, demonstrating that our reduction pipeline can preserve the properties of the smallest sources in the HUDF, while recovering the low surface brightness structures of the outskirts of the largest galaxies.

Systematic biases can dominate over the sky noise. It is for this reason that the noise level of the mosaics is not always a good proxy of the real depth of astronomical images. The measured value of the intensity dispersion of the sky dominated pixels it is not very sensitive to the effects of sky background over-subtraction. Hypothetically, an image reduced with a sky-subtraction process that completely fits and subtracts the sources on the field of view might obtain a similar surface brightness limiting magnitude (measured as the standard deviation of sky-noise level) as a reduction that preserves the outskirts of the largest sources. The latter image clearly contains more information and therefore is deeper than the over-subtracted version, despite of having the same formal surface brightness limiting magnitude. We have shown that, despite the small loss of exposure time and the corresponding slight increase of surface brightness limiting magnitudes, our mosaics contain more signal and information about the outskirts of galaxies than previous versions of the WFC3/IR HUDF.

Most, if not all of these problems will be found on the deep observations to be performed by HST near IR successor, the JWST. In particular, persistence will be present in its three image detectors (NIRCam, NIRISS, and MIRI). Mitigation of persistence effects on JWST deep cosmological surveys (Leisering et al. 2016) have to be based mainly on the following observational strategy: 1) careful scheduling of the previous observations and 2) large dithering patterns to avoid observing regions of the sky with those regions that are affected by persistence on all the exposures. In addition, deep and wide survey dedicated missions, (i.e., EUCLID, MESSIER) can improve their results using these techniques, which would enable a new generation of low surface brightness studies based on their legacy data.

Article number, page 28 of 36

Este documento incorpora firma electrónica, y es copia auténtica de un documento electrónico archivado por la ULL según la Ley 39/2015.
Su autenticidad puede ser contrastada en la siguiente dirección <https://sede.ull.es/validacion/>

Identificador del documento: 1630219

Código de verificación: NYPyuzSi

Fecha: 26/10/2018 14:33:01

Firmado por: ALEJANDRO SERRANO BORLAFF
 UNIVERSIDAD DE LA LAGUNA

Juan Esteban Beckman Abramson
 UNIVERSIDAD DE LA LAGUNA

MARIA DEL CARMEN ELICHE MORAL
 UNIVERSIDAD DE LA LAGUNA

JOAN FONT SERRA
 UNIVERSIDAD DE LA LAGUNA

26/10/2018 14:36:58

26/10/2018 15:46:09

26/10/2018 18:46:53

Borlaff et al.: The missing light of the Hubble Ultra Deep Field

In this paper we have reviewed many of these systematic effects and proposed solutions to them, applying the methods on the deepest image of the Universe ever taken, the HUDF, creating our own version called ABYSS: a low surface brightness dedicated reduction for the HUDF WFC3/IR mosaics. We make the results and the calibration files publicly available to the community - as well as the ABYSS pipeline,¹ hoping to promote further analysis and improvements to the proposed reduction methods.

Acknowledgements. The authors would like to thank the XDF and HUDF12 teams for their extraordinary work in which this contribution is based on, truly standing on the shoulders of giants. This work would not have been possible without the kind assistance of all the members of the STScI Help Desk. We specially thank Knox Long by its work on persistence effects and its extraordinary support during this work. Some/all of the data presented in this paper were obtained from the Mikulski Archive for Space Telescopes (MAST). STScI is operated by the Association of Universities for Research in Astronomy, Inc., under NASA contract NAS5-26555. I.T acknowledges the support from the SUNDIAL EU Network and from the European Union's Horizon 2020 research and innovation programme under Marie Skłodowska-Curie grant agreement No 721463 and the SUNDIAL ITN network. N.C acknowledged support from the Spanish Programa Nacional de Astronomía y Astrofísica under grant AYA2016-75808-R. C.G.G. acknowledges support from the European Research Council (ERC) Consolidator Grant funding scheme (project ConTExt, grant number 648179). Support for MAST for non-HST data is provided by the NASA Office of Space Science via grant NNX09AF08G and by other grants and contracts. This work was partly done using GNU Astronomy Utilities Gnuastro version 0.5. Gnuastro is a generic package for astronomical data manipulation and analysis which was primarily created and developed for research funded by the Monbukagakusho (Japanese government) scholarship and ERC advanced grant 339659-MUSICOS. Support for this work was provided by the Spanish Ministerio de Economía y Competitividad (MINECO, grant AYA 2016-77237-C3-1-P).

¹ ABYSS is a low surface brightness dedicated reduction for the HUDF WFC3/IR mosaics. It is freely/publicly available at <http://www.iac.es/proyecto/abyss/>

Este documento incorpora firma electrónica, y es copia auténtica de un documento electrónico archivado por la ULL según la Ley 39/2015.
Su autenticidad puede ser contrastada en la siguiente dirección <https://sede.ull.es/validacion/>

Identificador del documento: 1630219

Código de verificación: NYPyuzSi

Firmado por: ALEJANDRO SERRANO BORLAFF UNIVERSIDAD DE LA LAGUNA	Fecha: 26/10/2018 14:33:01
Juan Esteban Beckman Abramson UNIVERSIDAD DE LA LAGUNA	26/10/2018 14:36:58
MARIA DEL CARMEN ELICHE MORAL UNIVERSIDAD DE LA LAGUNA	26/10/2018 15:46:09
JOAN FONT SERRA UNIVERSIDAD DE LA LAGUNA	26/10/2018 18:46:53

A&A proofs: manuscript no. output

Appendix A: Surface brightness profiles of the objects commented in Section 3.2

In this appendix we show the surface brightness profiles for the five objects (HUDF-1, HUDF-2, ABYSS-1, ABYSS-2, and ABYSS-3, see Table 3) analysed on Sect. 3.2, comparing the results for the ABYSS, XDF, and HUDF12 versions on the mosaics.

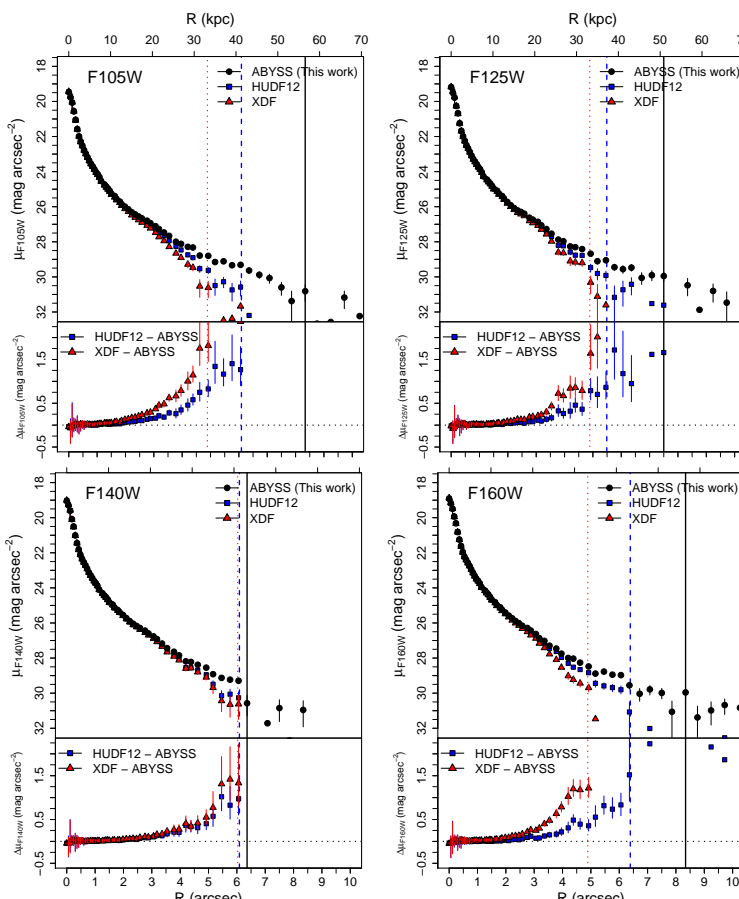


Fig. A.1: Comparison of the surface brightness profiles of the elliptical galaxy HUDF-1 ($\alpha = 53.16164, \delta = -27.78025$ Buitrago et al. 2016) for the F105W (top left), F125W (top right), F140W (bottom left), and F160W filters (bottom right), using our own reduction of the HUDF WFC3 mosaics (ABYSS, black dots), the HUDF12 (Koekemoer et al. 2012, blue squares), and the XDF (Illingworth et al. 2013, red triangles). The top plot of each panel shows the surface brightness profile for each reduction. Black solid, blue dashed, and red dotted lines represent the elliptical aperture with largest semi-major axis that presents a S/N ratio higher than 3 over the sky-level. The bottom plot represents the difference in magnitude of each previous reduction with the ABYSS version of the mosaics as a function of galactocentric radius. Consult the legend on the figure.

Article number, page 30 of 36

Este documento incorpora firma electrónica, y es copia auténtica de un documento electrónico archivado por la ULL según la Ley 39/2015.
Su autenticidad puede ser contrastada en la siguiente dirección <https://sede.ull.es/validacion/>

Identificador del documento: 1630219

Código de verificación: NYPyuzSi

Firmado por: ALEJANDRO SERRANO BORLAFF
 UNIVERSIDAD DE LA LAGUNA

Fecha: 26/10/2018 14:33:01

Juan Esteban Beckman Abramson
 UNIVERSIDAD DE LA LAGUNA

26/10/2018 14:36:58

MARIA DEL CARMEN ELICHE MORAL
 UNIVERSIDAD DE LA LAGUNA

26/10/2018 15:46:09

JOAN FONT SERRA
 UNIVERSIDAD DE LA LAGUNA

26/10/2018 18:46:53

Borlaff et al.: The missing light of the Hubble Ultra Deep Field

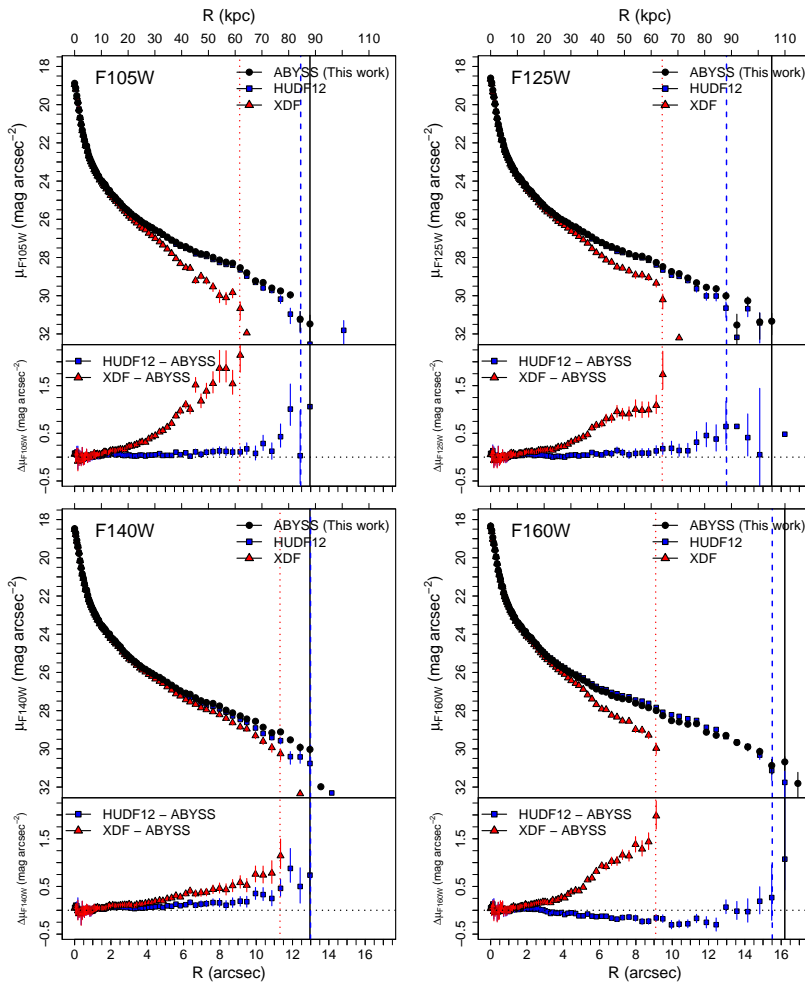


Fig. A.2: Comparison of the surface brightness profiles of the elliptical galaxy HUDF-2 ($\alpha = 53.17254, \delta = -27.78812$ Buitrago et al. 2016) for the F105W (top left), F125W (top right), F140W (bottom left), and F160W filters (bottom right), using our own reduction of the HUDF WFC3 mosaics (ABYSS, black dots), the HUDF12 (Koekemoer et al. 2012, blue squares) and the XDF (Illingworth et al. 2013, red triangles). The top plot of each panel shows the surface brightness profile for each reduction. Black solid, blue dashed and red dotted lines represent the elliptic aperture with largest semi-major axis that presents a signal-to-noise ratio higher than 3 over the sky-level. The bottom plot represents the difference in magnitude of each previous reduction with the ABYSS version of the mosaics as a function of galactocentric radius. Consult the legend on the figure.

Article number, page 31 of 36

Este documento incorpora firma electrónica, y es copia auténtica de un documento electrónico archivado por la ULL según la Ley 39/2015.
Su autenticidad puede ser contrastada en la siguiente dirección <https://sede.ull.es/validacion/>

Identificador del documento: 1630219

Código de verificación: NYPyuzSi

Firmado por: ALEJANDRO SERRANO BORLAFF
 UNIVERSIDAD DE LA LAGUNA

Fecha: 26/10/2018 14:33:01

Juan Esteban Beckman Abramson
 UNIVERSIDAD DE LA LAGUNA

26/10/2018 14:36:58

MARIA DEL CARMEN ELICHE MORAL
 UNIVERSIDAD DE LA LAGUNA

26/10/2018 15:46:09

JOAN FONT SERRA
 UNIVERSIDAD DE LA LAGUNA

26/10/2018 18:46:53

A&A proofs: manuscript no. output

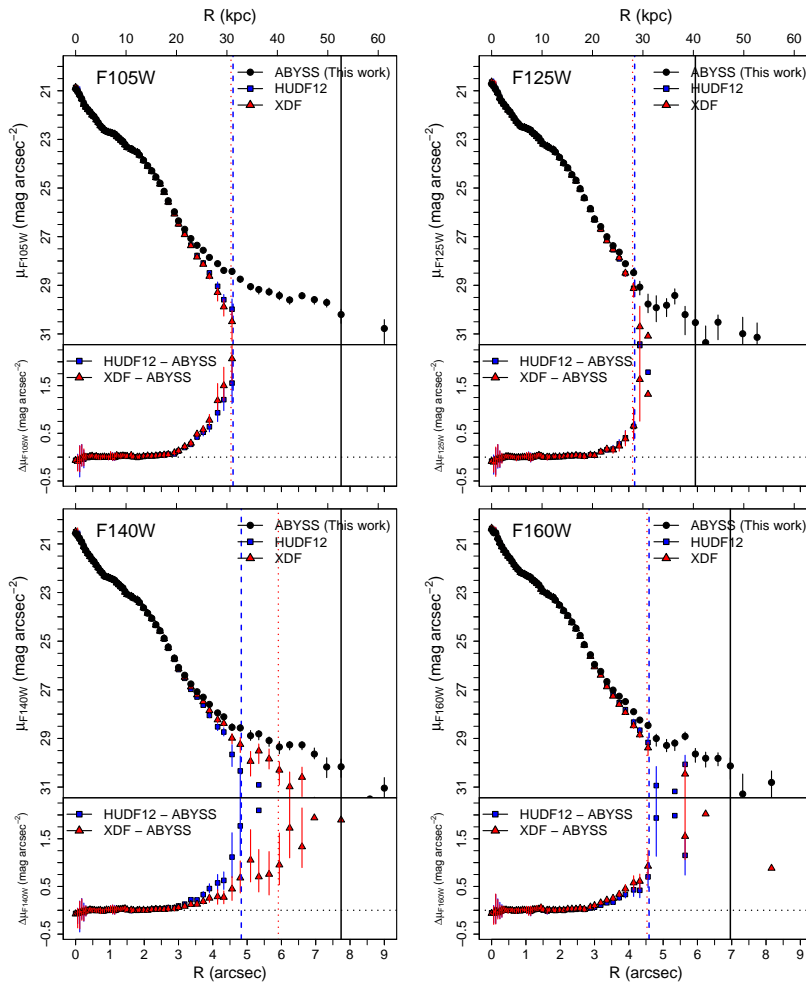


Fig. A.3: Comparison of the surface brightness profiles of the spiral galaxy ABYSS-1 ($\alpha = 53.16993$, $\delta = -27.77106$, Elmegreen et al. 2005) for the F105W (top left), F125W (top right), F140W (bottom left), and F160W filters (bottom right), using our own reduction of the HUDF WFC3 mosaics (ABYSS, black dots), the HUDF12 (Koekemoer et al. 2012, blue squares), and the XDF (Illingworth et al. 2013, red triangles). The top plot of each panel shows the surface brightness profile for each reduction. Black solid, blue dashed, and red dotted lines represent the elliptical aperture with largest semi-major axis that presents a S/N ratio higher than 3 over the sky-level. The bottom plot represents the difference in magnitude of each previous reduction with the ABYSS version of the mosaics as a function of galactocentric radius. Consult the legend on the figure.

Article number, page 32 of 36

Este documento incorpora firma electrónica, y es copia auténtica de un documento electrónico archivado por la ULL según la Ley 39/2015.
Su autenticidad puede ser contrastada en la siguiente dirección <https://sede.ull.es/validacion/>

Identificador del documento: 1630219

Código de verificación: NYPyuzSi

Firmado por: ALEJANDRO SERRANO BORLAFF
 UNIVERSIDAD DE LA LAGUNA

Fecha: 26/10/2018 14:33:01

Juan Esteban Beckman Abramson
 UNIVERSIDAD DE LA LAGUNA

26/10/2018 14:36:58

MARIA DEL CARMEN ELICHE MORAL
 UNIVERSIDAD DE LA LAGUNA

26/10/2018 15:46:09

JOAN FONT SERRA
 UNIVERSIDAD DE LA LAGUNA

26/10/2018 18:46:53

Borlaff et al.: The missing light of the Hubble Ultra Deep Field

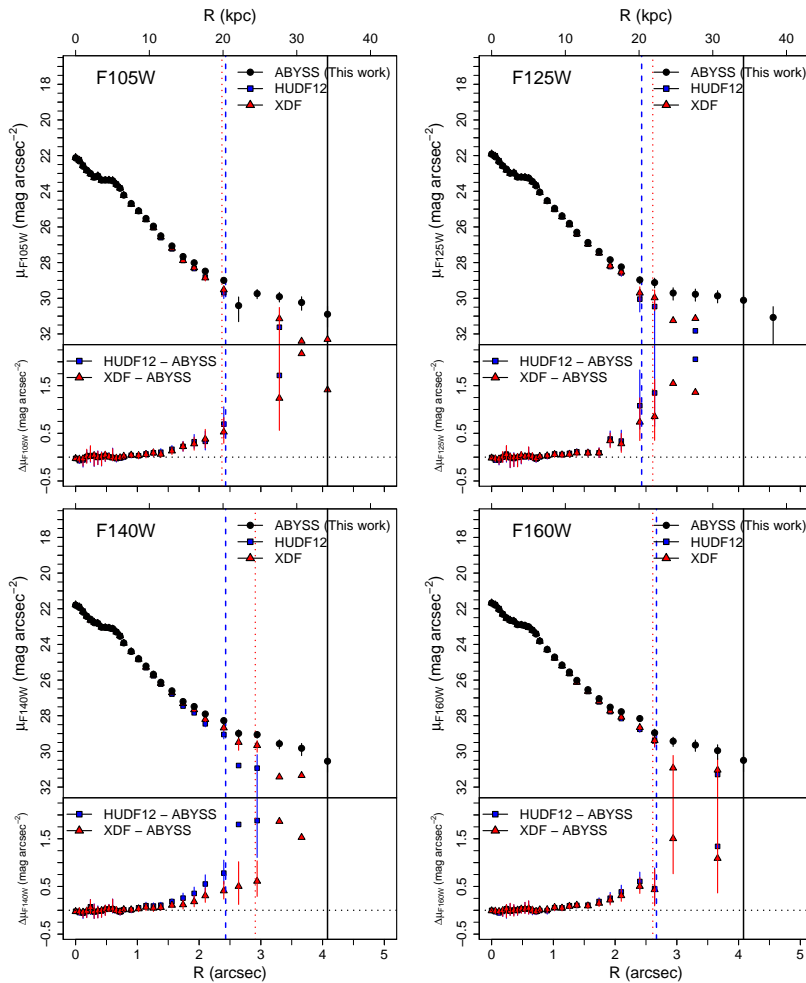


Fig. A.4: Comparison of the surface brightness profiles of the spiral galaxy ABYSS-2 ($\alpha = 53.17606$, $\delta = -27.77371$, Elmegreen et al. 2005) for the F105W (top left), F125W (top right), F140W (bottom left), and F160W filters (bottom right), using our own reduction of the HUDF WFC3 mosaics (ABYSS, black dots), the HUDF12 (Koekemoer et al. 2012, blue squares), and the XDF (Illingworth et al. 2013, red triangles). The top plot of each panel shows the surface brightness profile for each reduction. Black solid, blue dashed, and red dotted lines represent the elliptical aperture with largest semi-major axis that presents a S/N ratio higher than 3 over the sky-level. The bottom plot represents the difference in magnitude of each previous reduction with the ABYSS version of the mosaics as a function of galactocentric radius. Consult the legend on the figure.

Article number, page 33 of 36

Este documento incorpora firma electrónica, y es copia auténtica de un documento electrónico archivado por la ULL según la Ley 39/2015.
Su autenticidad puede ser contrastada en la siguiente dirección <https://sede.ull.es/validacion/>

Identificador del documento: 1630219

Código de verificación: NYPyuzSi

Firmado por: ALEJANDRO SERRANO BORLAFF
 UNIVERSIDAD DE LA LAGUNA

Fecha: 26/10/2018 14:33:01

Juan Esteban Beckman Abramson
 UNIVERSIDAD DE LA LAGUNA

26/10/2018 14:36:58

MARIA DEL CARMEN ELICHE MORAL
 UNIVERSIDAD DE LA LAGUNA

26/10/2018 15:46:09

JOAN FONT SERRA
 UNIVERSIDAD DE LA LAGUNA

26/10/2018 18:46:53

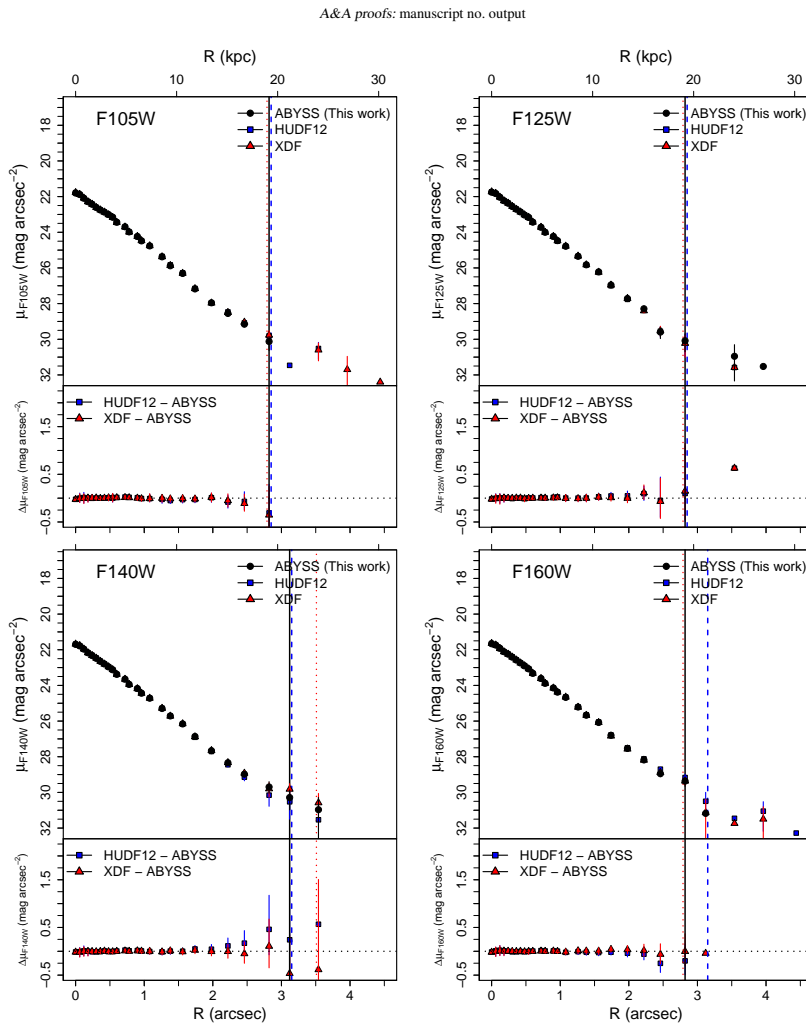


Fig. A.5: Comparison of the surface brightness profiles of the spiral galaxy ABYSS-3 ($\alpha = 53.15815$, $\delta = -27.78109$, Elmegreen et al. 2005) for the F105W (top left), F125W (top right), F140W (bottom left), and F160W filters (bottom right), using our own reduction of the HUDF WFC3 mosaics (ABYSS, black dots), the HUDF12 (Koekemoer et al. 2012, blue squares), and the XDF (Illingworth et al. 2013, red triangles). The top plot of each panel shows the surface brightness profile for each reduction. Black solid, blue dashed, and red dotted lines represent the elliptical aperture with largest semi-major axis that presents a S/N ratio higher than 3 over the sky-level. The bottom plot represents the difference in magnitude of each previous reduction with the ABYSS version of the mosaics as a function of galactocentric radius. Consult the legend on the figure.

Article number, page 34 of 36

Este documento incorpora firma electrónica, y es copia auténtica de un documento electrónico archivado por la ULL según la Ley 39/2015.
Su autenticidad puede ser contrastada en la siguiente dirección <https://sede.ull.es/validacion/>

Identificador del documento: 1630219

Código de verificación: NYPyuzSi

Firmado por: ALEJANDRO SERRANO BORLAFF
 UNIVERSIDAD DE LA LAGUNA

Fecha: 26/10/2018 14:33:01

Juan Esteban Beckman Abramson
 UNIVERSIDAD DE LA LAGUNA

26/10/2018 14:36:58

MARIA DEL CARMEN ELICHE MORAL
 UNIVERSIDAD DE LA LAGUNA

26/10/2018 15:46:09

JOAN FONT SERRA
 UNIVERSIDAD DE LA LAGUNA

26/10/2018 18:46:53

References

- Abadi, M. G., Navarro, J. F., & Steinmetz, M. 2005, Monthly Notices of the Royal Astronomical Society, Volume 365, Issue 3, pp. 747-758., 365, 747
- Aihara, H., Armstrong, R., Bickerton, S., et al. 2018, PASJ, 70, 88
- Akhlaghi, M. 2016, ArXiv e-prints
- Akhlaghi, M. & Ichikawa, T. 2015, ApJS, 220, 1
- Aravena, M., Decarli, R., Walter, F., et al. 2016a, The Astrophysical Journal, Volume 833, Issue 1, article id. 71, 22 pp. (2016), 833
- Aravena, M., Decarli, R., Walter, F., et al. 2016b, The Astrophysical Journal, Volume 833, Issue 1, article id. 71, 22 pp. (2016), 833
- Azzolini, R., Trujillo, I., & Beckman, J. E. 2008a, The Astrophysical Journal Letters, Volume 679, Issue 2, pp. L69 (2008)., 679, L69
- Azzolini, R., Trujillo, I., & Beckman, J. E. 2008b, The Astrophysical Journal, Volume 684, Issue 2, pp. 1026-1047 (2008)., 684, 1026
- Bacon, R., Consel, S., May, D., et al. 2017
- Beckwith, S. V. W., Stiavelli, M., Koekemoer, A. M., et al. 2006, AJ, 132, 1729
- Bertin, E. & Arnouts, S. 1996, Astronomy and Astrophysics Supplement Series, 117, 393
- Bohlin, R. C., Mack, J., & Biretta, J. 2008, Instrument Science Report WFPC2 2008-01, 7 pages
- Borlaff, A., Eliche-Moral, M. C., Beckman, J. E., et al. 2017, Astronomy & Astrophysics, Volume 604, id.A119, 71 pp., 604
- Borlaff, A., Eliche-Moral, M. C., Beckman, J. E., et al. 2018, A&A, 615, A26
- Borlaff, A., Eliche-Moral, M. C., Rodríguez-Pérez, C., et al. 2014, Astronomy & Astrophysics, Volume 570, id.A103, 30 pp., 570
- Bouwens, R. J., Illingworth, G. D., Oesch, P. A., et al. 2009, The Astrophysical Journal Letters, Volume 709, Issue 2, pp. L133-L137 (2010)., 709, L133
- Brammer, G., Pirzkal, N., McCullough, P., & MacKenty, J. 2014, Instrument Science Report WFPC3 2014-03, 14 pages
- Buitrago, F., Trujillo, I., Curtiss-Lake, E., et al. 2016, Monthly Notices of the Royal Astronomical Society, 466, stw3382
- Bullock, J. S. & Johnston, K. V. 2005, The Astrophysical Journal, Volume 635, Issue 2, pp. 931-949., 635, 931
- Bushouse, H. 2008, WFPC3 Instrument Science Report 2008-28, 14 pages
- Calvi, V. 2014
- Chonis, T. S., Martínez-Delgado, D., Gabany, R. J., et al. 2011, The Astronomical Journal, Volume 142, Issue 5, article id. 166, 15 pp. (2011)., 142
- Comastri, A., Ranalli, P., Iwasawa, K., et al. 2011, Astronomy and Astrophysics, Volume 526, id.L9, 6 pp., 526
- Comerón, S., Elmegreen, B. G., Salo, H., et al. 2012, The Astrophysical Journal, Volume 759, Issue 2, article id. 98, 29 pp. (2012)., 759
- Comerón, S., Elmegreen, B. G., Salo, H., et al. 2014, A&A, 571, A58
- Cooper, A. P., Cole, S., Frenk, C. S., et al. 2009, Monthly Notices of the Royal Astronomical Society, Volume 406, Issue 2, pp. 744-766., 406, 744
- Dressel, L. 2012, Wide Field Camera 3, HST Instrument Handbook
- Dunlop, J. S., McLure, R. J., Strick, C. B., et al. 2016
- Elmegreen, B. G., & Strick, C. B. 2016, The Astrophysical Journal, Volume 830, Issue 2, article id. 115, 8 pp. (2016)., 830
- Elmegreen, D. M., Elmegreen, B. G., Rubin, D. S., & Schaffer, M. A. 2005, The Astrophysical Journal, Volume 631, Issue 1, pp. 85-100., 631, 85
- Erwin, P., Beckman, J. E., & Pohlen, M. 2005, The Astrophysical Journal, Volume 626, Issue 2, pp. L81-184., 626, L81
- Erwin, P., Pohlen, M., & Beckman, J. E. 2007, The Astronomical Journal, Volume 135, Issue 1, pp. 20-54 (2008)., 135, 20
- Fowler, J., Markwardt, L., Bourque, M., & Anderson, J. 2017, Instrument Science Report WFPC3 2017-02 (v.1), 14 pages
- Fruchter, A. S. & Hooi, R. N. 1998, The Publications of the Astronomical Society of the Pacific, Volume 114, Issue 792, pp. 144-152., 114, 144
- Giacconi, R., Zirm, A., Wang, J., et al. 2002, The Astrophysical Journal Supplement Series, 139, 369
- Giavalisco, M., Team, t. G., Koekemoer, A. M., et al. 2003, The Astrophysical Journal, Volume 600, Issue 2, pp. L93-198., 600, L93
- Gonzaga, S., Hack, W., Fruchter, A., & Mack, J. 2012, The DrizzlePac Handbook, HST Data Handbook
- Greenfield, P. & Miller, T. 2016, Astronomy and Computing, 16, 41
- Gutierrez, L., Erwin, P., Aladro, R., & Beckman, J. E. 2011, The Astronomical Journal, Volume 142, Issue 5, article id. 145, 31 pp. (2011)., 142
- Herpich, J., Stinson, G. S., Dutton, A. A., et al. 2015a, Monthly Notices of the Royal Astronomical Society: Letters, Volume 448, Issue 1, p.L99-L103, 448, 199
- Herpich, J., Stinson, G. S., Rix, H.-W., Marin, M., & Dutton, A. A. 2015b, Monthly Notices of the Royal Astronomical Society, Volume 470, Issue 4, p.4941-4955, 470, 4941
- Horton, A., Spitler, L., Mathers, N., et al. 2016, Proceedings of the SPIE, Volume 9904, id. 99041Q 20 pp. (2016)., 9904
- Ibata, R., Mouchine, M., & Rejkuba, M. 2009, Monthly Notices of the Royal Astronomical Society, Volume 395, Issue 1, pp. 126-143., 395, 126
- Ibata, R. A., Lewis, G. F., McConnachie, A. W., et al. 2013, The Astrophysical Journal, Volume 780, Issue 2, article id. 128, 20 pp. (2014)., 780
- Illingworth, G. D., Magee, D., Oesch, P. A., et al. 2013, The Astrophysical Journal Supplement, Volume 209, Issue 1, article id. 6, 13 pp. (2013)., 209
- Ji, I., Hasan, I., Schmidt, S. J., & Tyson, J. A. 2018, PASP, 130, 084504
- Johnston, K. V., Bullock, J. S., Shima, S., et al. 2008, The Astrophysical Journal, Volume 689, Issue 2, pp. 936-957 (2008)., 689, 936
- Kazantzidis, S., Zehner, A. R., Kravtsov, A. V., Bullock, J. S., & Debattista, V. P. 2009, The Astrophysical Journal, Volume 700, Issue 2, pp. 1896-1920 (2009)., 700, 1896
- Koekemoer, A. M., Ellis, R. S., McLure, R. J., et al. 2012, The Astrophysical Journal Supplement, Volume 209, Issue 1, article id. 3, 14 pp. (2013)., 209
- Koekemoer, A. M. e. a. 2002, HST Dither Handbook, HST Data Handbooks
- Kozhurina-Platais, V., Dulude, M., Dahle, T., & Cox, C. 2012, Instrument Science Report WFC 2012-07, 13 pages
- Lahde, I., Oesch, P. A., Illingworth, G. D., et al. 2015, The Astrophysical Journal Supplement Series, Volume 221, Issue 2, article id. 23, 13 pp. (2015)., 221
- Laurikainen, E., & Salo, H. 2001, Monthly Notices of the Royal Astronomical Society, 324, 685
- Leisnering, J. M., Rieke, M., Misselt, K., & Robberto, M. 2016, in Proc. SPIE, Vol. 9915, High Energy, Optical, and Infrared Detectors for Astronomy VII, 99152N
- Long, K. S., Baggett, S., & Mackenty, J. W. 2013a
- Long, K. S., Baggett, S. M., & MacKenty, J. W. 2013b, WFC3 Instrument Science Report 2013-06, 10 pages
- Long, K. S., Baggett, S. M., & MacKenty, J. W. 2015, WFC3 Instrument Science Report 2015-15, 18 pages
- Long, K. S., Baggett, S. M., MacKenty, J. W., & Riess, A. G. 2012, in Space Telescopes and Instrumentation 2012: Optical, Infrared, and Millimeter Wave, Proceedings of the SPIE, Volume 8442, article id. 84421W, 9 pp. (2012)., ed. M. C. Clampin, G. G. Fazio, H. A. MacEwen, & J. M. Oschmann, Vol. 8442, 84421W
- Lucas, R. A. 2015, Instrument Science Report ACS 2015-05, 27 pages
- Lucas, R. A. & Hilbert, B. 2015, Instrument Science Report ACS 2015-04, 10 pages
- Luo, B., Brandt, W. N., Xue, Y., et al. 2016, The Astrophysical Journal Supplement Series, Volume 228, Issue 1, article id. 2, 30 pp. (2017)., 228
- Malby, D. T., Aragón-Salamanca, A., Gray, M. E., et al. 2014, Monthly Notices of the Royal Astronomical Society, Volume 447, Issue 2, p.1506-1530, 447, 1506
- Martínez-Delgado, D., Gabany, R. J., Penarrubia, J., et al. 2008a, The Astrophysical Journal, Volume 692, Issue 2, pp. 955-963 (2009)., 692, 955
- Martínez-Delgado, D., Penarrubia, J., Gabany, R. J., et al. 2008b, The Astrophysical Journal, Volume 689, Issue 1, pp. 184-193 (2008)., 689, 184
- McConnachie, A. W., Irwin, M. J., Ibata, R. A., et al. 2009, Nature, Volume 461, Issue 7260, pp. 66-69 (2009)., 461, 66
- Morales, G., Martínez-Delgado, D., Grebel, E. K., et al. 2018
- Nelson, D., Pillepich, A., Genel, S., et al. 2015, Astronomy and Computing, Volume 13, p. 12-37., 13, 12
- Oesch, P. A., Bouwens, R. J., Carollo, C. M., et al. 2009, The Astrophysical Journal Letters, Volume 709, Issue 1, pp. L21-L25 (2010)., 709, L21
- Oke, J. B. 1971, The Astrophysical Journal, 170, 193
- Peacock, M. B., Strader, J., Romanowsky, A. J., & Brodie, J. P. 2014, The Astrophysical Journal, Volume 800, Issue 1, article id. 13, 17 pp. (2015)., 800
- Penarrubia, J., McConnachie, A., & Babul, A. 2006, The Astrophysical Journal, Volume 650, Issue 1, pp. L33-L36., 650, L33
- Pirzkal, N. & Hilbert, B. 2012, Instrument Science Report WFC3 2012-15, 10 pages
- Pirzkal, N., Mack, J., Dahlen, T., & Sabbi, E. 2011, Sky Flats: Generating Improved WFC3 IR Flat-fields, Tech. rep.
- Pirzkal, N., Viana, A., & Rajan, A. 2010, Instrument Science Report WFC3 2010-06, 16 pages
- Pohlen, M. & Trujillo, I. 2006, Astronomy and Astrophysics, Volume 454, Issue 3, August II 2006, pp. 759-772., 454, 759
- Róskar, R., Debattista, V. P., Stinson, G. S., et al. 2007, The Astrophysical Journal Letters, Volume 675, Issue 2, pp. L65 (2008)., 675, L65
- Rujopakarn, W., Dunlop, J. S., Rieke, G. H., et al. 2016, The Astrophysical Journal, Volume 833, Issue 1, article id. 12, 11 pp. (2016)., 833
- Sandrin, C. 2014, Astronomy & Astrophysics, Volume 567, id.A97, 16 pp., 567
- Sandrin, C. 2015, Astronomy & Astrophysics, Volume 577, id.A106, 31 pp., 577
- Schröder, S. & Sauer, P. 1996, Publications of the Astronomical Society of the Pacific, 102, 615
- Smith, R. M., Zavodny, M., Rahmer, G., & Bonati, M. 2008a, in (International Society for Optics and Photonics), 702101
- Smith, R. M., Zavodny, M., Rahmer, G., & Bonati, M. 2008b, in (International Society for Optics and Photonics), 70210K
- Spergel, D. N., Bean, R., Doré, O., et al. 2006, The Astrophysical Journal Supplement Series, Volume 170, Issue 2, pp. 377-408., 170, 377

Article number, page 35 of 36

Este documento incorpora firma electrónica, y es copia auténtica de un documento electrónico archivado por la ULL según la Ley 39/2015.
Su autenticidad puede ser contrastada en la siguiente dirección <https://sede.ull.es/validacion/>

Identificador del documento: 1630219

Código de verificación: NYPyuzSi

Fecha: 26/10/2018 14:33:01

Firmado por: ALEJANDRO SERRANO BORLAFF
UNIVERSIDAD DE LA LAGUNAJuan Esteban Beckman Abramson
UNIVERSIDAD DE LA LAGUNAMARIA DEL CARMEN ELICHE MORAL
UNIVERSIDAD DE LA LAGUNAJOAN FONT SERRA
UNIVERSIDAD DE LA LAGUNA

Fecha: 26/10/2018 14:36:58

Fecha: 26/10/2018 15:46:09

Fecha: 26/10/2018 18:46:53

A&A proofs: manuscript no. output

- Steidel, C. C., Giavalisco, M., Dickinson, M., & Adelberger, K. L. 1996a, AJ, 112, 352
Steidel, C. C., Giavalisco, M., Pettini, M., Dickinson, M., & Adelberger, K. L. 1996b, ApJ, 462, L17
Steidel, C. C. & Hamilton, D. 1992, AJ, 104, 941
Struck, C. & Elmegreen, B. G. 2016, Monthly Notices of the Royal Astronomical Society, Volume 464, Issue 2, p.1482-1492, 464, 1482
Struck, C. & Elmegreen, B. G. 2017, Monthly Notices of the Royal Astronomical Society, Volume 469, Issue 1, p.1157-1165, 469, 1157
Tanaka, M., Chiba, M., Komiyama, Y., Guhathakurta, P., & Kalirai, J. S. 2011, The Astrophysical Journal, Volume 738, Issue 2, article id. 150, 9 pp. (2011), 738
Teplitz, H. I., Rafelski, M., Kurczynski, P., et al. 2013, The Astronomical Journal, Volume 146, Issue 6, article id. 159, 19 pp. (2013), 146
Trujillo, I. & Bakos, J. 2013, MNRAS, 431, 1121
Trujillo, I. & Fliri, J. 2016, ApJ, 823, 123
Valtorta-Gabaud, D. & Collaboration, M. 2016, Proceedings of the International Astronomical Union, 11, 199
Vogelsberger, M., Genel, S., Springel, V., et al. 2014, Nature, Volume 509, Issue 7499, pp. 177-182 (2014), 509, 177
Walter, F., Decarli, R., Aravena, M., et al. 2016, The Astrophysical Journal, Volume 833, Issue 1, article id. 67, 15 pp. (2016), 833
Wong, M. H. 2010, WFC3 Instrument Science Report 2010-04, 18 pages
Xue, Y. Q., Luo, B., Brandt, W. N., et al. 2011, The Astrophysical Journal Supplement, Volume 195, Issue 1, article id. 10, 31 pp. (2011), 195
Yang, B., Zhu, J., & Song, Y.-Y. 2002, Chinese Journal of Astronomy and Astrophysics, 2, 474
Younger, J. D., Cox, T. J., Seth, A. C., & Hernquist, L. 2007, The Astrophysical Journal, Volume 670, Issue 1, pp. 269-278, 670, 269
Zackrisson, E., de Jong, R. S., & Micheva, G. 2012, Monthly Notices of the Royal Astronomical Society, 421, 190

Article number, page 36 of 36

Este documento incorpora firma electrónica, y es copia auténtica de un documento electrónico archivado por la ULL según la Ley 39/2015.
Su autenticidad puede ser contrastada en la siguiente dirección <https://sede.ull.es/validacion/>

Identificador del documento: 1630219

Código de verificación: NYPyuzSi

Fecha: 26/10/2018 14:33:01

Firmado por: ALEJANDRO SERRANO BORLAFF
UNIVERSIDAD DE LA LAGUNA

Juan Esteban Beckman Abramson
UNIVERSIDAD DE LA LAGUNA

MARIA DEL CARMEN ELICHE MORAL
UNIVERSIDAD DE LA LAGUNA

JOAN FONT SERRA
UNIVERSIDAD DE LA LAGUNA

26/10/2018 14:36:58

26/10/2018 15:46:09

26/10/2018 18:46:53

6

Conclusions and future work

*We search among ghostly errors of measurement for landmarks that are scarcely more substantial.
The search will continue. Not until the empirical resources are exhausted, need we pass on to the dreamy realms of speculation.*

— Edwin Powell Hubble, *The Realm of the nebulae*

In this Chapter we summarise the main conclusions of the work presented on the PhD thesis. We have explored several effects related to the structure and photometry of galaxies, paying special attention to those that affect the outskirts of galactic discs. In particular, we have studied how different structural phenomena and systematic biases (such as projection effects due to inclination, PSF contamination, or sky background over-subtraction) can affect the shape of the surface brightness profiles of galaxies.

6.1 Type-II surface brightness profiles in edge-on galaxies produced by flares

In Chapter 2 (Borlaff et al. 2016) we study the effects of a variation of the vertical scale height with the galactocentric radius (effect known as flaring) on the surface brightness profiles depending on the inclination of the system with respect to the observer. We investigate if a fraction of the down-bending surface brightness profiles that have been observed in edge-on galaxies can be explained by the effect of flares. The main hypothesis can be summarised as follows: Imagine an observer who studies the surface brightness profile of an edge-on galaxy through a slit along the major axis. Now the same observer performs an identical profile on an equivalent galaxy that presents a flare in the outskirts of its disc. In the latter case, the stellar column density (surface brightness profile) in the slit would be lower (darker) in the case of a flared disc galaxy than in the case of a single exponential equivalent system (see Fig. 2.1).

123

Este documento incorpora firma electrónica, y es copia auténtica de un documento electrónico archivado por la ULL según la Ley 39/2015.
Su autenticidad puede ser contrastada en la siguiente dirección <https://sede.ull.es/validacion/>

Identificador del documento: 1630219

Código de verificación: NYPyuzSi

Firmado por: ALEJANDRO SERRANO BORLAFF UNIVERSIDAD DE LA LAGUNA	Fecha: 26/10/2018 14:33:01
Juan Esteban Beckman Abramson UNIVERSIDAD DE LA LAGUNA	26/10/2018 14:36:58
MARIA DEL CARMEN ELICHE MORAL UNIVERSIDAD DE LA LAGUNA	26/10/2018 15:46:09
JOAN FONT SERRA UNIVERSIDAD DE LA LAGUNA	26/10/2018 18:46:53

In Borlaff et al. (2016, Chapter 2) we tested this hypothesis by using 10,000 3D models of disc galaxies, based on observations of real photometric and structural parameters. We found several interesting results:

1. Flares can produce detectable down-bending surface brightness profiles of low-to-intermediate intensity on edge-on realistic disc galaxy models.
2. The distribution of inner-to-outer scale-length ratios (h_i/h_o) in edge-on flared models of galaxies reproduces the observations of breaks found by Martín-Navarro et al. (2012), who associated them with star formation thresholds.
3. Flares also explain the observed weakening of the Type-II profiles with increasing distance to the plane (Pohlen et al. 2007; Martinez-Lombilla et al. 2018).

In Fig. 6.1 we represent the variation of the inner (h_i) and outer (h_o) scale-length as a function of the normalised vertical distance from the galactic plane, comparing the results from our 3D models (flared and non-flared) with the observational results from Pohlen et al. (2007). We find that both h_i and h_o from our 3D models and the observations of edge-on galaxies present a tendency to increase at higher vertical distances, and this trend is clearer and more intense for h_o . However, this tendency is not observed in the non-flared single exponential models (represented as red lines). Moreover, the normalised increase ratios in h_i and h_o observed by Pohlen et al. (2007) are $h_i/h_{i,z=0} = 1.1 - 1.4$ and $h_o/h_{o,z=0} = 1.4 - 2.4$. These ratios are well reproduced by our flared models ($h_i/h_{i,z=0} = 1.14^{+0.23}_{-0.12}$, $h_o/h_{o,z=0} = 2.12^{+1.15}_{-0.70}$).

Following the results from Borlaff et al. (2016), we proposed an ultra-deep observation program with OSIRIS/GTC for three edge-on galaxies (proposal ID: 80-GTC61/18B, 8.4 hours, *Ultra-deep imaging of edge-on galaxies: Flares, satellites and stellar halos*). The main objective of this proposal is to detect possible flares in the outskirts of a sample of edge-on, relaxed disc galaxies. This proposal was recently accepted (July 2018) and it is currently being completed, with all the data already obtained for one of the galaxies. The SDSS *g* and *r* filters will allow us to obtain the surface brightness and stellar mass profiles down to 31 mag arcsec⁻² in the *g*-band and 30.5 in the *r*-band (3σ in 10×10 arcsec² boxes) using only 2 hours of exposure time per object. Even so, these observations will allow to study many interesting science cases. One of the secondary objectives is the detection and study of warps at the edges of galaxy discs. The passage of a galaxy through its surrounding intergalactic medium has been predicted to have effects on the warp shape (López-Corredoira et al. 2002). Ultra-deep observations of the outskirts of edge-on disc galaxies are the only available probe to test this effect. Linked to possible asymmetries of the outer disc is the population of satellite galaxies. A well-known problem is the excess of satellites of the predictions of Λ CDM models compared those which are detected (Klypin et al. 1999). There is evidence that the orbits of the satellites around the Milky way are concentrated into a plane (Lynden-Bell 1976; Pawłowski et al. 2015), and that the same phenomenon has been observed for M31 (Conn et al. 2013; Ibata et al. 2014) and more recently Centaurus A (Tully et al. 2015). This phenomenon is also very hard to account for in standard Λ CDM.

Este documento incorpora firma electrónica, y es copia auténtica de un documento electrónico archivado por la ULL según la Ley 39/2015.
Su autenticidad puede ser contrastada en la siguiente dirección <https://sede.ull.es/validacion/>

Identificador del documento: 1630219

Código de verificación: NYPyuzSi

Fecha: 26/10/2018 14:33:01

Firmado por: ALEJANDRO SERRANO BORLAFF UNIVERSIDAD DE LA LAGUNA	26/10/2018 14:36:58
Juan Esteban Beckman Abramson UNIVERSIDAD DE LA LAGUNA	26/10/2018 15:46:09
MARIA DEL CARMEN ELICHE MORAL UNIVERSIDAD DE LA LAGUNA	26/10/2018 18:46:53
JOAN FONT SERRA UNIVERSIDAD DE LA LAGUNA	

6.1 Type-II surface brightness profiles in edge-on galaxies produced by flail²⁵

Finally, the extreme depth of the images will allow us to detect the stellar halos around the edge-on galaxies. The observational strategy and the selected set of filters will allow the study of the stellar mass distribution of the galaxies and their halos. The selected filters were the SDSS g and r , optimized for the study of low surface brightness features and the estimation of the stellar mass (Bakos et al. 2008). The final results will be compared with the predictions from cosmological models and other observations.

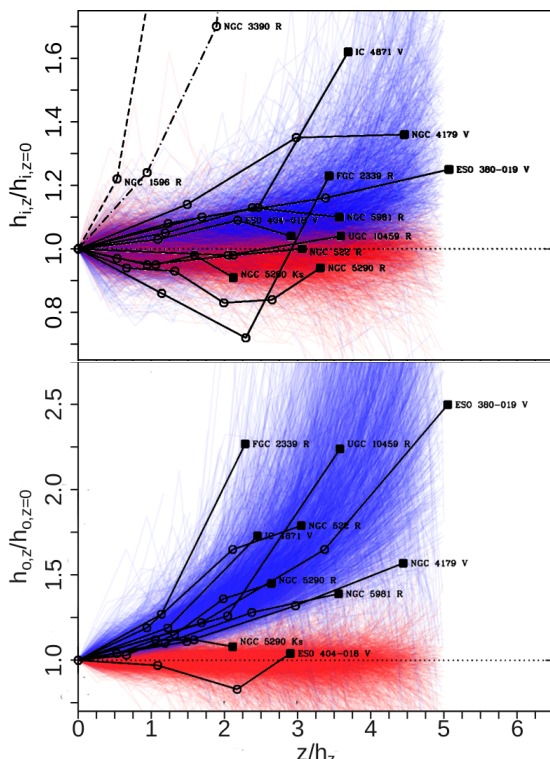


Figure 6.1: Variation of the normalised inner ($h_{i,z}/h_{i,z=0}$, top panel) and outer ($h_{o,z}/h_{o,z=0}$, bottom panel) scale-length to their respective in-plane scale-lengths as a function of the distance to the galactic plane (z). In the background we represent in blue (flared) and red (non-flared) the results for the models from Borlaff et al. (2016) and in black thick lines we represent the results from Pohlen et al. (2007) for observed individual edge-on galaxies.

Este documento incorpora firma electrónica, y es copia auténtica de un documento electrónico archivado por la ULL según la Ley 39/2015.
Su autenticidad puede ser contrastada en la siguiente dirección <https://sede.ull.es/validacion/>

Identificador del documento: 1630219

Código de verificación: NYPyuzSi

Firmado por: ALEJANDRO SERRANO BORLAFF
 UNIVERSIDAD DE LA LAGUNA

Fecha: 26/10/2018 14:33:01

Juan Esteban Beckman Abramson
 UNIVERSIDAD DE LA LAGUNA

26/10/2018 14:36:58

MARIA DEL CARMEN ELICHE MORAL
 UNIVERSIDAD DE LA LAGUNA

26/10/2018 15:46:09

JOAN FONT SERRA
 UNIVERSIDAD DE LA LAGUNA

26/10/2018 18:46:53

6.2 Evolution of the anti-truncated stellar profiles of S0 galaxies since $z = 0.6$ in the SHARDS survey. I & II

In Borlaff et al. (2017, 2018) we analysed a sample of galaxies from the red sequence with $0.2 < z < 0.6$ on the GOODS-N cosmological field. We have used the available HST/ACS images from 3DHST on the GOODS-N field, with the main objective of identifying the first sample of Type-III S0 galaxies beyond the local Universe. In the first part (Borlaff et al. 2017) we detailed the morphological classification, the corrections for PSF effects, cosmological dimming, K-correction, and dust reddening. Finally we developed an automated robust classification test to identify significant breaks in surface brightness profiles. In Borlaff et al. (2018) we compared the properties of the sample of Type-III S0 galaxies found in the previous article with a sample of objects of the same type at $z = 0$. We found several interesting results:

1. We identified 14 Type-III galaxies out of a sample of 50 S0 galaxies between $0.2 < z < 0.6$. The relative frequency of profile types is similar to that observed in the local Universe.
2. We found that a $\sim 30\%$ of the apparent Type-III S0 discs were caused by PSF contamination. In two cases, we found significant down-bending breaks (Type-II profile) after the PSF deconvolution of apparent Type-I exponential profile discs.
3. The structure of the local Universe Type-III S0 galaxies is compatible to that of the observed in objects of the same type at $0.4 < z < 0.6$, sharing compatible scaling relations and break radius R_{break} distributions.
4. Contrarily, there is a significant dimming of $\Delta\mu \sim 1.5 \text{ mag arcsec}^{-2}$ of the general structure of the Type-III S0 galaxies since $z \sim 0.6$, when compared to the local Universe sample.
5. There are no significant differences in the median colours of the inner and outer profiles, although some profiles show significant individual variations.
6. Based on the results from a grid of SSP models (EMILES, Vazdekis et al. 2016), we found that if the dominant stellar population of the Type-III S0 galaxies was produced in a single SFR burst, the burst must have taken place after $z \sim 1.2$. Otherwise, the surface brightness dimming since $z \sim 0.6$ to $z = 0$ would be smaller than $\mu \sim 1.5 \text{ mag arcsec}^{-2}$. Alternatively, the SFH of the Type-III S0 galaxies has to be more extended in time than an SSP, or should have experienced a combination of SFR bursts.

We must note that the results presented here require further observations and larger samples to be confirmed. In addition, the stellar population evolution analysis would greatly improve with the analysis of Type-III S0 galaxies at even higher z ranges ($z \sim 1$ and beyond). In order to do that, we propose to:

Este documento incorpora firma electrónica, y es copia auténtica de un documento electrónico archivado por la ULL según la Ley 39/2015.
Su autenticidad puede ser contrastada en la siguiente dirección <https://sede.ull.es/validacion/>

Identificador del documento: 1630219

Código de verificación: NYPyuzSi

Fecha: 26/10/2018 14:33:01

Firmado por: ALEJANDRO SERRANO BORLAFF
 UNIVERSIDAD DE LA LAGUNA

Juan Esteban Beckman Abramson
 UNIVERSIDAD DE LA LAGUNA

MARIA DEL CARMEN ELICHE MORAL
 UNIVERSIDAD DE LA LAGUNA

JOAN FONT SERRA
 UNIVERSIDAD DE LA LAGUNA

26/10/2018 14:36:58

26/10/2018 15:46:09

26/10/2018 18:46:53

- Expand the analysis presented in Borlaff et al. (2017, 2018) to the rest of the cosmological fields observed with HST/ACS (GOODS-S, AEGIS, COSMOS).
- Identify and compare the properties of the Type-III spiral galaxies. We note that this analysis should be performed carefully, due to the higher possibility of significant radial differences of the stellar populations.
- Continue the analysis to higher z ranges. Such scientific objective requires ultra-deep, high-spatial resolution NIR imaging (due to the combined effects of distance, redshift and cosmological dimming). This point is the main driven science case of the work presented in Chapter 5.

6.3 The missing light of the Hubble Ultra Deep Field

In Borlaff et al. (submitted) we explored the low surface brightness imaging capabilities of HST using the NIR observations of WFC3/IR in the HUDF. In order to do that, we have focused on the identification and correction of multiple systematic effects that can affect the accuracy of the analysis of extended low surface brightness structures on the largest objects of the HUDF. The proposed corrections to the reduction process can be summarised in:

1. Creation of robust sky flat fields per band using deep images obtained on the same epochs of the HUDF images.
2. Robust masking of sources, using non-parametric noise-based detection methods (Gnuastro/NoiseChisel, Akhlaghi & Ichikawa 2015).
3. Careful (two dimensional and flat) sky background subtraction, based on the described methods of masking and source detection.
4. Improved modelling of the NIR persistence contamination effects of the HgCdTe detectors of WFC3/IR (Long et al. 2015).

The main result of this work is the creation of the ABYSS mosaics¹, which are the deepest version of the WFC3/IR HUDF images up to date, taking into account the systematic effects of over subtraction on the extended sources. In the new version of the HUDF mosaics a significant amount of over-subtracted diffuse light is recovered, mainly around the largest objects. Such light was not detected by the previous versions of the mosaics. The integrated magnitude of the recovered light is equivalent to a $m \sim 19$ mag object for the XDF and $m \sim 20$ mag for the HUDF12 mosaics, comparable to the brightest galaxies on the image. Therefore we demonstrated that the XDF version of the HUDF WFC3/IR mosaics is dominated by a systematic bias in the form of a significant over-subtraction of the sky background around the objects with large angular size. We found that although the HUDF12 has less exposure time than the XDF, the systematic sky-oversubtraction is less dramatic in this reduction than in the XDF.

¹ABYSS: a low surface brightness dedicated reduction for the HUDF WFC3/IR mosaics:
<http://www.iac.es/proyecto/abyss/>

Este documento incorpora firma electrónica, y es copia auténtica de un documento electrónico archivado por la ULL según la Ley 39/2015.
Su autenticidad puede ser contrastada en la siguiente dirección <https://sede.ull.es/validacion/>

Identificador del documento: 1630219

Código de verificación: NYPyuzSi

Firmado por: ALEJANDRO SERRANO BORLAFF UNIVERSIDAD DE LA LAGUNA	Fecha: 26/10/2018 14:33:01
Juan Esteban Beckman Abramson UNIVERSIDAD DE LA LAGUNA	26/10/2018 14:36:58
MARIA DEL CARMEN ELICHE MORAL UNIVERSIDAD DE LA LAGUNA	26/10/2018 15:46:09
JOAN FONT SERRA UNIVERSIDAD DE LA LAGUNA	26/10/2018 18:46:53

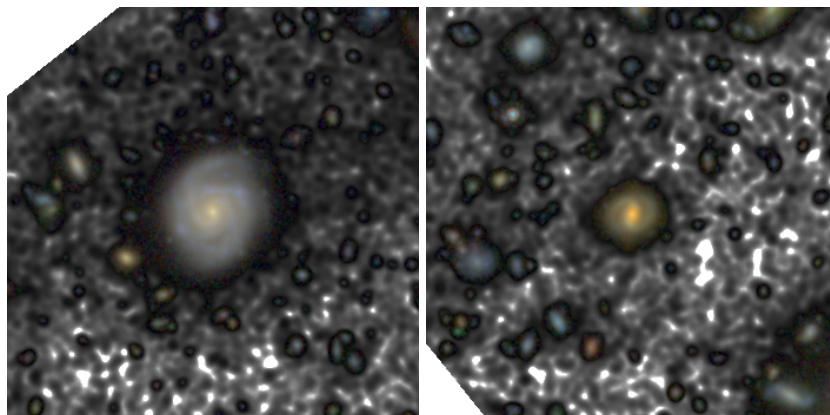


Figure 6.2: Luminance-RGB images of ABYSS-1 (left panel, $\alpha = 53.1699, \delta = 27.7711$) and ABYSS-4 (right panel, $\alpha = 53.1766, \delta = -27.7854$). The field of view is 21×21 arcsec in both images. The high signal-to-noise parts of the mosaics are represented with colours (*red*: F160W, *green*: mean of F125W and F140W bands, *blue*: F105W). The low signal-to-noise regions are represented as a black and white background (black regions are brighter than white regions) according to the mean image of the four mosaics (F105W, F125W, F140W, F160W).

The cause of this over subtraction is probably the highly aggressive two dimensional sky background subtraction method used in the previous versions. The creation of dedicated sky flat fields and accurate correction and masking of persistence contamination on images reduces the need for gradient corrections. Nevertheless, some residual gradients are not related to flat-field issues but to real light contamination (either external, such as moonlight and earthlight, or internal, such as NIR persistence). Due to this, we propose and test a sky background correction method, based on `Gnuastro/NoiseChisel` in order to robustly detect and flag the extended dim envelopes of the sources on the field of view. We found that this method can improve the sky background determination by up to 1-2 orders of magnitude. Finally, in Borlaff et al. (submitted) we study the surface brightness profiles of six objects in the HUDF, demonstrating that our reduction pipeline can preserve the properties of the smallest sources in the HUDF, while recovering the low surface brightness structures of the outskirts of the largest galaxies.

Nevertheless, as explained in the article, the surface brightness profiles presented in Borlaff et al. (submitted) (three elliptical galaxies and three spirals) were not corrected from PSF effects, and thus they are only a benchmark between different versions of the HUDF mosaics. In order to properly identify the true shape of the surface brightness profiles of the galaxies from the HUDF, we need to correct for PSF effects. Here we present a brief example of this future work, analysing two spiral galaxies from the HUDF (see Fig. 6.2).

Este documento incorpora firma electrónica, y es copia auténtica de un documento electrónico archivado por la ULL según la Ley 39/2015.
Su autenticidad puede ser contrastada en la siguiente dirección <https://sede.ull.es/validacion/>

Identificador del documento: 1630219

Código de verificación: NYPyuzSi

Fecha: 26/10/2018 14:33:01

Firmado por: ALEJANDRO SERRANO BORLAFF
UNIVERSIDAD DE LA LAGUNA

Juan Esteban Beckman Abramson
UNIVERSIDAD DE LA LAGUNA

MARIA DEL CARMEN ELICHE MORAL
UNIVERSIDAD DE LA LAGUNA

JOAN FONT SERRA
UNIVERSIDAD DE LA LAGUNA

26/10/2018 14:36:58

26/10/2018 15:46:09

26/10/2018 18:46:53

In Fig. 6.3 we present the PSF corrected profile of ABYSS-1 ($\alpha = 53.1699, \delta = 27.7711$, Elmegreen et al. 2005). ABYSS-1 is one of the three spiral galaxies at $z = 0.622$ (Bacon et al. 2017) used in Borlaff et al. (submitted) as a benchmark to compare the different reductions of the HUDF WFC3/IR (see left panel of Fig. 6.2). We follow the method of PSF correction described in Borlaff et al. (2017, 2018) to generate PSF corrected images using GALFIT3.0 (Peng et al. 2010) models (see Chapter 3). In order to estimate the shape of the PSF for the HUDF, we use the Tiny Tim PSF models for WFC3/IR (Krist et al. 2011), rotated to match the angle of the spikes from the final mosaics of the HUDF. In this case, we fit two Sérsic components modified with a spiral rotation function to match the irregular spiral pattern. Finally, we estimate the surface brightness profile using elliptical apertures ($PA = -15.9$ degrees, $q = 0.884$) and correct for sky background (see Sect 3.2 from Borlaff et al. submitted). Finally, we correct for cosmological dimming (see eq. 1.1). The resulting PSF corrected surface brightness profile shows an inner bulge like structure, with a clear down-bending profile at $R \sim 12$ kpc from the centre. At this radius the spiral pattern of ABYSS-1 is no longer visible in the images. The outer profile ($R > 12$ kpc) appears then as an external component, possibly an outer disc. The outskirts of the F105W and F140W profiles show hints of what could be an external component at $R \sim 20 - 25$ kpc ($p_{F105W} = 0.0077$, $p_{F125W} = 0.013$, $p_{F140W} = 6.6 \cdot 10^{-4}$, $p_{F160W} = 0.044$; possibly an anti-truncation or stellar halo), which is not detected in the F125W or F160W bands. In order to confirm this detection, we require a more accurate PSF model for the HUDF, to model and subtract of the surrounding objects –including their PSF– following the method described on Trujillo & Fliri (2016).

In Fig. 6.4 we present the PSF corrected profile of ABYSS-4 ($\alpha = 53.1766, \delta = -27.7854$, Elmegreen et al. 2005), a two-armed spiral galaxy at $z = 1.319$ (Bacon et al. 2017, see right panel of Fig. 6.2). We fit three different components to the model, an inner bulge, an extended disc component based on a Sérsic component modified with a spiral rotation function and different Fourier modes, in order to take into account the spiral arms. The position angle and axis ratio are $PA = -83.71$ and $q = 0.715$, using Gnuastro. The resulting surface brightness profile shows a similar structure in all the bands, consisting of an inner profile dominated by the bar and the spiral arms ($R < 8$ kpc) and an extended exponential outer disc ($R > 8$ kpc). Interestingly, the surface brightness profile of the non corrected image appears to be anti-truncated, but the apparent up-bending structure is completely removed after PSF correction. The detailed analysis of the structure of the disc galaxies in the HUDF requires a detailed analysis of the PSF of each HUDF mosaic well beyond the scope of this thesis, and it will be addressed in a forthcoming paper.

In addition to the structural analysis of the galaxies on the HUDF, the future application of the reduction techniques presented in this thesis and tested on the HUDF can allow exploration of the low surface brightness Universe from many projected space and ground observatories such as the LSST, EUCLID, JWST or MESSIER. Careful reduction techniques will enable multiple scientific objectives including: 1) the study of stellar halos as tracers of the dark matter distribution in galaxies, 2) unprecedented mapping

Este documento incorpora firma electrónica, y es copia auténtica de un documento electrónico archivado por la ULL según la Ley 39/2015.
Su autenticidad puede ser contrastada en la siguiente dirección <https://sede.ull.es/validacion/>

Identificador del documento: 1630219

Código de verificación: NYPyuzSi

Fecha: 26/10/2018 14:33:01

Firmado por: ALEJANDRO SERRANO BORLAFF UNIVERSIDAD DE LA LAGUNA	26/10/2018 14:36:58
Juan Esteban Beckman Abramson UNIVERSIDAD DE LA LAGUNA	26/10/2018 15:46:09
MARIA DEL CARMEN ELICHE MORAL UNIVERSIDAD DE LA LAGUNA	26/10/2018 18:46:53
JOAN FONT SERRA UNIVERSIDAD DE LA LAGUNA	

of the zodiacal light and Galactic dust cirrus, (specially interesting for the EUCLID mission, because of its possible impact on the weak lensing measurements due to its fine substructure), and 3) precise measurement of the anisotropies of the Cosmic Infrared Background. Nonetheless, such scientific objectives can be achieved only with a careful treatment and constant improvements to the methods that ensure the fiducial quality of the final astronomical images. We have made significant advances in this thesis which will underpin the future research described here.

6.4 Final conclusions

Here we summarise the main scientific results we have obtained in this thesis:

1. We have shown that flares can produce detectable down-bending surface brightness profiles of low-to-intermediate intensity in edge-on realistic disc galaxy models.
2. The distribution of inner-to-outer scale-length (h_i/h_o) in edge-on flared models of galaxies reproduces the observations of breaks found by Martín-Navarro et al. (2012), who associated them with star formation thresholds.
3. Flares can also explain the observed weakening of the Type-II profiles with increasing distance from the plane (Pohlen et al. 2007; Martinez-Lombilla et al. 2018).
4. We have found that PSF contamination can strongly affect the shape of the profile of S0 galaxies beyond the local Universe, making necessary a detailed correction for this effect to perform robust analysis.
5. The structure of the local Universe Type-III S0 galaxies is compatible to that of the observed in objects of the same type at $0.4 < z < 0.6$, sharing compatible scaling relations and break radius R_{break} distributions.
6. We found a significant dimming of the global structure of Type-III S0 galaxies since $z = 0.6$ to $z = 0$ of $\Delta\mu \sim 1.5 \text{ mag arcsec}^{-2}$ in the R -band. The dimming is compatible with the evolution in brightness of a SSP burst that takes place at $z \lesssim 1.2$.
7. We created a new version of the HUDF WFC3/IR, which accurately recovers the low surface brightness structure around the most extended galaxies. This new reduction of the images accurately corrects the significant sky oversubtraction detected in previous versions of the HUDF WFC3/IR mosaics, allowing the study of the outer structure of galaxies at an unprecedented ultra-low surface brightness regime ($\mu_{\text{lim}} \sim 33 \text{ mag arcsec}^{-2}$).

Este documento incorpora firma electrónica, y es copia auténtica de un documento electrónico archivado por la ULL según la Ley 39/2015.
Su autenticidad puede ser contrastada en la siguiente dirección <https://sede.ull.es/validacion/>

Identificador del documento: 1630219 Código de verificación: NYPyuzSi

Firmado por: ALEJANDRO SERRANO BORLAFF UNIVERSIDAD DE LA LAGUNA	Fecha: 26/10/2018 14:33:01
Juan Esteban Beckman Abramson UNIVERSIDAD DE LA LAGUNA	26/10/2018 14:36:58
MARIA DEL CARMEN ELICHE MORAL UNIVERSIDAD DE LA LAGUNA	26/10/2018 15:46:09
JOAN FONT SERRA UNIVERSIDAD DE LA LAGUNA	26/10/2018 18:46:53

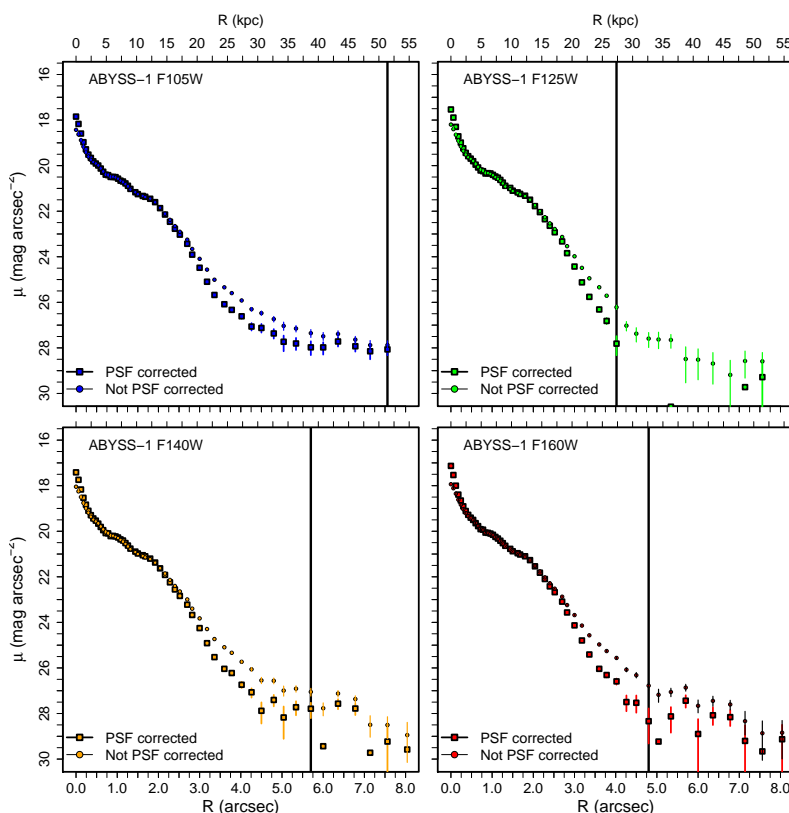


Figure 6.3: Surface brightness profiles of ABYSS-1 ($\alpha = 53.1699$, $\delta = 27.7711$, $z = 0.622$ Elmegreen et al. 2005; Bacon et al. 2017). Top left: F105W (blue). Top right: F125W (green). Bottom left: F140W (orange). Bottom right: F160W (red). The square points represent the PSF corrected profiles, compared to the uncorrected profiles (circles). Vertical black solid line represents the $S/N = 3$ limit of the surface brightness profile. The surface brightness magnitudes have been corrected for cosmological dimming.

Este documento incorpora firma electrónica, y es copia auténtica de un documento electrónico archivado por la ULL según la Ley 39/2015.
Su autenticidad puede ser contrastada en la siguiente dirección <https://sede.ull.es/validacion/>

Identificador del documento: 1630219

Código de verificación: NYPyuzSi

Firmado por: ALEJANDRO SERRANO BORLAFF
 UNIVERSIDAD DE LA LAGUNA

Fecha: 26/10/2018 14:33:01

Juan Esteban Beckman Abramson
 UNIVERSIDAD DE LA LAGUNA

26/10/2018 14:36:58

MARIA DEL CARMEN ELICHE MORAL
 UNIVERSIDAD DE LA LAGUNA

26/10/2018 15:46:09

JOAN FONT SERRA
 UNIVERSIDAD DE LA LAGUNA

26/10/2018 18:46:53

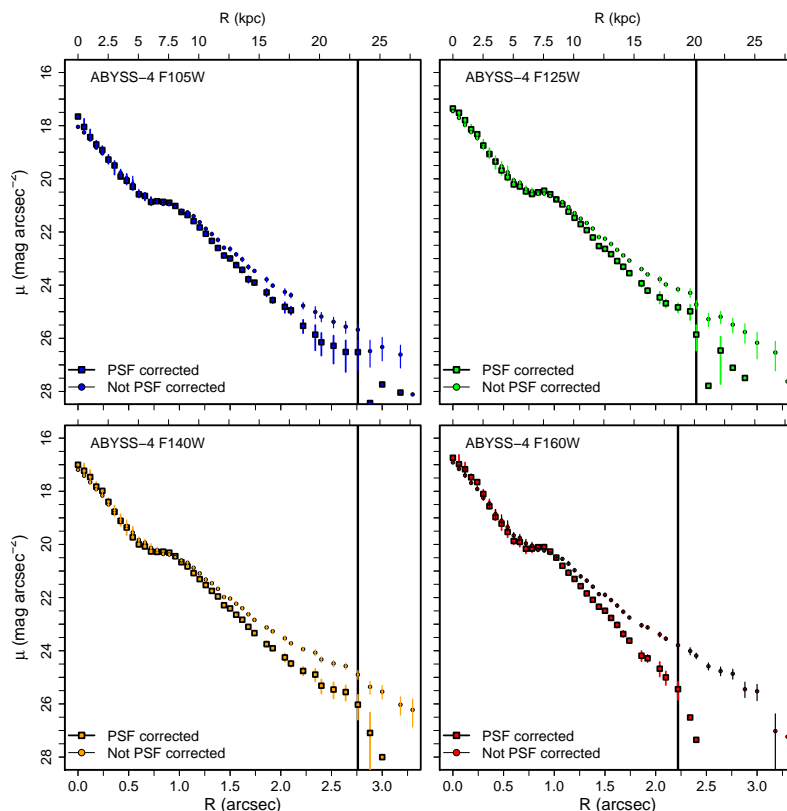


Figure 6.4: Surface brightness profiles of ABYSS-4] [Elmegreen2005, Bacon2017. *Top left:* F105W (blue). *Top right:* F125W (green). *Bottom left:* F140W (orange). *Bottom right:* F160W (red). The square points represent the PSF corrected profiles, compared to the uncorrected profiles (circles). Vertical black solid line represents the S/N= 3 limit of the surface brightness profile. The surface brightness magnitudes have been corrected for cosmological dimming.

Este documento incorpora firma electrónica, y es copia auténtica de un documento electrónico archivado por la ULL según la Ley 39/2015.
Su autenticidad puede ser contrastada en la siguiente dirección <https://sede.ull.es/validacion/>

Identificador del documento: 1630219

Código de verificación: NYPyuzSi

Firmado por: ALEJANDRO SERRANO BORLAFF
UNIVERSIDAD DE LA LAGUNA

Fecha: 26/10/2018 14:33:01

Juan Esteban Beckman Abramson
UNIVERSIDAD DE LA LAGUNA

26/10/2018 14:36:58

MARIA DEL CARMEN ELICHE MORAL
UNIVERSIDAD DE LA LAGUNA

26/10/2018 15:46:09

JOAN FONT SERRA
UNIVERSIDAD DE LA LAGUNA

26/10/2018 18:46:53

Bibliography

- Aarseth, S. J., & Fall, S. M. 1980, ApJ, 236, 43
- Ahn, C. P., Alexandroff, R., Allende Prieto, C., et al. 2012, ApJS, 203, 21
- Akhlaghi, M., & Ichikawa, T. 2015, doi:10.1088/0067-0049/220/1/1
- Annibali, F., Bressan, A., Rampazzo, R., et al. 2010, A&A, 519, A40
- Aragón-Salamanca, A., Bedregal, A. G., & Merrifield, M. R. 2006, A&A, 458, 101
- Aravena, M., Decarli, R., Walter, F., et al. 2016a, The Astrophysical Journal, Volume 833, Issue 1, article id. 68, 20 pp. (2016)., 833, arXiv:1607.06769
- . 2016b, The Astrophysical Journal, Volume 833, Issue 1, article id. 71, 22 pp. (2016)., 833, arXiv:1607.06772
- Athanassoula, E., Rodionov, S. A., Peschken, N., & Lambert, J. C. 2016, The Astrophysical Journal, Volume 821, Issue 2, article id. 90, 17 pp. (2016)., 821, arXiv:1602.03189
- Azzollini, R., Trujillo, I., & Beckman, J. E. 2008a, The Astrophysical Journal Letters, Volume 679, Issue 2, pp. L69 (2008)., 679, L69
- . 2008b, The Astrophysical Journal, Volume 684, Issue 2, pp. 1026-1047 (2008)., 684, 1026
- Bacon, R., Conseil, S., Mary, D., et al. 2017, arXiv:1710.03002
- Bakos, J., Trujillo, I., Pohlen, M., & ;. 2008, The Astrophysical Journal Letters, V683, Issue 2, article id. L103, pp. (2008)., 683, arXiv:0807.2776
- Baldry, I. K. 2008, Astronomy & Geophysics, Volume 49, Issue 5, pp. 5.25-5.26., 49, 5.25
- Barnaby, D., & Thronson, Jr., H. A. 1992, AJ, 103, 41
- Barro, G., Pérez-González, P. G., Gallego, J., et al. 2011a, ApJS, 193, 13
- . 2011b, ApJS, 193, 30

133

Este documento incorpora firma electrónica, y es copia auténtica de un documento electrónico archivado por la ULL según la Ley 39/2015.
Su autenticidad puede ser contrastada en la siguiente dirección <https://sede.ull.es/validacion/>

Identificador del documento: 1630219

Código de verificación: NYPyuzSi

Fecha: 26/10/2018 14:33:01

Firmado por: ALEJANDRO SERRANO BORLAFF
UNIVERSIDAD DE LA LAGUNA

Juan Esteban Beckman Abramson
UNIVERSIDAD DE LA LAGUNA

MARIA DEL CARMEN ELICHE MORAL
UNIVERSIDAD DE LA LAGUNA

JOAN FONT SERRA
UNIVERSIDAD DE LA LAGUNA

26/10/2018 14:36:58

26/10/2018 15:46:09

26/10/2018 18:46:53

- Barton, I. J., & Thompson, L. A. 1997, The Astronomical Journal, 114, 655
- Barway, S., Wadadekar, Y., Kembhavi, A. K., & Mayya, Y. D. 2009, MNRAS, 394, 1991
- Barway, S., Wadadekar, Y., Vaghmare, K., & Kembhavi, A. K. 2013, MNRAS, 432, 430
- Battaner, E., Florido, E., & Jimenez-Vicente, J. 2002, Astronomy and Astrophysics, v.388, p.213-218 (2002), 388, 213
- Battaner, E., Florido, E., & Sanchez-Saavedra, M. L. 1992a, A&A, 253, 89
- Battaner, E., Garrido, J. L., Membrado, M., & Florido, E. 1992b, Nature, 360, 652
- Beckwith, S. V. W., Stiavelli, M., Koekemoer, A. M., et al. 2006, AJ, 132, 1729
- Bekki, K., & Couch, W. J. 2011, Monthly Notices of the Royal Astronomical Society, Volume 415, Issue 2, pp. 1783-1796., 415, 1783
- Bekki, K., Couch, W. J., & Shioya, Y. 2002, ApJ, 577, 651
- Bekki, K., & Kenji. 1998, The Astrophysical Journal, Volume 502, Issue 2, pp. L133-L137., 502, L133
- . 2001, Astrophysics and Space Science, 276, 847
- Bell, E. F., McIntosh, D. H., Katz, N., & Weinberg, M. D. 2003, ApJS, 149, 289
- Berlind, A. A., Frieman, J., Weinberg, D. H., et al. 2006, ApJS, 167, 1
- Bernardi, M., Roche, N., Shankar, F., & Sheth, R. K. 2011a, MNRAS, 412, 684
- . 2011b, MNRAS, 412, L6
- Bernardi, M., Shankar, F., Hyde, J. B., et al. 2010, MNRAS, 404, 2087
- Bizyaev, D. V., Kautsch, S. J., Mosenkov, A. V., et al. 2014, ApJ, 787, 24
- Bland-Hawthorn, J., Vlajic, M., Freeman, K., & Draine, B. 2005, The Astrophysical Journal, Volume 629, Issue 1, pp. 239-249., 629, 239
- Block, D. L., Bertin, G., Stockton, A., et al. 1994, A&A, 288, 365
- Boissier, S., Boselli, A., Ferrarese, L., et al. 2016, A&A, 593, A126
- Borlaff, A., Carmen Eliche-Moral, M., Beckman, J., & Font, J. 2016, Astronomy and Astrophysics, 591, doi:10.1051/0004-6361/201628868
- Borlaff, A., Eliche-Moral, M. C., Beckman, J. E., et al. 2017, Astronomy & Astrophysics, Volume 604, id.A119, 71 pp., 604, arXiv:1705.05850
- Borlaff, A., Eliche-Moral, M. C., Rodríguez-Pérez, C., et al. 2014, Astronomy & Astrophysics, Volume 570, id.A103, 30 pp., 570, arXiv:1407.5097

Este documento incorpora firma electrónica, y es copia auténtica de un documento electrónico archivado por la ULL según la Ley 39/2015.
Su autenticidad puede ser contrastada en la siguiente dirección <https://sede.ull.es/validacion/>

Identificador del documento: 1630219

Código de verificación: NYPyuzSi

Fecha: 26/10/2018 14:33:01

Firmado por: ALEJANDRO SERRANO BORLAFF UNIVERSIDAD DE LA LAGUNA	26/10/2018 14:36:58
Juan Esteban Beckman Abramson UNIVERSIDAD DE LA LAGUNA	26/10/2018 15:46:09
MARIA DEL CARMEN ELICHE MORAL UNIVERSIDAD DE LA LAGUNA	26/10/2018 18:46:53
JOAN FONT SERRA UNIVERSIDAD DE LA LAGUNA	

6.4 BIBLIOGRAPHY

135

- Borlaff, A., Eliche-Moral, M. C., Beckman, J. E., et al. 2018, *Astronomy & Astrophysics*, Volume 615, id.A26, 26 pp., 615, arXiv:1803.00570
- Borlaff, A., Trujillo, I., Román, J., et al. submitted, ArXiv e-prints, arXiv:1810.00002
- Bothun, G. D., Impey, C. D., Malin, D. F., & Mould, J. R. 1987, *AJ*, 94, 23
- Bournaud, F., Elmegreen, B. G., & Elmegreen, D. M. 2007, *The Astrophysical Journal*, Volume 670, Issue 1, pp. 237-248., 670, 237
- Bournaud, F., Jog, C. J., & Combes, F. 2005, *Astronomy and Astrophysics*, Volume 437, Issue 1, July I 2005, pp.69-85, 437, 69
- Bournaud, F., Chapon, D., Teyssier, R., et al. 2011, *ApJ*, 730, 4
- Bouwens, R. J., Illingworth, G. D., Oesch, P. A., et al. 2009, *The Astrophysical Journal Letters*, Volume 709, Issue 2, pp. L133-L137 (2010)., 709, L133
- Bouwens, R. J., Illingworth, G. D., Oesch, P. A., et al. 2011, *ApJ*, 737, 90
- Brunetti, M., Chiappini, C., & Pfenniger, D. 2011, *Astronomy & Astrophysics*, Volume 534, id.A75, 10 pp., 534, arXiv:1108.5631
- Bruzual, G., & Charlot, S. 2003, *MNRAS*, 344, 1000
- Buitrago, F., Trujillo, I., Curtis-Lake, E., et al. 2017, *MNRAS*, 466, 4888
- Bullock, J. S., Dekel, A., Kolatt, T. S., et al. 2000, *The Astrophysical Journal*, Volume 555, Issue 1, pp. 240-257., 555, 240
- Bullock, J. S., & Johnston, K. V. 2005, *The Astrophysical Journal*, Volume 635, Issue 2, pp. 931-949., 635, 931
- Burstein, D. 1979, *ApJ*, 234, 829
- Byun, Y.-I. 1998, *Chinese Journal of Physics*, 36, 677
- Cappellari, M., Emsellem, E., Krajnović, D., et al. 2011, *MNRAS*, 416, 1680
- Cardamone, C., Schawinski, K., Sarzi, M., et al. 2009, *MNRAS*, 399, 1191
- Carlsten, S. G., Hau, G. K. T., & Zenteno, A. 2017, *MNRAS*, 472, 2889
- Cerulo, P., Couch, W. J., Lidman, C., et al. 2017, *MNRAS*, 472, 254
- Chilingarian, I. V., Di Matteo, P., Combes, F., Melchior, A.-L., & Semelin, B. 2010, *A&A*, 518, A61
- Comastri, A., Ranalli, P., Iwasawa, K., et al. 2011, *Astronomy and Astrophysics*, Volume 526, id.L9, 6 pp., 526, arXiv:1012.4011

Este documento incorpora firma electrónica, y es copia auténtica de un documento electrónico archivado por la ULL según la Ley 39/2015.
Su autenticidad puede ser contrastada en la siguiente dirección <https://sede.ull.es/validacion/>

Identificador del documento: 1630219

Código de verificación: NYPyuzSi

Firmado por: ALEJANDRO SERRANO BORLAFF UNIVERSIDAD DE LA LAGUNA	Fecha: 26/10/2018 14:33:01
Juan Esteban Beckman Abramson UNIVERSIDAD DE LA LAGUNA	26/10/2018 14:36:58
MARIA DEL CARMEN ELICHE MORAL UNIVERSIDAD DE LA LAGUNA	26/10/2018 15:46:09
JOAN FONT SERRA UNIVERSIDAD DE LA LAGUNA	26/10/2018 18:46:53

- Comerón, S., Elmegreen, B. G., Salo, H., et al. 2014, A&A, 571, A58
- Comerón, S., Elmegreen, B. G., Salo, H., et al. 2012, The Astrophysical Journal, Volume 759, Issue 2, article id. 98, 29 pp. (2012)., 759, arXiv:1209.1513
- Conn, A. R., Lewis, G. F., Ibata, R. A., & Parker, Q. A. e. a. 2013, The Astrophysical Journal, Volume 766, Issue 2, article id. 120, 16 pp. (2013)., 766, arXiv:1301.7131
- Crook, A. C., Huchra, J. P., Martimbeau, N., et al. 2007, ApJ, 655, 790
- Crowl, H. H., Kenney, J. D. P., van Gorkom, J. H., & Vollmer, B. 2005, AJ, 130, 65
- Dalcanton, J. J., & Bernstein, R. A. 2002, AJ, 124, 1328
- Dalcanton, J. J., Spergel, D. N., & Summers, F. J. 1996, The Astrophysical Journal, Volume 482, Issue 2, pp. 659-676., 482, 659
- de Grijs, R. 1998, MNRAS, 299, 595
- de Grijs, R., Kregel, M., & Wesson, K. H. 2001, MNRAS, 324, 1074
- de Grijs, R., & Peletier, R. F. 1997, A&A, 320, L21
- de Jong, R. S. 1996, Astronomy and Astrophysics Supplement, v.118, p.557-573, 118, 557
- de Jong, R. S., Seth, A. C., Radburn-Smith, D. J., et al. 2007, The Astrophysical Journal, Volume 667, Issue 1, pp. L49-L52., 667, L49
- de Paz, A. G., Madore, B. F., Boissier, S., et al. 2005, The Astrophysical Journal, Volume 627, Issue 1, pp. L29-L32., 627, L29
- de Vaucouleurs, G. 1959a, Handbuch der Physik, Volume 53, p.311, 53, 311
- . 1959b, The Astrophysical Journal, 130, 728
- . 1963, The Astrophysical Journal Supplement Series, 8, 31
- Dickinson, M., Giavalisco, M., & GOODS Team. 2003, in The Mass of Galaxies at Low and High Redshift, ed. R. Bender & A. Renzini, 324
- Disney, M. J. 1976, Nature, 263, 573
- Djorgovski, G. S. 1992, in Astrophysics and Space Science Library, Vol. 178, Morphological and Physical Classification of Galaxies, ed. G. Longo, M. Capaccioli, & G. Busarello, 337
- D'Onofrio, M., Marziani, P., & Buson, L. 2015, Frontiers in Astronomy and Space Sciences, 2, 4
- Dressler, A. 1980, ApJ, 236, 351

Este documento incorpora firma electrónica, y es copia auténtica de un documento electrónico archivado por la ULL según la Ley 39/2015.
Su autenticidad puede ser contrastada en la siguiente dirección <https://sede.ull.es/validacion/>

Identificador del documento: 1630219

Código de verificación: NYPyuzSi

Fecha: 26/10/2018 14:33:01

Firmado por: ALEJANDRO SERRANO BORLAFF
UNIVERSIDAD DE LA LAGUNA

Juan Esteban Beckman Abramson
UNIVERSIDAD DE LA LAGUNA

MARIA DEL CARMEN ELICHE MORAL
UNIVERSIDAD DE LA LAGUNA

JOAN FONT SERRA
UNIVERSIDAD DE LA LAGUNA

26/10/2018 14:36:58

26/10/2018 15:46:09

26/10/2018 18:46:53

6.4 BIBLIOGRAPHY

137

- Dressler, A., Oemler, Jr., A., Couch, W. J., et al. 1997, ApJ, 490, 577
- Dunlop, J. S., McLure, R. J., Biggs, A. D., et al. 2016, arXiv:1606.00227
- Dupraz, C., & Combes, F. 1986, A&A, 166, 53
- Ebrova, I. 2013, ArXiv e-prints, arXiv:1312.1643
- Efstathiou, G. 2000, Monthly Notices of the Royal Astronomical Society, Volume 317, Issue 3, pp. 697-719., 317, 697
- Eliche-Moral, M. C., Borlaff, A., Beckman, J. E., & Gutierrez, L. 2015, Astronomy & Astrophysics, Volume 580, id.A33, 18 pp., 580, arXiv:1505.04797
- Eliche-Moral, M. C., González-García, A. C., Aguerri, J. A. L., et al. 2012, A&A, 547, A48
- . 2013, A&A, 552, A67
- Eliche-Moral, M. C., Rodriguez-Perez, C., Borlaff, A., Querejeta, M., & Tapia, T. 2018, eprint arXiv:1806.06070, arXiv:1806.06070
- Eliche-Moral, M. C., Prieto, M., Gallego, J., et al. 2010, A&A, 519, A55
- Elmegreen, B. G., Elmegreen, D. M., Tompkins, B., & Jenks, L. G. 2017, ApJ, 847, 14
- Elmegreen, B. G., & Struck, C. 2013, The Astrophysical Journal Letters, Volume 775, Issue 2, article id. L35, 5 pp. (2013)., 775, arXiv:1308.5236
- . 2016, The Astrophysical Journal, Volume 830, Issue 2, article id. 115, 8 pp. (2016)., 830, arXiv:1607.07595
- Elmegreen, D. M., Elmegreen, B. G., Rubin, D. S., & Schaffer, M. A. 2005, The Astrophysical Journal, Volume 631, Issue 1, pp. 85-100., 631, 85
- Emsellem, E., Cappellari, M., Krajnović, D., et al. 2007, MNRAS, 379, 401
- Erwin, P., Beckman, J. E., & Pohlen, M. 2005, The Astrophysical Journal, Volume 626, Issue 2, pp. L81-L84., 626, L81
- Erwin, P., Gutiérrez, L., & Beckman, J. E. 2012, ApJ, 744, L11
- Erwin, P., Pohlen, M., & Beckman, J. E. 2008, AJ, 135, 20
- Erwin, P., Saglia, R. P., Fabricius, M., et al. 2015, MNRAS, 446, 4039
- Fasano, G., Poggianti, B. M., Couch, W. J., et al. 2000, ApJ, 542, 673
- Fathi, K. 2010, ApJ, 722, L120

Este documento incorpora firma electrónica, y es copia auténtica de un documento electrónico archivado por la ULL según la Ley 39/2015.
Su autenticidad puede ser contrastada en la siguiente dirección <https://sede.ull.es/validacion/>

Identificador del documento: 1630219

Código de verificación: NYPyuzSi

Fecha: 26/10/2018 14:33:01

Firmado por: ALEJANDRO SERRANO BORLAFF
UNIVERSIDAD DE LA LAGUNA

Juan Esteban Beckman Abramson
UNIVERSIDAD DE LA LAGUNA

MARIA DEL CARMEN ELICHE MORAL
UNIVERSIDAD DE LA LAGUNA

JOAN FONT SERRA
UNIVERSIDAD DE LA LAGUNA

26/10/2018 14:36:58

26/10/2018 15:46:09

26/10/2018 18:46:53

- Ferguson, A., & Clarke, C. 2001, Monthly Notices of the Royal Astronomical Society, Volume 325, Issue 2, pp. 781-791., 325, 781
- Finkelman, I., Brosch, N., Funes, J. G., Kniazev, A. Y., & Väisänen, P. 2010, MNRAS, 407, 2475
- Forbes, D. A., Beasley, M. A., Bekki, K., Brodie, J. P., & Strader, J. 2003, Science, 301, 1217
- Freeman, K. C. 1970, The Astrophysical Journal, 160, 811
- Giacconi, R., Zirm, A., Wang, J., et al. 2002, The Astrophysical Journal Supplement Series, 139, 369
- Giavalisco, M., Team, t. G., Koekemoer, A. M., et al. 2003, The Astrophysical Journal, Volume 600, Issue 2, pp. L93-L98., 600, L93
- Giavalisco, M., Ferguson, H. C., Koekemoer, A. M., et al. 2004, ApJ, 600, L93
- Governato, F., Willman, B., Mayer, L., et al. 2007, MNRAS, 374, 1479
- Governato, F., Brook, C. B., Brooks, A. M., et al. 2009, MNRAS, 398, 312
- Graham, A. W. 2013, Elliptical and Disk Galaxy Structure and Modern Scaling Laws, ed. T. D. Oswalt & W. C. Keel, 91
- Gunn, J. E. 1982, in Astrophysical Cosmology Proceedings, ed. H. A. Brueck, G. V. Coyne, & M. S. Longair, 233-259
- Gunn, J. E., & Gott, III, J. R. 1972, ApJ, 176, 1
- Gutierrez, L., Erwin, P., Aladro, R., & Beckman, J. E. 2011, The Astronomical Journal, Volume 142, Issue 5, article id. 145, 31 pp. (2011)., 142, arXiv:1108.3662
- Hernquist, L., & Quinn, P. J. 1988, ApJ, 331, 682
- Herpich, J., Stinson, G. S., Rix, H.-W., Martig, M., & Dutton, A. A. 2015, Monthly Notices of the Royal Astronomical Society, Volume 470, Issue 4, p.4941-4955, 470, 4941
- . 2017, Monthly Notices of the Royal Astronomical Society, Volume 470, Issue 4, p.4941-4955, 470, 4941
- Hohl, F. 1971, The Astrophysical Journal, 168, 343
- Holmberg, E. 1958, Lund Medd. Astron. Obs. Ser. II, Vol. 136, p. 1 (1958), 136, 1
- Hopkins, P. F., Cox, T. J., Hernquist, L., et al. 2013, MNRAS, 430, 1901
- Hopkins, P. F., Cox, T. J., Younger, J. D., & Hernquist, L. 2009a, The Astrophysical Journal, Volume 691, Issue 2, pp. 1168-1201 (2009)., 691, 1168

Este documento incorpora firma electrónica, y es copia auténtica de un documento electrónico archivado por la ULL según la Ley 39/2015.
Su autenticidad puede ser contrastada en la siguiente dirección <https://sede.ull.es/validacion/>

Identificador del documento: 1630219

Código de verificación: NYPyuzSi

Fecha: 26/10/2018 14:33:01

Firmado por: ALEJANDRO SERRANO BORLAFF
UNIVERSIDAD DE LA LAGUNA

Juan Esteban Beckman Abramson
UNIVERSIDAD DE LA LAGUNA

MARIA DEL CARMEN ELICHE MORAL
UNIVERSIDAD DE LA LAGUNA

JOAN FONT SERRA
UNIVERSIDAD DE LA LAGUNA

26/10/2018 14:36:58

26/10/2018 15:46:09

26/10/2018 18:46:53

6.4 BIBLIOGRAPHY

139

- Hopkins, P. F., Somerville, R. S., Cox, T. J., et al. 2009b, Monthly Notices of the Royal Astronomical Society, Volume 397, Issue 2, pp. 802-814., 397, 802
- Hubble, E. P. 1922, ApJ, 56, doi:10.1086/142698
- . 1925, Popular Astronomy, 33
- . 1926, ApJ, 64, doi:10.1086/143018
- . 1927, The Observatory., Vol. 50 (Editors of the Observatory]), 276-281
- . 1936, Realm of the Nebulae
- Huchra, J. P., & Geller, M. J. 1982, ApJ, 257, 423
- Hunter, D. A., Elmegreen, B. G., Oh, S.-H., et al. 2011, The Astronomical Journal, Volume 142, Issue 4, article id. 121, 26 pp. (2011)., 142, arXiv:1107.5587
- Ibata, R., Martin, N. F., Irwin, M., et al. 2007, ApJ, 671, 1591
- Ibata, R. A., Famaey, B., Lewis, G. F., Ibata, N. G., & Martin, N. 2014, The Astrophysical Journal, Volume 805, Issue 1, article id. 67, 10 pp. (2015)., 805, arXiv:1411.3718
- Illingworth, G. D., Magee, D., Oesch, P. A., et al. 2013, The Astrophysical Journal Supplement, Volume 209, Issue 1, article id. 6, 13 pp. (2013)., 209, arXiv:1305.1931
- Jog, C. J., & Combes, F. 2009, Phys. Rep., 471, 75
- Johnston, K. V., Bullock, J. S., Sharma, S., et al. 2008, The Astrophysical Journal, Volume 689, Issue 2, pp. 936-957 (2008)., 689, 936
- Kalberla, P. M. W., Kerp, J., Dedes, L., & Haud, U. 2014, The Astrophysical Journal, Volume 794, Issue 1, article id. 90, 5 pp. (2014)., 794, arXiv:1408.5334
- Kazantzidis, S., Zentner, A. R., Kravtsov, A. V., Bullock, J. S., & Debattista, V. P. 2009, The Astrophysical Journal, Volume 700, Issue 2, pp. 1896-1920 (2009)., 700, 1896
- Kennicutt, Robert C., J., C., R., & Jr. 1989, The Astrophysical Journal, 344, 685
- Kent, S. M. 1984, The Astrophysical Journal Supplement Series, 56, 105
- Khim, H.-g., Park, J., Seo, S.-W., et al. 2015, ApJS, 220, 3
- King, I. R. 1992, in Astrophysics and Space Science Library, Vol. 178, Morphological and Physical Classification of Galaxies, ed. G. Longo, M. Capaccioli, & G. Busarello, 371
- Klypin, A. A., Kravtsov, A. V., Valenzuela, O., & Prada, F. 1999, The Astrophysical Journal, Volume 522, Issue 1, pp. 82-92., 522, 82

Este documento incorpora firma electrónica, y es copia auténtica de un documento electrónico archivado por la ULL según la Ley 39/2015.
Su autenticidad puede ser contrastada en la siguiente dirección <https://sede.ull.es/validacion/>

Identificador del documento: 1630219

Código de verificación: NYPyuzSi

Fecha: 26/10/2018 14:33:01

Firmado por: ALEJANDRO SERRANO BORLAFF UNIVERSIDAD DE LA LAGUNA	26/10/2018 14:33:01
Juan Esteban Beckman Abramson UNIVERSIDAD DE LA LAGUNA	26/10/2018 14:36:58
MARIA DEL CARMEN ELICHE MORAL UNIVERSIDAD DE LA LAGUNA	26/10/2018 15:46:09
JOAN FONT SERRA UNIVERSIDAD DE LA LAGUNA	26/10/2018 18:46:53

- Koekemoer, A. M., Ellis, R. S., McLure, R. J., et al. 2012, The Astrophysical Journal Supplement, Volume 209, Issue 1, article id. 3, 14 pp. (2013)., 209, arXiv:1212.1448
- Koekemoer, A. M., Ellis, R. S., McLure, R. J., et al. 2013, ApJS, 209, 3
- Kormendy, J. 1993, in IAU Symposium, Vol. 153, Galactic Bulges, ed. H. Dejonghe & H. J. Habing, 209
- Kormendy, J., & Bender, R. 2012, ApJS, 198, 2
- Kormendy, J., & Kennicutt, Jr., R. C. 2004, ARA&A, 42, 603
- Krajnović, D., Emsellem, E., Cappellari, M., et al. 2011, MNRAS, 414, 2923
- Kregel, M., van der Kruit, P. C., & de Grijs, R. 2002, MNRAS, 334, 646
- Krist, J. E., Hook, R. N., & Stoehr, F. 2011, in Proc. SPIE, Vol. 8127, Optical Modeling and Performance Predictions V, 81270J
- Kylafis, N. D., & Bahcall, J. N. 1987, ApJ, 317, 637
- Labbe, I., Oesch, P. A., Illingworth, G. D., et al. 2015, The Astrophysical Journal Supplement Series, Volume 221, Issue 2, article id. 23, 13 pp. (2015)., 221, arXiv:1507.08313
- Larson, R. B., Tinsley, B. M., & Caldwell, C. N. 1980, ApJ, 237, 692
- Laurikainen, E., & Salo, H. 2001, Monthly Notices of the Royal Astronomical Society, 324, 685
- Laurikainen, E., Salo, H., Buta, R., et al. 2006, AJ, 132, 2634
- Laurikainen, E., Salo, H., Buta, R., & Knapen, J. H. 2011, MNRAS, 418, 1452
- Laurikainen, E., Salo, H., Buta, R., Knapen, J. H., & Comerón, S. 2010, MNRAS, 405, 1089
- Lin, D. N. C., & Pringle, J. E. 1987, The Astrophysical Journal, 320, L87
- Long, K. S., Baggett, S. M., & MacKenty, J. W. 2015, WFC3 Instrument Science Report 2015-15, 18 pages
- López-Corredoira, M., Betancort-Rijo, J., & Beckman, J. E. 2002, A&A, 386, 169
- López-Corredoira, M., & Molgó, J. 2014, A&A, 567, A106
- Luo, B., Brandt, W. N., Xue, Y. Q., et al. 2016, The Astrophysical Journal Supplement Series, Volume 228, Issue 1, article id. 2, 30 pp. (2017)., 228, arXiv:1611.03501
- Lynden-Bell, D. 1976, Monthly Notices of the Royal Astronomical Society, 174, 695
- Malin, D. F., & Carter, D. 1980, Nature, 285, 643

Este documento incorpora firma electrónica, y es copia auténtica de un documento electrónico archivado por la ULL según la Ley 39/2015.
Su autenticidad puede ser contrastada en la siguiente dirección <https://sede.ull.es/validacion/>

Identificador del documento: 1630219

Código de verificación: NYPyuzSi

Fecha: 26/10/2018 14:33:01

Firmado por: ALEJANDRO SERRANO BORLAFF
UNIVERSIDAD DE LA LAGUNA

Juan Esteban Beckman Abramson
UNIVERSIDAD DE LA LAGUNA

MARIA DEL CARMEN ELICHE MORAL
UNIVERSIDAD DE LA LAGUNA

JOAN FONT SERRA
UNIVERSIDAD DE LA LAGUNA

26/10/2018 14:36:58

26/10/2018 15:46:09

26/10/2018 18:46:53

6.4 BIBLIOGRAPHY

141

- Maltby, D. T., Hoyos, C., Gray, M. E., Aragón-Salamanca, A., & Wolf, C. 2012, Monthly Notices of the Royal Astronomical Society, 420, 2475
- Martín-Navarro, I., Bakos, J., Trujillo, I., Knapen, J. H., & Athanassoula, E. e. a. 2012, Monthly Notices of the Royal Astronomical Society, Volume 427, Issue 2, pp. 1102-1134., 427, 1102
- Martínez-Delgado, D., Peñarrubia, J., Gabany, R. J., et al. 2008, ApJ, 689, 184
- Martínez-Delgado, D., Pohlen, M., Gabany, R. J., et al. 2009, ApJ, 692, 955
- Martínez-Delgado, D., Gabany, R. J., Crawford, K., et al. 2010, AJ, 140, 962
- Martinez-Lombilla, C., Trujillo, I., & Knapen, J. H. 2018, eprint arXiv:1804.01546, arXiv:1804.01546
- Marzke, R. O., Geller, M. J., Huchra, J. P., & Corwin, Jr., H. G. 1994, AJ, 108, 437
- Mestel, L. 1963, Monthly Notices of the Royal Astronomical Society, 126, 553
- Mihos, J. C., & Hernquist, L. 1994, ApJ, 437, 611
- Minchev, I., Famaey, B., Quillen, A. C., et al. 2012, Astronomy & Astrophysics, Volume 548, id.A126, 24 pp., 548, arXiv:1203.2621
- Minchev, I., Martig, M., Streich, D., et al. 2015, The Astrophysical Journal Letters, Volume 804, Issue 1, article id. L9, 5 pp. (2015)., 804, arXiv:1502.06606
- Miyamoto, M., & Nagai, R. 1975, PASJ, 27, 533
- Moore, B., Katz, N., Lake, G., Dressler, A., & Oemler, A. 1996, Nature, 379, 613
- Muñoz-Mateos, J. C., de Paz, A. G., Boissier, S., et al. 2006, The Astrophysical Journal, Volume 658, Issue 2, pp. 1006-1026., 658, 1006
- Naeslund, M., & Joersaeter, S. 1997, A&A, 325, 915
- Narayan, C. A., & Jog, C. J. 2002, A&A, 390, L35
- Nelson, A. H. 1988, MNRAS, 233, 115
- Oort, J. H. 1940, ApJ, 91, 273
- Patterson, F. S. 1940, Harvard College Observatory Bulletin, 914, 9
- Pawlowski, M. S., McGaugh, S. S., & Jerjen, H. 2015, Monthly Notices of the Royal Astronomical Society, Volume 453, Issue 1, p.1047-1061, 453, 1047
- Peñarrubia, J., McConnachie, A., & Babul, A. 2006, The Astrophysical Journal, Volume 650, Issue 1, pp. L33-L36., 650, L33

Este documento incorpora firma electrónica, y es copia auténtica de un documento electrónico archivado por la ULL según la Ley 39/2015.
Su autenticidad puede ser contrastada en la siguiente dirección <https://sede.ull.es/validacion/>

Identificador del documento: 1630219

Código de verificación: NYPyuzSi

Fecha: 26/10/2018 14:33:01

Firmado por: ALEJANDRO SERRANO BORLAFF
UNIVERSIDAD DE LA LAGUNA

Juan Esteban Beckman Abramson
UNIVERSIDAD DE LA LAGUNA

MARIA DEL CARMEN ELICHE MORAL
UNIVERSIDAD DE LA LAGUNA

JOAN FONT SERRA
UNIVERSIDAD DE LA LAGUNA

26/10/2018 14:36:58

26/10/2018 15:46:09

26/10/2018 18:46:53

- Peng, C. Y., Ho, L. C., Impey, C. D., & Rix, H.-W. 2002, AJ, 124, 266
- . 2010, AJ, 139, 2097
- Perez, I. 2004, Astronomy and Astrophysics, v.427, p.L17-L20 (2004), 427, L17
- Pérez-González, P. G., Cava, A., Barro, G., et al. 2013, ApJ, 762, 46
- Peschken, N., Athanassoula, E., & Rodionov, S. A. 2017, Monthly Notices of the Royal Astronomical Society, Volume 468, Issue 1, p.994-1004, 468, 994
- Poggianti, B. M., Fasano, G., Bettoni, D., et al. 2009, ApJ, 697, L137
- Pohlen, M., Beckman, J. E., Hüttemeister, S., et al. 2004, in Astrophysics and Space Science Library, Vol. 319, Penetrating Bars Through Masks of Cosmic Dust, ed. D. L. Block, I. Puerari, K. C. Freeman, R. Groess, & E. K. Block, 713
- Pohlen, M., Dettmar, R.-J., Lütticke, R., & Aronica, G. 2002, Astronomy & Astrophysics, 392, 807
- Pohlen, M., & Trujillo, I. 2006, Astronomy and Astrophysics, Volume 454, Issue 3, August II 2006, pp.759-772, 454, 759
- Pohlen, M., Zaroubi, S., Peletier, R. F., & Dettmar, R. J. 2007, Monthly Notices of the Royal Astronomical Society, Volume 378, Issue 2, pp. 594-616., 378, 594
- Pranger, F., Trujillo, I., Kelvin, L. S., & Cebrián, M. 2017, MNRAS, 467, 2127
- Querejeta, M., Eliche-Moral, M., Tapia, T., et al. 2015a, Astronomy and Astrophysics, 573, doi:10.1051/0004-6361/201424303
- . 2015b, Astronomy and Astrophysics, 579, doi:10.1051/0004-6361/201526354
- Quinn, P. J. 1984, ApJ, 279, 596
- Radburn-Smith, D. J., Roskar, R., Debattista, V. P., et al. 2012, The Astrophysical Journal, Volume 753, Issue 2, article id. 138, 8 pp. (2012)., 753, arXiv:1206.1057
- Ravikumar, C. D., Barway, S., Kembhavi, A., Mobasher, B., & Kuriakose, V. C. 2006, A&A, 446, 827
- Reshetnikov, V., & Combes, F. 1999, Astronomy and Astrophysics Supplement Series, 138, 101
- Reshetnikov, V. P., Mosenkov, A. V., Moiseev, A. V., Kotov, S. S., & Savchenko, S. S. 2016, MNRAS, 461, 4233
- Reynolds, J. H. 1913, MNRAS, 74, 132
- Rix, H.-W., & Zaritsky, D. 1995, ApJ, 447, 82

Este documento incorpora firma electrónica, y es copia auténtica de un documento electrónico archivado por la ULL según la Ley 39/2015.
Su autenticidad puede ser contrastada en la siguiente dirección <https://sede.ull.es/validacion/>

Identificador del documento: 1630219

Código de verificación: NYPyuzSi

Fecha: 26/10/2018 14:33:01

Firmado por: ALEJANDRO SERRANO BORLAFF
UNIVERSIDAD DE LA LAGUNA

Juan Esteban Beckman Abramson
UNIVERSIDAD DE LA LAGUNA

MARIA DEL CARMEN ELICHE MORAL
UNIVERSIDAD DE LA LAGUNA

JOAN FONT SERRA
UNIVERSIDAD DE LA LAGUNA

26/10/2018 14:36:58

26/10/2018 15:46:09

26/10/2018 18:46:53

6.4 BIBLIOGRAPHY

143

- Rodionov, S. A., Athanassoula, E., & Peschken, N. 2017, Astronomy & Astrophysics, Volume 600, id.A25, 14 pp., 600, arXiv:1701.02685
- Rodríguez Del Pino, B., Bamford, S. P., Aragón-Salamanca, A., et al. 2014, MNRAS, 438, 1038
- Roškar, R., Debattista, V. P., Quinn, T. R., Stinson, G. S., & Wadsley, J. 2008a, ApJ, 684, L79
- Roškar, R., Debattista, V. P., Stinson, G. S., et al. 2008b, ApJ, 675, L65
- Ruiz-Lara, T., Few, C. G., Florido, E., et al. 2017, Astronomy & Astrophysics, Volume 608, id.A126, 11 pp., 608, arXiv:1709.06968
- Rujopakarn, W., Dunlop, J. S., Rieke, G. H., et al. 2016, The Astrophysical Journal, Volume 833, Issue 1, article id. 12, 11 pp. (2016)., 833, arXiv:1607.07710
- Sanchez-Saavedra, M. L., Battaner, E., & Florido, E. 1990, MNRAS, 246, 458
- Sandage, A. 1961, Washington: Carnegie Institution, 1961
- Sandin, C. 2014, Astronomy & Astrophysics, Volume 567, id.A97, 16 pp., 567, arXiv:1406.5508
- . 2015, Astronomy & Astrophysics, Volume 577, id.A106, 31 pp., 577, arXiv:1502.07244
- Schechter, P. 1976, ApJ, 203, 297
- Schweizer, F., Whitmore, B. C., & Rubin, V. C. 1983, AJ, 88, 909
- Sérsic, J. L. 1963, Boletín de la Asociacion Argentina de Astronomia La Plata Argentina, 6, 41
- Shaw, M. A., & Gilmore, G. 1990, MNRAS, 242, 59
- Sil'chenko, O. K., Proshina, I. S., Shulga, A. P., & Koposov, S. E. 2012, MNRAS, 427, 790
- Skelton, R. E., Whitaker, K. E., Momcheva, I. G., et al. 2014, ApJS, 214, 24
- Smith, B. J., Struck, C., Hancock, M., et al. 2007, AJ, 133, 791
- Spitzer, Lyman, J., & Baade, W. 1951, The Astrophysical Journal, 113, 413
- Struck, C., & Elmegreen, B. G. 2017, Monthly Notices of the Royal Astronomical Society, Volume 469, Issue 1, p.1157-1165, 469, 1157
- Tapia, T., Eliche-Moral, M. C., Aceves, H., et al. 2017, Astronomy & Astrophysics, Volume 604, id.A105, 20 pp., 604, arXiv:1706.03803

Este documento incorpora firma electrónica, y es copia auténtica de un documento electrónico archivado por la ULL según la Ley 39/2015.
Su autenticidad puede ser contrastada en la siguiente dirección <https://sede.ull.es/validacion/>

Identificador del documento: 1630219

Código de verificación: NYPyuzSi

Firmado por: ALEJANDRO SERRANO BORLAFF UNIVERSIDAD DE LA LAGUNA	Fecha: 26/10/2018 14:33:01
Juan Esteban Beckman Abramson UNIVERSIDAD DE LA LAGUNA	26/10/2018 14:36:58
MARIA DEL CARMEN ELICHE MORAL UNIVERSIDAD DE LA LAGUNA	26/10/2018 15:46:09
JOAN FONT SERRA UNIVERSIDAD DE LA LAGUNA	26/10/2018 18:46:53

- Teplitz, H. I., Rafelski, M., Kurczynski, P., et al. 2013, The Astronomical Journal, Volume 146, Issue 6, article id. 159, 19 pp. (2013)., 146, arXiv:1305.1357
- Thilker, D. A., Bianchi, L., Boissier, S., et al. 2004, The Astrophysical Journal, Volume 619, Issue 1, pp. L79-L82., 619, L79
- Thilker, D. A., Bianchi, L., Meurer, G., et al. 2007, The Astrophysical Journal Supplement Series, Volume 173, Issue 2, pp. 538-571., 173, 538
- Tolman, R. C. 1930, Proceedings of the National Academy of Science, 16, 511
- . 1934, Relativity, Thermodynamics, and Cosmology
- Toomre, A. 1978, Science, 202, 510
- Toomre, A., & Toomre, J. 1972, ApJ, 178, 623
- Toth, G., & Ostriker, J. P. 1992, The Astrophysical Journal, 389, 5
- Trujillo, I., & Bakos, J. 2013, MNRAS, 431, 1121
- Trujillo, I., & Fliri, J. 2016, ApJ, 823, 123
- Tsikoudi, V. 1979, ApJ, 234, 842
- Tully, R. B., Libeskind, N. I., Karachentsev, I. D., et al. 2015, The Astrophysical Journal Letters, Volume 802, Issue 2, article id. L25, 5 pp. (2015)., 802, arXiv:1503.05599
- Vaghmare, K., Barway, S., Mathur, S., & Kembhavi, A. K. 2015, MNRAS, 450, 873
- van den Bergh, S. 1976, ApJ, 206, 883
- . 1990, ApJ, 348, 57
- van der Kruit, P. C. 1979, A&AS, 38, 15
- . 1987, A&A, 173, 59
- van der Kruit, P. C., & Searle, L. 1981a, A&A, 95, 105
- . 1981b, A&A, 95, 116
- . 1982, A&A, 110, 61
- Vazdekis, A., Koleva, M., Ricciardelli, E., Röck, B., & Falcón-Barroso, J. 2016, MNRAS, 463, 3409
- Vlajić, M., Bland-Hawthorn, J., & Freeman, K. C. 2009, The Astrophysical Journal, Volume 697, Issue 1, pp. 361-372 (2009)., 697, 361
- . 2011, The Astrophysical Journal, Volume 732, Issue 1, article id. 7, 10 pp. (2011)., 732, arXiv:1101.0607

Este documento incorpora firma electrónica, y es copia auténtica de un documento electrónico archivado por la ULL según la Ley 39/2015.
Su autenticidad puede ser contrastada en la siguiente dirección <https://sede.ull.es/validacion/>

Identificador del documento: 1630219

Código de verificación: NYPyuzSi

Fecha: 26/10/2018 14:33:01

Firmado por: ALEJANDRO SERRANO BORLAFF UNIVERSIDAD DE LA LAGUNA	26/10/2018 14:36:58
Juan Esteban Beckman Abramson UNIVERSIDAD DE LA LAGUNA	26/10/2018 15:46:09
MARIA DEL CARMEN ELICHE MORAL UNIVERSIDAD DE LA LAGUNA	26/10/2018 18:46:53
JOAN FONT SERRA UNIVERSIDAD DE LA LAGUNA	

6.4 BIBLIOGRAPHY

145

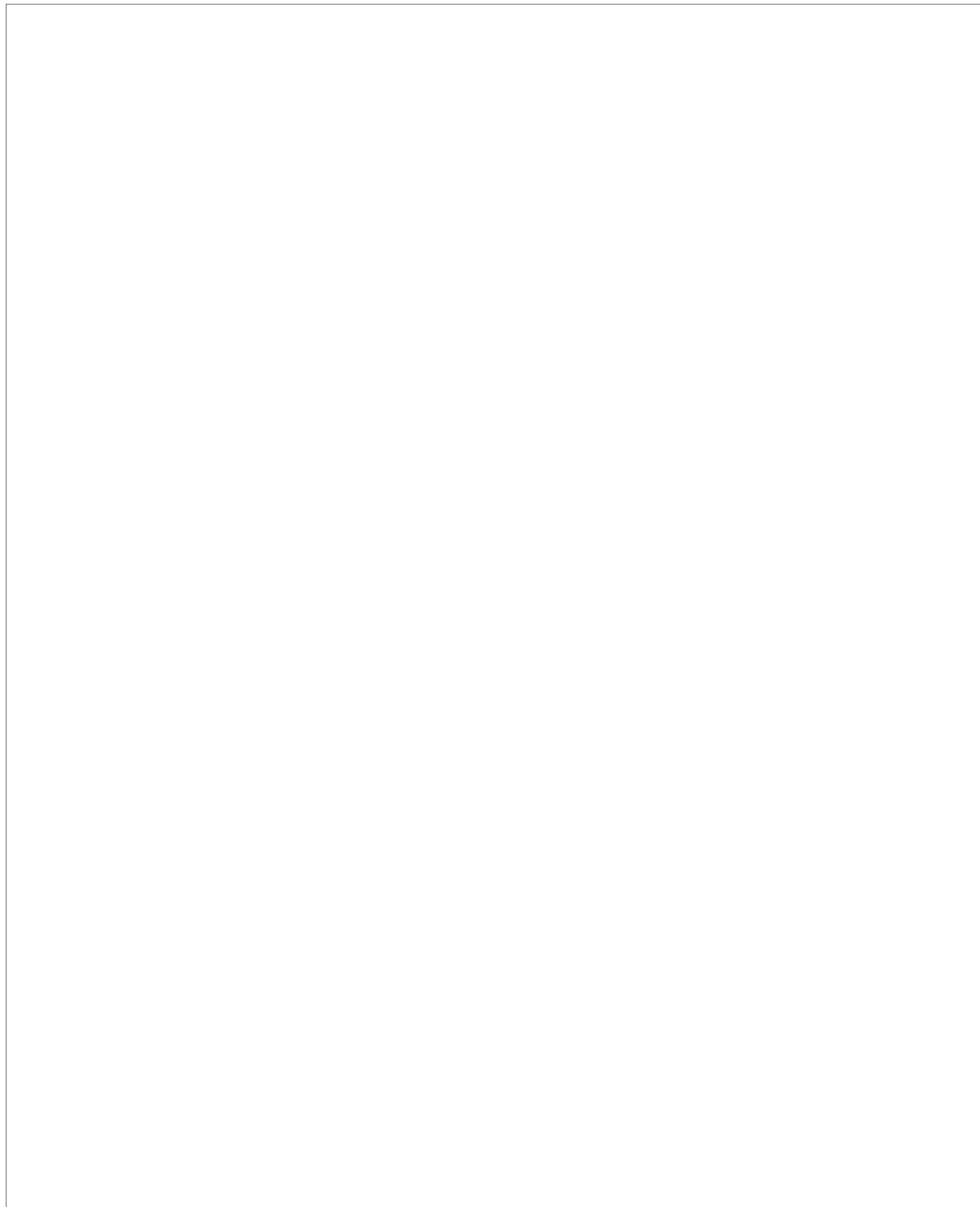
- Vollmer, B., Huchtmeier, W., & van Driel, W. 2005, A&A, 439, 921
- Vollmer, B., Soida, M., Braine, J., et al. 2012, A&A, 537, A143
- Walter, F., Decarli, R., Aravena, M., et al. 2016, The Astrophysical Journal, Volume 833, Issue 1, article id. 67, 15 pp. (2016)., 833, arXiv:1607.06768
- Wang, J., Zheng, Z., D'Souza, R., et al. 2018, Monthly Notices of the Royal Astronomical Society, Advance Access, arXiv:1806.09353
- Weiner, B. J., Williams, T. B., van Gorkom, J. H., & Sellwood, J. A. 2000, The Astrophysical Journal, Volume 546, Issue 2, pp. 916-930., 546, 916
- Whitaker, K. E., van Dokkum, P. G., Brammer, G., & Franx, M. 2012, ApJ, 754, L29
- Whitaker, K. E., Labbé, I., van Dokkum, P. G., et al. 2011, ApJ, 735, 86
- White, S. D. M. 1978, MNRAS, 184, 185
- Wilman, D. J., Oemler, Jr., A., Mulchaey, J. S., et al. 2009, ApJ, 692, 298
- Xue, Y. Q., Luo, B., Brandt, W. N., et al. 2011, The Astrophysical Journal Supplement, Volume 195, Issue 1, article id. 10, 31 pp. (2011)., 195, arXiv:1105.5643
- Yoshii, Y., & Sommer-Larsen, J. 1989, Monthly Notices of the Royal Astronomical Society, 236, 779
- Younger, J. D., Cox, T. J., Seth, A. C., & Hernquist, L. 2007, The Astrophysical Journal, Volume 670, Issue 1, pp. 269-278., 670, 269
- Zaritsky, D., Salo, H., Laurikainen, E., et al. 2013, ApJ, 772, 135
- Zheng, Z., Thilker, D., Heckman, T., et al. 2014, The Astrophysical Journal, Volume 800, Issue 2, article id. 120, 26 pp. (2015)., 800, arXiv:1412.3209

Este documento incorpora firma electrónica, y es copia auténtica de un documento electrónico archivado por la ULL según la Ley 39/2015.
Su autenticidad puede ser contrastada en la siguiente dirección <https://sede.ull.es/validacion/>

Identificador del documento: 1630219

Código de verificación: NYPyuzSi

Firmado por: ALEJANDRO SERRANO BORLAFF UNIVERSIDAD DE LA LAGUNA	Fecha: 26/10/2018 14:33:01
Juan Esteban Beckman Abramson UNIVERSIDAD DE LA LAGUNA	26/10/2018 14:36:58
MARIA DEL CARMEN ELICHE MORAL UNIVERSIDAD DE LA LAGUNA	26/10/2018 15:46:09
JOAN FONT SERRA UNIVERSIDAD DE LA LAGUNA	26/10/2018 18:46:53



Este documento incorpora firma electrónica, y es copia auténtica de un documento electrónico archivado por la ULL según la Ley 39/2015. <i>Su autenticidad puede ser contrastada en la siguiente dirección https://sede.ull.es/validacion/</i>	
Identificador del documento: 1630219	Código de verificación: NYPyuzSi
Firmado por: ALEJANDRO SERRANO BORLAFF UNIVERSIDAD DE LA LAGUNA	Fecha: 26/10/2018 14:33:01
Juan Esteban Beckman Abramson UNIVERSIDAD DE LA LAGUNA	26/10/2018 14:36:58
MARIA DEL CARMEN ELICHE MORAL UNIVERSIDAD DE LA LAGUNA	26/10/2018 15:46:09
JOAN FONT SERRA UNIVERSIDAD DE LA LAGUNA	26/10/2018 18:46:53

BIBLIOGRAPHY

147

Este documento incorpora firma electrónica, y es copia auténtica de un documento electrónico archivado por la ULL según la Ley 39/2015.
Su autenticidad puede ser contrastada en la siguiente dirección <https://sede.ull.es/validacion/>

Identificador del documento: 1630219

Código de verificación: NYPyuzSi

Firmado por: ALEJANDRO SERRANO BORLAFF UNIVERSIDAD DE LA LAGUNA	Fecha: 26/10/2018 14:33:01
Juan Esteban Beckman Abramson UNIVERSIDAD DE LA LAGUNA	26/10/2018 14:36:58
MARIA DEL CARMEN ELICHE MORAL UNIVERSIDAD DE LA LAGUNA	26/10/2018 15:46:09
JOAN FONT SERRA UNIVERSIDAD DE LA LAGUNA	26/10/2018 18:46:53

A

Appendix A

148

Este documento incorpora firma electrónica, y es copia auténtica de un documento electrónico archivado por la ULL según la Ley 39/2015.
Su autenticidad puede ser contrastada en la siguiente dirección <https://sede.ull.es/validacion/>

Identificador del documento: 1630219 Código de verificación: NYPyuzSi

Firmado por: ALEJANDRO SERRANO BORLAFF UNIVERSIDAD DE LA LAGUNA	Fecha: 26/10/2018 14:33:01
Juan Esteban Beckman Abramson UNIVERSIDAD DE LA LAGUNA	26/10/2018 14:36:58
MARIA DEL CARMEN ELICHE MORAL UNIVERSIDAD DE LA LAGUNA	26/10/2018 15:46:09
JOAN FONT SERRA UNIVERSIDAD DE LA LAGUNA	26/10/2018 18:46:53

A. Borlaff et al.: Anti-truncated stellar profiles on S0 galaxies at $0.2 < z < 0.6$

Appendix A: Global properties of the initial sample of galaxies on the red sequence at $0.2 < z < 0.6$ in the GOODS-N field

Table A.1. Properties of the initial red sample and morphological classification.

Number	SHARDS ID	α ($^{\circ}$)	δ ($^{\circ}$)	Morph type	z_{phot}	z_{spec}	$\log_{10}(M_{\star}/M_{\odot})$	SFR M_{\odot}/yr	M_V [mag]	M_K [mag]	A_{F775W} $[10^{-2} \text{ mag}]$	$R - F775W$ [mag]
(1)	(2)	(3)	(4)	(5)	(6)	(7)	(8)	(9)	(10)	(11)	(12)	(13)
1	SHARDS10000327	189.3624	62.2135	E/S0	0.46	0.4755	10.177 \pm 0.073	-2.210	-19.42	-20.25	-2.54 $^{+0.11}_{-0.13}$	-0.433
2	SHARDS10000478	189.3746	62.2169	E	0.52	0.5117	11.02 \pm 0.10	-4.308	-21.27	-22.25	-2.52 $^{+0.13}_{-0.15}$	-
3	SHARDS10000488	189.3237	62.2208	DF	0.38	-	8.73 \pm 0.13	-0.595	-16.34	-17.45	-2.564 $^{+0.086}_{-0.151}$	-
4	SHARDS10000536	189.4163	62.2231	CPSTB	0.23	-	8.31 \pm 0.18	0.112	-14.58	-15.98	-2.52 $^{+0.13}_{-0.13}$	-
5	SHARDS10000737	189.3396	62.2263	E	0.47	0.4747	11.188 \pm 0.081	-3.615	-21.48	-22.72	-2.54 $^{+0.11}_{-0.13}$	-
6	SHARDS10000762	189.3593	62.2297	S0	0.47	0.4742	10.755 \pm 0.092	2.484	-21.16	-22.40	-2.54 $^{+0.13}_{-0.13}$	-0.430
7	SHARDS10000827	189.4341	62.2329	S0	0.51	0.5116	10.223 \pm 0.060	2.398	-20.56	-22.08	-2.50 $^{+0.13}_{-0.13}$	-0.491
8	SHARDS10000840	189.4244	62.2330	E/S0	0.52	0.5118	10.901 \pm 0.054	-2.725	-20.97	-21.95	-2.52 $^{+0.13}_{-0.13}$	-0.493
9	SHARDS10000845	189.4441	62.2332	S0	0.36	0.5123	11.247 \pm 0.062	4.570	-21.83	-22.82	-2.50 $^{+0.13}_{-0.13}$	-0.493
10	SHARDS10000849	189.3590	62.2342	S0	0.47	0.4746	10.736 \pm 0.084	-2.371	-20.63	-22.03	-2.54 $^{+0.11}_{-0.13}$	-0.432
11	SHARDS10001013	189.2899	62.2399	S0	0.47	0.4753	10.793 \pm 0.063	-1.976	-20.49	-21.73	-2.59 $^{+0.11}_{-0.13}$	-0.433
12	SHARDS10001052	189.2839	62.2396	Sp	0.57	0.5639	11.091 \pm 0.092	9.220	-21.52	-22.92	-2.59 $^{+0.13}_{-0.13}$	-
13	SHARDS10001058	189.4457	62.2420	CPSTB	0.47	-	8.970 \pm 0.100	-1.100	-16.90	-17.00	-2.50 $^{+0.13}_{-0.13}$	-
14	SHARDS10001235	189.4768	62.2475	OM	0.38	0.4620	9.939 \pm 0.080	-1.521	-18.81	-19.87	-2.50 $^{+0.13}_{-0.13}$	-
15	SHARDS10001269	189.4690	62.2470	S0	0.51	0.5116	10.958 \pm 0.074	-4.443	-21.61	-22.89	-2.50 $^{+0.13}_{-0.13}$	-0.492
16	SHARDS10001314	189.2334	62.2486	S0	0.31	0.3215	9.662 \pm 0.057	-0.510	-18.42	-19.50	-2.586 $^{+0.086}_{-0.086}$	-0.183
17	SHARDS10001344	189.2864	62.2504	S0	0.57	0.5673	10.375 \pm 0.086	2.813	-20.19	-21.30	-2.586 $^{+0.086}_{-0.086}$	-0.584
18	SHARDS10001350	189.4721	62.2483	S0	0.50	0.5106	10.935 \pm 0.071	-4.234	-21.55	-22.83	-2.50 $^{+0.13}_{-0.13}$	-0.492
19	SHARDS10001629	189.4774	62.2575	E	0.45	0.4566	10.846 \pm 0.058	-1.869	-20.62	-21.86	-2.50 $^{+0.13}_{-0.13}$	-
20	SHARDS10001648	189.4680	62.2582	S0	0.45	0.4540	10.501 \pm 0.080	-1.874	-20.47	-21.75	-2.50 $^{+0.13}_{-0.13}$	-0.397
21	SHARDS10001727	189.2911	62.2567	S0	0.22	0.2013	10.113 \pm 0.046	-0.984	-19.62	-21.15	-2.607 $^{+0.086}_{-0.086}$	0.014
22	SHARDS10001847	189.4818	62.2618	S0	0.46	0.4598	10.761 \pm 0.096	2.576	-21.12	-22.40	-2.50 $^{+0.13}_{-0.13}$	-0.408
23	SHARDS10001928	189.4598	62.2647	S0	0.44	0.4553	9.824 \pm 0.051	-1.959	-19.48	-21.01	-2.52 $^{+0.13}_{-0.13}$	-0.398
24	SHARDS10001971	189.4888	62.2633	E	0.46	0.4574	11.072 \pm 0.088	3.896	-21.19	-22.43	-2.50 $^{+0.13}_{-0.13}$	-
25	SHARDS10002351	189.5065	62.2742	S0	0.48	0.4834	10.483 \pm 0.047	-1.745	-20.23	-21.51	-2.48 $^{+0.13}_{-0.13}$	-0.446
26	SHARDS10002730	189.3097	62.2823	S0	0.44	0.4472	10.339 \pm 0.062	-1.660	-20.11	-21.20	-2.63 $^{+0.11}_{-0.11}$	-0.386
27	SHARDS10002769	189.4826	62.2824	E/S0	0.44	0.4417	10.539 \pm 0.074	1.187	-20.06	-21.05	-2.52 $^{+0.24}_{-0.24}$	-0.378
28	SHARDS10002901	189.3599	62.2869	E/S0	0.57	0.5642	10.23 \pm 0.14	5.088	-19.73	-21.11	-2.61 $^{+0.13}_{-0.13}$	-0.579
29	SHARDS10002942	189.3608	62.2871	S0	0.57	0.5644	10.77 \pm 0.12	-4.363	-20.84	-21.80	-2.61 $^{+0.13}_{-0.13}$	-0.578
30	SHARDS10003216	189.2486	62.3041	E/S0	0.49	0.4974	10.024 \pm 0.059	-2.081	-19.28	-20.20	-2.650 $^{+0.108}_{-0.108}$	-0.468
31	SHARDS10003299	189.1697	62.3019	DF	0.32	-	8.50 \pm 0.20	-0.289	-15.19	-16.06	-2.63 $^{+0.13}_{-0.13}$	-
32	SHARDS10003312	189.2352	62.3012	E/S0	0.49	0.4973	10.731 \pm 0.084	-2.475	-20.54	-21.53	-2.650 $^{+0.108}_{-0.086}$	-0.468
33	SHARDS10003402	189.4151	62.2974	S0	0.20	0.2133	10.817 \pm 0.062	-1.592	-20.07	-21.31	-2.59 $^{+0.13}_{-0.13}$	-0.007
34	SHARDS10003647	189.1583	62.2914	S0	0.56	0.5553	10.926 \pm 0.068	-4.616	-21.11	-22.51	-2.61 $^{+0.13}_{-0.13}$	-0.563
35	SHARDS10004066	189.3262	62.3433	E	0.25	0.2544	10.357 \pm 0.052	0.649	-20.23	-21.76	-2.69 $^{+0.13}_{-0.13}$	-
36	SHARDS10004234	189.3083	62.3435	E	0.53	0.5323	11.064 \pm 0.061	1.750	-21.63	-22.58	-2.71 $^{+0.13}_{-0.13}$	-
37	SHARDS10004423	189.3738	62.3263	Sp	0.32	0.3186	10.58 \pm 0.41	1.968	-21.03	-22.37	-2.65 $^{+0.19}_{-0.19}$	-
38	SHARDS10004592	189.3917	62.3270	E	0.27	0.2733	10.435 \pm 0.070	1.140	-20.67	-22.04	-2.65 $^{+0.19}_{-0.19}$	-
39	SHARDS10004719	189.3806	62.3472	GP	0.30	-	8.31 \pm 0.30	-0.328	-14.58	-15.98	-2.69 $^{+0.17}_{-0.17}$	-
40	SHARDS10004777	189.2822	62.3143	S0	0.24	0.2010	10.219 \pm 0.041	1.133	-19.88	-21.41	-2.67 $^{+0.11}_{-0.11}$	0.014
41	SHARDS10005029	189.2326	62.2485	E/S0	0.30	-	9.155 \pm 0.069	-0.341	-17.45	-18.27	-2.586 $^{+0.108}_{-0.086}$	-0.147
42	SHARDS10005391	189.4568	62.2852	CPSTB	0.23	-	8.614 \pm 0.084	-0.161	-14.55	-15.82	-2.54 $^{+0.17}_{-0.17}$	-
43	SHARDS10005533	189.3450	62.2152	CPSTB	0.46	-	8.58 \pm 0.18	-1.399	-16.60	-17.08	-2.54 $^{+0.11}_{-0.11}$	-
44	SHARDS10006598	189.3552	62.2282	DF	0.38	-	8.46 \pm 0.18	-0.584	-15.81	-16.89	-2.54 $^{+0.11}_{-0.11}$	-
45	SHARDS10006521	189.3817	62.2372	DF	0.46	-	9.04 \pm 0.22	-1.208	-16.12	-16.98	-2.54 $^{+0.11}_{-0.11}$	-
46	SHARDS10006744	189.4309	62.2823	CPSTB	0.22	-	7.51 \pm 0.24	-0.327	-13.08	-14.03	-2.56 $^{+0.19}_{-0.19}$	-

Notes. Columns: (1) ID sample, (2) ID SHARDS (release DR2 beta), (3) Right ascension (degrees). (4) Declination (degrees). (5) Morphological classification: E (elliptical), E/S0, S0, Sp (spiral), CPSTB (compact post-starburst), OM (ongoing merger), GP (green pea), DF (diffuse galaxy). (6) Photometric redshift. (7) Spectroscopic redshift (when available). (8) Decimal logarithm of the stellar mass. (9) Total SFR (from the emission in 24 μm and 2800 \AA provided in the Rainbow database, following the procedure described in Barro et al. 2013). Negative values correspond to upper limits following the notation on the Rainbow Database (see Sect. 3). (10) Absolute synthetic rest-frame magnitude in Johnson V band from the Rainbow database (Sect. 2.5). (11) Absolute rest-frame synthetic magnitude in the K_s band from the Rainbow database (Sect. 2.5). (12) Milky Way extinction in the $F775\text{W}$ band (magnitudes). (13) Estimated K-correction for the $F775\text{W}$ filters to the Steidel R band for the redshift of each galaxy, considering the fit in Eq. (8) (see Sect. 2.5).

A119, page 23 of 71

Este documento incorpora firma electrónica, y es copia auténtica de un documento electrónico archivado por la ULL según la Ley 39/2015. Su autenticidad puede ser contrastada en la siguiente dirección https://sede.ull.es/validacion/	
Identificador del documento: 1630219 Código de verificación: NYPyuzSi	
Firmado por: ALEJANDRO SERRANO BORLAFF UNIVERSIDAD DE LA LAGUNA	Fecha: 26/10/2018 14:33:01
Juan Esteban Beckman Abramson UNIVERSIDAD DE LA LAGUNA	26/10/2018 14:36:58
MARIA DEL CARMEN ELICHE MORAL UNIVERSIDAD DE LA LAGUNA	26/10/2018 15:46:09
JOAN FONT SERRA UNIVERSIDAD DE LA LAGUNA	26/10/2018 18:46:53

A&A 604, A119 (2017)

Table A.1. continued.

Number	SHARDS ID	α ($^{\circ}$)	δ ($^{\circ}$)	Morph type	z_{phot}	z_{spec}	$\log_{10}(M_{\star}/M_{\odot})$	SFR M_{\odot}/yr	M_V [mag]	M_K [mag]	A_{F775W} $[10^{-2} \text{ mag}]$	$R - F775W$ [mag]
(1)	(2)	(3)	(4)	(5)	(6)	(7)	(8)	(9)	(10)	(11)	(12)	(13)
47	SHARDS10006819	189.4873	62.2901	DF	0.25	–	7.92 ± 0.21	-0.167	-13.69	-14.93	-2.52 ^{+0.24} _{-0.15}	–
48	SHARDS10006931	189.4216	62.3015	OM	0.37	–	8.05 ± 0.23	-0.336	-14.66	-15.55	-2.59 ^{+0.17} _{-0.17}	–
49	SHARDS10007413	189.3688	62.3567	CPSTB	0.24	–	8.34 ± 0.21	-0.129	-14.61	-15.53	-2.71 ^{+0.17} _{-0.17}	–
50	SHARDS10007672	189.4374	62.2383	DF	0.20	–	7.77 ± 0.36	-0.112	-13.18	-14.47	-2.50 ^{+0.13} _{-0.13}	–
51	SHARDS10007737	189.1887	62.2536	GP	0.26	–	7.13 ± 0.30	-0.229	-12.96	-13.76	-2.59 ^{+0.11} _{-0.11}	–
52	SHARDS10007846	189.2103	62.2692	CPSTB	0.20	–	7.97 ± 0.15	-0.074	-13.25	-14.59	-2.61 ^{+0.11} _{-0.11}	–
53	SHARDS10007883	189.5146	62.2755	GP	0.26	–	8.05 ± 0.12	-0.194	-14.37	-15.48	-2.48 ^{+0.15} _{-0.15}	–
54	SHARDS10007902	189.2121	62.2778	CPSTB	0.26	–	8.39 ± 0.33	-0.224	-14.52	-15.62	-2.61 ^{+0.15} _{-0.11}	–
55	SHARDS10008552	189.4493	62.2348	SO	0.38	–	9.372 ± 0.099	-0.761	-17.55	-18.99	-2.50 ^{+0.13} _{-0.13}	-0.279
56	SHARDS10008997	189.3576	62.2331	DF	0.41	–	8.71 ± 0.13	-0.669	-15.67	-16.76	-2.54 ^{+0.11} _{-0.13}	–
57	SHARDS10009032	189.4216	62.2412	CPSTB	0.25	–	8.13 ± 0.26	-0.202	-14.12	-15.52	-2.52 ^{+0.13} _{-0.13}	–
58	SHARDS10009131	189.4763	62.2589	DF	0.39	–	8.50 ± 0.12	-0.543	-15.22	-16.28	-2.50 ^{+0.13} _{-0.13}	–
59	SHARDS10009411	189.3849	62.2949	DF	0.30	–	8.29 ± 0.26	-0.311	-14.20	-15.51	-2.61 ^{+0.13} _{-0.19}	–
60	SHARDS10009577	189.3581	62.3522	DF	0.28	–	8.42 ± 0.22	-0.189	-14.52	-15.84	-2.71 ^{+0.17} _{-0.17}	–
61	SHARDS10009610	189.1626	62.3059	SO	0.55	0.5568	11.209 ± 0.069	-5.768	-21.53	-22.77	-2.65 ^{+0.13} _{-0.13}	-0.565
62	SHARDS10009819	189.2794	62.2468	CPSTB	0.27	–	8.40 ± 0.26	-0.206	-14.04	-15.28	-2.586 ^{+0.108} _{-0.086}	–
63	SHARDS10009927	189.1876	62.2756	DF	0.21	–	7.84 ± 0.18	-0.080	-13.71	-14.00	-2.61 ^{+0.11} _{-0.11}	–
64	SHARDS10010084	189.2336	62.3079	DF	0.34	–	8.24 ± 0.20	-0.443	-14.57	-15.62	-2.672 ^{+0.086} _{-0.108}	–
65	SHARDS10010282	189.3884	62.2943	DF	0.36	–	8.50 ± 0.19	-0.431	-14.81	-15.91	-2.59 ^{+0.17} _{-0.17}	–
66	SHARDS10010726	189.3233	62.2166	DF	0.54	–	8.72 ± 0.10	-2.152	-16.02	-16.51	-2.54 ^{+0.11} _{-0.13}	–
67	SHARDS10010775	189.4558	62.2429	DF	0.34	–	8.23 ± 0.11	-0.471	-14.32	-15.24	-2.59 ^{+0.13} _{-0.13}	–
68	SHARDS10011094	189.3024	62.3716	CPSTB	0.57	–	8.99 ± 0.18	-2.633	-17.38	-17.82	-2.76 ^{+0.12} _{-0.13}	–
69	SHARDS10011171	189.3521	62.2071	CPSTB	0.32	–	7.80 ± 0.17	-0.265	-13.97	-14.11	-2.52 ^{+0.11} _{-0.13}	–
70	SHARDS10011229	189.2272	62.2494	DF	0.43	–	7.97 ± 0.23	-0.991	-15.11	-15.86	-2.586 ^{+0.108} _{-0.086}	–
71	SHARDS10011544	189.3378	62.2820	GP	0.24	–	7.40 ± 0.20	-0.166	-13.62	-14.44	-2.61 ^{+0.13} _{-0.15}	–
72	SHARDS10012012	189.4063	62.2628	DF	0.35	–	7.63 ± 0.28	-0.496	-14.26	-15.02	-2.56 ^{+0.13} _{-0.13}	–
73	SHARDS20000593	189.1656	62.1385	SO	0.24	0.2470	9.766 ± 0.038	-0.407	-19.07	-20.32	-2.43 ^{+0.15} _{-0.13}	-0.060
74	SHARDS20000668	189.0924	62.1440	CPSTB	0.33	–	9.351 ± 0.087	-1.754	-17.53	-18.91	-2.46 ^{+0.11} _{-0.11}	–
75	SHARDS20000827	189.0355	62.1475	SO	0.40	0.4090	11.177 ± 0.079	-4.065	-20.97	-22.21	-2.435 ^{+0.108} _{-0.086}	-0.324
76	SHARDS20000858	189.2628	62.1502	SO	0.55	0.5600	10.391 ± 0.056	4.298	-19.77	-21.17	-2.46 ^{+0.10} _{-0.19}	-0.571
77	SHARDS20001051	189.1201	62.1564	SO	0.52	0.5183	10.602 ± 0.061	-2.607	-20.52	-21.81	-2.46 ^{+0.11} _{-0.11}	-0.502
78	SHARDS20001223	189.0208	62.1619	GP	0.23	–	7.88 ± 0.16	-0.157	-13.72	-14.93	-2.456 ^{+0.086} _{-0.086}	–
79	SHARDS20001534	189.2412	62.1702	SO	0.40	0.4101	10.249 ± 0.062	-1.112	-19.15	-20.01	-2.50 ^{+0.13} _{-0.13}	-0.327
80	SHARDS20002147	189.1471	62.1861	SO	0.40	0.4101	10.190 ± 0.057	-1.183	-20.19	-21.47	-2.50 ^{+0.13} _{-0.11}	-0.327
81	SHARDS20002235	189.2818	62.1867	E/SO	0.40	0.4714	10.583 ± 0.057	-1.989	-20.42	-21.48	-2.52 ^{+0.11} _{-0.15}	-0.426
82	SHARDS20002542	189.1283	62.1996	DF	0.32	–	8.30 ± 0.11	-0.328	-15.45	-16.78	-2.500 ^{+0.129} _{-0.066}	–
83	SHARDS20002550	189.0022	62.1988	E/SO	0.55	0.5616	11.139 ± 0.090	-7.355	-21.86	-22.86	-2.478 ^{+0.086} _{-0.084}	-0.573
84	SHARDS20002599	189.0414	62.2324	DF	0.22	–	7.914 ± 0.073	-0.143	-14.97	-15.83	-2.500 ^{+0.129} _{-0.065}	–
85	SHARDS20002889	189.2019	62.2213	SO	0.47	0.4760	9.25 ± 0.12	-1.681	-18.12	-19.64	-2.564 ^{+0.086} _{-0.086}	-0.434
86	SHARDS20002935	189.2003	62.2192	SO	0.47	0.4745	10.924 ± 0.068	3.046	-20.82	-22.06	-2.564 ^{+0.086} _{-0.086}	-0.431
87	SHARDS20002966	189.1671	62.2182	SO	0.49	0.4854	10.953 ± 0.066	-2.720	-20.89	-22.13	-2.543 ^{+0.108} _{-0.086}	-0.449
88	SHARDS20002995	189.1044	62.2168	SO	0.52	0.5185	10.958 ± 0.072	2.404	-20.90	-22.14	-2.521 ^{+0.108} _{-0.086}	-0.503
89	SHARDS20003119	189.2360	62.2126	Sp	0.52	0.5178	10.67 ± 0.10	4.251	-20.94	-22.19	-2.564 ^{+0.096} _{-0.151}	–
90	SHARDS20003134	189.0956	62.2166	SO	0.47	0.4725	10.807 ± 0.071	9.135	-20.99	-21.94	-2.521 ^{+0.116} _{-0.086}	-0.427
91	SHARDS20003210	189.2522	62.2096	SO	0.56	0.5631	10.800 ± 0.063	-2.855	-20.53	-21.39	-2.564 ^{+0.086} _{-0.086}	-0.576
92	SHARDS20003217	189.1158	62.2113	SO	0.52	0.5153	10.808 ± 0.066	-2.485	-20.53	-21.77	-2.521 ^{+0.108} _{-0.086}	-0.499
93	SHARDS20003377	189.0637	62.2060	SO	0.32	0.3198	9.930 ± 0.061	-0.568	-19.54	-20.82	-2.500 ^{+0.13} _{-0.065}	-0.180
94	SHARDS20003678	189.1938	62.1976	E/SO	0.50	0.5039	10.421 ± 0.061	-2.014	-19.77	-20.75	-2.52 ^{+0.11} _{-0.11}	-0.480
95	SHARDS20003814	189.1394	62.2842	E	0.46	0.4543	10.100 ± 0.091	-1.459	-19.52	-20.77	-2.61 ^{+0.13} _{-0.13}	–
96	SHARDS20003909	189.1583	62.2709	E	0.53	0.5290	10.581 ± 0.081	-2.256	-20.40	-21.27	-2.59 ^{+0.13} _{-0.13}	–
97	SHARDS20003969	189.1071	62.2617	CPSTB	0.20	–	8.339 ± 0.080	-0.107	-14.45	-15.07	-2.56 ^{+0.13} _{-0.13}	–
98	SHARDS20004069	189.0768	62.2552	OM	0.27	–	7.93 ± 0.22	-0.233	-14.36	-14.62	-2.54 ^{+0.11} _{-0.11}	–
99	SHARDS20004113	189.1728	62.2557	CPSTB	0.27	–	7.93 ± 0.30	-0.256	-13.79	-14.85	-2.59 ^{+0.11} _{-0.11}	–
100	SHARDS20004273	189.1426	62.2425	SO	0.52	0.5184	10.758 ± 0.086	5.286	-21.11	-22.39	-2.56 ^{+0.11} _{-0.11}	-0.502
101	SHARDS20004275	189.1439	62.2424	CPSTB	0.26	–	9.60 ± 0.14	1.078	-17.02	-18.30	-2.56 ^{+0.11} _{-0.11}	–
102	SHARDS20004328	189.1245	62.2393	CPSTB	0.52	0.5195	9.920 ± 0.049	9.615	-18.95	-20.34	-2.54 ^{+0.11} _{-0.11}	–
103	SHARDS20004359	189.2638	62.2383	SO	0.51	0.5120	10.597 ± 0.091	-2.385	-20.66	-21.51	-2.59 ^{+0.11} _{-0.11}	-0.493
104	SHARDS20004420	189.1728	62.2341	E/SO	0.55	0.5556	10.774 ± 0.069	-3.640	-20.95	-21.94	-2.56 ^{+0.11} _{-0.11}	-0.565

Este documento incorpora firma electrónica, y es copia auténtica de un documento electrónico archivado por la ULL según la Ley 39/2015. Su autenticidad puede ser contrastada en la siguiente dirección https://sede.ull.es/validacion/												
Identificador del documento: 1630219										Código de verificación: NYPyuzSi		
Firmado por: ALEJANDRO SERRANO BORLAFF UNIVERSIDAD DE LA LAGUNA										Fecha: 26/10/2018 14:33:01		
Juan Esteban Beckman Abramson UNIVERSIDAD DE LA LAGUNA												

A. Borlaff et al.: Anti-truncated stellar profiles on S0 galaxies at $0.2 < z < 0.6$

Table A.1. continued.

Number	SHARDS ID	α ($^{\circ}$)	δ ($^{\circ}$)	Morph type	z_{phot}	z_{spec}	$\log_{10}(M_{\star}/M_{\odot})$	SFR M_{\odot}/yr	M_V [mag]	M_K [mag]	A_{F775W} $[10^{-2} \text{ mag}]$	$R - F775W$ [mag]
(1)	(2)	(3)	(4)	(5)	(6)	(7)	(8)	(9)	(10)	(11)	(12)	(13)
105	SHARDS20004440	189.0736	62.2290	E/S0	0.53	0.5337	10.649 ± 0.085	3.126	-20.89	-22.14	-2.521 ^{+0.108} _{-0.086}	-0.527
106	SHARDS20004586	189.1416	62.1314	OM	0.46	-	9.01 ± 0.27	-3.901	-17.23	-17.75	-2.43 ^{+0.13} _{-0.17}	-
107	SHARDS20004857	189.0668	62.1637	CPSTB	0.44	-	8.77 ± 0.20	-1.145	-16.01	-17.07	-2.456 ^{+0.108} _{-0.065}	-
108	SHARDS20005328	189.2706	62.1944	OM	0.30	-	7.95 ± 0.16	-0.345	-13.99	-14.26	-2.52 ^{+0.13} _{-0.15}	-
109	SHARDS20005718	189.1152	62.2396	DF	0.29	-	7.848 ± 0.098	-0.216	-14.77	-15.20	-2.54 ^{+0.11} _{-0.11}	-
110	SHARDS20006178	189.1600	62.1373	CPSTB	0.26	-	8.25 ± 0.21	-0.211	-14.55	-15.51	-2.43 ^{+0.13} _{-0.13}	-
111	SHARDS20006262	189.1689	62.1475	DF	0.23	-	8.04 ± 0.25	-0.161	-13.75	-14.76	-2.46 ^{+0.13} _{-0.15}	-
112	SHARDS20006283	189.2127	62.1492	CPSTB	0.35	-	8.774 ± 0.094	-0.537	-15.87	-16.50	-2.46 ^{+0.13} _{-0.13}	-
113	SHARDS20006429	189.0748	62.1624	CPSTB	0.27	-	7.99 ± 0.22	-0.138	-14.97	-16.49	-2.456 ^{+0.108} _{-0.096}	-
114	SHARDS20006437	189.0413	62.1627	CPSTB	0.43	-	8.40 ± 0.11	-1.042	-16.19	-16.94	-2.456 ^{+0.086} _{-0.086}	-
115	SHARDS20006480	188.9992	62.1661	CPSTB	0.24	-	8.36 ± 0.25	-0.172	-14.54	-15.55	-2.456 ^{+0.086} _{-0.086}	-
116	SHARDS20006824	188.9935	62.1913	CPSTB	0.27	-	7.63 ± 0.12	-0.171	-13.37	-14.59	-2.478 ^{+0.086} _{-0.043}	-
117	SHARDS20006985	189.1612	62.2029	CPSTB	0.24	-	7.86 ± 0.16	-0.164	-13.86	-14.67	-2.521 ^{+0.108} _{-0.096}	-
118	SHARDS20007009	189.1015	62.2041	DF	0.36	-	8.24 ± 0.14	-0.535	-15.20	-15.76	-2.500 ^{+0.129} _{-0.095}	-
119	SHARDS20007308	189.1162	62.2174	DF	0.37	-	8.13 ± 0.13	-0.408	-15.14	-16.25	-2.521 ^{+0.129} _{-0.086}	-
120	SHARDS20007309	189.2036	62.2174	GP	0.22	-	7.80 ± 0.19	-0.152	-13.90	-14.71	-2.564 ^{+0.086} _{-0.108}	-
121	SHARDS20007395	189.1077	62.2634	DF	0.47	-	9.57 ± 0.13	4.176	-17.45	-18.32	-2.56 ^{+0.13} _{-0.13}	-
122	SHARDS20007536	189.0747	62.2394	OM	0.56	-	9.10 ± 0.17	23.937	-17.28	-18.30	-2.521 ^{+0.129} _{-0.129}	-
123	SHARDS20007647	189.1417	62.1105	CPSTB	0.25	-	8.29 ± 0.14	-0.122	-14.25	-15.38	-2.39 ^{+0.108} _{-0.15}	-
124	SHARDS20008604	189.2621	62.2185	CPSTB	0.52	-	8.46 ± 0.11	-1.583	-15.94	-16.92	-2.564 ^{+0.086} _{-0.129}	-
125	SHARDS20008789	189.2519	62.2283	OM	0.35	-	8.01 ± 0.17	-0.539	-14.49	-14.62	-2.59 ^{+0.13} _{-0.13}	-
126	SHARDS20008811	189.2151	62.2298	CPSTB	0.22	-	8.22 ± 0.11	-0.145	-13.49	-14.82	-2.586 ^{+0.086} _{-0.108}	-
127	SHARDS20009039	189.1674	62.2450	CPSTB	0.30	-	8.52 ± 0.28	-0.258	-14.34	-15.57	-2.56 ^{+0.13} _{-0.11}	-
128	SHARDS20009057	189.1712	62.2444	GP	0.36	-	8.24 ± 0.17	-0.586	-15.34	-15.94	-2.56 ^{+0.13} _{-0.11}	-
129	SHARDS20009101	189.1076	62.2419	DF	0.46	-	8.90 ± 0.11	-1.254	-16.53	-17.63	-2.54 ^{+0.13} _{-0.11}	-
130	SHARDS20009404	189.1496	62.2593	CPSTB	0.59	-	9.06 ± 0.16	-2.542	-16.67	-17.96	-2.59 ^{+0.13} _{-0.13}	-
131	SHARDS20009676	189.0200	62.1704	CPSTB	0.54	-	9.23 ± 0.13	-2.136	-17.23	-18.61	-2.456 ^{+0.086} _{-0.065}	-
132	SHARDS20009942	189.1314	62.1832	DF	0.44	-	8.21 ± 0.23	-0.947	-15.29	-16.44	-2.50 ^{+0.13} _{-0.11}	-
133	SHARDS20010138	189.1646	62.2442	DF	0.29	-	7.84 ± 0.13	-0.313	-14.35	-14.96	-2.56 ^{+0.13} _{-0.11}	-
134	SHARDS20010154	189.0798	62.2310	CPSTB	0.56	-	9.315 ± 0.087	-3.841	-17.44	-18.82	-2.521 ^{+0.108} _{-0.086}	-
135	SHARDS20010466	189.0968	62.2099	CPSTB	0.46	-	8.04 ± 0.25	1.105	-15.84	-16.14	-2.500 ^{+0.129} _{-0.065}	-
136	SHARDS20010555	189.2050	62.2566	DF	0.26	-	8.11 ± 0.21	-0.164	-14.63	-15.24	-2.61 ^{+0.13} _{-0.13}	-
137	SHARDS20010777	189.2606	62.2381	CPSTB	0.22	-	7.84 ± 0.21	-0.083	-14.06	-14.69	-2.59 ^{+0.13} _{-0.11}	-
138	SHARDS20010793	189.2710	62.2300	DF	0.33	-	7.53 ± 0.24	-0.448	-13.92	-14.44	-2.59 ^{+0.13} _{-0.13}	-
139	SHARDS20010969	189.1317	62.1697	CPSTB	0.43	-	8.07 ± 0.24	-0.841	-15.15	-16.12	-2.48 ^{+0.15} _{-0.11}	-
140	SHARDS20011001	188.9709	62.1863	DF	0.50	-	8.87 ± 0.34	-0.995	-16.11	-16.74	-2.478 ^{+0.086} _{-0.065}	-
141	SHARDS20011033	188.9454	62.1989	CPSTB	0.27	-	8.30 ± 0.21	-0.287	-14.39	-15.40	-2.478 ^{+0.108} _{-0.043}	-
142	SHARDS20011279	189.1110	62.2383	CPSTB	0.51	-	8.93 ± 0.14	-1.873	-15.83	-17.07	-2.54 ^{+0.11} _{-0.11}	-
143	SHARDS20011817	189.0578	62.1248	SO	0.50	-	10.843 ± 0.054	-2.207	-20.62	-21.86	-2.41 ^{+0.11} _{-0.11}	-0.472
144	SHARDS20011862	189.0222	62.1519	OM	0.42	-	8.82 ± 0.22	2.370	-15.51	-16.83	-2.456 ^{+0.086} _{-0.065}	-
145	SHARDS20012018	189.2125	62.2069	DF	0.35	-	8.08 ± 0.11	-0.522	-14.23	-14.77	-2.54 ^{+0.13} _{-0.13}	-
146	SHARDS20012798	189.0583	62.2140	CPSTB	0.34	-	8.24 ± 0.20	-0.469	-14.54	-15.41	-2.500 ^{+0.129} _{-0.065}	-
147	SHARDS20013012	189.0228	62.2195	CPSTB	0.57	-	8.84 ± 0.17	-1.565	-15.72	-16.56	-2.500 ^{+0.108} _{-0.065}	-
148	SHARDS20013475	189.1848	62.2321	CPSTB	0.22	-	7.83 ± 0.15	-0.109	-13.24	-14.25	-2.56 ^{+0.11} _{-0.11}	-
149	SHARDS20013783	189.1933	62.2540	DF	0.24	-	8.01 ± 0.22	-0.166	-13.57	-14.67	-2.57 ^{+0.11} _{-0.11}	-
150	SHARDS20014088	189.1593	62.2771	OM	0.20	-	7.93 ± 0.21	-0.095	-13.01	-14.18	-2.61 ^{+0.13} _{-0.15}	-

Este documento incorpora firma electrónica, y es copia auténtica de un documento electrónico archivado por la ULL según la Ley 39/2015. Su autenticidad puede ser contrastada en la siguiente dirección https://sede.ull.es/validacion/										
Identificador del documento: 1630219										Código de verificación: NYPyuzSi
Firmado por: ALEJANDRO SERRANO BORLAFF UNIVERSIDAD DE LA LAGUNA										Fecha: 26/10/2018 14:33:01
Juan Esteban Beckman Abramson UNIVERSIDAD DE LA LAGUNA										26/10/2018 14:36:58
MARIA DEL CARMEN ELICHE MORAL UNIVERSIDAD DE LA LAGUNA										26/10/2018 15:46:09
JOAN FONT SERRA UNIVERSIDAD DE LA LAGUNA										26/10/2018 18:46:53

B

Appendix B

152

Este documento incorpora firma electrónica, y es copia auténtica de un documento electrónico archivado por la ULL según la Ley 39/2015.
Su autenticidad puede ser contrastada en la siguiente dirección <https://sede.ull.es/validacion/>

Identificador del documento: 1630219 Código de verificación: NYPyuzSi

Firmado por: ALEJANDRO SERRANO BORLAFF UNIVERSIDAD DE LA LAGUNA	Fecha: 26/10/2018 14:33:01
Juan Esteban Beckman Abramson UNIVERSIDAD DE LA LAGUNA	26/10/2018 14:36:58
MARIA DEL CARMEN ELICHE MORAL UNIVERSIDAD DE LA LAGUNA	26/10/2018 15:46:09
JOAN FONT SERRA UNIVERSIDAD DE LA LAGUNA	26/10/2018 18:46:53

Appendix B: Profile parameters of the sample of S0 and E/S0 galaxies at $0.2 < z < 0.6$

Table B.1. Profile classification and photometric parameters of S0 and E/S0 galaxies at $0.2 < z < 0.6$ in the GOODS-N field.

#	ID	Profile type	i	μ_{break}	R_{break}	μ_{01}	μ_{03}	h_i	h_o	p_h	p_{ho}	R_{23}	R_{lim}
(1)	(2)	(3)	(4)	(5)	(6)	(7)	(8)	(9)	(10)	(11)	(12)	(13)	(14)
1	SHARDS10000327	III	54	23.05 ^{+0.29} _{-0.68}	5.45 ^{+0.66} _{-0.98}	18.96 ^{+0.21} _{-0.17}	1.42 ^{+0.12} _{-0.12}	20.86 ^{+0.56} _{-0.42}	2.61 ^{+0.65} _{-0.26}	3.0 ^{+0.67} _{-0.26}	5.42 ^{+0.22} _{-0.18}	10.34	
2	SHARDS10000762	I	64	—	—	19.19 ^{+0.13} _{-0.13}	4.50 ^{+0.16} _{-0.16}	—	—	2.0 ^{+0.10} _{-0.10}	16.06 ^{+0.39} _{-0.45}	24.19	
3	† SHARDS10000827	III	55	22.44 ^{+1.31} _{-0.53}	8.08 ^{+4.44} _{-0.53}	18.63 ^{+0.18} _{-0.16}	2.59 ^{+0.21} _{-0.15}	20.23 ^{+1.23} _{-0.44}	3.92 ^{+1.98} _{-0.44}	2.4 ^{+0.10} _{-0.07}	10.18 ^{+1.42} _{-0.59}	15.20	
4	SHARDS10000840	III	48	21.96 ^{+0.33} _{-0.32}	6.10 ^{+0.77} _{-0.84}	18.18 ^{+0.21} _{-0.16}	1.73 ^{+0.15} _{-0.15}	19.67 ^{+0.44} _{-0.26}	2.83 ^{+0.13} _{-0.13}	2.3 ^{+0.07} _{-0.07}	8.72 ^{+0.25} _{-0.27}	13.72	
5	SHARDS10000845	II	84	19.71 ^{+0.29} _{-0.30}	8.86 ^{+0.75} _{-0.66}	16.68 ^{+0.21} _{-0.21}	3.15 ^{+0.38} _{-0.21}	15.41 ^{+0.23} _{-0.13}	2.23 ^{+0.11} _{-0.11}	3.4 ^{+0.10} _{-0.10}	15.89 ^{+0.62} _{-0.45}	18.17	
6	SHARDS10000849	III	69	23.23 ^{+0.18} _{-0.36}	8.36 ^{+0.69} _{-0.60}	18.36 ^{+0.18} _{-0.16}	1.97 ^{+0.12} _{-0.12}	21.09 ^{+0.84} _{-0.82}	4.4 ^{+2.2} _{-1.11}	3.1 ^{+0.04} _{-0.04}	8.45 ^{+0.21} _{-0.18}	12.10	
7	SHARDS10001013	I	45	—	—	17.35 ^{+0.075} _{-0.075}	1.132 ^{+0.018} _{-0.018}	—	—	2.4 ^{+0.10} _{-0.10}	5.87 ^{+0.15} _{-0.15}	7.48	
8	SHARDS10001269	I	67	—	—	17.75 ^{+0.14} _{-0.13}	2.75 ^{+0.087} _{-0.076}	—	—	1.8 ^{+0.10} _{-0.10}	1.8 ^{+0.10} _{-0.10}	13.12 ^{+0.27} _{-0.29}	18.54
9	SHARDS10001314	I	49	—	—	20.12 ^{+0.13} _{-0.13}	1.843 ^{+0.068} _{-0.068}	—	—	3.9 ^{+0.10} _{-0.10}	4.60 ^{+0.14} _{-0.14}	9.81	
10	SHARDS10001344	III	54	22.57 ^{+1.31} _{-0.50}	10.21 ^{+7.30} _{-0.43}	19.70 ^{+0.48} _{-0.43}	3.64 ^{+0.10} _{-0.10}	21.16 ^{+0.98} _{-0.32}	6.99 ^{+3.31} _{-0.43}	1.6 ^{+0.10} _{-0.10}	12.41 ^{+0.64} _{-0.81}	24.22	
11	SHARDS10001350	II	45	21.64 ^{+0.42} _{-0.26}	10.21 ^{+2.22} _{-0.87}	18.89 ^{+0.21} _{-0.16}	4.02 ^{+0.59} _{-0.22}	17.40 ^{+0.26} _{-0.26}	2.61 ^{+0.16} _{-0.16}	5.8 ^{+0.10} _{-0.10}	13.52 ^{+0.21} _{-0.19}	17.77	
12	SHARDS10001648	III	72	23.01 ^{+0.52} _{-0.53}	7.7 ^{+1.1} _{-1.1}	17.99 ^{+0.38} _{-0.38}	1.60 ^{+0.15} _{-0.15}	20.63 ^{+0.87} _{-0.87}	3.23 ^{+0.16} _{-0.34}	2.9 ^{+0.10} _{-0.10}	7.70 ^{+0.20} _{-0.20}	13.90	
13	SHARDS10001727	I	84	—	—	17.44 ^{+0.052} _{-0.052}	2.104 ^{+0.029} _{-0.027}	—	—	1.6 ^{+0.10} _{-0.10}	11.08 ^{+0.14} _{-0.14}	16.14	
14	SHARDS10001847	II	75	21.33 ^{+0.59} _{-0.37}	9.9 ^{+1.4} _{-1.0}	17.92 ^{+0.16} _{-0.16}	3.148 ^{+0.259} _{-0.24}	16.84 ^{+0.24} _{-0.69}	2.39 ^{+0.13} _{-0.69}	4.0 ^{+0.10} _{-0.10}	13.68 ^{+0.20} _{-0.25}	21.34	
15	SHARDS10002351	I	86	—	—	19.70 ^{+0.27} _{-0.27}	3.64 ^{+0.10} _{-0.10}	21.16 ^{+0.98} _{-0.32}	6.99 ^{+3.31} _{-0.43}	1.6 ^{+0.10} _{-0.10}	12.41 ^{+0.64} _{-0.81}	24.22	
16	SHARDS10002730	III	53	23.49 ^{+1.10} _{-0.85}	6.8 ^{+1.7} _{-1.2}	18.20 ^{+0.12} _{-0.12}	1.361 ^{+0.45} _{-0.24}	19.76 ^{+2.88} _{-0.64}	1.92 ^{+2.78} _{-0.23}	7.8 ^{+0.10} _{-0.10}	13.52 ^{+0.21} _{-0.19}	17.77	
17	SHARDS10002769	I	39	—	—	20.41 ^{+0.15} _{-0.15}	3.79 ^{+0.19} _{-0.19}	—	—	9.1 ^{+0.10} _{-0.10}	11.28 ^{+0.84} _{-0.77}	16.07	
18	SHARDS10002942	III	21	22.01 ^{+1.69} _{-0.34}	5.70 ^{+2.81} _{-0.57}	17.70 ^{+0.22} _{-0.22}	1.40 ^{+0.19} _{-0.19}	19.08 ^{+2.00} _{-0.96}	2.06 ^{+1.41} _{-0.31}	3.2 ^{+0.10} _{-0.10}	7.54 ^{+0.24} _{-0.24}	10.90	
19	SHARDS10003216	I	19	—	—	18.66 ^{+0.17} _{-0.17}	1.049 ^{+0.060} _{-0.060}	—	—	4.2 ^{+0.10} _{-0.10}	4.16 ^{+0.15} _{-0.15}	5.84	
20	SHARDS10003312	III	38	23.85 ^{+0.031} _{-0.039}	10.43 ^{+0.22} _{-0.22}	19.64 ^{+0.17} _{-0.17}	2.71 ^{+0.16} _{-0.15}	21.79 ^{+0.42} _{-0.30}	5.60 ^{+1.51} _{-0.68}	2.6 ^{+0.10} _{-0.10}	8.31 ^{+0.31} _{-0.32}	17.90	
21	SHARDS10003402	II	84	20.09 ^{+0.19} _{-0.29}	3.96 ^{+0.25} _{-0.41}	17.78 ^{+0.14} _{-0.11}	1.88 ^{+0.13} _{-0.10}	16.36 ^{+0.13} _{-0.19}	1.161 ^{+0.13} _{-0.19}	8.0 ^{+0.10} _{-0.10}	7.06 ^{+0.17} _{-0.19}	10.62	
22	SHARDS10003647	III	66	22.40 ^{+1.43} _{-0.36}	8.88 ^{+0.95} _{-0.95}	17.57 ^{+0.33} _{-0.24}	1.92 ^{+0.24} _{-0.24}	19.64 ^{+2.02} _{-0.13}	3.26 ^{+0.69} _{-0.24}	4.6 ^{+0.10} _{-0.10}	10.41 ^{+0.34} _{-0.35}	16.23	
23	SHARDS10004777	II	62	24.85 ^{+0.076} _{-0.066}	12.92 ^{+0.37} _{-1.18}	9.939 ^{+0.064} _{-0.058}	1.875 ^{+0.064} _{-0.058}	18.37 ^{+0.44} _{-1.18}	2.11 ^{+0.19} _{-0.18}	<1.0 ^{+0.10} _{-0.10}	8.22 ^{+0.14} _{-0.14}	16.29	

Notes. Columns: (1) Numerical ID in our final sample of S0 and E/S0 galaxies at $0.2 < z < 0.6$; (2) ID SHARDS (recess D2' best); (3) Profile type; (4) Galaxy inclination (degrees); (5) Surface brightness of the profile at the break radius (R_{break}) in mag arcsec $^{-2}$; (6) Break radius (R_{break}) in kpc; (7) Central surface brightness of the inner profile (μ_{01}) in mag arcsec $^{-2}$; (8) Scale-length of the outer profile (h_o) in kpc; (9) Central profile type; (10) Isophotal radius for 25 mag arcsec $^{-2}$ of the object in the corrected Steidel R band in kpc; (11) Elbow P -value for the likelihood that h_i and h_o are equal; (12) Elbow P -value for the likelihood that μ_{01} and μ_{03} are equal; (13) Isophotal radius for 25 mag arcsec $^{-2}$ of the object in the corrected Steidel R band in kpc; (14) Limiting radius of the profile in kpc. The objects flagged with an † symbol after their ID SHARDS correspond to those objects in the AGN subsample (see Sect. 2.8).

Este documento incorpora firma electrónica, y es copia auténtica de un documento electrónico archivado por la ULL según la Ley 39/2015. Su autenticidad puede ser contrastada en la siguiente dirección https://sede.ull.es/validacion/													
Identificador del documento: 1630219													
Código de verificación: NYPyuzSi													
Firmado por: ALEJANDRO SERRANO BORLAFF	UNIVERSIDAD DE LA LAGUNA												Fecha: 26/10/2018 14:33:01
Juan Esteban Beckman Abramson	UNIVERSIDAD DE LA LAGUNA												26/10/2018 14:36:58
MARIA DEL CARMEN ELICHE MORAL	UNIVERSIDAD DE LA LAGUNA												26/10/2018 15:46:09
JOAN FONT SERRA	UNIVERSIDAD DE LA LAGUNA												26/10/2018 18:46:53

A. Borlaff et al.: Anti-truncated stellar profiles on S0 galaxies at $0.2 < z < 0.6$

#	ID	Profile type	i	μ_{break}	R_{break}	μ_{hi}	h_i	μ_{lo}	h_o	p_h	p_{μ_0}	R_{33}	R_{lim}
(1)	(2)	(3)	(4)	(5)	(6)	(7)	(8)	(9)	(10)	(11)	(12)	(13)	(14)
24	SHARDIS0009610	III	53	22.54 ^{+0.31} _{-0.38}	10.27 ^{+1.21} _{-0.99}	17.80 ^{+0.23} _{-0.24}	2.32 ^{+0.17} _{-0.17}	20.03 ^{+0.47} _{-0.34}	4.31 ^{+0.66} _{-0.36}	1.2 × 10 ⁻⁴	12.11 ^{+0.29} _{-0.38}	20.51	
25	SHARDIS2000593	III	46	23.10 ^{+0.27} _{-0.21}	6.09 ^{+0.60} _{-0.60}	20.32 ^{+0.15} _{-0.15}	2.34 ^{+0.12} _{-0.17}	21.17 ^{+0.15} _{-0.11}	3.36 ^{+0.17} _{-0.12}	3.8 × 10 ⁻³	3.8 × 10 ⁻³	5.79 ^{+0.15} _{-0.16}	
26	SHARDIS2000827	III	84	22.79 ^{+0.31} _{-0.38}	10.90 ^{+0.35} _{-0.44}	17.83 ^{+0.14} _{-0.14}	2.01 ^{+0.29} _{-0.37}	20.17 ^{+2.29} _{-0.57}	4.34 ^{+0.24} _{-0.36}	1.5 × 10 ⁻⁵	11.67 ^{+0.39} _{-0.39}	17.66	
27	SHARDIS20001051	I	27	—	—	18.40 ^{+0.83} _{-0.84}	1.689 ^{+0.038} _{-0.036}	1.257 ^{+0.019} _{-0.017}	—	—	4.3 × 10 ⁻¹	4.3 × 10 ⁻¹	7.21 ^{+0.21} _{-0.22}
28	SHARDIS20001534	I	63	—	—	18.50 ^{+0.58} _{-0.56}	1.207 ^{+0.019} _{-0.017}	1.312 ^{+0.056} _{-0.055}	—	—	4.9 × 10 ⁻¹	4.9 × 10 ⁻¹	5.24 ^{+0.17} _{-0.17}
29	† SHARDIS2002147	I	24	—	—	18.63 ^{+0.15} _{-0.15}	1.205 ^{+0.014} _{-0.012}	2.256 ^{+0.080} _{-0.077}	—	—	8.8 × 10 ⁻²	8.8 × 10 ⁻²	5.25 ^{+0.30} _{-0.29}
30	SHARDIS2002235	I	31	—	—	19.05 ^{+0.12} _{-0.10}	1.196 ^{+0.012} _{-0.010}	—	—	2.9 × 10 ⁻²	2.9 × 10 ⁻²	8.06 ^{+0.24} _{-0.29}	11.70
31	SHARDIS2002550	I	38	—	—	19.22 ^{+0.16} _{-0.14}	4.74 ^{+0.21} _{-0.21}	—	—	4.9 × 10 ⁻²	4.9 × 10 ⁻²	16.34 ^{+0.47} _{-0.40}	24.49
32	SHARDIS2002889	I	17	—	—	20.07 ^{+0.18} _{-0.14}	1.292 ^{+0.077} _{-0.062}	—	—	1.8 × 10 ⁻¹	1.8 × 10 ⁻¹	3.42 ^{+0.18} _{-0.18}	
33	SHARDIS2002935	I	38	—	—	19.36 ^{+0.13} _{-0.12}	2.99 ^{+0.11} _{-0.10}	—	—	1.6 × 10 ⁻²	1.6 × 10 ⁻²	9.59 ^{+0.24} _{-0.24}	15.30
34	SHARDIS2002966	I	47	—	—	18.34 ^{+0.091} _{-0.096}	2.184 ^{+0.054} _{-0.048}	—	—	2.3 × 10 ⁻¹	2.3 × 10 ⁻¹	9.50 ^{+0.25} _{-0.25}	13.70
35	SHARDIS2002995	II	31	22.67 ^{+0.08} _{-0.14}	10.7 ^{+1.12} _{-1.00}	19.25 ^{+0.14} _{-0.11}	3.40 ^{+0.15} _{-0.15}	17.66 ^{+0.62} _{-1.00}	2.32 ^{+0.27} _{-0.33}	6.0 × 10 ⁻⁴	5.8 × 10 ⁻⁴	11.50 ^{+0.23} _{-0.23}	
36	SHARDIS2003134	II	78	20.40 ^{+1.14} _{-0.97}	5.47 ^{+0.99} _{-1.11}	16.38 ^{+0.84} _{-0.54}	1.53 ^{+0.73} _{-0.24}	12.7 ^{+1.2} _{-1.5}	0.78 ^{+0.12} _{-0.10}	2.0 × 10 ⁻²	7.6 × 10 ⁻⁴	7.54 ^{+0.18} _{-0.18}	
37	SHARDIS2003210	III	22	22.06 ^{+0.35} _{-0.39}	5.69 ^{+0.68} _{-1.04}	17.95 ^{+0.27} _{-0.26}	1.46 ^{+0.15} _{-0.15}	20.21 ^{+0.32} _{-0.28}	3.13 ^{+0.36} _{-0.26}	9.9 × 10 ⁻⁴	9.9 × 10 ⁻⁴	8.06 ^{+0.26} _{-0.26}	
38	SHARDIS2003217	I	28	—	—	17.78 ^{+0.60} _{-0.60}	1.359 ^{+0.038} _{-0.030}	—	—	2.8 × 10 ⁻¹	2.7 × 10 ⁻¹	6.57 ^{+0.19} _{-0.19}	
39	† SHARDIS2003377	I	68	—	—	18.70 ^{+0.18} _{-0.21}	1.313 ^{+0.060} _{-0.059}	—	—	2.1 × 10 ⁻³	2.2 × 10 ⁻²	4.95 ^{+0.16} _{-0.14}	
40	SHARDIS2003678	I	38	—	—	19.56 ^{+0.25} _{-0.25}	1.392 ^{+0.088} _{-0.088}	—	—	1.8 × 10 ⁻²	1.8 × 10 ⁻²	4.11 ^{+0.22} _{-0.22}	
41	SHARDIS2004359	I	40	—	—	19.97 ^{+0.22} _{-0.16}	3.56 ^{+0.19} _{-0.17}	—	—	1.1 × 10 ⁻²	1.1 × 10 ⁻²	9.82 ^{+0.25} _{-0.20}	
42	SHARDIS2004420	I	42	—	—	19.81 ^{+0.17} _{-0.15}	4.13 ^{+0.27} _{-0.19}	—	—	8.2 × 10 ⁻²	8.2 × 10 ⁻²	11.84 ^{+0.36} _{-0.34}	
43	† SHARDIS2004440	I	34	—	—	18.13 ^{+0.15} _{-0.15}	1.668 ^{+0.067} _{-0.066}	—	—	1.3 × 10 ⁻²	1.3 × 10 ⁻²	7.46 ^{+0.27} _{-0.24}	
44	SHARDIS20011817	I	82	—	—	16.283 ^{+0.077} _{-0.076}	1.097 ^{+0.022} _{-0.020}	—	—	2.6 × 10 ⁻¹	2.5 × 10 ⁻¹	6.83 ^{+0.35} _{-0.31}	

Table B.1. continued.

Este documento incorpora firma electrónica, y es copia auténtica de un documento electrónico archivado por la ULL según la Ley 39/2015. Su autenticidad puede ser contrastada en la siguiente dirección https://sede.ull.es/validacion/	
Identificador del documento: 1630219 Código de verificación: NYPyuzSi	
Firmado por: ALEJANDRO SERRANO BORLAFF UNIVERSIDAD DE LA LAGUNA	Fecha: 26/10/2018 14:33:01
Juan Esteban Beckman Abramson UNIVERSIDAD DE LA LAGUNA	26/10/2018 14:36:58
MARIA DEL CARMEN ELICHE MORAL UNIVERSIDAD DE LA LAGUNA	26/10/2018 15:46:09
JOAN FONT SERRA UNIVERSIDAD DE LA LAGUNA	26/10/2018 18:46:53

C

Appendix C

155

Este documento incorpora firma electrónica, y es copia auténtica de un documento electrónico archivado por la ULL según la Ley 39/2015.
Su autenticidad puede ser contrastada en la siguiente dirección <https://sede.ull.es/validacion/>

Identificador del documento: 1630219 Código de verificación: NYPyuzSi

Firmado por: ALEJANDRO SERRANO BORLAFF UNIVERSIDAD DE LA LAGUNA	Fecha: 26/10/2018 14:33:01
Juan Esteban Beckman Abramson UNIVERSIDAD DE LA LAGUNA	26/10/2018 14:36:58
MARIA DEL CARMEN ELICHE MORAL UNIVERSIDAD DE LA LAGUNA	26/10/2018 15:46:09
JOAN FONT SERRA UNIVERSIDAD DE LA LAGUNA	26/10/2018 18:46:53

A&A 604, A119 (2017)

Appendix C: Specific comments on images, surface brightness profiles and disc profile analysis for the S0 and E/S0 galaxies at $z < 0.6$

Here we detail some of the most important characteristics of the S0 and E/S0 objects within our sample (see Table B.1), accounting for their PSF-corrected photometric profiles. Only the first galaxy is provided in the printed edition.

SHARDS10000327: E/S0 galaxy with a Type-III profile, with no nearby galaxies, and medium inclination (see Table B.1). The object shows a clear Type-III break at 5.4 kpc from the centre. The PDDs for h and μ_0 show two clearly separated peaks corresponding to the two sections of the surface brightness profile.

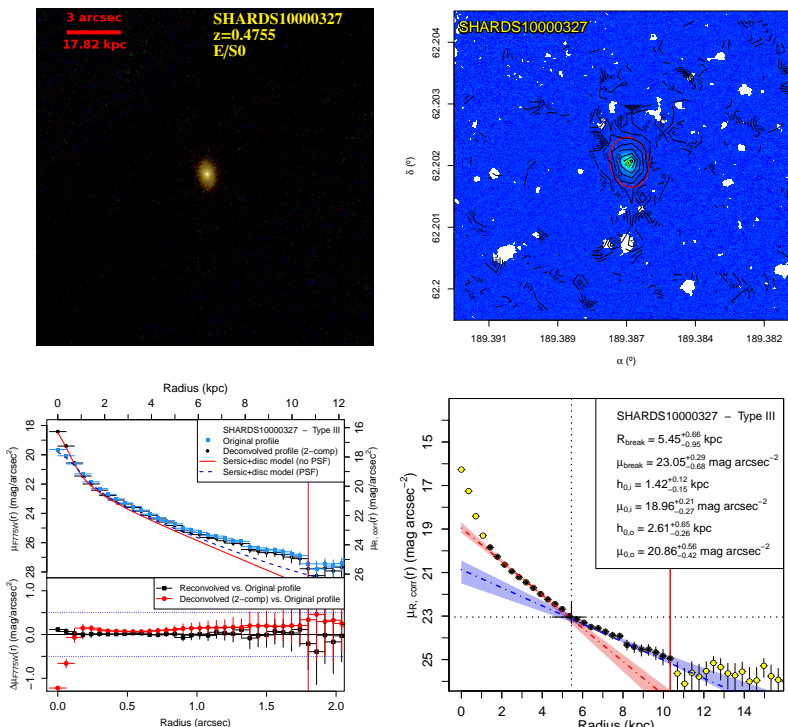


Fig. C.1. *Upper row, left panel:* masked false RGB image centred on the source (red: F775W, green: F606W, blue: F435W). The red segment represents 3 arcsec. *Upper row, right panel:* deconvolved F775W image. The black lines represent the isophotal contours of the image in magnitudes. The white regions represent the masked areas. The red ellipse indicates the limiting radius. *Lower row, left panel:* surface brightness profiles of the original image (blue) and the PSF-corrected image (black) for the observed F775W band (left axis) and for the rest-frame Steidel R band (right axis). The red solid and blue dashed lines correspond to the models fitted during the deconvolution and used for checking the visual morphological selection (see the legend). *The lower panel* represents the differences between the original and the PSF-corrected profiles (red circles) and the difference between the original profile and the reconvolved PSF-corrected image profile (black squares). The vertical red line represents the limiting radius. *Lower row, right panel:* surface brightness profile in the rest-frame Steidel R band corrected for dust extinction, cosmological dimming and K-correction. The dashed lines and the shaded areas correspond to the exponential fittings of the inner and outer profiles in red and blue colours, respectively. The vertical and horizontal black dotted lines correspond to the peak of the PDD for the break radius and the surface brightness value at that location (R_{break} and μ_{break}). The results of the break analysis are provided in the panel.

A119, page 28 of 71

Este documento incorpora firma electrónica, y es copia auténtica de un documento electrónico archivado por la ULL según la Ley 39/2015.
Su autenticidad puede ser contrastada en la siguiente dirección <https://sede.ul.es/validacion/>

Identificador del documento: 1630219

Código de verificación: NYPyuzSi

Firmado por: ALEJANDRO SERRANO BORLAFF
 UNIVERSIDAD DE LA LAGUNA

Fecha: 26/10/2018 14:33:01

Juan Esteban Beckman Abramson
 UNIVERSIDAD DE LA LAGUNA

26/10/2018 14:36:58

MARIA DEL CARMEN ELICHE MORAL
 UNIVERSIDAD DE LA LAGUNA

26/10/2018 15:46:09

JOAN FONT SERRA
 UNIVERSIDAD DE LA LAGUNA

26/10/2018 18:46:53

A. Borlaff et al.: Anti-truncated stellar profiles on S0 galaxies at $0.2 < z < 0.6$

SHARDS10000762: we classify this object as S0 galaxy with a Type-I profile. It presents a medium to high inclination (see Table B.1). There are not any nearby galaxies. The inner profile shows a slight bump in the inner region, possibly a lens component. We apply masking to a small source of $\mu_{F775W} \sim 23$ mag arcsec $^{-2}$ on the north direction along the semimajor axis. After masking the lens dominated part of the profile, the PDDs do not show any noticeable break.

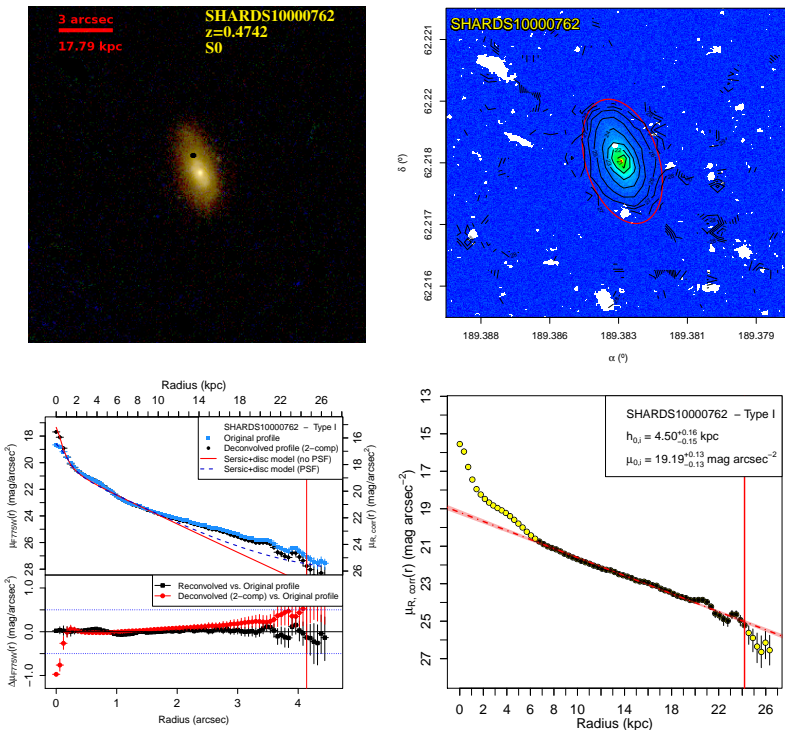


Fig. C.2. See caption of Fig. 1.

A119, page 29 of 71

Este documento incorpora firma electrónica, y es copia auténtica de un documento electrónico archivado por la ULL según la Ley 39/2015.
Su autenticidad puede ser contrastada en la siguiente dirección <https://sede.ull.es/validacion/>

Identificador del documento: 1630219

Código de verificación: NYPyuzSi

Firmado por: ALEJANDRO SERRANO BORLAFF
 UNIVERSIDAD DE LA LAGUNA

Fecha: 26/10/2018 14:33:01

Juan Esteban Beckman Abramson
 UNIVERSIDAD DE LA LAGUNA

26/10/2018 14:36:58

MARIA DEL CARMEN ELICHE MORAL
 UNIVERSIDAD DE LA LAGUNA

26/10/2018 15:46:09

JOAN FONT SERRA
 UNIVERSIDAD DE LA LAGUNA

26/10/2018 18:46:53

A&A 604, A119 (2017)

SHARDS10000827: S0 galaxy with Type-III profile. The object presents a medium inclination (see Table B.1). It was flagged as an AGN source (see Sect. 2.8). A high level of masking was needed due to a low surface brightness field object to the SW. To avoid any contamination, we calculated the surface brightness profile by using the opposite part of the galaxy and performing a manual aggressive masking to the whole FoV. The isophotal curves are centred around the main object, they do not present any large perturbations or deviations and show a position angle and ellipticity that is almost constant.

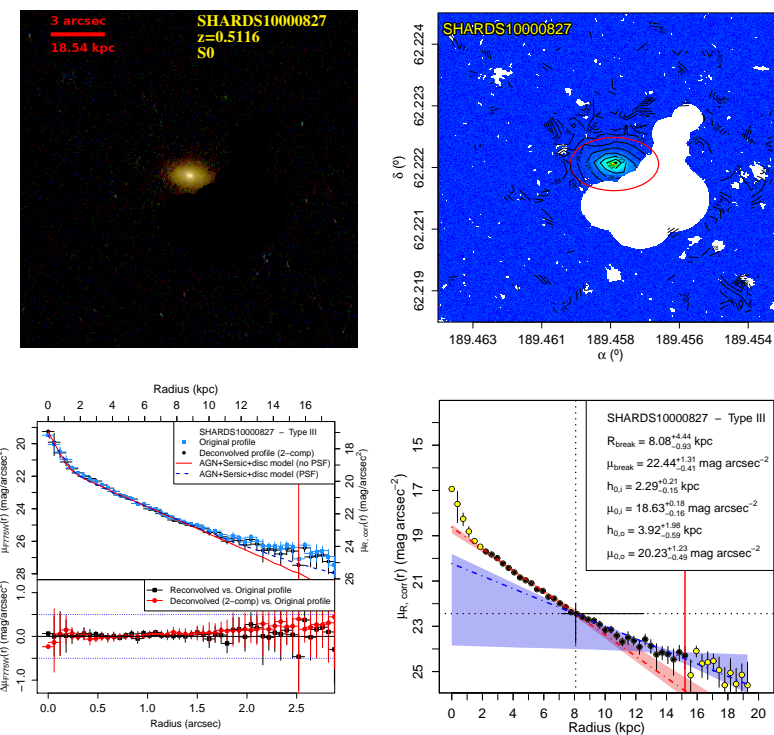


Fig. C.3. See caption of Fig. 1.

A. Borlaff et al.: Anti-truncated stellar profiles on S0 galaxies at $0.2 < z < 0.6$

SHARDS10000840: E/S0 galaxy with Type-III profile. The object presents a medium to low inclination (see Table B.1). The image needed an aggressive level of masking due to two nearby edge on field galaxies to the NE, including manual masking and revision of the whole FoV. We do not find any significant perturbations in the isophotes that could be due to the field objects. The PDDs for h and μ_0 show two clearly separated peaks corresponding to the two profiles.

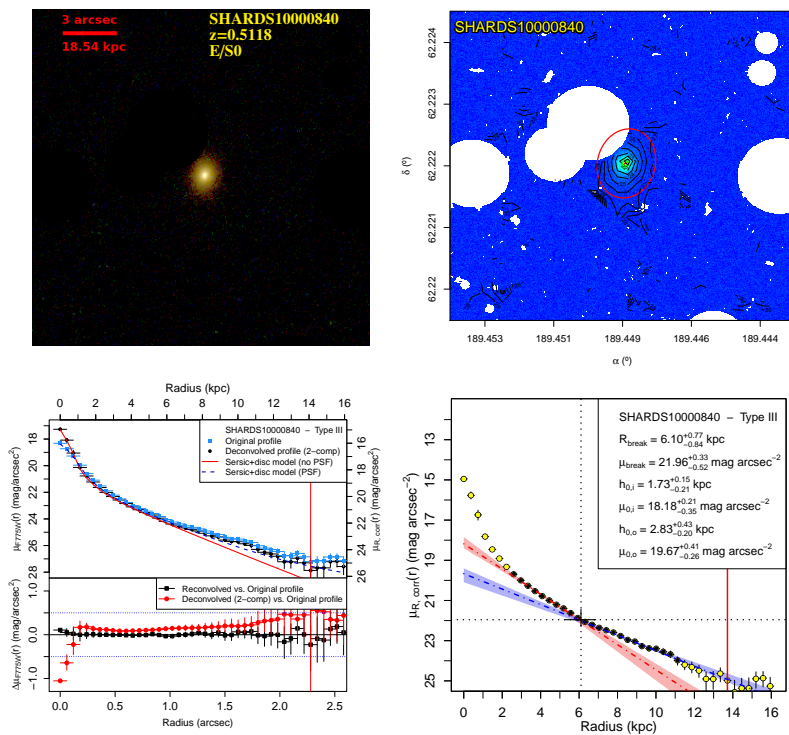


Fig. C.4. See caption of Fig. 1.

A&A 604, A119 (2017)

SHARDS10000845: S0 galaxy with Type-II profile. Its profile was generated by ISOFIT instead of ellipse due to its completely edge on orientation (see Table B.1). The object appears to be isolated, therefore manual masking was not needed. The profile shows a clear and compact bulge component. The PDDs for h and μ_0 show two clearly separated peaks corresponding to the two profiles. The corresponding PDDs for R_{break} and μ_{break} appear to be clearly Gaussian and narrow.

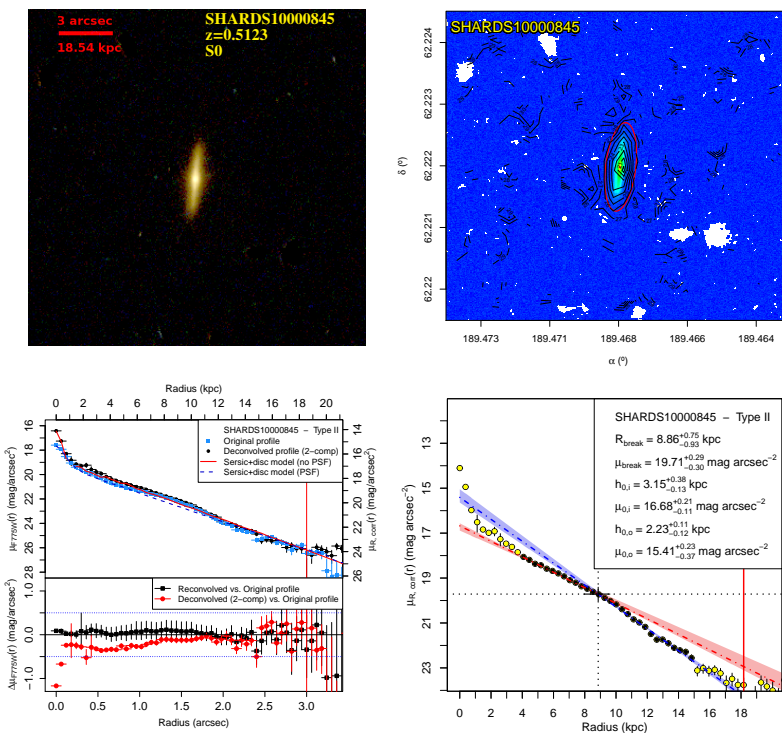


Fig. C.5. See caption of Fig. 1.

A. Borlaff et al.: Anti-truncated stellar profiles on S0 galaxies at $0.2 < z < 0.6$

SHARDS10000849: S0 galaxy with Type-III profile. The object presents medium to high inclination (see Table B.1). We have applied manual masking to two main sources in the FoV and a smaller one. Nevertheless, no source appears to be close enough to distort the profile and any contribution to the outer parts of our profile was discarded. The PDDs for h and μ_0 show two clearly separated distributions, although the outer profile is somewhat skewed due to deviations from a pure exponential profile.

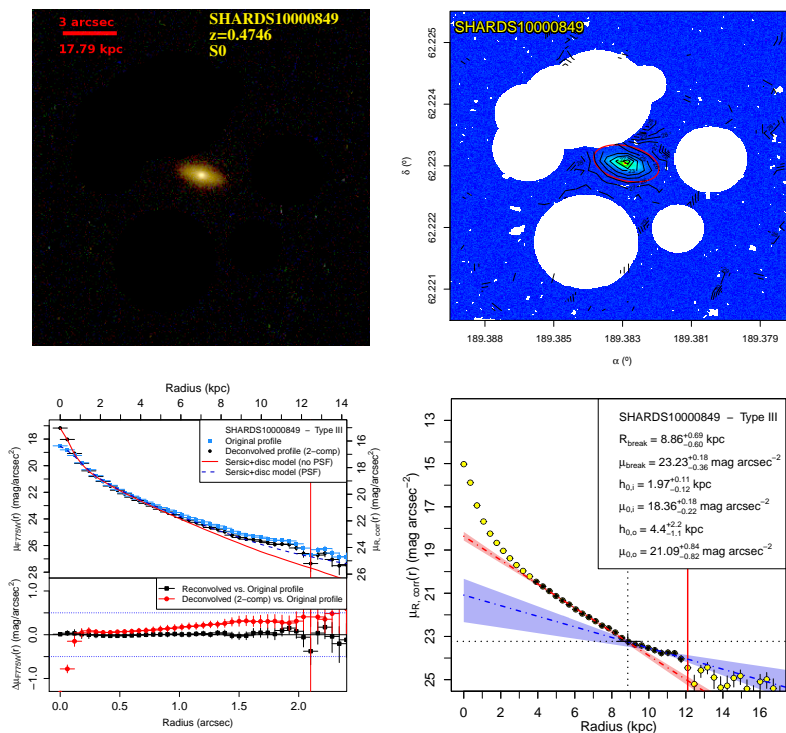


Fig. C.6. See caption of Fig. 1.

A&A 604, A119 (2017)

SHARDS10001013: small S0 galaxy with Type-I profile. The original surface brightness profile appears to be almost bulgeless. It presents medium inclination and small apparent size (~ 1.4 arcsec to $S/N = 3$). There are not any nearby galaxies or FoV objects. The resolution is not high enough to resolve any possible detail apart from the disc itself. Elbow does not reveal significant differences of any part on the disc.

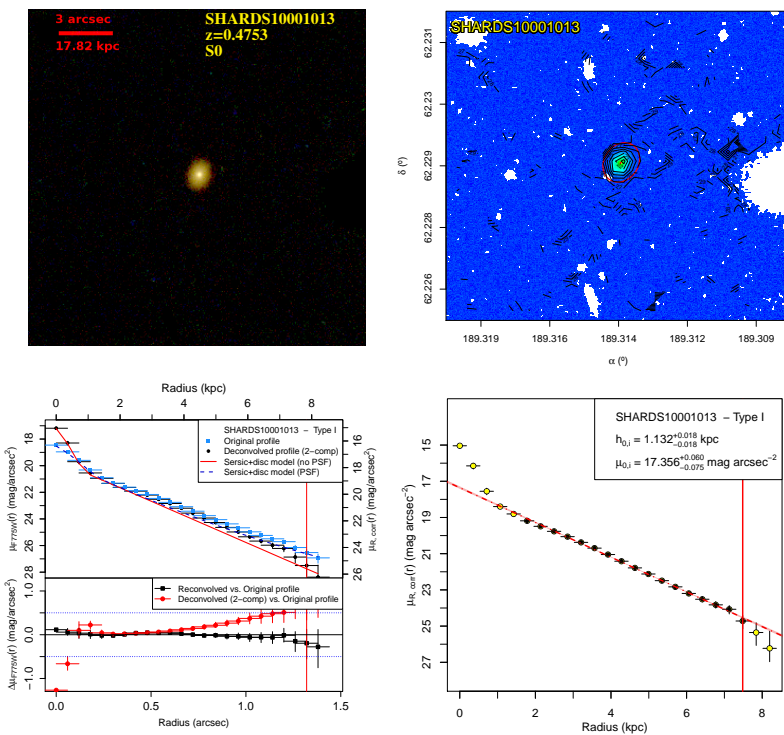


Fig. C.7. See caption of Fig. 1.

A119, page 34 of 71

Este documento incorpora firma electrónica, y es copia auténtica de un documento electrónico archivado por la ULL según la Ley 39/2015.
 Su autenticidad puede ser contrastada en la siguiente dirección <https://sede.ull.es/validacion/>

Identificador del documento: 1630219

Código de verificación: NYPyuzSi

Firmado por: ALEJANDRO SERRANO BORLAFF
 UNIVERSIDAD DE LA LAGUNA

Fecha: 26/10/2018 14:33:01

Juan Esteban Beckman Abramson
 UNIVERSIDAD DE LA LAGUNA

26/10/2018 14:36:58

MARIA DEL CARMEN ELICHE MORAL
 UNIVERSIDAD DE LA LAGUNA

26/10/2018 15:46:09

JOAN FONT SERRA
 UNIVERSIDAD DE LA LAGUNA

26/10/2018 18:46:53

A. Borlaff et al.: Anti-truncated stellar profiles on S0 galaxies at $0.2 < z < 0.6$

SHARDS10001269: S0 galaxy with Type-I profile. The object presents medium to high inclination (see Table B.1). Some close field objects to the NW along the major axis required extensive manual masking, although only few masked pixels finally were within inside the fitting region. An apparent excess of light dominates at the very outer parts of the galaxy, but it is not significant after PSF subtraction ($p \sim 0.018$). This is quite similar case to SHARDS10000845. The PDDs of h and μ_0 reveal a clear inner disc profile in contrast with the wider and skewed PDD of the outer profile.

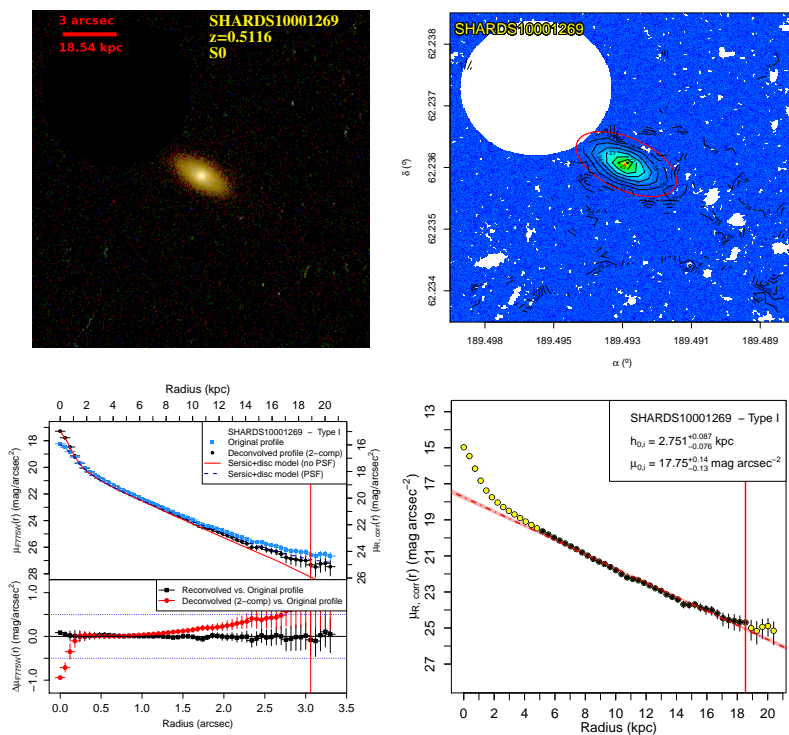


Fig. C.8. See caption of Fig. 1.

A&A 604, A119 (2017)

SHARDS10001314: S0 galaxy, apparently in interaction or at least overlapped with another source of similar size. The galaxy does not seem to be highly disturbed or asymmetric. High contamination from a close object required extensive masking of almost 30% of the galaxy, leaving the other 70% to analyse the surface brightness profile. The non-PSF corrected image shows an excess of light with almost constant surface brightness at 9–12 kpc from the centre, which results negligible after PSF subtraction. The exponential profile appears to be slightly bended, but the break parameters present high uncertainties. The probabilities of the both distributions (inner and outer profile for being equal) are slightly lower than 5% both in μ and h . We finally classified this object as Type I.

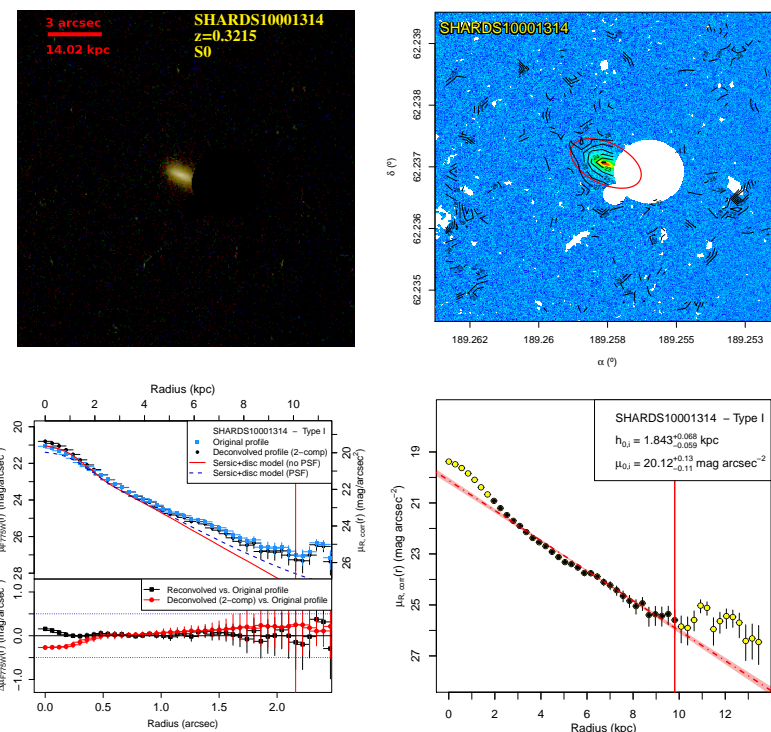


Fig. C.9. See caption of Fig. 1.

A119, page 36 of 71

Este documento incorpora firma electrónica, y es copia auténtica de un documento electrónico archivado por la ULL según la Ley 39/2015.
Su autenticidad puede ser contrastada en la siguiente dirección <https://sede.ull.es/validacion/>

Identificador del documento: 1630219

Código de verificación: NYPyuzSi

Firmado por: ALEJANDRO SERRANO BORLAFF
 UNIVERSIDAD DE LA LAGUNA

Fecha: 26/10/2018 14:33:01

Juan Esteban Beckman Abramson
 UNIVERSIDAD DE LA LAGUNA

26/10/2018 14:36:58

MARIA DEL CARMEN ELICHE MORAL
 UNIVERSIDAD DE LA LAGUNA

26/10/2018 15:46:09

JOAN FONT SERRA
 UNIVERSIDAD DE LA LAGUNA

26/10/2018 18:46:53

A. Borlaff et al.: Anti-truncated stellar profiles on S0 galaxies at $0.2 < z < 0.6$

SHARDS10001344: S0 Type-III galaxy with medium inclination (see Table B.1) and a very bright central component ($\mu_R = 16$ mag arcsec $^{-2}$) in contrast with the low surface brightness of the disc structure. We applied an extensive masking to a nearby region to the N-EE and a small close source to the N-NW. The PDDs for h and μ_0 show two separated peaks corresponding to the two profiles. The PDDs of the inner disc profile appear with two peaks and distorted due to the low statistics that result from the aggressive masking performed to the central bulge to avoid contamination.

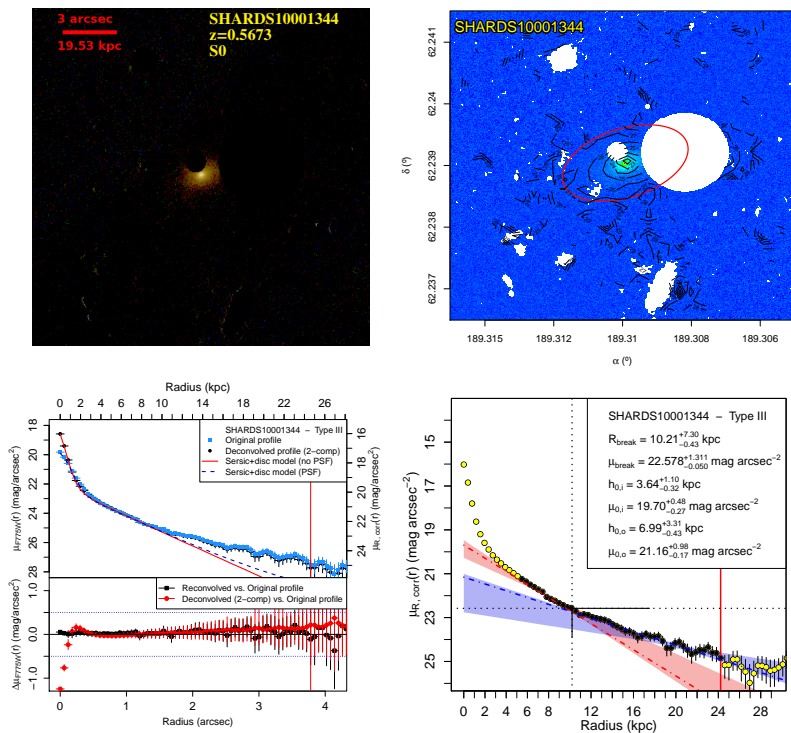


Fig. C.10. See caption of Fig. 1.

A&A 604, A119 (2017)

SHARDS10001350: S0 galaxy with a Type-II profile. The image shows a nearby galaxy to the main object, similar in size, that was carefully masked to prevent any flux contribution to the outer profile. Finally, the masked region was outside the limiting radius. We find no significant perturbations on the isophotes that could be due to the field objects, which are all beyond the fitting region. The PDDs for h and μ_0 show two clearly separated peaks corresponding to the two profiles.

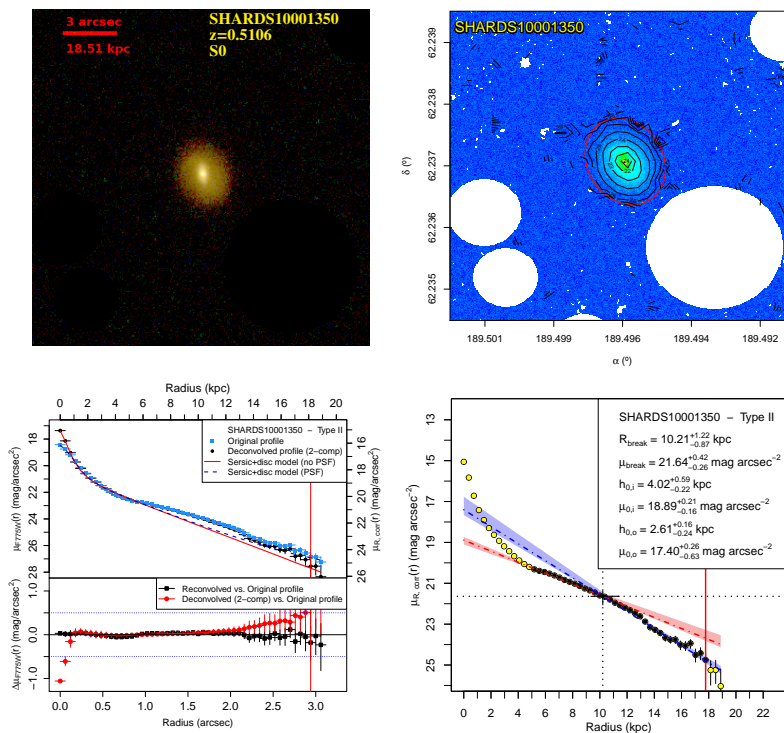


Fig. C.11. See caption of Fig. 1.

A. Borlaff et al.: Anti-truncated stellar profiles on S0 galaxies at $0.2 < z < 0.6$

SHARDS10001648: isolated Type-III S0 galaxy with medium inclination (see Table B.1). The PDDs of h and μ_0 reveal that the excess of light found at $R_{\text{break}} = 8-14$ kpc is significant and compatible with an outer exponential profile, different from the inner disc profile.

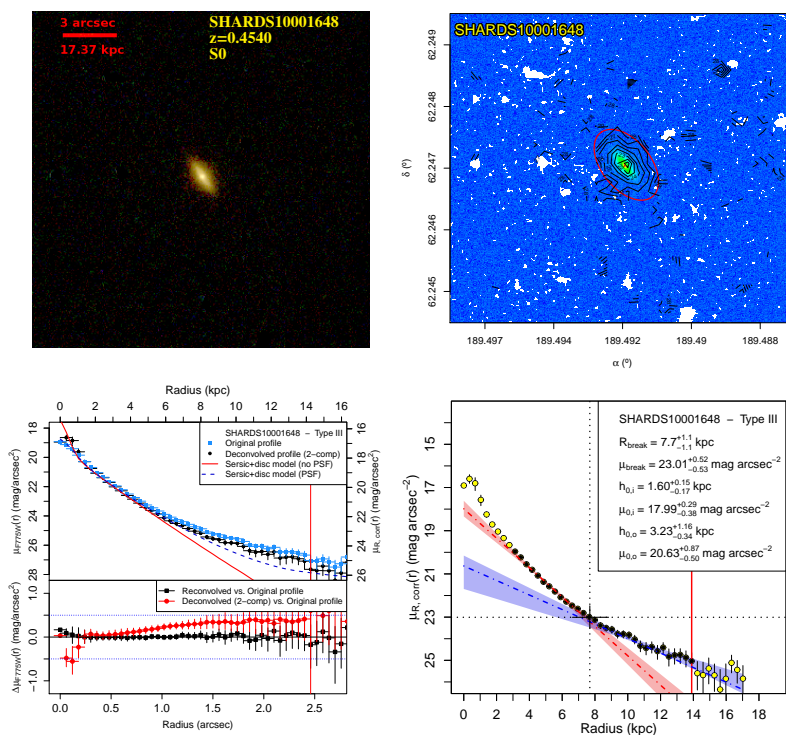


Fig. C.12. See caption of Fig. 1.

A&A 604, A119 (2017)

SHARDS10001727: S0 galaxy with Type-I profile. It was analysed by ISOFIT instead of ellipse due to its completely edge-on orientation (see Table B.1). The PDDs of h and μ_0 show no significant break, and the general profile can be successfully modelled as a single exponential function.

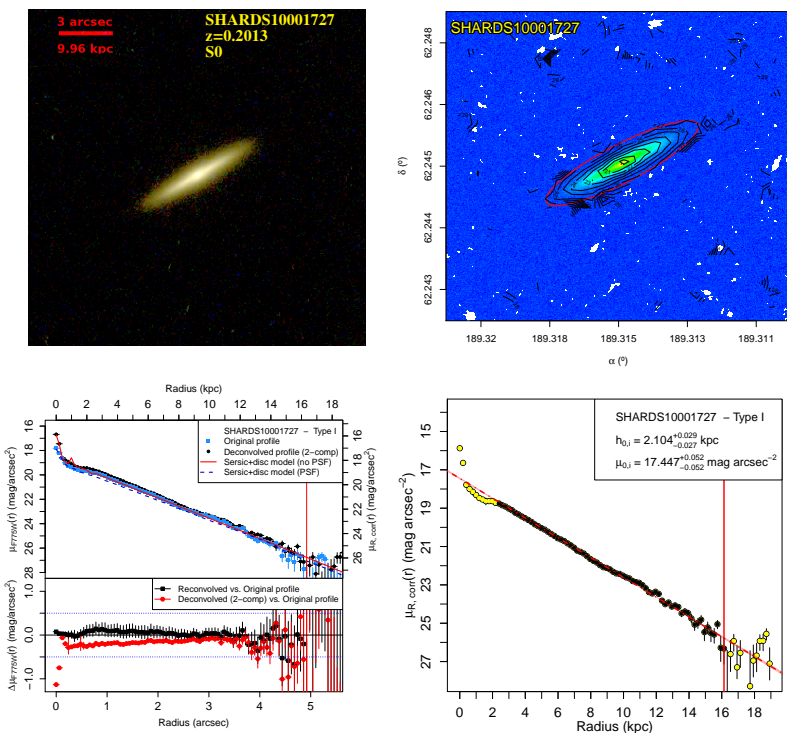


Fig. C.13. See caption of Fig. 1.

A119, page 40 of 71

Este documento incorpora firma electrónica, y es copia auténtica de un documento electrónico archivado por la ULL según la Ley 39/2015.
Su autenticidad puede ser contrastada en la siguiente dirección <https://sede.ull.es/validacion/>

Identificador del documento: 1630219

Código de verificación: NYPyuzSi

Firmado por: ALEJANDRO SERRANO BORLAFF
 UNIVERSIDAD DE LA LAGUNA

Fecha: 26/10/2018 14:33:01

Juan Esteban Beckman Abramson
 UNIVERSIDAD DE LA LAGUNA

26/10/2018 14:36:58

MARIA DEL CARMEN ELICHE MORAL
 UNIVERSIDAD DE LA LAGUNA

26/10/2018 15:46:09

JOAN FONT SERRA
 UNIVERSIDAD DE LA LAGUNA

26/10/2018 18:46:53

A. Borlaff et al.: Anti-truncated stellar profiles on S0 galaxies at $0.2 < z < 0.6$

SHARDS10001847: S0 galaxy with Type II profile (see Table B.1). The galaxy appears at a medium to high inclination. The limits for the profiles were chosen by hand, based several fittings performed varying the initial configurations, with the aim to reduce multiple peaks that appeared on the PDDs of h and μ_0 . The profile show a Type-II break which is statistically significant. The outskirts present an apparent excess of light, but it is not statistically significant after PSF subtraction.

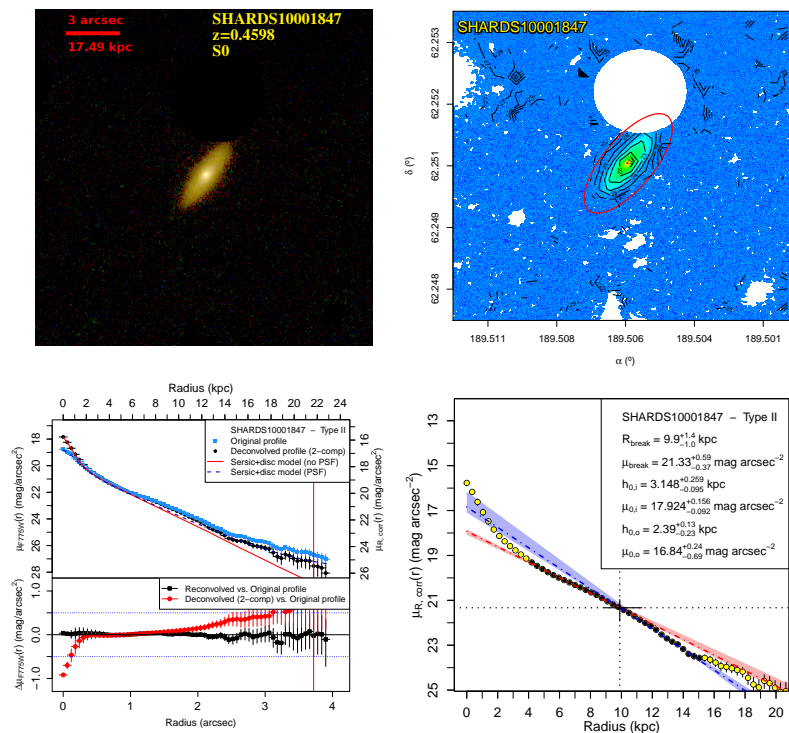


Fig. C.14. See caption of Fig. 1.

A&A 604, A119 (2017)

SHARDS10002351: small S0 galaxy with pure exponential profile (Type I). It was analysed by ISOFIT instead of ellipse due to its edge-on orientation. The object is almost isolated. The PDDs of h and μ_0 show no statistically significant differences between any parts of the disc.

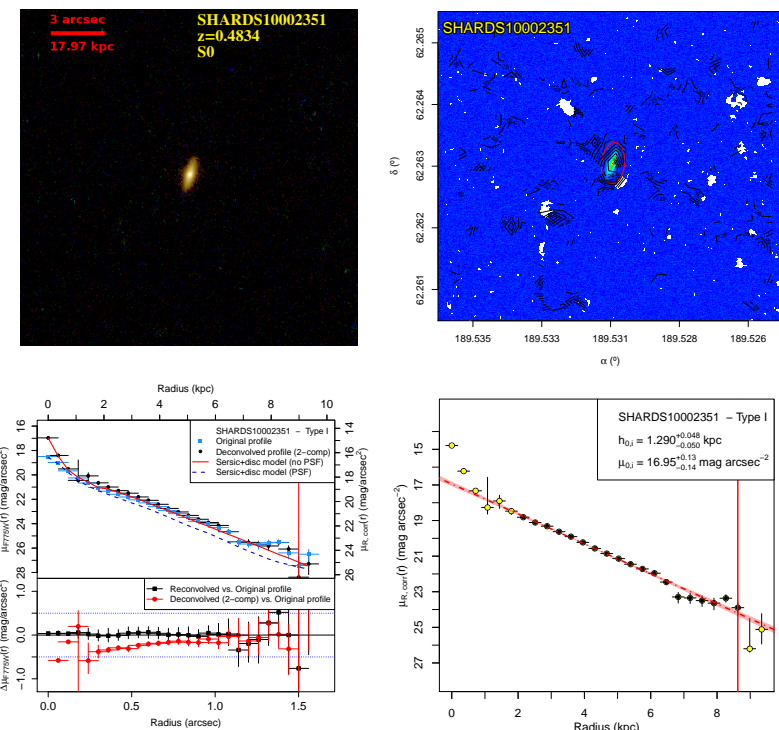


Fig. C.15. See caption of Fig. 1.

A119, page 42 of 71

Este documento incorpora firma electrónica, y es copia auténtica de un documento electrónico archivado por la ULL según la Ley 39/2015.
Su autenticidad puede ser contrastada en la siguiente dirección <https://sede.ull.es/validacion/>

Identificador del documento: 1630219

Código de verificación: NYPyuzSi

Firmado por: ALEJANDRO SERRANO BORLAFF
 UNIVERSIDAD DE LA LAGUNA

Fecha: 26/10/2018 14:33:01

Juan Esteban Beckman Abramson
 UNIVERSIDAD DE LA LAGUNA

26/10/2018 14:36:58

MARIA DEL CARMEN ELICHE MORAL
 UNIVERSIDAD DE LA LAGUNA

26/10/2018 15:46:09

JOAN FONT SERRA
 UNIVERSIDAD DE LA LAGUNA

26/10/2018 18:46:53

A. Borlaff et al.: Anti-truncated stellar profiles on S0 galaxies at $0.2 < z < 0.6$

SHARDS10002730: small S0 galaxy with Type-III profile. It has a medium inclination (see Table B.1). It required extensive masking, but no masked pixel finally was inside the fitting region. The automated break analysis reveals that the excess of light shown at the outermost part of the galaxy is statistically significant as a Type-III break despite the PSF subtraction, although the probability of being a Type I is ~ 0.008 .

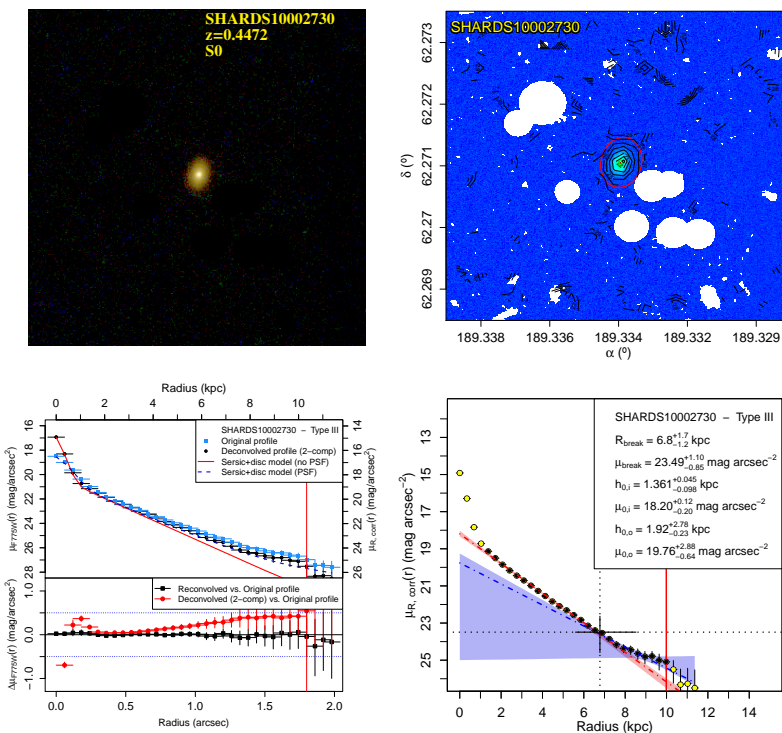


Fig. C.16. See caption of Fig. 1.

A&A 604, A119 (2017)

SHARDS10002769: E/S0 galaxy with Type-I profile and a low to medium inclination (see Table B.1). Manual and extensive masking was required due to multiple close field objects. The profile shows a very bright bulge and a wavy exponential profile. The PDDs of h and μ_0 reveal multiple Gaussian peaked distributions, due to the irregularities along the radius. None of them is compatible with a double exponential profile.

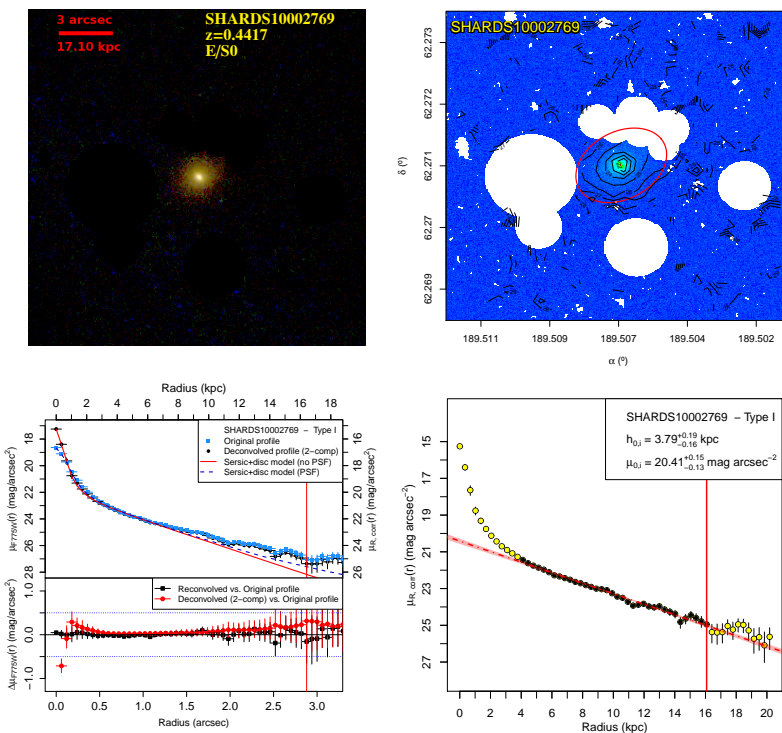


Fig. C.17. See caption of Fig. 1.

A119, page 44 of 71

Este documento incorpora firma electrónica, y es copia auténtica de un documento electrónico archivado por la ULL según la Ley 39/2015.
Su autenticidad puede ser contrastada en la siguiente dirección <https://sede.ull.es/validacion/>

Identificador del documento: 1630219

Código de verificación: NYPyuzSi

Firmado por: ALEJANDRO SERRANO BORLAFF
 UNIVERSIDAD DE LA LAGUNA

Fecha: 26/10/2018 14:33:01

Juan Esteban Beckman Abramson
 UNIVERSIDAD DE LA LAGUNA

26/10/2018 14:36:58

MARIA DEL CARMEN ELICHE MORAL
 UNIVERSIDAD DE LA LAGUNA

26/10/2018 15:46:09

JOAN FONT SERRA
 UNIVERSIDAD DE LA LAGUNA

26/10/2018 18:46:53

A. Borlaff et al.: Anti-truncated stellar profiles on S0 galaxies at $0.2 < z < 0.6$

SHARDS10002942: Type-III S0 galaxy with face on orientation (see Table B.1). Multiple and extensive masking was required due to the presence of nearby objects. The profile shows a bulge and Type-III disc composition, as the small excess of light at the outermost part of the galaxy is proved to be statistically significant by the automatic break analysis after the PSF subtraction.

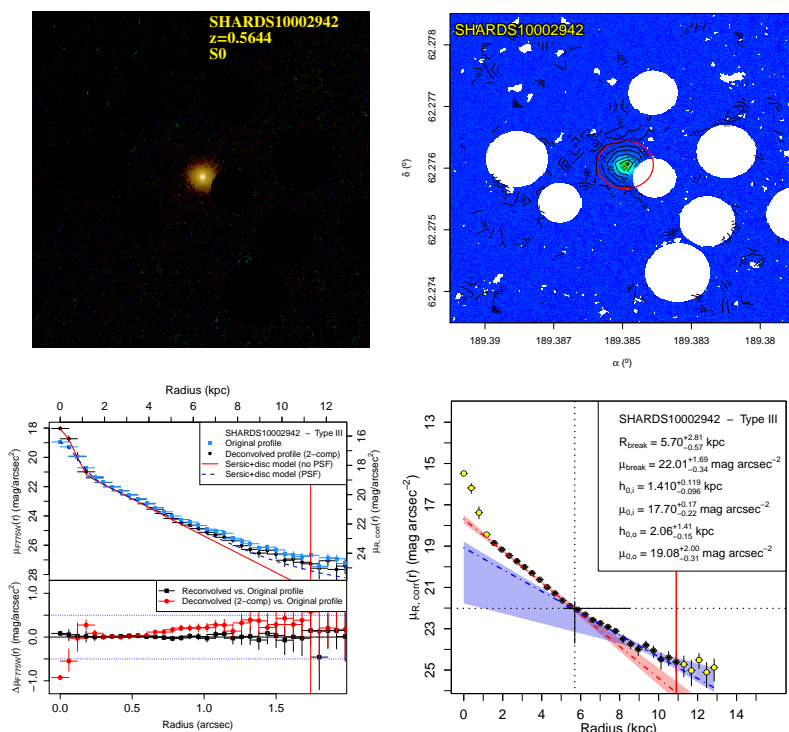


Fig. C.18. See caption of Fig. 1.

A&A 604, A119 (2017)

SHARDS10003216: E/S0 galaxy with very small size. The profile appears to be almost featureless, with no visible bulge or break, so it was classified as a Type I.

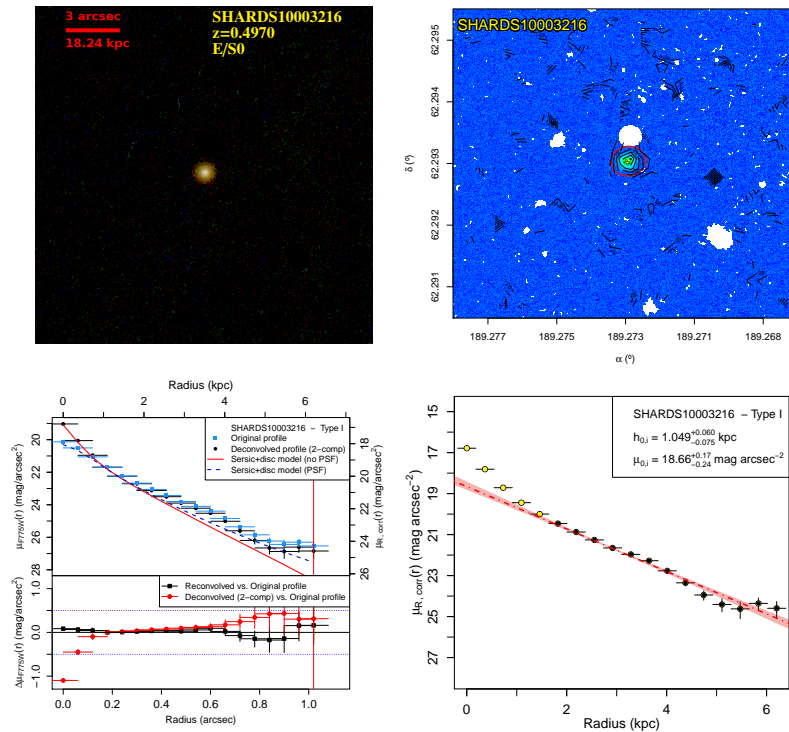


Fig. C.19. See caption of Fig. 1.

A. Borlaff et al.: Anti-truncated stellar profiles on S0 galaxies at $0.2 < z < 0.6$

SHARDS10003312: E/S0 galaxy with Type-III profile. It has a medium inclination (see Table B.1) and it is almost isolated, so no manual masking was needed. The automated break analysis successfully detected two exponential profiles, with narrow and separated PDDs, although the distributions associated with the outer profile presented higher dispersions due to the irregularities found in the profile.

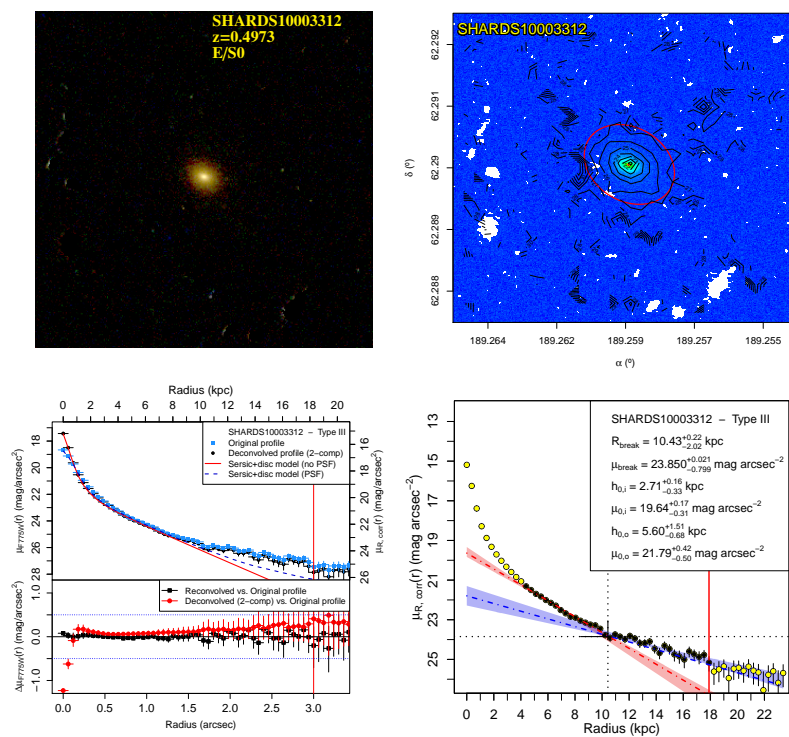


Fig. C.20. See caption of Fig. 1.

A119, page 47 of 71

<p>Este documento incorpora firma electrónica, y es copia auténtica de un documento electrónico archivado por la ULL según la Ley 39/2015. <i>Su autenticidad puede ser contrastada en la siguiente dirección https://sede.ull.es/validacion/</i></p>	
Identificador del documento: 1630219	Código de verificación: NYPyuzSi
Firmado por: ALEJANDRO SERRANO BORLAFF UNIVERSIDAD DE LA LAGUNA	Fecha: 26/10/2018 14:33:01
Juan Esteban Beckman Abramson UNIVERSIDAD DE LA LAGUNA	26/10/2018 14:36:58
MARIA DEL CARMEN ELICHE MORAL UNIVERSIDAD DE LA LAGUNA	26/10/2018 15:46:09
JOAN FONT SERRA UNIVERSIDAD DE LA LAGUNA	26/10/2018 18:46:53

A&A 604, A119 (2017)

SHARDS10003402: S0 galaxy with a Type-II profile. Manual masking was required due to the presence of multiple field objects, none of them inside the fitting region. It was analysed by ISOFIT instead of ellipse due to its completely edge-on orientation (see Table B.1). The outer region ($R > 9$ kpc) was removed from the profile analysis due to the presence of several irregularities. The PDDs show two close, but clearly separated distributions for h and μ_0 , thus the disc is well represented by a Type-II profile.

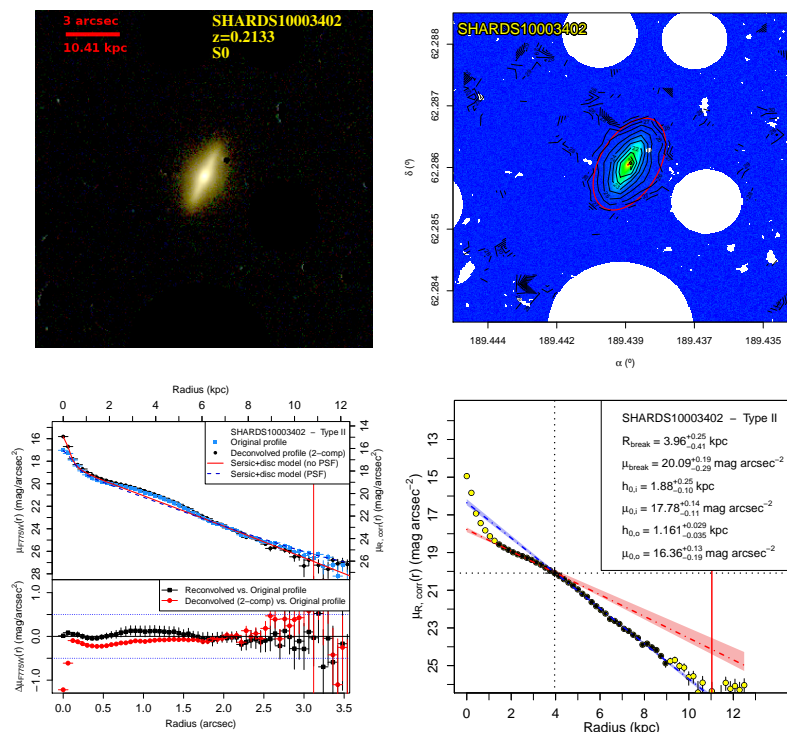


Fig. C.21. See caption of Fig. 1.

A. Borlaff et al.: Anti-truncated stellar profiles on S0 galaxies at $0.2 < z < 0.6$

SHARDS10003647: S0 galaxy with a Type-III profile. It shows a medium inclination (see Table B.1). Manual masking was required to avoid contamination from small field objects. The outermost region of the disc profile seems to be wavy, distorting the PDDs. The PDD of h and μ_0 appear to be clearly separated for the inner and outer profiles, although the outer profile is clearly skewed and wider than the inner one. The object present a significant Type-III profile despite the wide distribution of the outer profile.

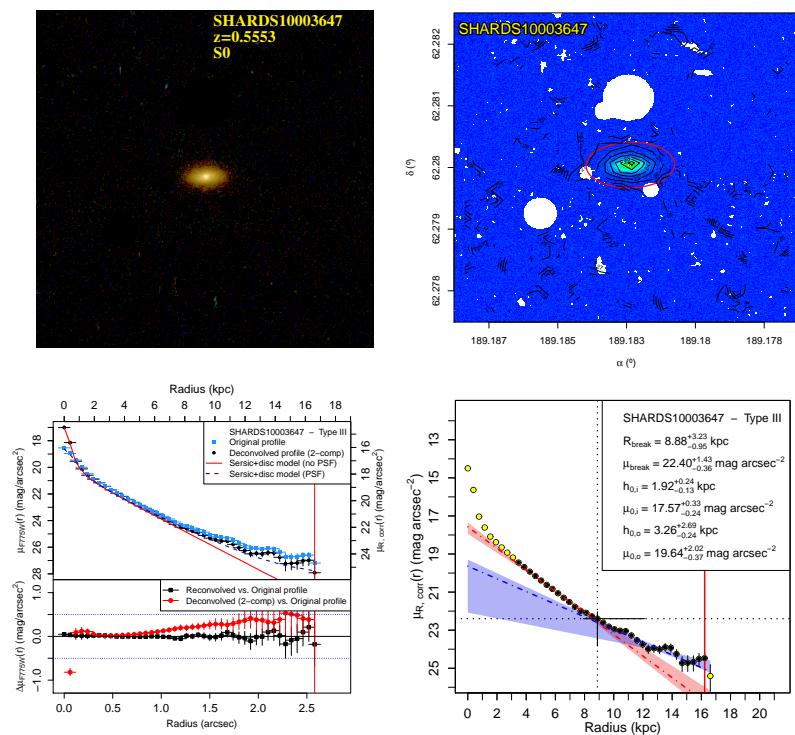


Fig. C.22. See caption of Fig. 1.

A119, page 49 of 71

Este documento incorpora firma electrónica, y es copia auténtica de un documento electrónico archivado por la ULL según la Ley 39/2015.
 Su autenticidad puede ser contrastada en la siguiente dirección <https://sede.ull.es/validacion/>

Identificador del documento: 1630219

Código de verificación: NYPyuzSi

Firmado por: ALEJANDRO SERRANO BORLAFF
 UNIVERSIDAD DE LA LAGUNA

Fecha: 26/10/2018 14:33:01

Juan Esteban Beckman Abramson
 UNIVERSIDAD DE LA LAGUNA

26/10/2018 14:36:58

MARIA DEL CARMEN ELICHE MORAL
 UNIVERSIDAD DE LA LAGUNA

26/10/2018 15:46:09

JOAN FONT SERRA
 UNIVERSIDAD DE LA LAGUNA

26/10/2018 18:46:53

A&A 604, A119 (2017)

SHARDS10004777: S0 galaxy with a Type-II profile. The galaxy presents a medium inclination (see Table B.1). Manual masking was applied to small sources at the outermost region (SE). We avoided the inner bump in the fit, because it probably traces a lens component, rather than a disc. The PDDs for h and μ_0 show clearly separated peaks corresponding to the outermost Type-II break.

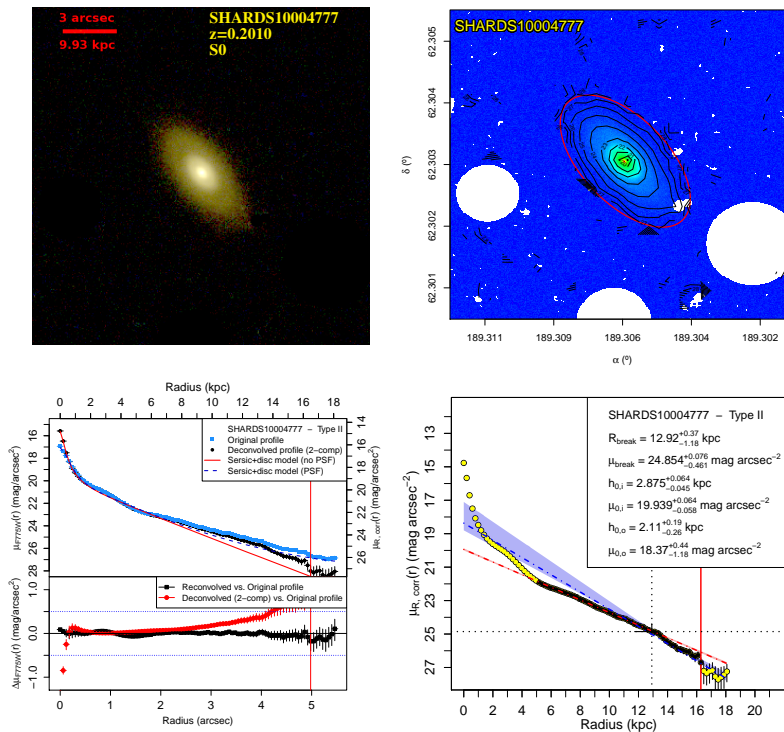


Fig. C.23. See caption of Fig. 1.

A. Borlaff et al.: Anti-truncated stellar profiles on S0 galaxies at $0.2 < z < 0.6$

SHARDS10009610: S0 galaxy with a Type-III profile. Manual masking was applied to multiple sources, but none of them finally laid within in the final fitting region. The PDDs for h and μ_0 show two clearly separated peaks corresponding to the inner and outer profiles. The outer profile PDD seems to be slightly wider than the inner one due to small distortions at high radius (see Table B.1).

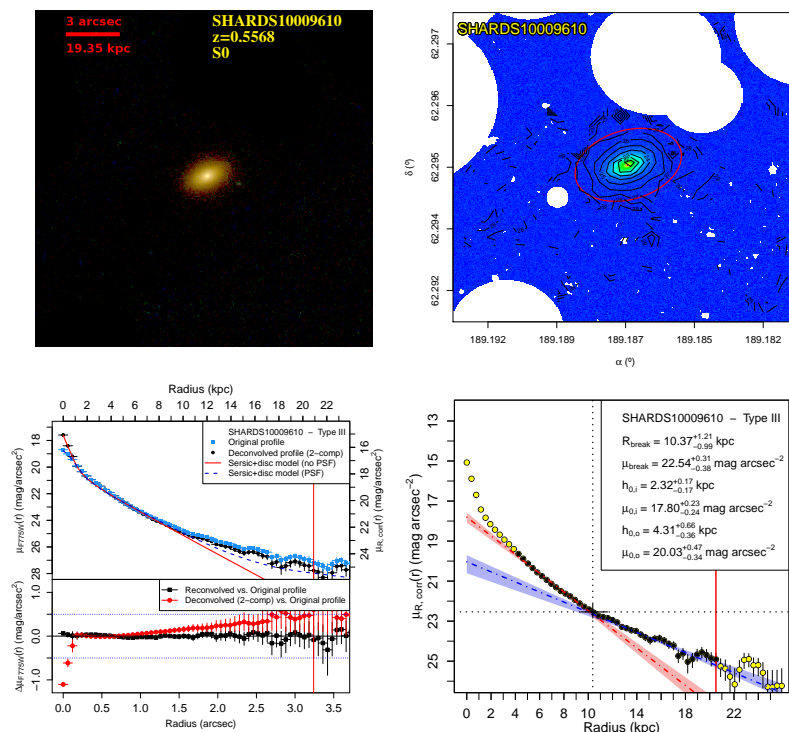


Fig. C.24. See caption of Fig. 1.

A&A 604, A119 (2017)

SHARDS20000593: Type-III S0 galaxy. The central bulge is very bright, and the ellipticity is low, but there is a prominent exponential component in the surface brightness profile that led us to classify it as S0, instead of elliptical. Extensive masking in the low emission regions. The disc profile presents a significant excess of emission beyond $R \sim 6$ kpc with respect to the inner exponential section of the disc that cannot be explained by PSF contribution. The PDDs for h and μ_0 show two clearly separated peaks corresponding to the two profiles.

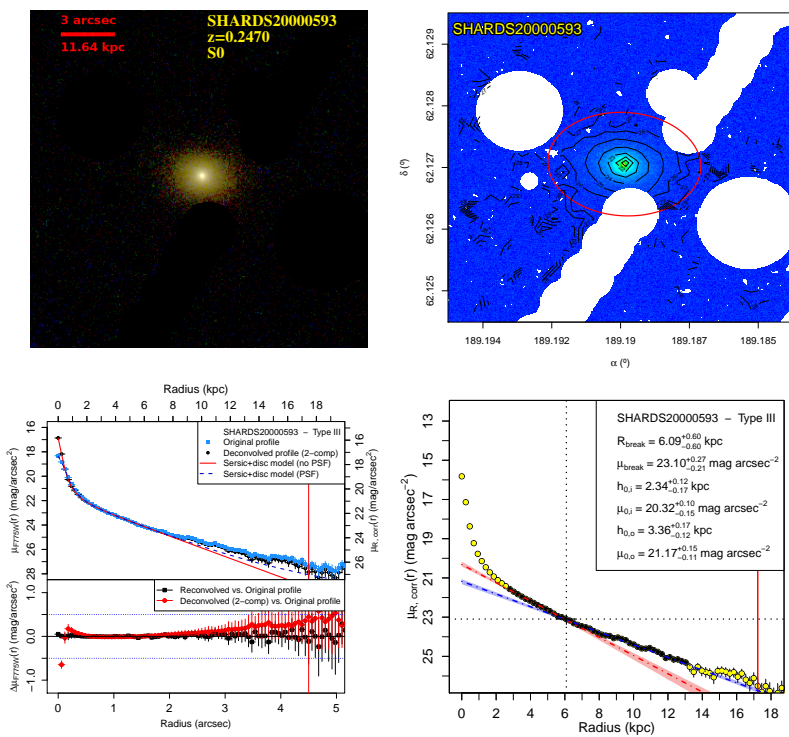


Fig. C.25. See caption of Fig. 1.

A. Borlaff et al.: Anti-truncated stellar profiles on S0 galaxies at $0.2 < z < 0.6$

SHARDS20000827: Type-III S0 galaxy. It is highly inclined (see Table B.1) so it was analysed with ISOFIT instead of Ellipse. The profile presents a significative excess of emission since $R \sim 10$ kpc that cannot be explained by PSF contribution. The PDDs for h and μ_0 show two clearly separated peaks corresponding to the two profiles, although they present large uncertainties for the outer profile fit.

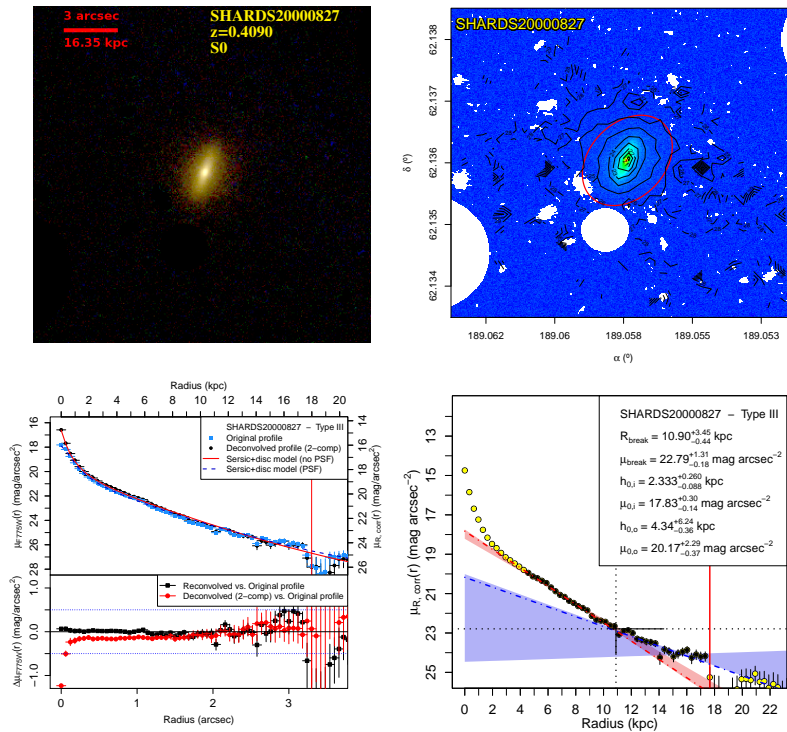


Fig. C.26. See caption of Fig. 1.

A&A 604, A119 (2017)

SHARDS20001051: small S0 galaxy with a Type-I profile. The object appears to be completely face on (see Table B.1), but inspection of the surface brightness profile reveals a typical bulge + exponential disc distribution. The disc appears to be featureless, and Elbow reveals no significant breaks within the observed disc region.

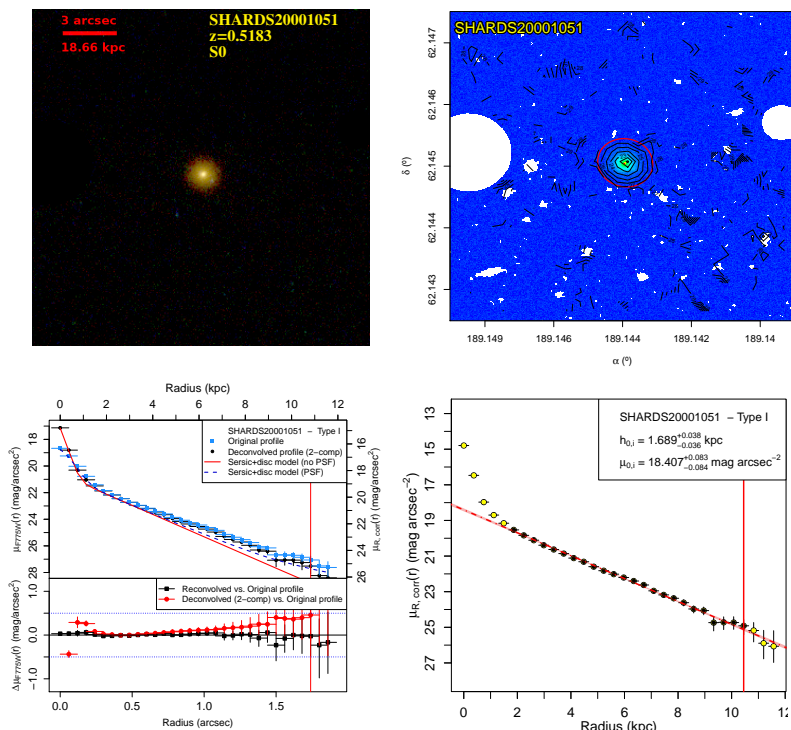


Fig. C.27. See caption of Fig. 1.

A119, page 54 of 71

Este documento incorpora firma electrónica, y es copia auténtica de un documento electrónico archivado por la ULL según la Ley 39/2015.
Su autenticidad puede ser contrastada en la siguiente dirección <https://sede.ull.es/validacion/>

Identificador del documento: 1630219

Código de verificación: NYPyuzSi

Firmado por: ALEJANDRO SERRANO BORLAFF
 UNIVERSIDAD DE LA LAGUNA

Fecha: 26/10/2018 14:33:01

Juan Esteban Beckman Abramson
 UNIVERSIDAD DE LA LAGUNA

26/10/2018 14:36:58

MARIA DEL CARMEN ELICHE MORAL
 UNIVERSIDAD DE LA LAGUNA

26/10/2018 15:46:09

JOAN FONT SERRA
 UNIVERSIDAD DE LA LAGUNA

26/10/2018 18:46:53

A. Borlaff et al.: Anti-truncated stellar profiles on S0 galaxies at $0.2 < z < 0.6$

SHARDS20001534: small S0 galaxy with a Type-I profile. It has a very similar profile to SHARDS20001051, but in this case, the object reveals a clear disc structure with medium to high inclination (see Table B.1). After inspection of the surface brightness profile, we detected a typical bulge + exponential disc distribution. The disc appears to be featureless, and the automatic break analysis does not reveal any significant breaks within the limiting radius.

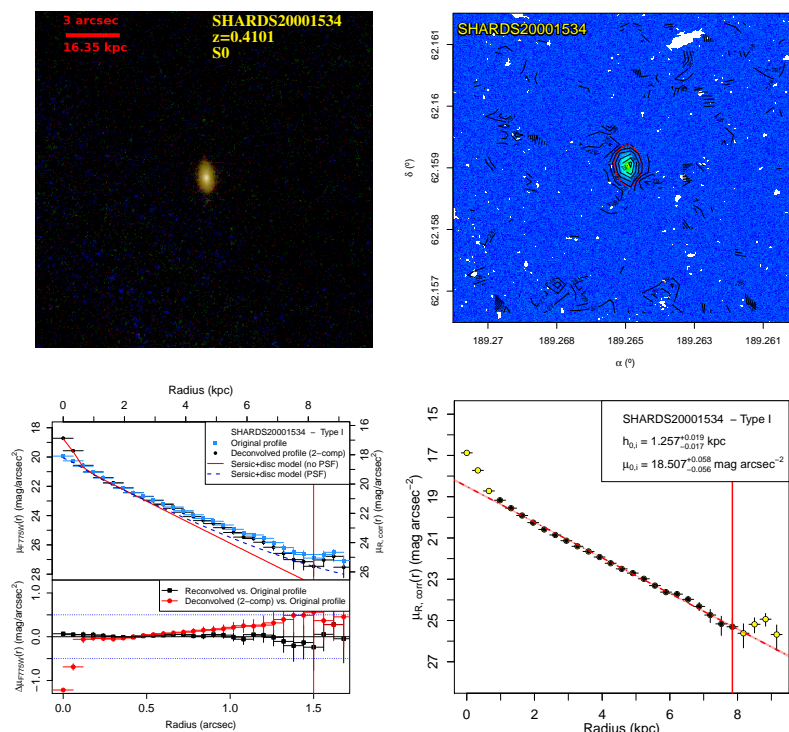


Fig. C.28. See caption of Fig. 1.

A&A 604, A119 (2017)

SHARDS20002147: small S0 galaxy with a Type-I disc and with very similar morphology to SHARDS20001051. It was flagged as an AGN source (see Sect. 2.8). The image presents some small isophotal irregularities, but they all are outside the fitting region. Masking was applied to two sources (to the N and SW of the main object). The surface brightness profile presents as typical of a bulge + exponential disc shape. The automatic break analysis reveals that, despite of the large uncertainties associated with the break parameters, the probability for this object of being compatible with a Type-I profile is $p = 0.022$, thus we classified it as Type I.

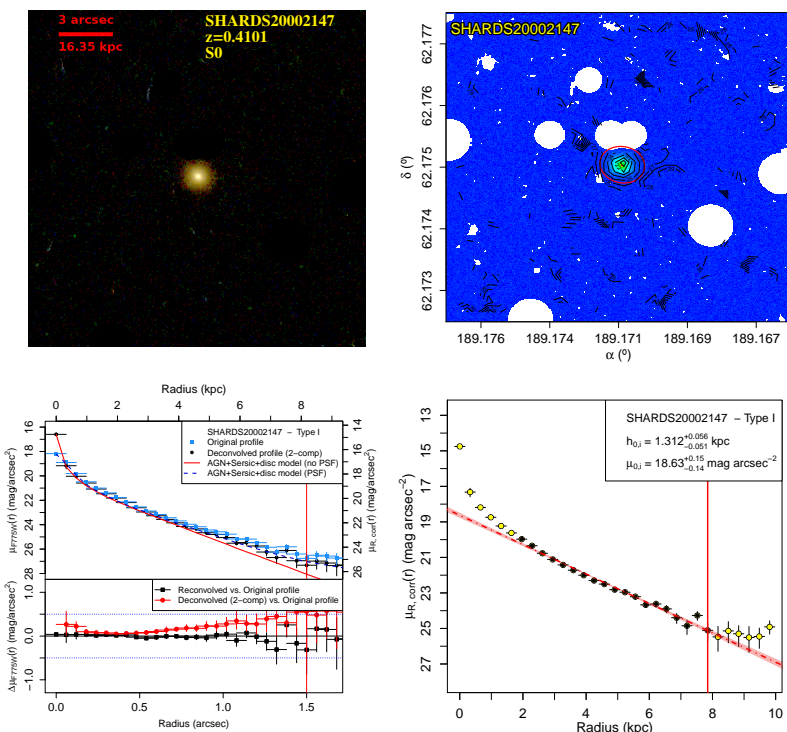


Fig. C.29. See caption of Fig. 1.

A. Borlaff et al.: Anti-truncated stellar profiles on S0 galaxies at $0.2 < z < 0.6$

SHARDS20002235: E/S0 galaxy of Type-I disc partially overlapped with a galaxy of similar apparent size. Extensive manual masking has been applied to this object in order to extract the surface brightness profile from the farthest regions of the companion. Inspection of the surface brightness profile reveals a typical bulge + exponential disc distribution. The disc appears to be featureless, and the automatic break analysis detects no significant breaks within the limiting radius.

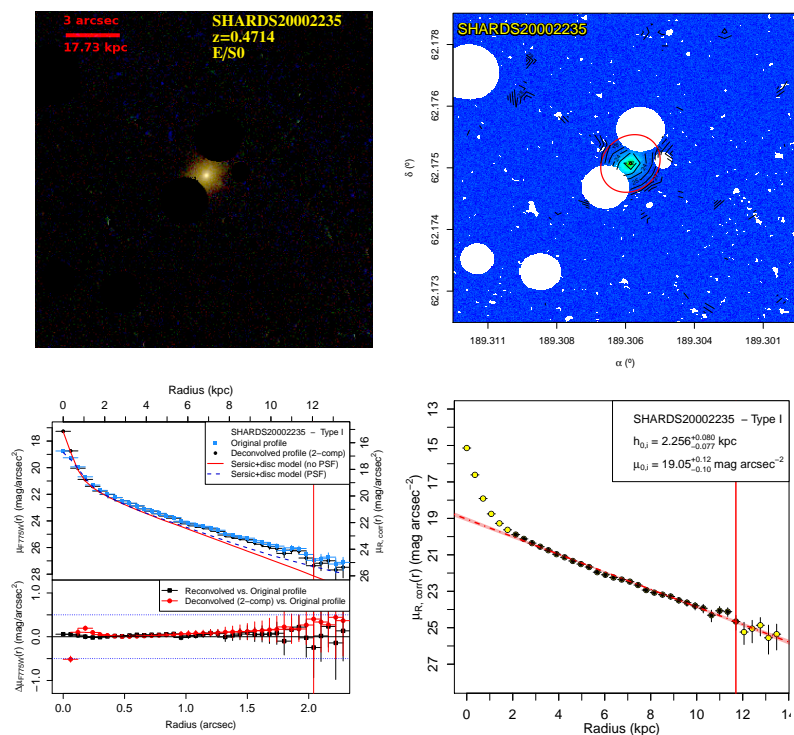


Fig. C.30. See caption of Fig. 1.

A&A 604, A119 (2017)

SHARDS20002550: E/S0 galaxy with a Type-I profile. The image required extensive masking due to the presence of a nearby saturated star. The masked area lies outside the final fitting region. It shows a clear bulge + exponential surface brightness profile. The automated break analysis revealed a noticeable change of profile in the transition zone between the bulge and the main disc, but we discarded it as it was too close to the centre, in order to avoid bulge contributions. (see Table B.1)

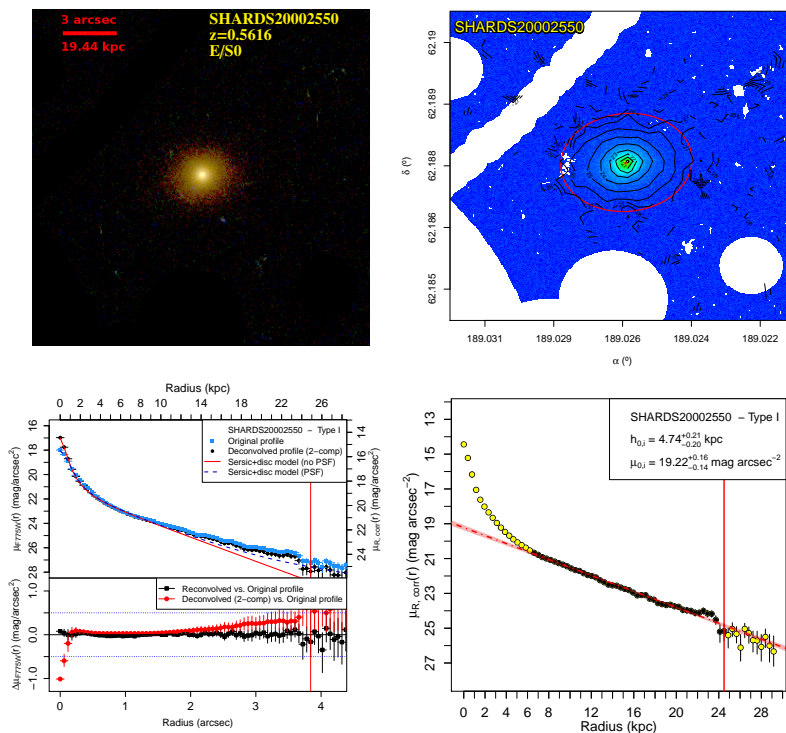


Fig. C.31. See caption of Fig. 1.

A119, page 58 of 71

Este documento incorpora firma electrónica, y es copia auténtica de un documento electrónico archivado por la ULL según la Ley 39/2015.
Su autenticidad puede ser contrastada en la siguiente dirección <https://sede.ull.es/validacion/>

Identificador del documento: 1630219

Código de verificación: NYPyuzSi

Fecha: 26/10/2018 14:33:01

Firmado por: ALEJANDRO SERRANO BORLAFF
 UNIVERSIDAD DE LA LAGUNA

Juan Esteban Beckman Abramson
 UNIVERSIDAD DE LA LAGUNA

MARIA DEL CARMEN ELICHE MORAL
 UNIVERSIDAD DE LA LAGUNA

JOAN FONT SERRA
 UNIVERSIDAD DE LA LAGUNA

26/10/2018 14:36:58

26/10/2018 15:46:09

26/10/2018 18:46:53

A. Borlaff et al.: Anti-truncated stellar profiles on S0 galaxies at $0.2 < z < 0.6$

SHARDS20002889: small S0 galaxy with Type-I profile. The original surface brightness profile appears to be almost bulgeless. It has a medium inclination and small apparent size. It has no nearby galaxies or field objects. The resolution is not enough to resolve any possible detail besides the disc itself. Automatic break analysis reveals no significant differences between any part of the disc.

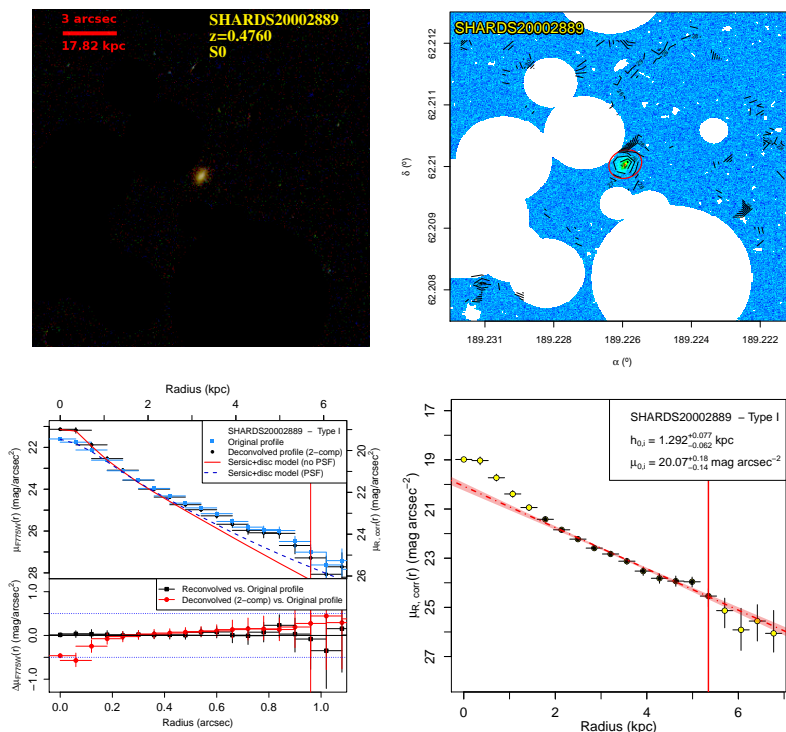


Fig. C.32. See caption of Fig. 1.

A&A 604, A119 (2017)

SHARDS20002935: S0 galaxy with a face-on orientation (see Table B.1). We classified it as Type-I profile despite the noticeable bump found in the outskirts that cannot be explained by PSF dispersed light. Multiple and extensive masking was required due to the presence of multiple field objects. The profile shows a simple bulge + exponential disc structure. The small excess of light at the outermost part of the galaxy is not compatible with an exponential component.

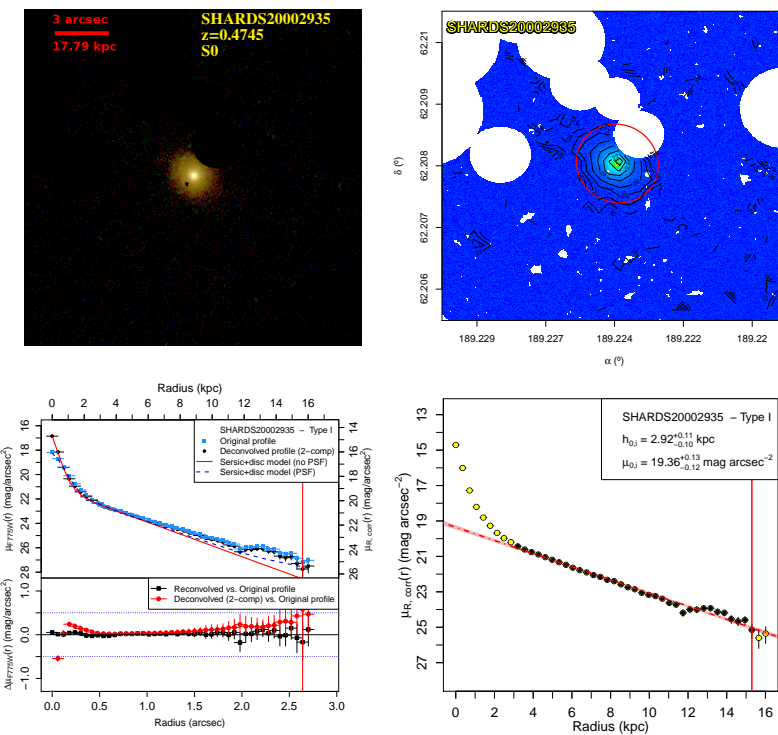


Fig. C.33. See caption of Fig. 1.

A119, page 60 of 71

Este documento incorpora firma electrónica, y es copia auténtica de un documento electrónico archivado por la ULL según la Ley 39/2015.
Su autenticidad puede ser contrastada en la siguiente dirección <https://sede.ull.es/validacion/>

Identificador del documento: 1630219

Código de verificación: NYPyuzSi

Fecha: 26/10/2018 14:33:01

Firmado por: ALEJANDRO SERRANO BORLAFF
 UNIVERSIDAD DE LA LAGUNA

Juan Esteban Beckman Abramson
 UNIVERSIDAD DE LA LAGUNA

MARIA DEL CARMEN ELICHE MORAL
 UNIVERSIDAD DE LA LAGUNA

JOAN FONT SERRA
 UNIVERSIDAD DE LA LAGUNA

26/10/2018 14:36:58

26/10/2018 15:46:09

26/10/2018 18:46:53

A. Borlaff et al.: Anti-truncated stellar profiles on S0 galaxies at $0.2 < z < 0.6$

SHARDS20002966: S0 galaxy with a Type-I profile. The object presents medium inclination (see Table B.1). The image did not require any masking inside the final fitting region. After inspection of the surface brightness profile, we found a typical bulge + exponential disc distribution. The disc appears to be featureless. The automatic break analysis reveals no significant breaks.

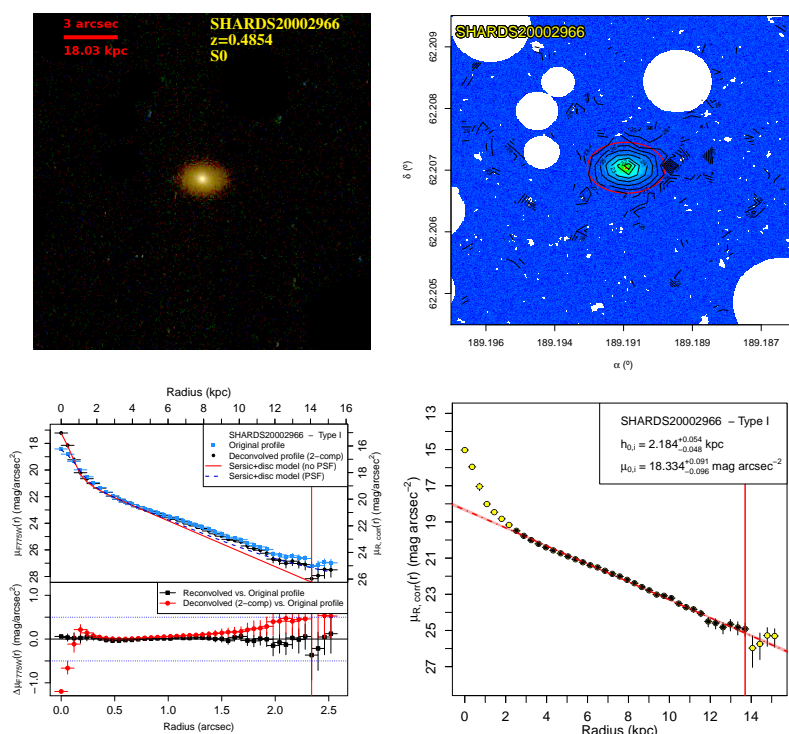


Fig. C.34. See caption of Fig. 1.

Este documento incorpora firma electrónica, y es copia auténtica de un documento electrónico archivado por la ULL según la Ley 39/2015.
Su autenticidad puede ser contrastada en la siguiente dirección <https://sede.ul.es/validacion/>

Identificador del documento: 1630219

Código de verificación: NYPyuzSi

Firmado por: ALEJANDRO SERRANO BORLAFF
 UNIVERSIDAD DE LA LAGUNA

Fecha: 26/10/2018 14:33:01

Juan Esteban Beckman Abramson
 UNIVERSIDAD DE LA LAGUNA

26/10/2018 14:36:58

MARIA DEL CARMEN ELICHE MORAL
 UNIVERSIDAD DE LA LAGUNA

26/10/2018 15:46:09

JOAN FONT SERRA
 UNIVERSIDAD DE LA LAGUNA

26/10/2018 18:46:53

A&A 604, A119 (2017)

SHARDS20002995: S0 galaxy with a Type-II profile. Manual masking was required for three nearby sources, one of them an apparent satellite in accretion. The smooth surface brightness profile free from spikes ensure us that the masking was enough and successful. The inner region was removed for the fit to avoid possible contamination from the bulge or an inner lens. The outer profile presents some irregularities at the outskirts ($\sim 13\text{--}15$ kpc). The break presents smooth and statistically significant PDDs.

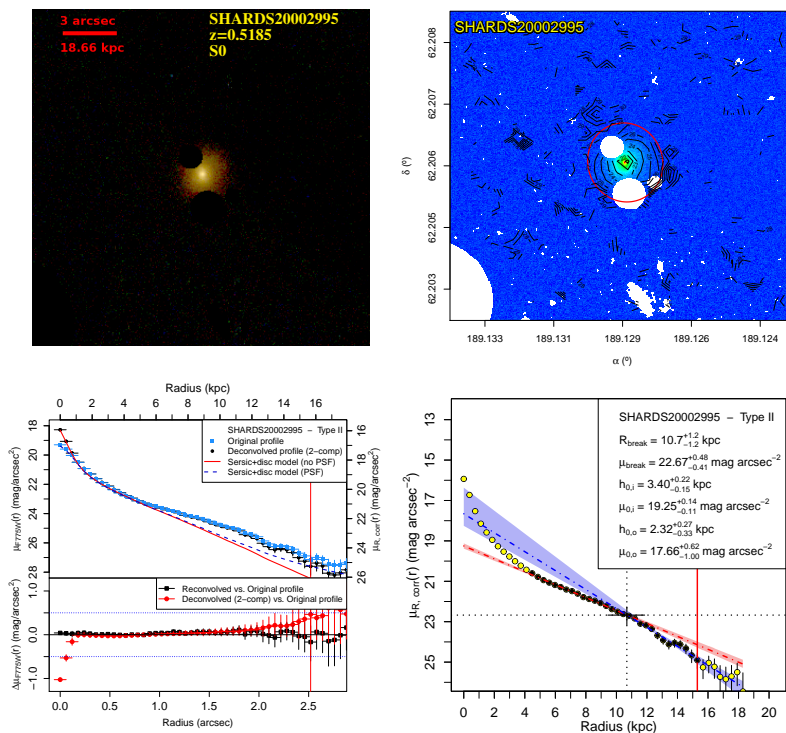


Fig. C.35. See caption of Fig. 1.

A. Borlaff et al.: Anti-truncated stellar profiles on S0 galaxies at $0.2 < z < 0.6$

SHARDS20003134: S0 galaxy with a Type-II profile. Manual masking was required to avoid the contamination by compact bright object located to the W. It was analysed by ISOFIT instead of ellipse due to its edge-on orientation (see Table B.1). The PDDs for h and μ_0 show two clearly separated peaks corresponding to the two profiles.

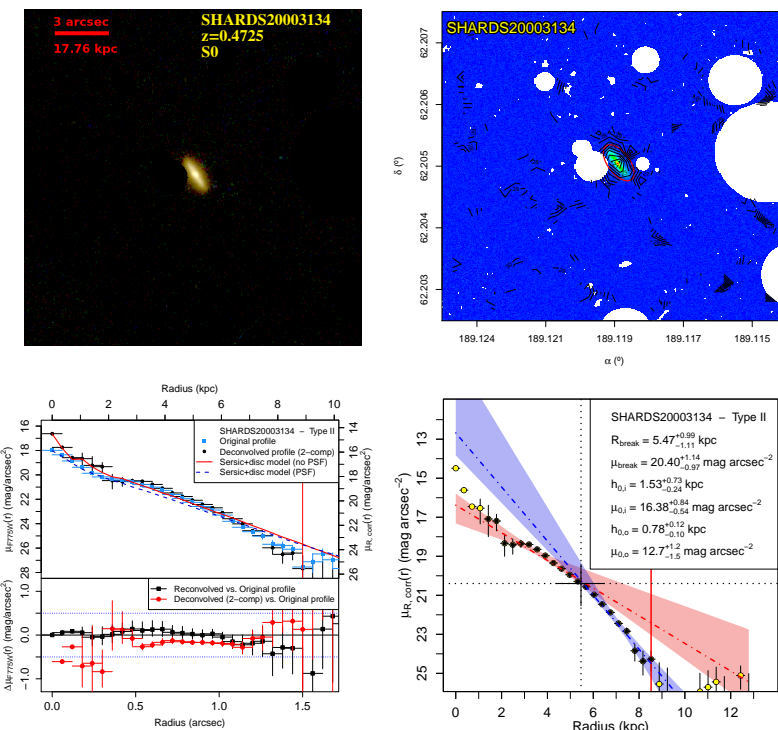


Fig. C.36. See caption of Fig. 1.

A&A 604, A119 (2017)

SHARDS20003210: S0 galaxy with a Type-III profile. The object presents a face-on orientation (see Table B.1). The profile reveal a clear bulge + double exponential structure. The PDDs for h and μ_0 show two clearly separated peaks corresponding to the two profiles.

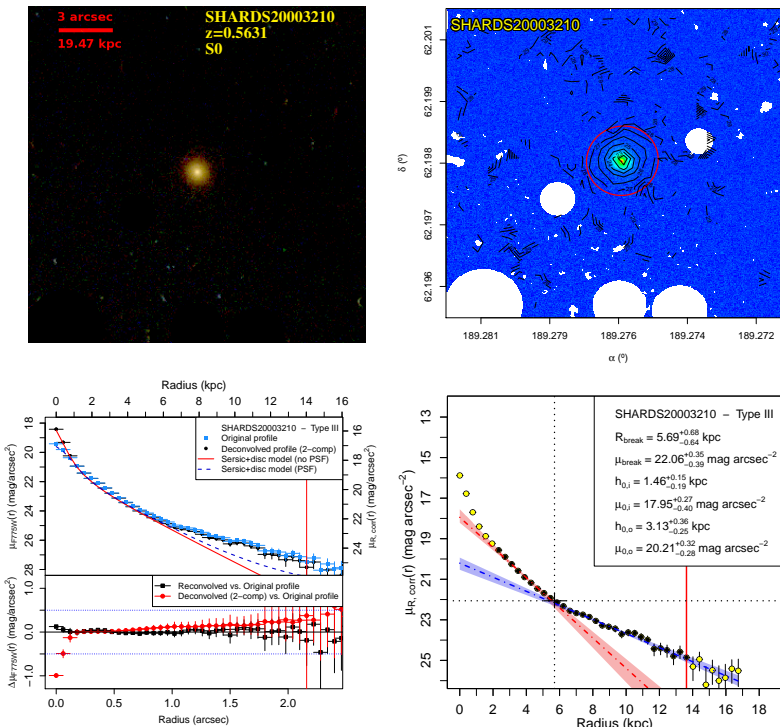


Fig. C.37. See caption of Fig. 1.

A. Borlaff et al.: Anti-truncated stellar profiles on S0 galaxies at $0.2 < z < 0.6$

SHARDS20003217: S0 galaxy with a Type-I profile (see Table B.1). The object presents a very low inclination, but shows a clear bulge + exponential structure. A small bump at $\sim 3-4$ kpc in the surface brightness profile originates double peaked PDDs when performing automated break analysis, but the p -values associated to this bump were negligible.

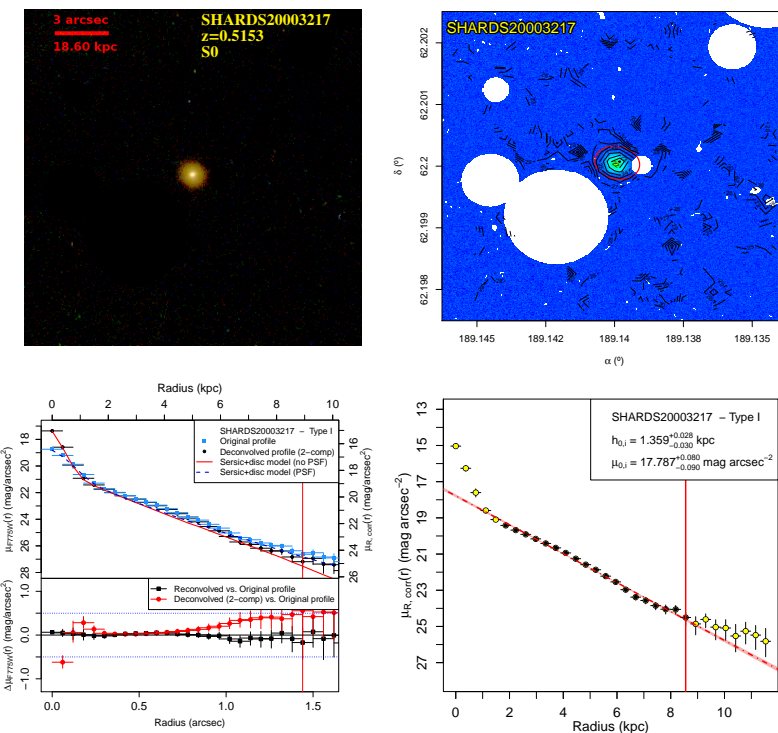


Fig. C.38. See caption of Fig. 1.

A&A 604, A119 (2017)

SHARDS20003377: S0 galaxy with a Type-I profile. It has a medium to high inclination (see Table B.1). It was flagged as an AGN source (see Sect. 2.8). The profile shows a simple bulge and exponential disc composition. The disc appears to be clear and featureless, with a small deviation from the exponential profile in the middle region ($\sim 4\text{--}6$ kpc). The automatic break analysis reveals no significant breaks.

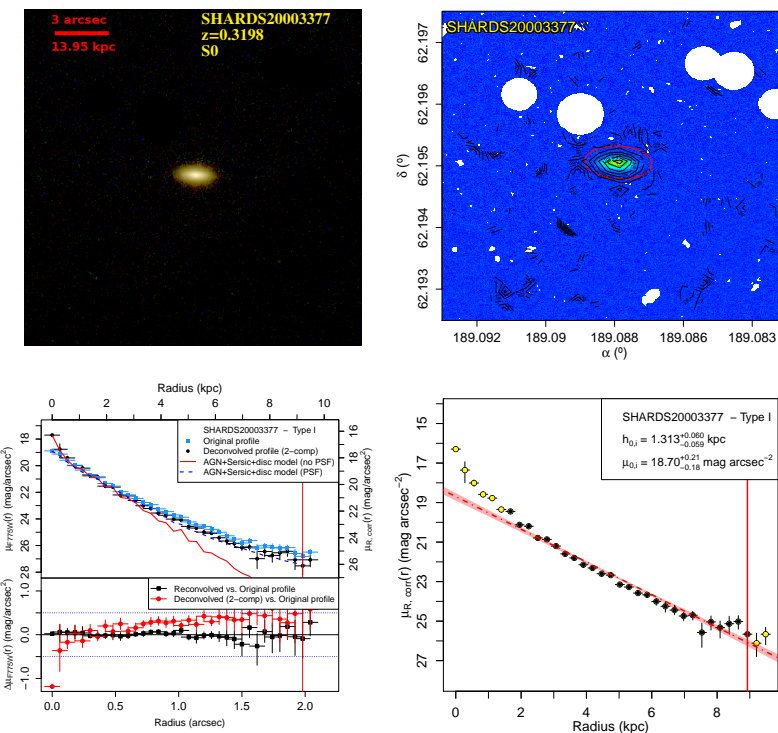


Fig. C.39. See caption of Fig. 1.

A. Borlaff et al.: Anti-truncated stellar profiles on S0 galaxies at $0.2 < z < 0.6$

SHARDS20003678: small E/S0 galaxy with a Type-I disc and very low inclination (see Table B.1). The profile shows a profile with a bulge + exponential disc structure. Due to the low resolution in this galaxy, the radial extension of the inner bulge is uncertain.

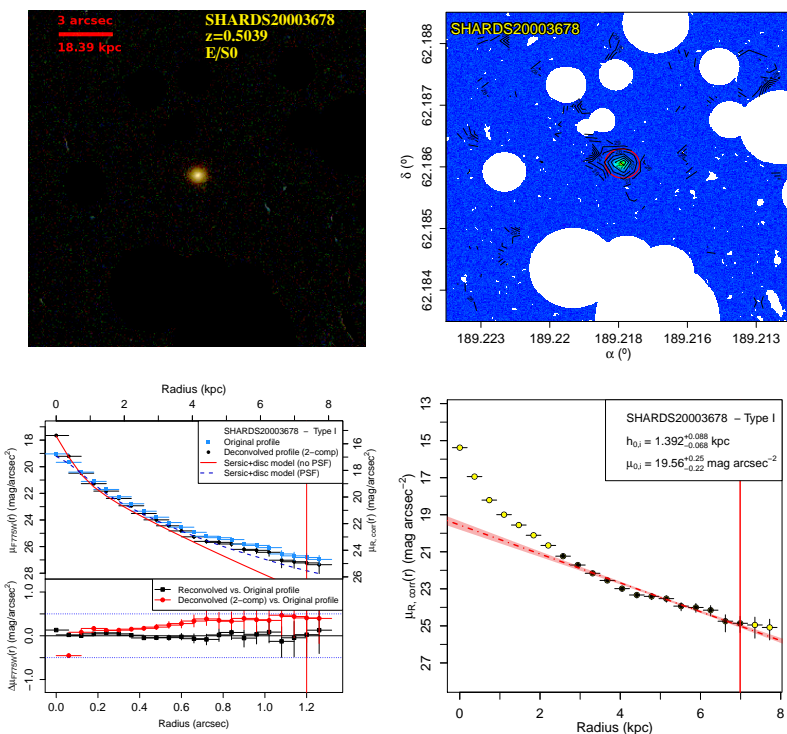


Fig. C.40. See caption of Fig. 1.

A&A 604, A119 (2017)

SHARDS20004359: S0 galaxy with a Type-I profile. The object presents low inclination (see Table B.1). Manual masking was applied to the image in many regions to avoid contamination from a tadpole irregular galaxy located to the N. The model greatly reduces residuals when adding an exponential profile to the free Sersic model, so we discarded the elliptical morphology for it. The profile generates too noisy PDDs to detect any statistically significant break. The visual analysis of the isophotes reveals a distortion between $\mu_{F775W} \sim 25\text{--}26 \text{ mag arcsec}^{-2}$, that coincides with a step observed in the surface brightness profile at $\sim 14\text{--}16 \text{ kpc}$. Finally the object was classified as a Type-I disc.

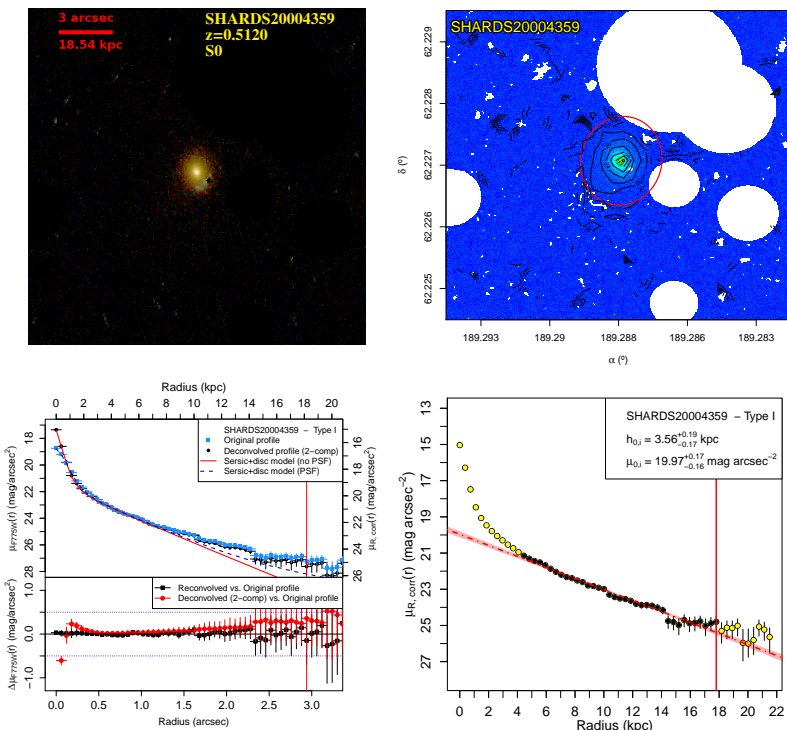


Fig. C.41. See caption of Fig. 1.

A119, page 68 of 71

Este documento incorpora firma electrónica, y es copia auténtica de un documento electrónico archivado por la ULL según la Ley 39/2015.
Su autenticidad puede ser contrastada en la siguiente dirección <https://sede.ull.es/validacion/>

Identificador del documento: 1630219

Código de verificación: NYPyuzSi

Firmado por: ALEJANDRO SERRANO BORLAFF
 UNIVERSIDAD DE LA LAGUNA

Fecha: 26/10/2018 14:33:01

Juan Esteban Beckman Abramson
 UNIVERSIDAD DE LA LAGUNA

26/10/2018 14:36:58

MARIA DEL CARMEN ELICHE MORAL
 UNIVERSIDAD DE LA LAGUNA

26/10/2018 15:46:09

JOAN FONT SERRA
 UNIVERSIDAD DE LA LAGUNA

26/10/2018 18:46:53

A. Borlaff et al.: Anti-truncated stellar profiles on S0 galaxies at $0.2 < z < 0.6$

SHARDS20004420: E/S0 galaxy with a Type-I profile. The object presents low inclination (see Table B.1). Manual masking was applied to several small field objects to avoid contamination. The innermost part of the galaxy present higher ellipticity than the outer parts when performing visual inspection of the image. The model greatly improves when adding an exponential disc to a free Sersic profile, so we classified it as an E/S0 instead of an elliptical. The PDDs of h and μ_0 present a two peaked distribution, although no significant no significant break is detected. We note the small spike at ~ 14 kpc.

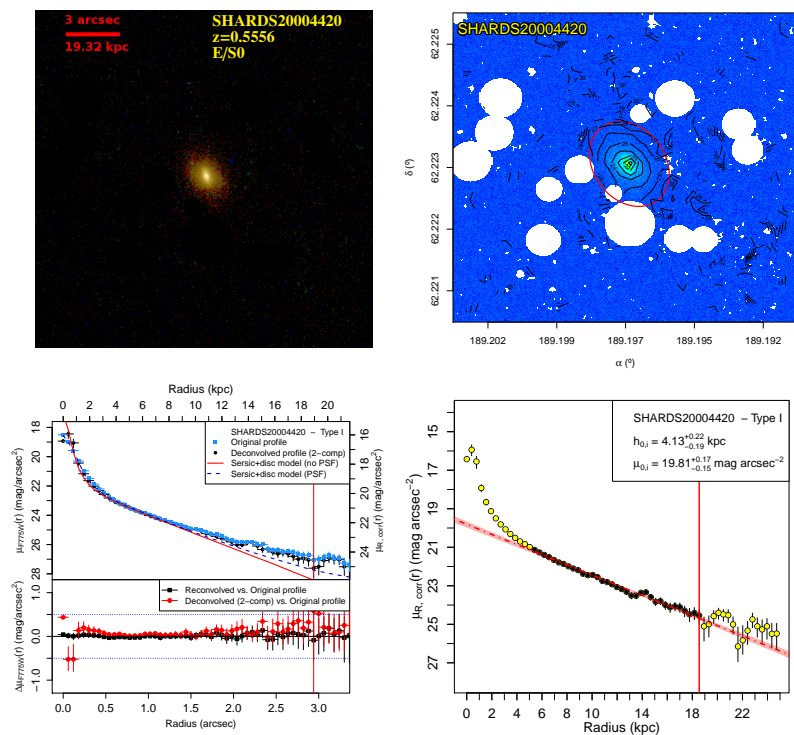


Fig. C.42. See caption of Fig. 1.

A&A 604, A119 (2017)

SHARDS20004440: E/S0 galaxy with a Type-I profile. It was flagged as an AGN source (see Sect. 2.8). It has a low inclination (see Table B.1). Multiple and extensive masking was applied to the outer parts of the galaxy, where tiny spot-like objects were detected through smoothing and re-masking. The excess of light detected before PSF correction appears to be caused by the dispersed light from the centre. The automatic break analysis reveals no significant breaks.

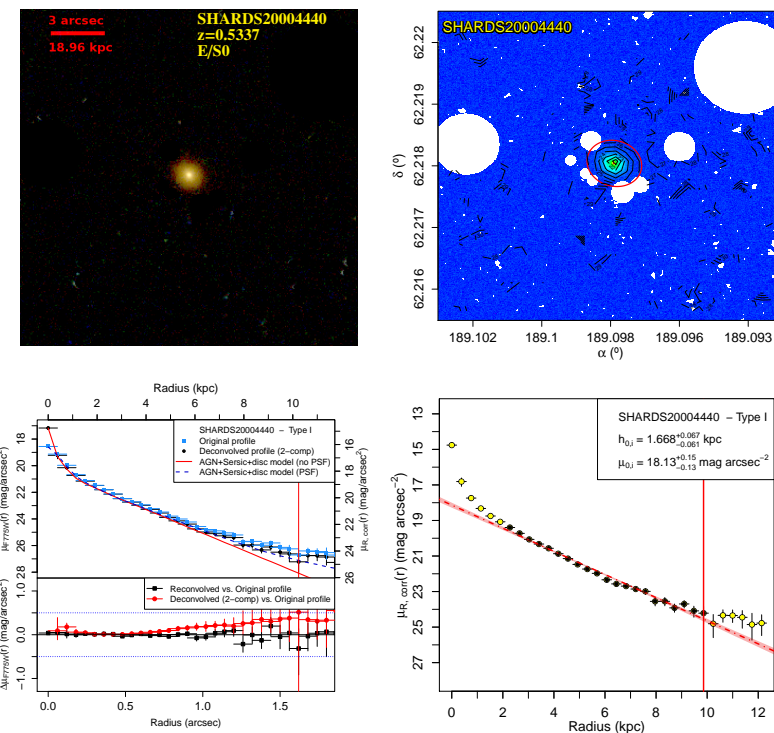


Fig. C.43. See caption of Fig. 1.

A. Borlaff et al.: Anti-truncated stellar profiles on S0 galaxies at $0.2 < z < 0.6$

SHARDS20011817: small S0 galaxy with a Type-I profile. The orientation is edge-on (see Table B.1). No masking was needed into the fitting region. The surface brightness profile presents a small bulge + exponential disc distribution. The disc appears to be clear and featureless. Elbow reveals no any significant breaks.

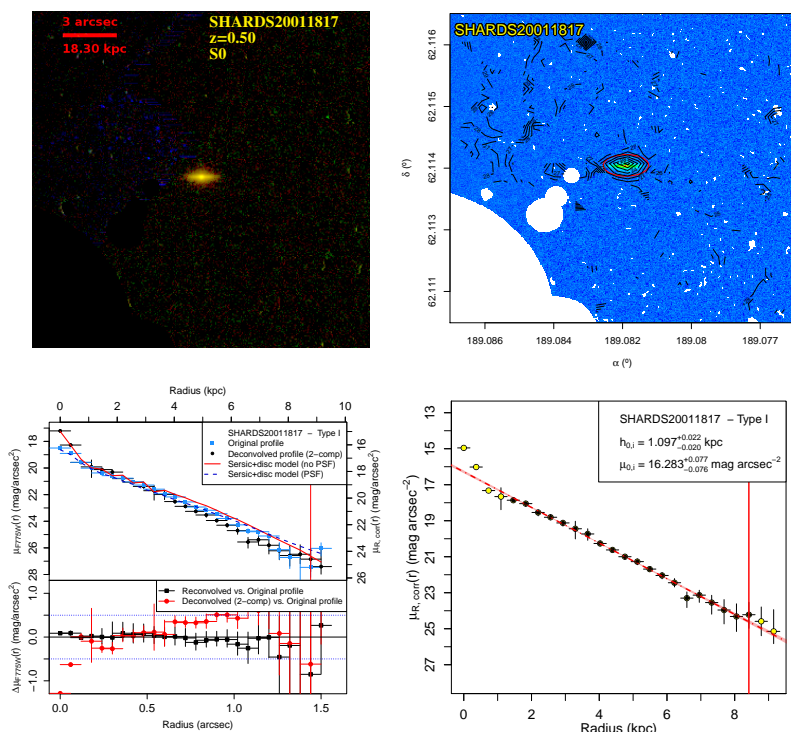


Fig. C.44. See caption of Fig. 1.

Publications during this thesis:

- Beckman, J. E., Font, J., Borlaff, A., & García-Lorenzo, B. 2018, ApJ, 854, 182
- Borlaff, A., Eliche-Moral, M. C., Beckman, J., & Font, J. 2016, A&A, 591, L7
- Borlaff, A., Eliche-Moral, M. C., Beckman, J. E., et al. 2017, A&A, 604, A119
- . 2018a, A&A, 615, A26
- Borlaff, A., Trujillo, I., Román, J., et al. 2018b, ArXiv e-prints, arXiv:1810.00002
- Camps-Fariña, A., Beckman, J. E., Font, J., et al. 2016, MNRAS, 461, L87
- Eliche-Moral, M. C., Borlaff, A., Beckman, J. E., & Gutiérrez, L. 2015, A&A, 580, A33
- Font, J., Beckman, J. E., Martínez-Valpuesta, I., et al. 2017, ApJ, 835, 279
- Lumbreras-Calle, A., Muñoz-Tuñón, C., Méndez-Abreu, J., et al. 2018, ArXiv e-prints, arXiv:1803.08045
- Querejeta, M., Eliche-Moral, M. C., Tapia, T., et al. 2015a, A&A, 573, A78
- . 2015b, A&A, 579, L2
- San Roman, I., Cenarro, A. J., Díaz-García, L. A., et al. 2018, A&A, 609, A20
- Tapia, T., Eliche-Moral, M. C., Aceves, H., et al. 2017, A&A, 604, A105
- Trujillo, I., Beasley, M. A., Borlaff, A., et al. 2018, ArXiv e-prints, arXiv:1806.10141
- Zaragoza-Cardiel, J., Beckman, J., Font, J., et al. 2017, MNRAS, 465, 3461

200

Este documento incorpora firma electrónica, y es copia auténtica de un documento electrónico archivado por la ULL según la Ley 39/2015.
Su autenticidad puede ser contrastada en la siguiente dirección <https://sede.ull.es/validacion/>

Identificador del documento: 1630219 Código de verificación: NYPyuzSi

Firmado por: ALEJANDRO SERRANO BORLAFF UNIVERSIDAD DE LA LAGUNA	Fecha: 26/10/2018 14:33:01
Juan Esteban Beckman Abramson UNIVERSIDAD DE LA LAGUNA	26/10/2018 14:36:58
MARIA DEL CARMEN ELICHE MORAL UNIVERSIDAD DE LA LAGUNA	26/10/2018 15:46:09
JOAN FONT SERRA UNIVERSIDAD DE LA LAGUNA	26/10/2018 18:46:53

Proceedings published during this thesis:

Beckman, J., Borlaff, A., Eliche-Moral, M. C., Font, J., & Erwin, P. 2017, in IAU Symposium, Vol. 321, Formation and Evolution of Galaxy Outskirts, ed. A. Gil de Paz, J. H. Knapen, & J. C. Lee, 190–192

Borlaff, A., Eliche-Moral, M. C., Beckman, J., & Font, J. 2017a, in IAU Symposium, Vol. 321, Formation and Evolution of Galaxy Outskirts, ed. A. Gil de Paz, J. H. Knapen, & J. C. Lee, 272–272

Borlaff, A., Eliche-Moral, M. C., Beckman, J., Pérez-González, P. G., & Font, J. 2017b, in IAU Symposium, Vol. 321, Formation and Evolution of Galaxy Outskirts, ed. A. Gil de Paz, J. H. Knapen, & J. C. Lee, 280–280

Eliche-Moral, C., Serrano-Borlaff, A., Beckman, J. E., & Gutierrez, L. 2015, IAU General Assembly, 22, 2253634

Querejeta, M., Eliche-Moral, M., Tapia, T., et al. 2015, Galaxies, 3, 202

Querejeta, M., Eliche-Moral, M. C., Tapia, T., et al. 2017, in IAU Symposium, Vol. 321, Formation and Evolution of Galaxy Outskirts, ed. A. Gil de Paz, J. H. Knapen, & J. C. Lee, 114–116

Tapia, T., Eliche-Moral, M. C., Querejeta, M., et al. 2015, IAU General Assembly, 22, 2253560

201

Este documento incorpora firma electrónica, y es copia auténtica de un documento electrónico archivado por la ULL según la Ley 39/2015.
Su autenticidad puede ser contrastada en la siguiente dirección <https://sede.ull.es/validacion/>

Identificador del documento: 1630219 Código de verificación: NYPyuzSi

Firmado por: ALEJANDRO SERRANO BORLAFF UNIVERSIDAD DE LA LAGUNA	Fecha: 26/10/2018 14:33:01
Juan Esteban Beckman Abramson UNIVERSIDAD DE LA LAGUNA	26/10/2018 14:36:58
MARIA DEL CARMEN ELICHE MORAL UNIVERSIDAD DE LA LAGUNA	26/10/2018 15:46:09
JOAN FONT SERRA UNIVERSIDAD DE LA LAGUNA	26/10/2018 18:46:53

Agradecimientos

Sin ninguna duda, la parte más difícil de esta tesis es intentar agradecer en una página a todas las personas que la han hecho posible. En primer lugar, quiero agradecer a mi familia, que me han educado para ser siempre curioso con la naturaleza y el mundo que nos rodea. A mi padre por grabarme en vídeo *El mundo de Beakman* cuando era pequeño. A mi madre por apoyarme todos estos años y hacer de los problemas grandes pequeñas listas a resolver. A mi hermano por enseñarme a hacer todas esas locuras que sin duda han acabado haciendo de mi un científico. Espero que el pequeño Ian estudie algo que le guste tanto como a mí lo que he estado haciendo estos años.

A Carmen, gracias por darme una oportunidad y guiarme desde que estaba en la carrera para convertirme en un científico. Solo ahora consigo empezar a darme cuenta de todos los sacrificios que te costó aquello. Espero poder ser algún día tan buen maestro como lo has sido tu todos estos años.

A John, gracias por ser el ejemplo de científico en el que me quiero convertir. En los momentos de duda, cuando no sé cuál es el siguiente paso a dar, siempre acabo pensando en las miles de aventuras que has tenido y espero tener una vida así. Cuando sea mayor quiero ser como tú.

A Nacho, por ser el incansable astrónomo que me ha dedicado tanto tiempo y del que he aprendido tanto. Tienes un equipo de alumnos espectacular y espero que hagamos muchos más trabajos juntos.

Cuando empecé la tesis en el Instituto de Astrofísica de Canarias, nunca me imaginé que acabaría teniendo una pequeña gran familia por aquí. La hora del almuerzo con vosotros es lo más parecido al "recreo" que he tenido desde el colegio. ¿Es toda una experiencia hacer una tesis, verdad? Eso es lo que significa ser doctorando. En la cafetería del IAC hemos visto cosas que no creeríais. Refírse a carcajadas que se oían mas allá del corralón. Hemos visto rayos microondas calentar tappers de arroz con pollo mas grandes que un *coconut crab*. Todos esos momentos son parte de nosotros y no se van a perder nunca. Ahora nos toca a todos repartirnos por el mundo, pero eso solo significa que siempre que aterraremos tendremos a un amigo cerca. Ahora toca la mejor parte de la tesis: ¡ir a de turista a veros a todos!

Y por último a Ro, mi compañera y mi constante. Gracias por haber estado a mi lado todo este tiempo. Pero no nos vamos a relajar porque ahora vienen nuevas aventuras, así que prepárate. Ahora te toca a ti, pero no tengo ninguna duda de que vas a ser una gran científica. Esta tesis te la dedico a ti, mi estrellita pequeña – pero firme – que se dobla antes que partirse.

Firmado por: ALEJANDRO SERRANO BORLAFF UNIVERSIDAD DE LA LAGUNA	Fecha: 26/10/2018 14:33:01
Juan Esteban Beckman Abramson UNIVERSIDAD DE LA LAGUNA	26/10/2018 14:36:58
MARIA DEL CARMEN ELICHE MORAL UNIVERSIDAD DE LA LAGUNA	26/10/2018 15:46:09
JOAN FONT SERRA UNIVERSIDAD DE LA LAGUNA	26/10/2018 18:46:53